Plasma Self-organized Pattern and the Coupling Processes at Plasma-liquid Interface

by

Zimu Yang

A dissertation submitted in partial fulfillment
of the requirements for the degree of
Doctor of Philosophy
(Nuclear Engineering and Radiological Sciences)
in the University of Michigan
2024

Doctoral Committee:

Professor John Edison Foster, Chair
Professor Mark Kushner
Professor Xiaodong Sun
Doctor Zhehui Wang

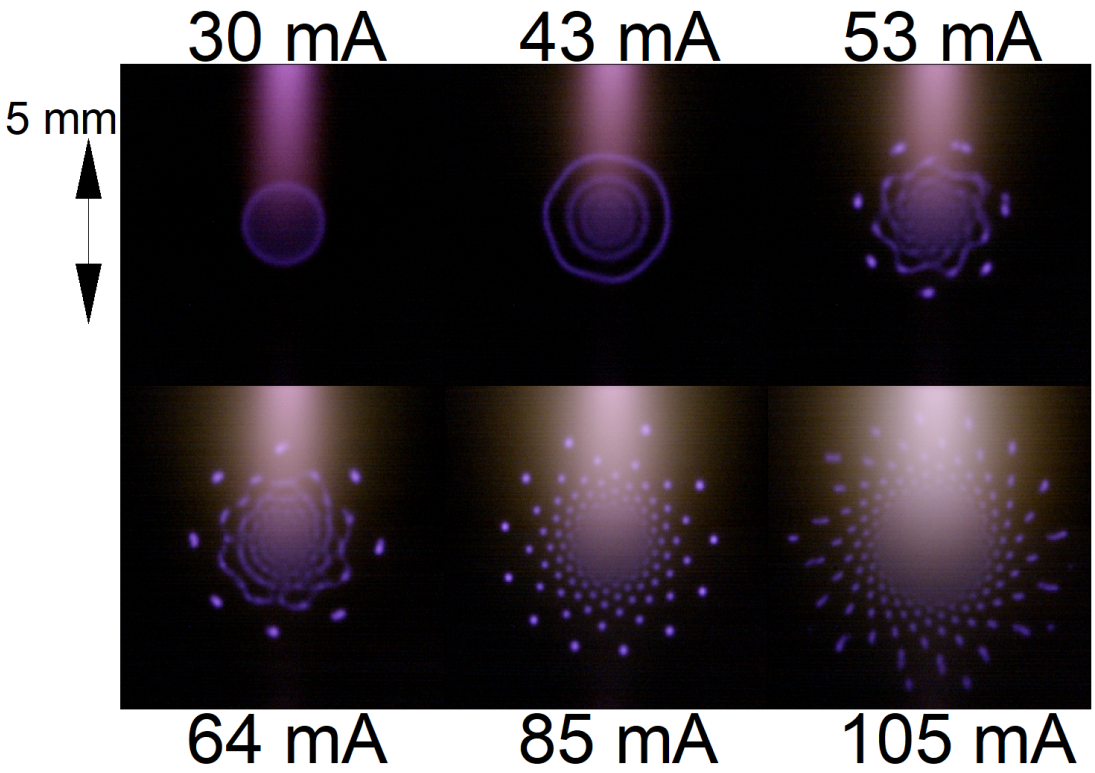
30 mA
43 mA
53 mA
5 mm
64 mA
85 mA
105 mA

Zimu Yang
zimuy@umich.edu
ORCID iD: 0000-0003-4043-8413

ACKNOWLEDGEMENTS

Since I started to observe and learn the routine and development of society, I have always wondered what is the motivation behind the deeds, good or bad. Various reasons could be found in individuals, but what is the macroscopic initiative of humankind or other sentient life? In physical nature, physicist Erwin Schrödinger suggests that life functions as a dissipative system that interacts with the environment to maintain a low entropy. This however means a finite system does not support life to expand indefinitely while our desire and imagination have no limits. For a long time, it inflicts confusion and desperation in my mind. The harsh conflict between the nature of life and deficient resources caused many losses throughout history, yet we are still going down this road with progress and uncertainty. Research, on the other hand, does not only serve the need to liberate ourselves from restriction but also satisfy the curiosity to understand nature. The information we receive and change justifies our existence and fulfills humanity. For myself, this work brings me an invaluable chance to observe and learn from a fascinating phenomenon that is part of exquisite nature. The path is foggy while the journey is exceptional and pure. I would consider this work an appreciation and acknowledgment of Mother Nature's greatness.

It is my greatest honor and privilege to have Professor John Foster's mentorship and friendship during the beginning period of my research career. As my advisor, his passion, creativity, wisdom, and curiosity in science enthuse me in my graduate program and inspire motivation for my future career. I sincerely appreciate his generosity and kindness for including me in his research group when I was a master's student knowing little about plasma science. During my doctoral program, he always cared about my progress and mentored me to advance. I could not achieve my current state if it were not for him. From my perspective, he is also a nice friend who would discuss many subjects aside from work and provide help to others in need. I can feel his awareness and dedication to the responsibility and morality towards society and humanity which would be the aspiration in his career. I admire and respect his spirit and pledge to follow his example in my future career.

Next, I would like to express my sincere gratitude to my dissertation committee, Prof. Mark Kushner, Prof. Xiaodong Sun, and Dr. Zhehui Wang for the suggestions and time they provide to refine my thesis. The class on plasma chemistry and plasma surface interactions taught by Prof. Kushner enlightened me on the mechanism of kinetic theory in plasma and helped me shape

many ideas in this thesis. I also enjoy very much from his teaching and enthusiasm for research. Prof. Sun is a distinguished scientist in thermohydraulics who is devoted to developing the corresponding research in the Nuclear Engineering & Radiological Sciences department and raising its impact. The knowledge and suggestions he shares on the dynamics of liquid in this work are instrumental. Last but not least, I want to express my special thank to Dr. Wang from Los Alamos National Laboratory for his help in the recognition of the jet droplets mechanism in plasma-liquid interactions. He is passionate and ambitious in the high-speed and innovative imaging and measurement systems in many disciplines. The chapter on jet droplets would not be done without his constructive ideas and the critical instruments he lent to us.

I am very grateful that Prof. María C. García from the University of Córdoba taught me a lot about spectroscopy and data analysis during her visit. She directly demonstrated and instructed the spectroscopy experiments and instigated the idea of implementing the spatially resolved optical emission spectroscopy measurement in this work. Dr. Shurik Yatom from Princeton Plasma Physics Laboratory helped me extensively with the laser photodetachment experiment. It was a great honor and a pleasant memory for me to work with him and many other profound scientists at PPPL.

Many financial support from funding and fellowships helped me through the doctoral program. This includes funding from the U.S. Department of Energy (DOE), Office of Fusion Energy Sciences under Grant No. DE-SC0018058, and National Science Foundation (NSF) ECosystem for Leading Innovation in Plasma Science and Engineering (ECLIPSE) program Award No. 2206039. This work is also supported by the U.S. Department of Energy under Contract No. 89233218CNA000001 in collaboration with Dr. Zhehui Wang from Los Alamos National Laboratory. I also want to acknowledge the collaboration from the Princeton Collaborative Research Facility (PCRF), which is supported by the U.S. Department of Energy (DOE) under Contract No. DE-AC02-09CH11466. During the 2020 Fall semester, the Don Kania and Renee Dubois Fellowship founded my tuition and financial aid for which I want to express my thankfulness.

I also want to sincerely thank my colleagues in the Plasma Science and Technology Laboratory at the University of Michigan. It is a unique and precious experience to work with them and their generous help and relaxing atmosphere always relieve my tiredness and loneliness. Numerous discussions and sharing of insights help me improve this thesis. They are the best friends and colleagues I could ever ask for.

The success that I achieved during my doctoral program also relies on the fundamental support of the University of Michigan and its Nuclear Engineering & Radiological Sciences department. The inclusive culture, dynamic atmosphere, and well-organized institution make it a wonderful community to work and live in. I would like to thank everyone who committed themselves to the development of this flourishing community.

Finally, I want to give my wholehearted gratitude to my parents for their selfless support in the development of my well-being. They extensively provide financial and emotional support during my study in the U.S. while they bear the loneliness of my absence. They prioritize my dream and happiness over theirs and their love has made me who I am today. Every good thing I have comes from them.

Zimu Yang
January 2024

TABLE OF CONTENTS

LIST OF FIGURES

FIGURE

LIST OF TABLES

TABLE

LIST OF ACRONYMS

I-V current–voltage

SOP self-organized pattern

OES optical emission spectroscopy

PIV particle imaging velocimetry

EEDF electron energy distribution function

LIST OF SYMBOLS

c	Speed of light in vacuum	299792458 $\mathrm{m/s}$
t	Time	s
g	Standard gravity	9.8 $\mathrm{m/s^2}$
$\mathrm{k_B}$	Boltzmann constant	$1.380649 \times 10^{-23}\mathrm{J/K}$
h	Planck constant	$6.62607015 \times 10^{-34}\mathrm{J/Hz}$
p	Pressure	Pa
T_e	Electron temperature	eV
T_i	Ion temperature	eV
T_g	Gas temperature	K
n_e	Electron density	$\mathrm{cm^{-3}}$
n_-	Negative ion density	$\mathrm{cm^{-3}}$
N	Neutral gas density	$\mathrm{cm^{-3}}$
R	Radius	$\mathrm{s^{-1}}$
γ	Surface tension	$\mathrm{N/m}$
σ	Cross section of interaction	$\mathrm{m^2}$
ν	Collision frequency	$\mathrm{s^{-1}}$
ρ	Density of matter	$\mathrm{kg/m^3}$

ABSTRACT

It is known that under certain conditions, the DC atmospheric pressure plasma attachment at the liquid surface can self-organize both spatially and temporally into coherent and complex patterns, called self-organized pattern (SOP). The mechanism of SOP formation remains poorly understood. Such SOP is also observed in DC glows with metal anodes as well, taking the form of organized arrays of dot-like attachments. However, the liquid anode SOP is typically more complex. SOP formation is also subject to more complicated processes including liquid phase evaporation, fluid dynamics, sophisticated chemical reactions, species interaction, and local sheath electric field. In the community of plasma-liquid interactions, a conclusive understanding of many of these processes is still elusive due to their nonlinear nature and limited by currently available diagnostics methods. On the other hand, one can assert that the patterns are a consequence of dynamical coupling and feedback among the aforementioned processes. By unfolding this coupling and understanding the feedback pathways it may be possible to elucidate the nature of pattern formation and dynamics.

In this work, multiple diagnostics were introduced to investigate the coupling processes in an atmospheric pressure DC glow discharge and plasma-liquid interface. The current–voltage (I-V) characteristics of the discharge and the corresponding shape and surface area of the self-organized pattern (SOP) were examined to correlate the changes in bulk plasma discharge properties with pattern dynamics. Various pattern morphology and the associated operating conditions necessary to realize the dynamic SOP were documented and it was found that both the oxygen entrainment and liquid properties had the most significant effect on the pattern dynamics. Specifically, a larger discharge gap or lower inert gas flow support more complex SOP dynamics and liquid conductivity was found to heavily affect the current density and attachment surface area of SOP. Schlieren imaging and control of ambient oxygen level in the air reveal that oxygen is critical for the establishment of a pattern.

The importance of electronegative gas, including species such as oxygen, is then further examined through the examination of the negative ion hypothesis by laser photodetachment. Because the discharge operates in an ambient atmosphere, gases from this atmosphere can have a significant impact on gas-phase chemistry and inelastic processes taking place in the actual plasma column driven by heat and mass transfer. A gas-phase glow discharge strongly depends on gas-phase

chemistry, heat, and mass transfer. By decreasing ambient oxygen concentration in a purge box, the SOP became featureless when the oxygen volume fraction dropped below $\approx 7\%$. A qualitative investigation of the gas density change by Schlieren imaging showed that discharge gap and inert flow rate strongly shape the convection boundary and thus the rate of air entrainment. In the literature, there is significant speculation that negative ions are necessary for pattern formation. It was found in this work that the mere presence of negative ions was not a sufficient condition for the appearance of SOP. Here by using detachment spectroscopy, negative ions in the discharge were detached by laser and the SOP showed no change implying that negative ions are not the cause of pattern dynamics.

The coupling between the gas phase and plasma-liquid interface was further investigated by spatially resolved optical emission spectroscopy (OES). The emission map of major species in the plasma is obtained by scanning the plasma with a focusing lens and an imaging spectrometer. Gas temperatures and electron densities are estimated from the rotational temperature of nitrogen second positive system $\mathrm{N}_2(C-B)$ and Stark broadening of H_β line, respectively. The result of the gas temperature distribution near the liquid anode had a steep gradient which is one of the important cooling mechanisms. The corresponding change in temperature profiles is more sensitive to the gas phase heating than the variation of liquid conditions. The radial profile of electron density has a profound coupling with excited species including $\mathrm{H}(4d)$ and $\mathrm{He}(3d)$ whose productions are heavily dependent on the energetic electrons.

Next, the thermodynamic and hydrodynamic processes at the plasma-liquid interface were examined via particle image velocimetry. Substantial convective flow at the plane vertical to the plasma-liquid interface was observed under SOP and driven by plasma gas heating and water evaporation at the interface. Interestingly, convection parallel to the interface is also observed and induces an unstable convective flow at a high electrical current where dynamic SOP is formed. It is assumed that this shear flow is either due to an anode sheath electric field or Marangoni flow (fluid motion due to surface tension gradient).

Last, a fast, but non-trivial mass transport process at the plasma-liquid interface was observed: droplet generation was investigated via high-speed imaging cameras and OES. Unlike the droplets generated from the Taylor cone on the liquid cathode, the droplet generation from the liquid anode was observed due to gas bubbles bursting at the interface. Although it is not inherently a plasma process, the driving forces are the discharge gas heating. Additionally, these droplets can enhance the mass transport of liquid-phase species toward the gas phase. This was confirmed by OES that droplets' emissions are from salt particles in the electrolyte and excited OH radicals from the water molecule dissociation. These findings substantiate a new approach to the mass transfer from the liquid and control of discharge by dispersing plasma-activate liquid into the gas phase and chemically and ionically enriching the plasma–liquid interaction.

From the aforementioned diagnostics, the couplings of pattern dynamics with gas phase operation, heat, and chemical dynamics were examined and found to provide useful insights into the SOP mechanism. In addition, this work, by using diagnostics, elucidated the complex coupling of the liquid phase to the gas phase driving discharge. At its core, the SOP problem is a manifestation of an interfacial process driven far from equilibrium–nonequilibrium thermodynamics. It is hoped that the data acquired by the suite of diagnostics in this thesis not only facilitates the understanding of SOP formation but also provides modelers with the parameters necessary to model this very complex system.

CHAPTER 1

Introduction

1.1 Non-Thermal Atmospheric Pressure Plasma

Plasma, distinct from solid, liquid, and gas, is colloquially considered the fourth fundamental state of matter. But in general, there is no distinct phase transition between for example a hot gaseous state and a plasma. Nevertheless, the physical properties of the plasma state are distinctly different from common states of matter. The name plasma was first used by physicist Irving Langmuir [1] in direct analogy with blood plasma. Plasma can be described as a cloud of ions and electrons with or without neutral particles. Counterintuitively, it is the most abundant form of visible ordinary matter in the universe, and vastly exists in stars and the intergalactic medium [2]. Yet the plasma occurrence in Earth's natural environment is less energetic than stars', as observed in lightning, aurora, and the ionosphere. Since plasma comprises energetic particles that respond to electromagnetic fields and participate in sophisticated interactions, many technologies exploit such control allowing for the realization of numerous applications such as fluorescent lamps, surface modification, etching processes, plasma chemistry, beam source, etc [3].

Plasma is generally classified into two categories: low-temperature plasma and high-temperature plasma. Here, "temperature" refers to the thermodynamic temperature which is defined in terms of the average kinetic energy (velocity) of a gas or collection of particles in its thermal equilibrium. The most probable velocity distribution at thermal equilibrium is described as *Maxwellian distribution*:

Maxwellian distribution

$$f(v) = n(\frac{m}{2\mathrm{k_B}T})^{\frac{3}{2}}\exp(-\frac{mv^2}{2\mathrm{k_B}T}) \tag{1.1}$$

where v, n, m, and T are the particle's kinetic velocity, number density, mass, and thermodynamic temperature, respectively. By integrating the distribution with kinetic energy and then

dividing by density, the average kinetic energy is $\langle\epsilon\rangle = \frac{3}{2}\mathrm{k_B}T$. Nonetheless, it is the usual practice to consider $T = \frac{2\langle\epsilon\rangle}{3\mathrm{k_B}}$ even at non-equilibrium.

High-temperature plasma means nearly all the particles are ionized and they are in thermal equilibrium with electrons. It is usually found in Q-machine plasma, star, or fusion plasma. Low-temperature plasma usually refers to particles' temperature $T < 10^6\mathrm{K}$ and can be further subdivided into thermal plasma and non-thermal plasma [4]. Thermal plasma is in local thermal equilibrium (quasi-equilibrium) where the heavy particles reach almost the same temperature as electrons via elastic collisions even though not ionized. Such conditions can be achieved in arc discharge and combustion plasma. Non-thermal plasma, on the other hand, refers to the non-equilibrium between electrons and heavy particles ($T_e \gg T_i \geqslant T_g$) due to less frequent elastic collisions and low ionization rate. Most of the plasma in laboratories or industries can be classified into non-thermal plasma, such as glow discharge, radio frequency discharge, and pulsed discharge.

Among the variety of non-thermal plasma applications, atmospheric pressure plasma draws increasing attention for its low cost and simplicity. Operating a plasma in atmospheric pressure means no need for a vacuum chamber or working gas, hence it can be relatively easy to adapt with line processing or fabrication industry. However, at atmospheric pressure, a large portion of energy transfer between electrons and neutral gas ends up heating the gas through excitation, dissociation, and relaxation. Many of these processes are exothermic and exponentially dependent on gas temperature thus inducing thermal instability [5]. The lack of working gas and chamber wall also limits the cooling rate of the plasma. Because of this, many plasma sources have been developed or modified to overcome this issue, including nanosecond pulse discharge, dielectric barrier discharge, helium discharge, micro discharge, and fast-flow discharge [6]. The background of this work originates from the effort to innovate an efficient atmospheric non-thermal plasma where a DC glow discharge operates with helium gas and a liquid electrode.

1.2 DC Glow Discharge at Atmospheric Pressure

A glow discharge is initiated by seed electrons near the cathode which are then accelerated by the external electric field towards the anode and producing electron-ion pairs along the way. This process will multiply and create an "avalanche". Energetic ions drift to the cathode and produce secondary electron emissions by overcoming the cathode work function. When the number of secondary electrons emitted at the cathode equals the electron current collected at the anode, the discharge is self-sustaining where typically it is luminous. In this case, the discharge has experienced a breakdown. A large number of charged particles will form space charge and thus perturb the local electric field then re-organize the distribution of the particles. Fig 1.1 shows the normal glow discharge visual structure and species distribution. The non-homogeneous structure origi-

nates from the aforementioned charged particles' energy and density distribution.

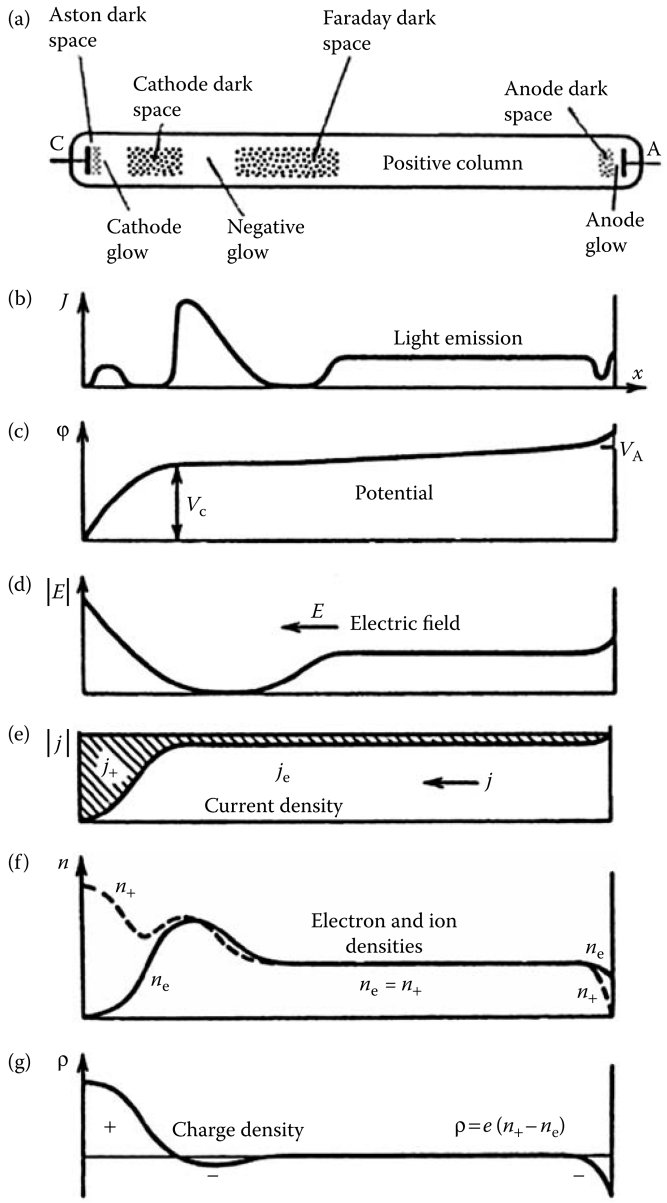

Figure 1.1: Physical parameters distribution in a glow discharge: (a) structure, (b) light emission, (c) potential, (d) electric field, (e) current density, (f) electron and ion densities, (g) charge density [5]

1) *Cathode fall region*

The cathode fall region starts from the cathode and ends at the negative glow region. Adjacent to the cathode is the Aston dark space where secondary electrons accumulate before being accelerated by the cathode sheath potential. Cathode glow represents neutral gas excitation and

electron-ion recombination when low-energy electrons meet drifting ions. Then at the cathode dark space, an external electric field further accelerates the electrons to cause the negative glow region by inelastic collisions with neutral gas. This region's thickness is inversely proportional to the pressure because it is correlated with collisional mean free path $\lambda = \frac{1}{N\sigma}$ and can be estimated by simple numerical calculations as Eq 1.2 [5]. At Faraday dark space, electrons will re-accelerate and establish quasi-neutrality ($n_e \approx n_+$).

$$d(\mathrm{cm}) \approx 0.05\mathrm{cm}/p(\mathrm{Torr}) \tag{1.2}$$

2) *Positive column*

The plasma in this region is rather uniform and satisfies quasi-neutrality. The acceleration of electrons from the electric field is balanced by the loss of energy including ionization, excitation, electron–neutral elastic scattering collision, and ambipolar diffusion. In a sense, it can be seen as a "resistor" that consumes energy by Joule heating.

3) *Anode region*

Wherever the positive column reaches the anode electrode, an anode sheath will be formed by the presence of space charges. Electrons will be accelerated across the sheath potential at the anode dark space and excite neutral gas at anode glow region.

Fig 1.2 illustrates the I-V characteristics and different discharge regimes of DC plasma. At very low voltages (region *AB*, dark discharge), there are not enough charged particles to produce a self-sustaining discharge, and the current is measured in random bursts. The region *BCD* is often called the Townsend discharge region where the voltage is high enough to form an avalanche of electrons. Here, the discharge current grows exponentially and is controlled by an external impedance either from the power supply or a resistor. An increase in voltage or decrease of the external resistance leads to the growth of the discharge current, plasma density, and reconstruction of the electric field. Once the voltage is across the breakdown threshold (point *D*), the plasma density will become stabilized with the fully reconstructed electric field shown in Fig 1.1. At the plateau near *G*, the plasma becomes more electrically conductive and its current is unlimited by the applied voltage which is the basic feature of normal glow discharge ($10^{-4} - 0.1\mathrm{A}$). The further current increment will be distributed as the radial expansion of the cathode/anode spot and plasma column because the plasma current density is constant. However, the size of the plasma is limited by particle diffusion, volumetric electron loss, or recombination at the chamber wall and once the expansion stops further current growth requires a voltage increase to provide higher current density. This is called the abnormal glow discharge at the interval *HI*. Beyond the abnormal glow (region *IJK*), the high current density would cause intense Joule heating and ion bombardment of

the cathode and lead to thermionic emission electron which is more efficient than the secondary electron emissions. Thus the discharge operates in a high current and low voltage mode called an arc. The plasma column will contract into hot filaments due to overheating.

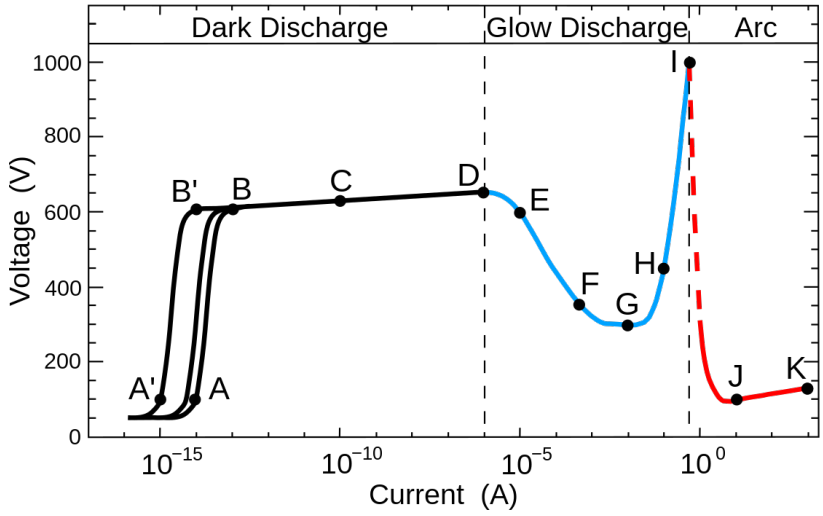

Figure 1.2: Current-voltage characteristics of a DC discharge [7]

Analogously, direct current plasma at atmospheric pressure is observed to form with morphologies nearly identical to a low-pressure glow discharge. Such discharge provides some attributes that can compete with the traditional atmospheric plasma source. It is more uniform than those filaments formed in pulsed discharge and a DC high voltage power supply is cheaper and readily available. A normal glow discharge can expand its volume either axially via increasing discharge gap and voltage or radially when the total current increases. Having a large volume of nonequilibrium plasma at atmospheric pressure could enable a low-cost and mass-production capability in the plasma processing industry. Although most of the glow discharges run at 10 mTorr to a few Torr, operating a DC glow discharge at atmospheric pressure was proved to be possible yet problematic [8, 9].

The foremost concern is the glow-to-arc transition where the current density goes beyond a certain threshold and the plasma becomes thermalized. This difficulty comes from both the heating process and cooling process. Unlike atomic species, nitrogen and oxygen molecules in the air feature more complex collisional processes and many of them are exothermic. Popov pointed out that the most prominent fast heating processes are dissociation of O_2 by electron impact and quenching of electronically excited $N_2(B^3\Pi_g, C^3\Pi_u, a'^1\Sigma_u^-)$ molecules by oxygen and excited $O(^1D)$ atoms by nitrogen [10]. Here "fast" means the reaction happens quicker than vibrational-translational re-

laxation which is also an important heating process that typically happens in $\sim$100 µs. In addition, these processes' rate coefficients are exponentially dependent on the gas temperature which can lead to positive feedback and thermal instability.

Running at atmospheric pressure means the electron-neutral collision frequency is high ($10^{10} - 10^{12}\mathrm{s}^{-1}$) and so as those exothermic reactions. On the other hand, the cooling mechanism of atmospheric plasma is more limited since there is no chamber wall for heat conduction and the heavy molecule species have longer diffusion time ($\tau_D = R^2/D$) than the light atoms. Here R is the positive column radius and D is the diffusion coefficient of ions and neutrals which depends on the mean free path $D \propto T_g^{3/2}/p$ [5]. To achieve a heat balance, the current density is limited by the heat transfer rate which is correlated with the gas diffusion rate. The atmospheric pressure deteriorates the neutrals' diffusion rate posing a challenge to cooling and restricting the current density. Overall, the high gas temperature and thermal instability limit the area of atmospheric pressure plasma applications and have to be resolved.

On account of the thermal issue, many methods have been proposed. To reduce the overheating from exothermic reactions, light atoms such as helium have faster diffusion time, high thermal conductivity, and do not have vibrational or rotational states which make them more efficient to be ionized [11]. At the positive column, introducing helium can increase the ionization efficiency and suppress the Joule heating and thermal instability. Alternatively, high-speed air can be used to increase the cooling rate by decreasing the gas residence time and a stable glow discharge is attainable [12]. The thermal instability that leads to the glow-to-arc transition usually starts near the cathode driven by the strong electric field. Using an external electron emitter, a micro hollow cathode discharge, to replace the secondary electron emission mechanism can avoid the cathode fall region and stabilize the glow discharge at atmospheric pressure [13]. Electrodes can also be cooled by water to extend the current threshold of atmospheric glow discharge [8]. A liquid electrode could also support a stable atmospheric glow discharge [14] and can be useful in electrolysis [15]. In fact, applying a liquid electrode in an atmospheric glow discharge proved to not only help cooling but also coincide with a rich area for plasma-liquid interactions. The introduction of liquid opens up multiple coupling channels of processes and the potential for applications.

1.3 Plasma-liquid Interaction in DC Glow Discharge

Plasma-liquid interaction involves complicated coupling processes encompassing many fields such as plasma science, fluid dynamics, heat and mass transport, multiphase chemistry, photolysis, and aerosol science, hence a multidisciplinary community of research is being cultivated along the growing interest [16]. Plasma-liquid interaction had its early start centering around electrolysis. Gubkin first explored electrical discharge interactions with liquids using glow discharge electrol-

ysis to extract silver particles from $\mathrm{AgNO_3}$ solution [17]. The discharges provide free electrons that recombine with the silver ions at the plasma-liquid interface and this mechanism is still the foundation of the synthesis of nanoparticles to this date. In recent years, progress has been made involving environmental [18] and biological [19] applications which also reveal more and more mysteries in the plasma-liquid interactions.

In an atmospheric glow discharge with liquid anode, the major coupling processes are mass and heat transfer, fluid dynamics, species transport, and chemical reaction. Although these processes feature different lengths and time scales, a series of mechanisms couple them together and thus comprehensive diagnostics are required to uncover them. When a glow discharge is initiated above the liquid, the gas heating from exothermic processes will raise the gas temperature to $2000\mathrm{K}$, and the thermal energy is dissipated to the ambient air and liquid electrode. The Joule heating in the gas phase is highly localized ($> 300\mathrm{W/cm^3}$) which drives gas expansion and affects the plasma size. One of the major heat transfer mechanisms is the natural convection of air accompanied by forced convection if an injected working gas is used [20]. At the plasma-liquid interface, heat transported by vapor from the heated water balances the incoming heat deposition. These vapor molecules would quench the major species in the plasma and affect their excitation lifetime which sometimes poses issues for inferring excited states population using optical diagnostics [21]. The anode sheath thickness is correlated with the Debye length ($\sim 100\,\mu\mathrm{m}$ at atmospheric pressure), and the introduction of vapor would reduce the electron temperature by additional attachment loss and raise the field strength at the anode. The gas convection also affects the air entrainment and vapor concentration in the plasma column which has an impact on chemical reaction and gas heating [22]. In addition, many of the exothermic reaction coefficients are exponentially dependent on the gas temperature whose profile would be altered by evaporation and air cooling. In the liquid phase, the evaporation drives convection flow right under the plasma attachment which mixes the aqueous species and enhances their transport [23][24]. Such coupling among the species collision process, thermal dynamics, mass and heat transfer only partially represents the whole picture in Fig 1.3.

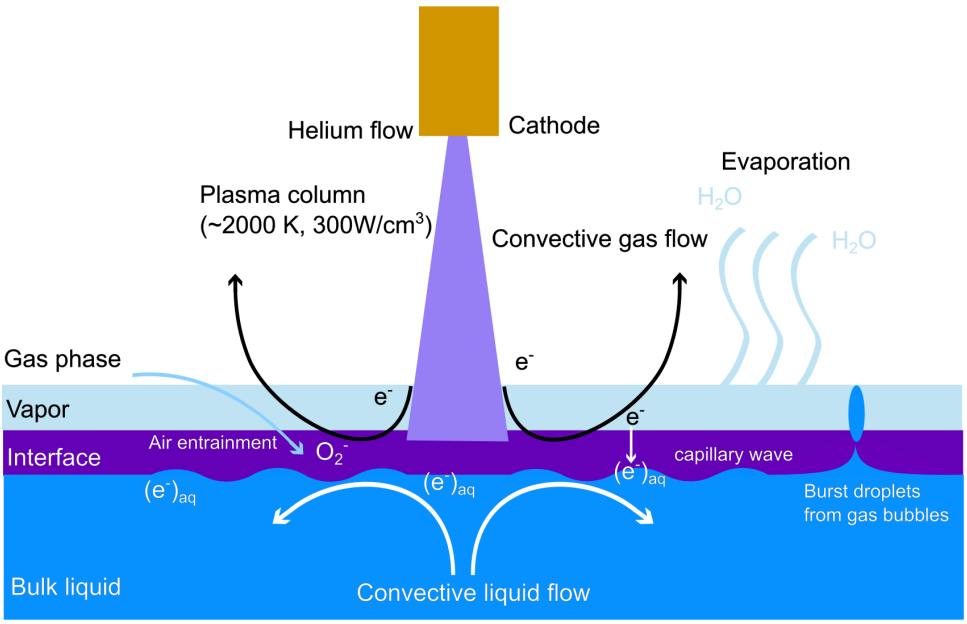

Figure 1.3: Schematic of the major dynamics and mechanisms for atmospheric DC glow discharge in contact with water

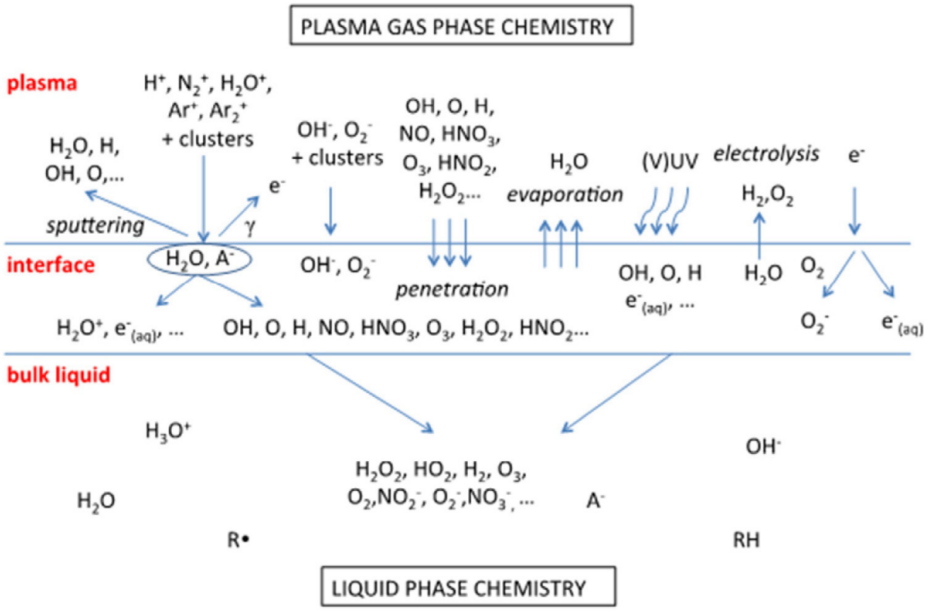

Figure 1.4: Schematic diagram of some of the most important species and mechanisms for an Ar/air plasma in contact with water [16]

The plasma chemistry is more complex in the plasma-liquid interaction due to the presence of

air, vapor, and interfacial regions. Fig 1.4 describes some of the major species and their reaction channels in the plasma-liquid interactions. At the gas phase, the water vapor from evaporation greatly enhances the corresponding species production rate such as O, H, hydroxyl radical, and H_2O_2. Macroscopic droplets can be ejected from the liquid phase by the burst of bubbles [25] and function as vehicles for sending the aqueous species such as salt ions [26] or escort the gas phase species to the liquid phase [27]. On the microscopic scale, the water molecules would form clusters with ions and change their mobility and reaction path. The nucleation of molecules in the vapor is an important subject in nanoparticle synthesis and aerosol science [28] and has great potential in applications [29]. At the plasma-liquid interface, energetic electrons become solvated electrons and form additional pathways for aqueous species including $(OH^-)_{aq}, (O_2^-)_{aq}, H_2, H_2O_2$ [30]. The *in situ* diagnostics of chemistry in plasma-liquid interface and liquid phase is always challenging due to the presence of short-lived species and small length scale [31, 32].

1.4 Self-organization in DC Glow Discharge with a Liquid Anode

One particular phenomenon that draws our attention is the highly dynamic self-organized pattern found to form under certain conditions on the surface of a DC glow discharge with liquid anode as shown in Fig 1.5. Plenty of self-organization phenomena can be found in nature. Fig 1.6a shows the hexagonal north pole of Saturn, which is hypothesized to be related to the intense jet stream interactions with the otherwise atmospheric uniform composition. Fig 1.6b reveals the Fibonacci sequence in fingerprint patterns and snail shell morphology.

In general, self-organization is the spontaneous formation of spatial, temporal, structures or functions in systems composed of few or many components. "Spontaneous" means the interactions among the system's components are executed using only local information, without reference to the global pattern [33]. One of the classic theories on self-organization in chemistry was proposed by Alan Turing, which was referred to as *reaction-diffusion system* [34]. Reaction-diffusion systems usually are comprised of two components where an activator provides a reaction and the inhibitor neutralizes the products or their diffusion. Feedback governs their growth and interaction and these local interactions form a coherent pattern in space or time. Such systems are ubiquitous and so in plasma science. Pattern formation however is not unique in atmospheric pressure DC glow discharge and can be observed in low-pressure cathode surface [35][36]. It is believed that some bifurcation events due to small changes of controlling parameters such as normal current density and electrode properties prompt different configurations of cathode area [37]. In nanosecond pulsed discharge, the plasma filaments can form SOP and affect the performance and efficiency of

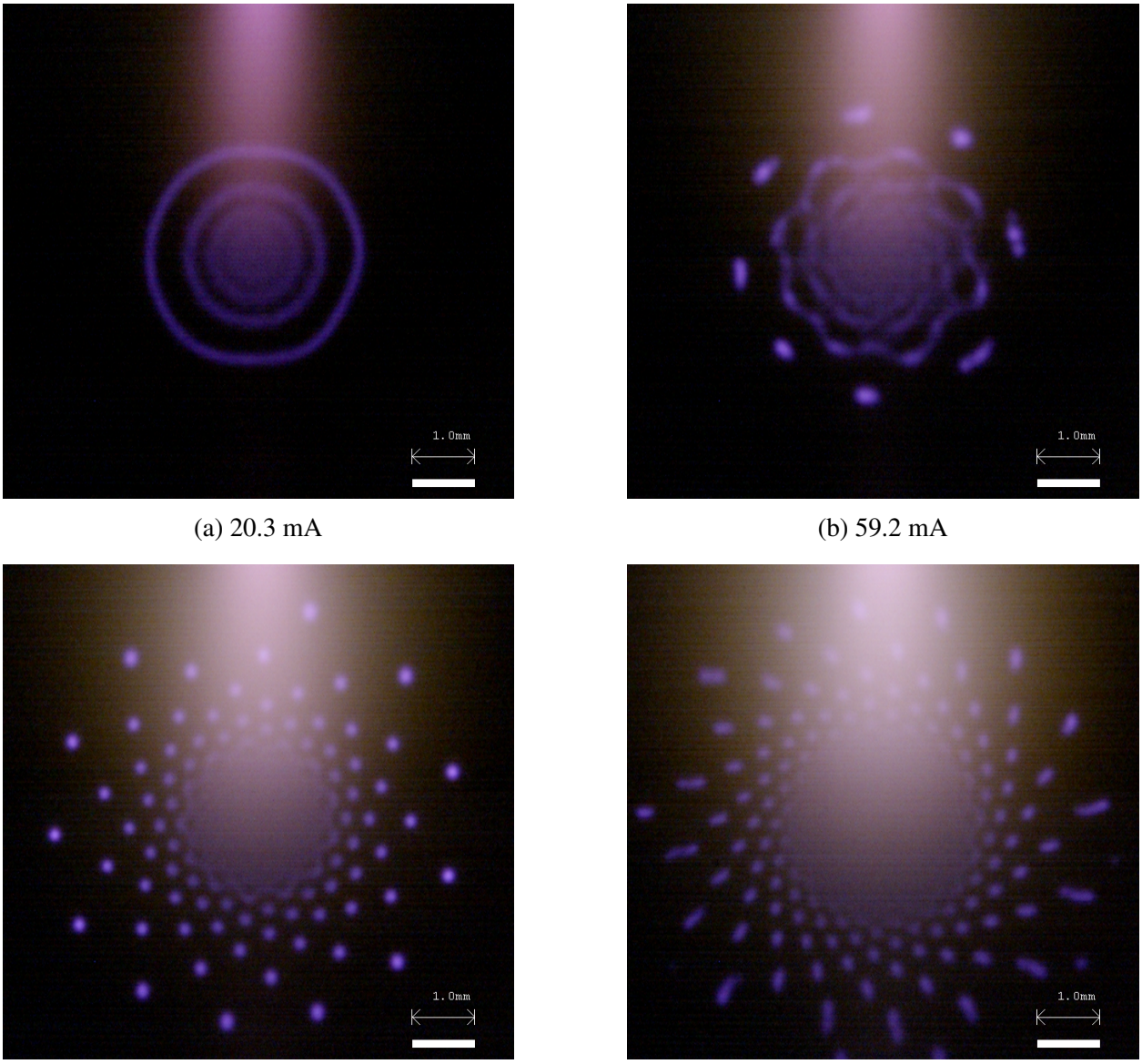

(a) 20.3 mA

(b) 59.2 mA

(c) 85.5 mA

(d) 105.6 mA

Figure 1.5: Self-organized pattern on the liquid anode of a DC glow discharge at various discharge currents

its applications. In the context of the reaction-diffusion hypothesis, the ionization in the applied field enhanced by the surface memory charges function as the activator while the inhibitor is due to the charging of the dielectric which limits the radial diffusion of a filament [38].

Coupled with the plasma-liquid interaction, the SOP of DC glow discharge with liquid anode is more complicated. This phenomenon was reported firstly without a working gas in [41][42] where the pattern is mainly shown as a "rim" at the edge of an unstable conical plasma column. Then, Shirai *et al* observed a stable and evolving pattern when a miniature helium flow is applied

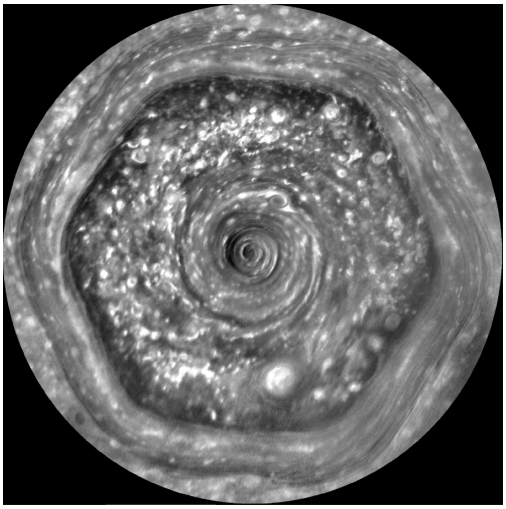

(a) Saturn's Hexagon pole [39]

(b) Fibonacci sequence found in shell and fingerprint [40]

Figure 1.6: Self-organization in nature

[43]. He pointed out the importance of air entrainment in the pattern formation. Verreycken *et al* reported the pattern area would increase at low liquid conductivity [44]. A more comprehensive study was conducted by Shirai *et al* which suggested that many electrical conditions including discharge gap, helium flow rate, liquid conductivity, temperature, and discharge current can affect the pattern dynamics [45][46][47]. More importantly, oxygen in the air was found to be critical for SOP formation since the nitrogen shielding gas will preclude the self-organized pattern as shown in Fig 1.7. Zhang *et al* observed the variation of pattern shape with different acids and it was possibly a result of electronegative gases from electrolysis at plasma-liquid interface [48]. In addition, the electrolyte composition could also affect the morphology complexity of the pattern in Fig 1.8 which may be related to the ionic strength of solution [49, 50]. The time scale of the establishment of SOP (100 µs) was reported in [51]. This time scale is not within the transient collisional and relaxation process but is more similar to timescales of gas convection, evaporation, and gas heating. The above findings show the sophisticated correlations between SOP and the coupling processes in plasma-liquid interactions.

Besides the experimental efforts, many theoretical models have been examined to reproduce the pattern dynamics. Trelles showed a plasma pattern appearing on the surface of solid anodes in arc discharges using a time-dependent 3D fluid model and the results qualitatively match with the experimental case [52]. Bieniek applied the multiple solution theory and reported that the simulated pattern spots behave like mini-cathode spots, in that the sign of the current density and electric field is reversed [53]. Rumbach *et al* treated the SOP as a reaction-diffusion system where electron impact ionization serves as an autocatalytic reaction [54]. Due to the complexity of plasma-liquid

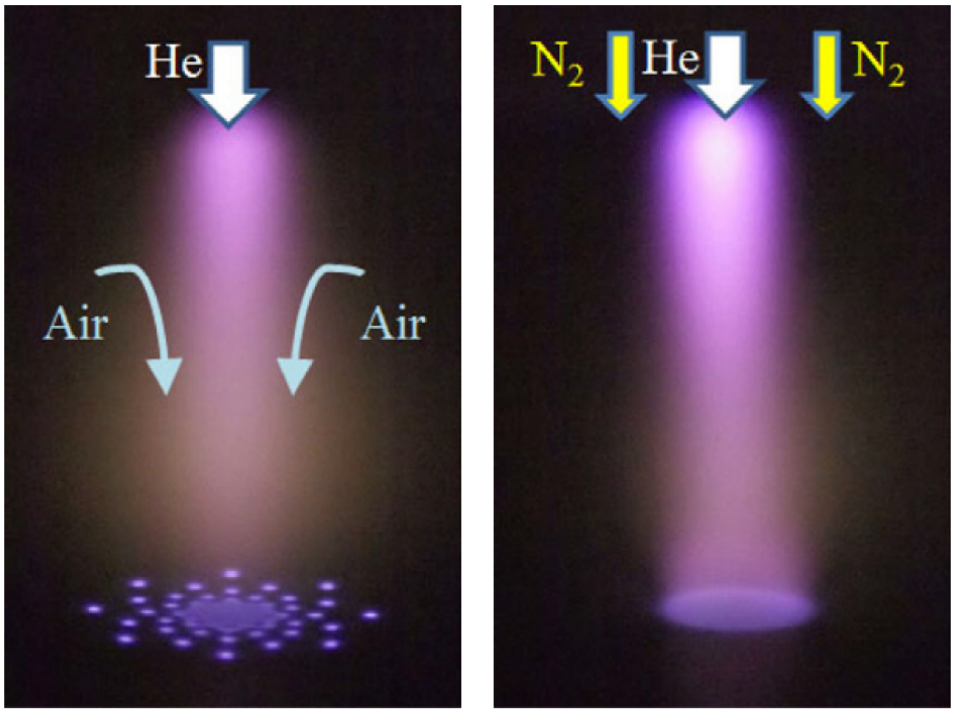

Figure 1.7: Dependence of the pattern formation on the gas species around the discharge. (a) Without a sheath flow (helium flows through ambient air). (b) With an nitrogen sheath flow of 1000 sccm[47]

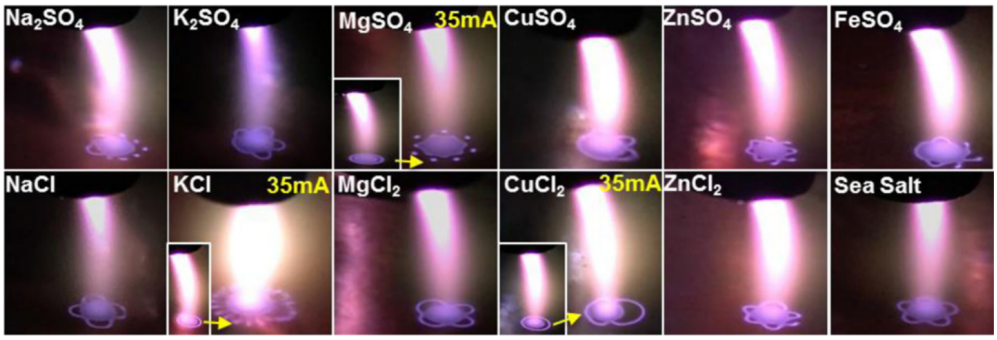

Figure 1.8: Dependence of the pattern formation on the electrolyte composition [49]

interactions, it is challenging to include all the dynamic processes when simulating the pattern mechanism. Recently, a one-dimensional multiphase model was presented [55]. It includes a comprehensive reaction network for both plasma and water chemistry and species transport between

the two phases.

1.5 Thesis Overview

The overarching goal of this thesis is to understand the role of the coupling processes prevailing at the plasma-liquid interface that ultimately give rise to the formation of self-organized patterns. Specifically, the summary of findings from the experimental investigation of five scientific questions will be presented in this manuscript.

1) What are the discharge operating conditions that give rise to and affect the self-organized pattern dynamics? Candidates explored in this work include discharge current, discharge gap, work gas flow rate, the cathode's orifice diameter for gas injection, liquid phase conductivity, and liquid temperature.

2) How do plasma discharge conditions change with the onset of self-organization of the anode attachment and subsequent dynamical behavior (gas temperature, electron density, electron temperature)? Are local or global plasma parameters more important to SOP formation?

3) Does the presence of electronegative gas (oxygen in the air) serve as a critical "ingredient" for the establishment of SOP? Are negative ions important to pattern formation?

4) What role does plasma-induced liquid phase convection play in species mass and liquid transport and how do these processes couple with the dynamics of SOP?

5) What is the origin of the aerosol droplets observed to form during the operation of DC glow discharge with liquid anode? Their presence in the discharge along with electrons, negative and positive ions constitute a complex plasma. How does the plasma interact with them?

The diagnostics in this work strive to examine each component of the coupling processes by analyzing their importance and answering the above scientific questions. Chapter 2 will illustrate the experimental setup and design that aims to satisfy the following investigation. In Chapter 3, the basic plasma properties including I-V characteristic curve, reduced electric field, and current density at the anode are recorded to map the threshold for various pattern modes. In Chapter 4, the importance of oxygen, which can form negative ions in the discharge is explored. Negative ions percentage is estimated experimentally to determine directly if there is a relation between their presence and pattern formation. Chapter 5 focuses on the spatially resolved OES diagnostics of

the plasma column. Specifically, the profiles of gas temperatures at various discharge conditions are examined to find the temperature profile that favors the pattern. In Chapter 6, the plasma-induced convective flow established in the liquid electrode is characterized using particle image velocimetry. The morphology of the observed liquid phase convection was found to be coupled to the pattern. Lastly, a fast, and non-trivial mass transport process at the plasma-liquid interface was investigated in Chapter 7. The jet droplet originating from bubbles was found to drive this transport process and can be facilitated by an air sprayer. The impact of droplets on the plasma properties was also examined by OES.

References

[1] Irving Langmuir. Oscillations in ionized gases. *Proceedings of the National Academy of Sciences*, 14(8):627–637, 1928.

[2] Paul K Chu and XinPei Lu. *Low temperature plasma technology: methods and applications*. CRC press, 2013.

[3] H Conrads and M Schmidt. Plasma generation and plasma sources. *Plasma Sources Science and Technology*, 9(4):441, 2000.

[4] Claire Tendero, Christelle Tixier, Pascal Tristant, Jean Desmaison, and Philippe Leprince. Atmospheric pressure plasmas: A review. *Spectrochimica Acta Part B: Atomic Spectroscopy*, 61(1):2–30, 2006.

[5] Alexander Fridman and Lawrence A Kennedy. *Plasma physics and engineering*. CRC press, 2004.

[6] Alexander Fridman, A Gutsol, and YI Cho. Non-thermal atmospheric pressure plasma. *Advances in Heat Transfer*, 40:1–142, 2007.

[7] Chetvorno Wikigian. Glow discharge current-voltage curve — Wikipedia, the free encyclopedia, 2013. Available online at: https://en.m.wikipedia.org/wiki/File:Glow_discharge_current-voltage_curve_English.svg, last accessed on 11.05.2023.

[8] Hsu Yun Fan. The transition from glow discharge to arc. *Physical Review*, 55(8):769, 1939.

[9] Erich E Kunhardt. Generation of large-volume, atmospheric-pressure, nonequilibrium plasmas. *IEEE transactions on plasma science*, 28(1):189–200, 2000.

[10] NA Popov. Fast gas heating in a nitrogen–oxygen discharge plasma: I. kinetic mechanism. *Journal of Physics D: Applied Physics*, 44(28):285201, 2011.

[11] T Yokoyama, Moriwaki Kogoma, T Moriwaki, and S Okazaki. The mechanism of the stabilisation of glow plasma at atmospheric pressure. *Journal of Physics D: Applied Physics*, 23(8):1125, 1990.

[12] Lan Yu, Christophe O Laux, Denis M Packan, and Charles H Kruger. Direct-current glow discharges in atmospheric pressure air plasmas. *Journal of applied physics*, 91(5):2678–2686, 2002.

[13] Robert H Stark and Karl H Schoenbach. Direct current high-pressure glow discharges. *Journal of applied physics*, 85(4):2075–2080, 1999.

[14] Peter Bruggeman, Jingjing Liu, Joris Degroote, Michael G Kong, Jan Vierendeels, and Christophe Leys. Dc excited glow discharges in atmospheric pressure air in pin-to-water electrode systems. *Journal of Physics D: Applied Physics*, 41(21):215201, 2008.

[15] A Hickling and MD Ingram. Contact glow-discharge electrolysis. *Transactions of the Faraday Society*, 60:783–793, 1964.

[16] Peter J Bruggeman, Mark J Kushner, Bruce R Locke, Johannes GE Gardeniers, WG Graham, David B Graves, RCHM Hofman-Caris, Dragana Maric, Jonathan P Reid, Elisa Ceriani, et al. Plasma–liquid interactions: a review and roadmap. *Plasma sources science and technology*, 25(5):053002, 2016.

[17] J Gubkin. Electrolytiche metallabscheidung an der freien oberfl ache einer salz osung. *Ann. Phys. Chem. NF*, 32:114–115, 1887.

[18] John E Foster. Plasma-based water purification: Challenges and prospects for the future. *Physics of Plasmas*, 24(5), 2017.

[19] Kristian Wende, Thomas von Woedtke, Klaus-Dieter Weltmann, and Sander Bekeschus. Chemistry and biochemistry of cold physical plasma derived reactive species in liquids. *Biological Chemistry*, 400(1):19–38, 2018.

[20] Vadim P Stepaniuk, Tindaro Ioppolo, M Volkan Ötügen, and Valery A Sheverev. Measurement of gas temperature and convection velocity profiles in a dc atmospheric glow discharge. *Journal of Applied Physics*, 102(12), 2007.

[21] Peter Bruggeman, Daan C Schram, Michael G Kong, and Christophe Leys. Is the rotational temperature of oh (a–x) for discharges in and in contact with liquids a good diagnostic for determining the gas temperature? *Plasma Processes and Polymers*, 6(11):751–762, 2009.

[22] Alexander Lindsay, Carly Anderson, Elmar Slikboer, Steven Shannon, and David Graves. Momentum, heat, and neutral mass transport in convective atmospheric pressure plasma-liquid systems and implications for aqueous targets. *Journal of Physics D: Applied Physics*, 48(42):424007, 2015.

[23] Tetsuji Shimizu, Yutaka Iwafuchi, Gregor E Morfill, and Takehiko Sato. Formation of thermal flow fields and chemical transport in air and water by atmospheric plasma. *New Journal of Physics*, 13(5):053025, 2011.

[24] Zimu Yang, Yao Kovach, and John Foster. Visualization and analysis of coupling between plasmas self-organization and plasma-induced fluid circulation in 1 atm dc glows with liquid anode. *Journal of Applied Physics*, 129(16), 2021.

[25] Zimu Yang, Yao Kovach, Zhehui Wang, and John Foster. On the nature of droplet production in dc glows with a liquid anode: mechanisms and potential applications. *Plasma Sources Science and Technology*, 31(11):115008, 2022.

[26] Naoki Shirai, Goju Suga, and Koichi Sasaki. Mechanism of droplet generation and optical emission of metal atoms in atmospheric-pressure dc glow discharge employing liquid cathode. *Plasma Sources Science and Technology*, 29(2):025007, 2020.

[27] R Burlica, K-Y Shih, and BR Locke. Formation of h2 and h2o2 in a water-spray gliding arc nonthermal plasma reactor. *Industrial & Engineering Chemistry Research*, 49(14):6342–6349, 2010.

[28] Myungjoon Kim, Saho Osone, Taesung Kim, Hidenori Higashi, and Takafumi Seto. Synthesis of nanoparticles by laser ablation: A review. *KONA Powder and Particle Journal*, 34:80–90, 2017.

[29] Davide Mariotti and R Mohan Sankaran. Perspectives on atmospheric-pressure plasmas for nanofabrication. *Journal of Physics D: Applied Physics*, 44(17):174023, 2011.

[30] Bruce C Garrett, David A Dixon, Donald M Camaioni, Daniel M Chipman, Mark A Johnson, Charles D Jonah, Gregory A Kimmel, John H Miller, Thomas N Rescigno, Peter J Rossky, et al. Role of water in electron-initiated processes and radical chemistry: Issues and scientific advances. *Chemical reviews*, 105(1):355–390, 2004.

[31] Peter J Bruggeman, Renee R Frontiera, Uwe R Kortshagen, Mark J Kushner, Suljo Linic, George C Schatz, Himashi Andaraarachchi, Stephen Exarhos, Leighton O Jones, Chelsea M Mueller, et al. Plasma-driven solution electrolysis. *Journal of Applied Physics*, 129(20), 2021.

[32] Paul Rumbach, David M Bartels, R Mohan Sankaran, and David B Go. The solvation of electrons by an atmospheric-pressure plasma. *Nature communications*, 6(1):7248, 2015.

[33] James Sneyd, Guy Theraula, EricVE Bonabeau, Jean-Louis Deneubourg, and Nigel R Franks. *Self-organization in biological systems*. Princeton university press, 2001.

[34] Alan Mathison Turing. The chemical basis of morphogenesis. *Bulletin of mathematical biology*, 52:153–197, 1990.

[35] Yu S Akishev, AA Deryugin, IV Kochetov, AP Napartovich, and NI Trushkin. Dc glow discharge in air flow at atmospheric pressure in connection with waste gases treatment. *Journal of Physics D: Applied Physics*, 26(10):1630, 1993.

[36] Hans-Georg Jürgen Purwins and Jürgen Berkemeier. Self-organized patterns in planar low-temperature dc gas discharge. *IEEE Transactions on Plasma Science*, 39(11):2116–2117, 2011.

[37] MS Benilov. Multiple solutions in the theory of dc glow discharges and cathodic part of arc discharges. application of these solutions to the modeling of cathode spots and patterns: a review. *Plasma Sources Science and Technology*, 23(5):054019, 2014.

[38] Thierry Callegari, B Bernecker, and Jean-Pierre Boeuf. Pattern formation and dynamics of plasma filaments in dielectric barrier discharges. *Plasma Sources Science and Technology*, 23(5):054003, 2014.

[39] NASA. Saturn's perplexing hexagon, 2017. Available online at: https://science.nasa.gov/_ipx/w_1536&f_webp/https://smd-cms.nasa.gov/wp-content/uploads/2023/07/saturn_hexagon_black_and_white.gif%3Fw=2000, last accessed on 11.08.2023.

[40] artcatalyst. Fibonacci sequence mathematics nature, 2014. Available online at: artcatalyst.blogspot.com/2011/04/fibonacci-sequence-mathematics-nature.html.

[41] Alyssa Wilson, David Staack, Tanvir Farouk, Alexander Gutsol, Alexander Fridman, and Bakhtier Farouk. Self-rotating dc atmospheric-pressure discharge over a water-surface electrode: regimes of operation. *Plasma Sources Science and Technology*, 17(4):045001, 2008.

[42] Shu Yi Miao, Chun Sheng Ren, Yu Tao Zhang, Bing Qi, You Nian Wang, et al. Conical dc discharge in ambient air using water as an electrode. *IEEE transactions on plasma science*, 36(1):126–130, 2008.

[43] Naoki Shirai, Shinji Ibuka, and Shozo Ishii. Self-organization pattern in the anode spot of an atmospheric glow microdischarge using an electrolyte anode and axial miniature helium flow. *Applied Physics Express*, 2(3):036001, 2009.

[44] Tiny Verreycken, Peter Bruggeman, and Christophe Leys. Anode pattern formation in atmospheric pressure air glow discharges with water anode. *Journal of Applied Physics*, 105(8), 2009.

[45] Naoki Shirai, Satoshi Uchida, Fumiyoshi Tochikubo, and Shozo Ishii. Self-organized anode pattern on surface of liquid or metal anode in atmospheric dc glow discharges. *IEEE Transactions on Plasma Science*, 39(11):2652–2653, 2011.

[46] Naoki Shirai, Kosuke Ichinose, Satoshi Uchida, and Fumiyoshi Tochikubo. Influence of liquid temperature on the characteristics of an atmospheric dc glow discharge using a liquid electrode with a miniature helium flow. *Plasma Sources Science and Technology*, 20(3):034013, 2011.

[47] Naoki Shirai, Satoshi Uchida, and Fumiyoshi Tochikubo. Influence of oxygen gas on characteristics of self-organized luminous pattern formation observed in an atmospheric dc glow discharge using a liquid electrode. *Plasma Sources Science and Technology*, 23(5):054010, 2014.

[48] Shiqiang Zhang and Thierry Dufour. Self-organized patterns by a dc pin liquid anode discharge in ambient air: Effect of liquid types on formation. *Physics of Plasmas*, 25(7), 2018.

[49] Yao E Kovach, Maria C Garcia, and John E Foster. The variation in self-organized anode plasma pattern structure with solution electrolyte type in 1 atm dc glow discharge. *Plasma Sources Science and Technology*, 30(1):015007, 2021.

[50] John E Foster, Yao E Kovach, Janis Lai, and Maria C Garcia. Self-organization in 1 atm dc glows with liquid anodes: Current understanding and potential applications. *Plasma Sources Science and Technology*, 29(3):034004, 2020.

[51] Tanubhav Srivastava, Marien Simeni Simeni, Gaurav Nayak, and Peter J Bruggeman. Self-organized patterns at the plasma–liquid anode interface in a helium glow discharge: temporal development and mechanisms. *Plasma Sources Science and Technology*, 31(8):085010, 2022.

[52] Juan Pablo Trelles. Formation of self-organized anode patterns in arc discharge simulations. *Plasma Sources Science and Technology*, 22(2):025017, 2013.

[53] MS Bieniek, PGC Almeida, and MS Benilov. Self-consistent modeling of self-organized patterns of spots on anodes of dc glow discharges. *Plasma Sources Science and Technology*, 27(5):05LT03, 2018.

[54] Paul Rumbach, Alan E Lindsay, and David B Go. Turing patterns on a plasma-liquid interface. *Plasma Sources Science and Technology*, 28(10):105014, 2019.

[55] Shane Keniley, Necip B Uner, Elizabeth Perez, R Mohan Sankaran, and Davide Curreli. Multiphase modeling of the dc plasma–water interface: application to hydrogen peroxide generation with experimental validation. *Plasma Sources Science and Technology*, 31(7):075001, 2022.

CHAPTER 2

Atmospheric DC Glow Discharge with Liquid Anode

2.1 Discharge Instrument and Liquid Circulatory

The experimental setup described in this section constitutes the core experiment component for the following chapters where additional parts are added for individual diagnostics. The discharge is a gas phase DC glow discharge with a pin-to-water configuration as illustrated in Fig 2.1. The plasma is powered by a high-voltage DC power supply (Gamma High Voltage Research RR3-333R) which can output up to 3 kV ($< \pm 0.01\%$) and 333 mA ($< \pm 0.005\%$). Note that the AC component in the DC power supply can produce periodic voltage fluctuations that look like ripples. In our case, the ripples have a scale of 0.05% at 60 Hz. It is possible that these fluctuations could potentially provoke some dynamics of the SOPs such as the random rotation and drift although this is not explored thoroughly in this work. In a normal glow discharge regime, raising the discharge power or current does not inflict a corresponding change in the discharge voltage. On the other hand, the power supply is voltage-regulated thus requiring a ballast resistor. A 15 $\mathrm{k}\Omega$ resistor is installed between the power supply output pin and charged electrode to allocate the additional voltage drop when the plasma current is increased. In addition, the resistor protects the power supply from potential short circuit events. Occasionally, a smaller resistance (5 $\mathrm{k}\Omega$) is installed instead when a deionized liquid anode dissipates high voltage drop. The discharge voltage is measured at the charged electrode by a high voltage divider (Tektronix P6015A, maximum error $< \pm 3\%$) that attenuates the electrode voltage by 1000 times. The current is measured by a Hall effect DC/AC current sensor (Tektronix TCP030A, maximum error $< \pm 3\%$). Both probes' signals are analyzed and recorded by an oscilloscope (Tektronix MDO 3054). The charged high-voltage electrode is a brass rod of 6 mm in diameter and 120 mm in length. The rod electrode is hollow inside and functions as a nozzle that allows the working gas to flow through. The electrode has an orifice (diameter 0.5 and 1 mm) at the end and different orifice sizes have been shown to affect SOP dynamics. Helium gas is used as working gas and its flow rate (100-500 sccm) is regulated by a flow controller (Alicat MC-10SLPM). The discharge gap is controlled by a linear motion stage

(Velmex Motorized XSlide) where the brass electrode is installed. A silicon plate is connected to the earth ground and immersed inside the liquid phase to collect the return current. Conventional metallic electrodes would experience corrosion from the charge exchange process when immersed in the water. The electrolysis reaction would release metal ions into the liquid and affect the conductivity and purity. Interestingly, obvious erosion was observed on a silicon ground plate. This is due to the continuous bubble formation which leaves acoustic cavitation [1]. Still, the silicon plate is a stable and economical choice for an immersive liquid electrode.

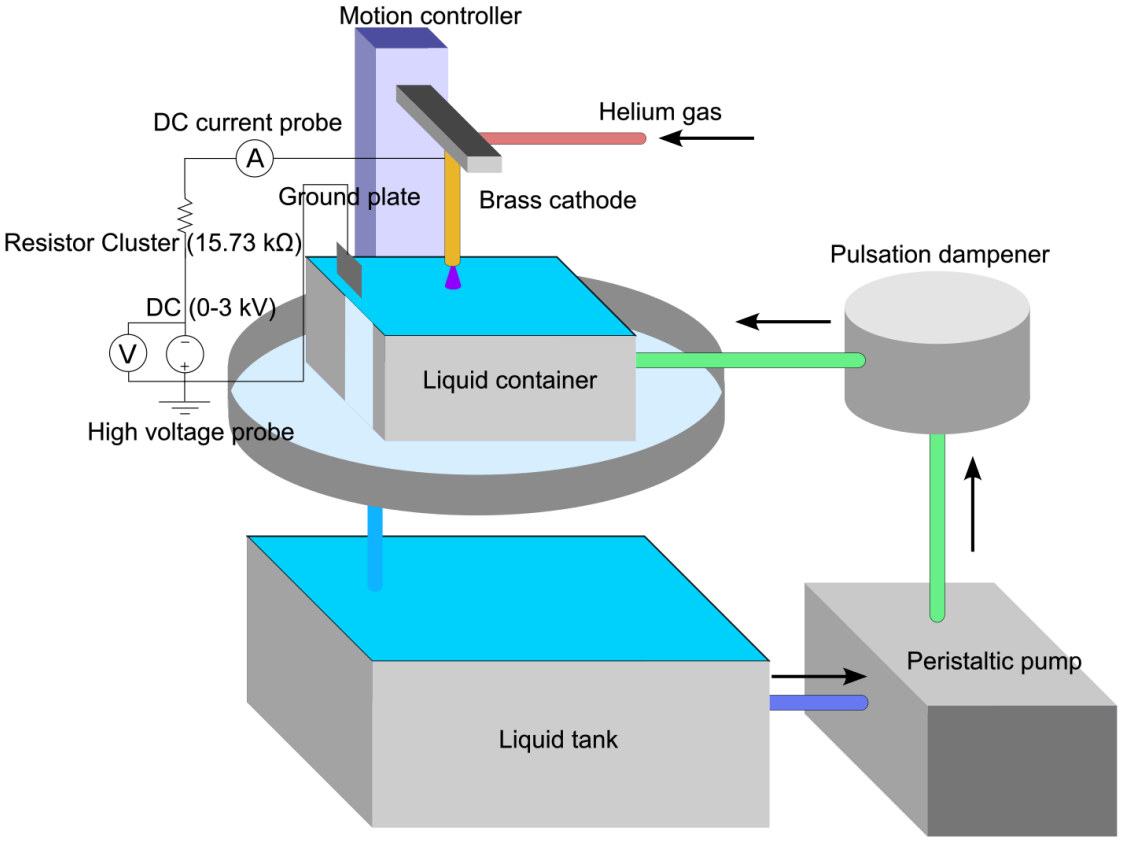

Figure 2.1: Schematic diagram of glow discharge and liquid phase circulatory setup

The liquid phase is held in a lucite cubic container (2.25 inch side length) which enables optical diagnostics. Discharge with liquid can change the liquid properties on a time scale of seconds. It was found that the temperature near the liquid surface could reach $80\,^{\circ}\mathrm{C}$ in a few minutes given that the container volume was not large. More importantly, the SOP is sensitive to the liquid properties which should be a controlled variable in the experiment. Given that, a water circulatory system is built to circulate the container so that the liquid properties can be controlled and stay constant. A bigger liquid tank is used to store the known properties of liquid and is pumped by a peristaltic pump. The peristaltic pump works as its rotary rollers compress the flexible tube without

contacting the liquid inside. Note that the pump's mechanism causes a discontinuous flow at the low pumping rate but this issue is resolved by installing a pulsation dampener just after the outlet of the pump. After the liquid is circulated into the container, it overflows and leaks into an underneath Petri dish and then drains back to the tank. When strictly controlled liquid properties are required, the liquid is not recycled but fed from a tank only. The external tank provides a larger heat sink to help maintain the temperature of the liquid container. With the circulation loop, the relaxation time of the liquid phase properties including temperature and conductivity is greatly extended ($\sim$ 30 min). In addition, a low liquid temperature would prevent vaporization on the anode surface which leads to a large increase in the resistance [2]. Most importantly, the circulation enables the overflow to keep the liquid surface level stable and constant so that the discharge gap is strictly controlled for operational parameter sensitivity analysis and spatially resolved OES.

2.2 Nitrogen Purge Box for Controlling the Ambient Oxygen

It is known that the SOP is sensitive to oxygen gas when added as a mixture in the feed gas [3]. Many gas-heating reactions are related to the presence of oxygen, including the dissociation of oxygen, and vibrational-translational relaxation between nitrogen molecules and atomic oxygen. Although the oxygen variable could be controlled by a mixing working gas or nitrogen shielding gas, the forced gas flow would interfere with the convection, cooling rate, gas residence time, and plasma thermal balance. Running the shielding nitrogen gas not only lowers the oxygen fraction but also increases the convective cooling rate which makes it difficult to investigate the gas heating contribution from the oxygen gas alone. On the other hand, adjusting the ambient oxygen fraction via running the discharge in a sealed box would preclude the influence of other variables as far as possible. As shown in Fig 2.2, a purge box was built with 30.5 cm width (1.27 cm thickness) cast acrylic plates and a detachable wall at the front. At the back panel, various ports provided feedthroughs for electrical connection, signal communication, gas inlet, and a purge valve to release excess pressure. When the ambient oxygen fraction needs to be controlled, the front plate is installed with a sealing rubber gasket and held by two latches which isolates the discharge gas phase from room air. The dry nitrogen gas is fed through a port at a high position and the excess gas is released by a purge valve at the bottom position. A fluorescence-based optical oxygen sensor (GasLab SAN-20 Oxygen Safety Monitor) was installed inside to indicate the oxygen level. In future work, a glow discharge with liquid electrodes could also be operated in a few Torr inside the purge box by depressurization.

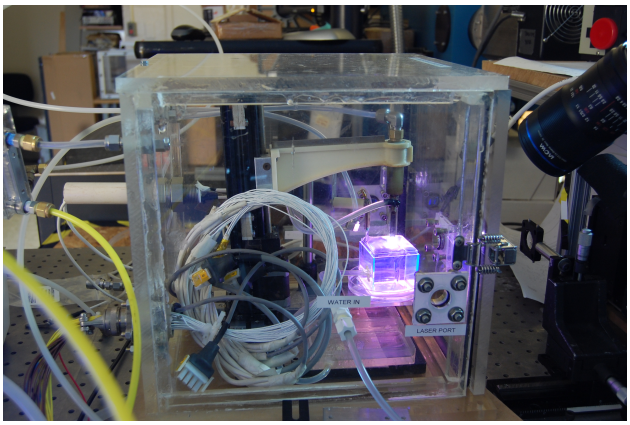

(a) Glow discharge in the purge box

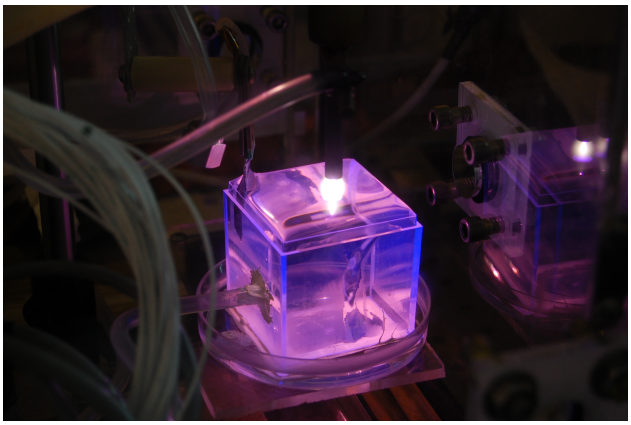

(b) Glow discharge on liquid surface

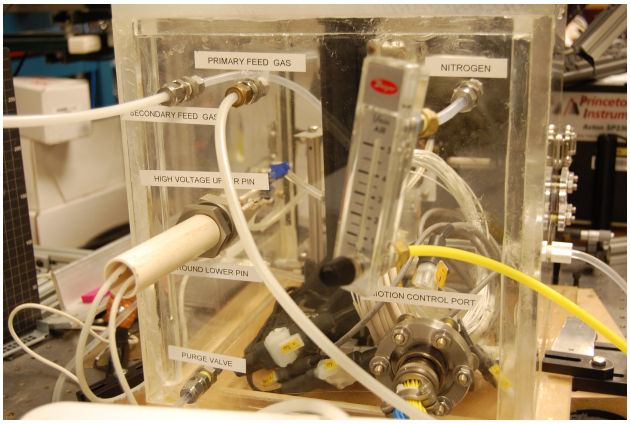

(c) Back panel with various ports

Figure 2.2: Purge box for controlling the ambient oxygen

References

[1] Andrea Angulo, Peter van der Linde, Han Gardeniers, Miguel Modestino, and David Fernández Rivas. Influence of bubbles on the energy conversion efficiency of electrochemical reactors. *Joule*, 4(3):555–579, 2020.

[2] Herbert H Kellogg. Anode effect in aqueous electrolysis. *Journal of the electrochemical society*, 97(4):133, 1950.

[3] Naoki Shirai, Satoshi Uchida, and Fumiyoshi Tochikubo. Influence of oxygen gas on characteristics of self-organized luminous pattern formation observed in an atmospheric dc glow discharge using a liquid electrode. *Plasma Sources Science and Technology*, 23(5):054010, 2014.

CHAPTER 3

Sensitivity of Self-organized Pattern to Operation Variables

3.1 Introduction

Operating an atmospheric glow discharge follows the fundamental mechanism of low pressure plasma yet it is necessary to analyze and optimize the parameters to fit its application needs. Two major elements feature the most important differences: 1) Operating at atmospheric pressure is cheaper yet overheating and thermal instability can be problematic. The air and humidity in the gas phase complicate the plasma species composition and associated chemical reactions; 2) The presence of liquid electrodes establishes many new coupling processes and channels for reactive species. Many parameters in the liquid and plasma-liquid interface are non-linear with the operating variables. As reviewed in section 1.4, SOP is sensitive to many variables including oxygen fraction [1], liquid conductivity [2], liquid temperature [3], and discharge current [4]. Conducting comprehensive diagnostics on the correlations between the variables and pattern dynamics would be paramount.

Research on the characteristics of glow discharge over a liquid electrode is not scarce. Staack *et al* investigated a glow discharge over a metallic electrode and found that the radius of such discharge is the result of balancing heat generation and cooling by particle diffusion [5]. Titov *et al* reported the electric field at the positive column of 900 V/cm and the independence of the N_2 vibrational temperature of discharge current [6]. Verreycken *et al* measured the change of plasma current density and the correlations of SOP with the discharge current [2]. Results indicated that the pattern spots linearly increase with elevated current and the pattern diameter increases as the water conductivity decreases. A conical shape DC glow discharge over a water anode was reported by Miao *et al* who investigated the discharge structure's change with the variation of liquid conductivity, cathode diameter, and air gap [7]. Zhang *et al* showed that different acid electrolytes can stimulate distinctive pattern shapes and hypothesized that it is attributed to the electronegative gas from electrolysis [8]. Another research on the impact of electrolyte type was conducted by

Kovach *et al* suggested that SOP presents varying degrees of complexity on different electrolytes, especially in the unstable lower current regime [9]. Shirai *et al* conducted several experiments to show that a larger discharge gap, higher liquid temperature, the presence of oxygen, and high liquid conductivity all favor the formation of a pattern [10, 4, 1].

Importantly, consistent characteristics of the plasma and the associated SOP can be found across the board in the aforementioned research studies though they were conducted under different experimental conditions. On the other hand, strict control over experimental variables is necessary when investigating their individual impact. For instance, the Joule heating at the plasma column evaporates the water at a rate of 1.28 mL/min, leading to liquid surface level drops and thus an increase in the air gap. The liquid conductivity and temperature rise at the same time and affect the pattern dynamics [11]. The pattern and plasma could respond to not only the actively adjusted parameters but also these passive dynamics. The goal of this chapter is to perform a comprehensive measurement of the plasma properties and pattern dynamics on the change of various parameters including discharge gap, current, working gas flow rate, nozzle orifice size, liquid conductivity, and liquid temperature. Current-voltage characteristic curve, electric field, and the SOP area will be measured and their sensitivity with the above parameters will be investigated. In addition, a Schlieren diagnostic is implemented to visualize the fluid convection at the periphery of the plasma column where heat transfer and air entrainment are coupled. Combining the above measurements, the coupling mechanisms among the gas phase, liquid phase, and plasma physics and their importance in pattern dynamics are discussed.

3.2 Diagnostics Method

3.2.1 Electrical Parameters

A typical I-V characteristic curve is shown in Fig 3.1 where the black curve is the total voltage including the plasma column and liquid phase. The error of voltage and current is within $\pm 3\%$ and applied to all the following I-V measurements. The impedance of the liquid phase and silicon ground plate contribution was measured by immersing the cathode in liquid which was then subtracted from the total voltage. The red curve represents the plasma-only impedance. The red curve now presents a negative slope at low current attributed to the gas temperature rise which is known in the glow discharge operation. Note that the measured liquid impedance (blue curve) would not be the same as those in plasma operation since the contact area, liquid convection, and electrolysis process will be different. On the other hand, the liquid impedance mostly depends on the liquid conductivity as demonstrated in Fig 3.2, thus this method is reliable to deduce the I-V characteristic curve. Besides the plasma impedance, the estimation of the electric field should also

be included for it governs the energy input into the electrons. However, it is the usual practice to use the reduced electric field E/N because it also includes the electron-neutral collision loss which balances with the ionization. In our case, the reduced electric field is measured with the change of discharge voltage when the discharge gap is varied. The neutral density is estimated by the rotational temperature of the nitrogen second positive system spectra $\mathrm{N_2(C-B)}$ that is fitted with a kinetic model [12].

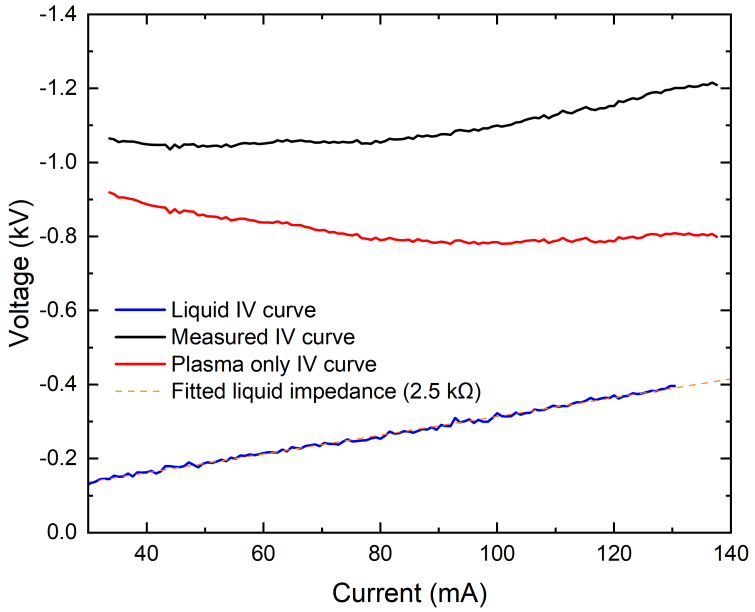

Figure 3.1: Current-voltage curve of glow discharge and liquid phase (liquid conductivity: 1.05 mS/cm, temperature: 28 °C)

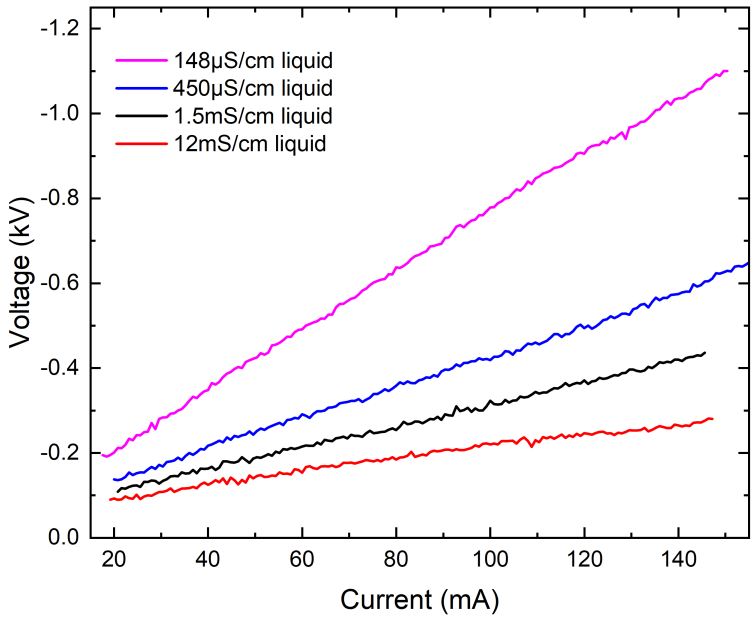

Figure 3.2: Current-voltage curve of liquid phase at different conductivities

3.2.2 Imaging of the Self-organized Pattern

The documentation and diagnostics of a SOP usually rely on a conventional imaging recording device. In this case, a CMOS camera (Photron FASTCAM miniUX100, resolution 1280x1024, exposure time 20 μs) is used to capture the SOP image. An issue for the pattern image acquisition was noted when the electrode obstructed the normal angle line of sight of the pattern. Thus, the camera was pointed at the SOP with a 45 degree angle, and the perspective distortion was fixed by the keystone correction method [13] in the post-processing function as shown in Fig 3.3. The emission from a SOP is the anode glow where energetic electrons accelerated by the anode fall electric field excite nitrogen molecules. Estimation of its surface area can provide insights into the anode current density and how it affects the plasma operations. Fig 3.4 presents the post-processing of the pattern image. First, the histogram equalization method is used to increase the global contrast of the image. The bright positive column superposes the pattern and interferes with the area estimation. This is addressed by stretching the color spectrum. This enhances the color separation across highly correlated channels and the pattern area is much more visible than the positive column. Finally, a color spectrum filter is applied to isolate those pixels representing a SOP. Specifically, the pixels' blue channel value smaller than 60% of the channel size are filtered out which leaves the pattern image. Counting the number of the rest pixels and times the pixel length scale indicates the pattern area. Unfortunately, such a method is not ideal at a current higher than 80 mA where the volumetric heating causes extensive vapor and bright emission from

the positive column. They heavily interfere with the pattern image and deteriorate the accuracy and precision. It is also worth noting that sometimes the streaking shape in a dynamic pattern is a motion blur which causes difficulties in surface area estimation. In addition, the pattern may not fully represent the conductive channel of the anode since the positive column lacks the self-organized shape yet the extent of the pattern is correlated with the column size. Therefore, the estimation of pattern size and anode current density is based on the perimeter (SOP footprint) but not the emission area.

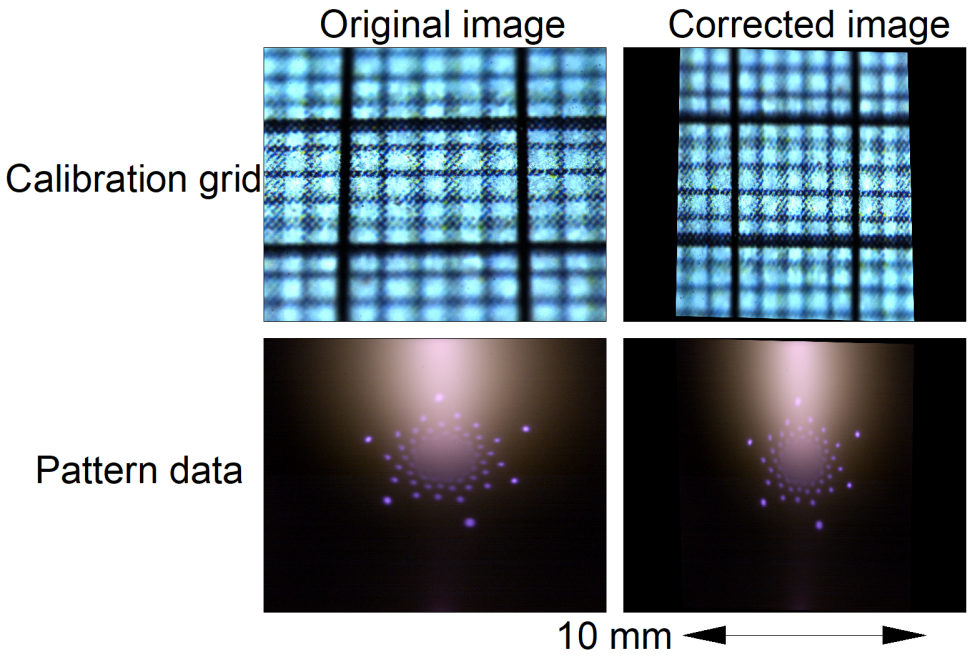

Figure 3.3: Keystone correction for the acquired image

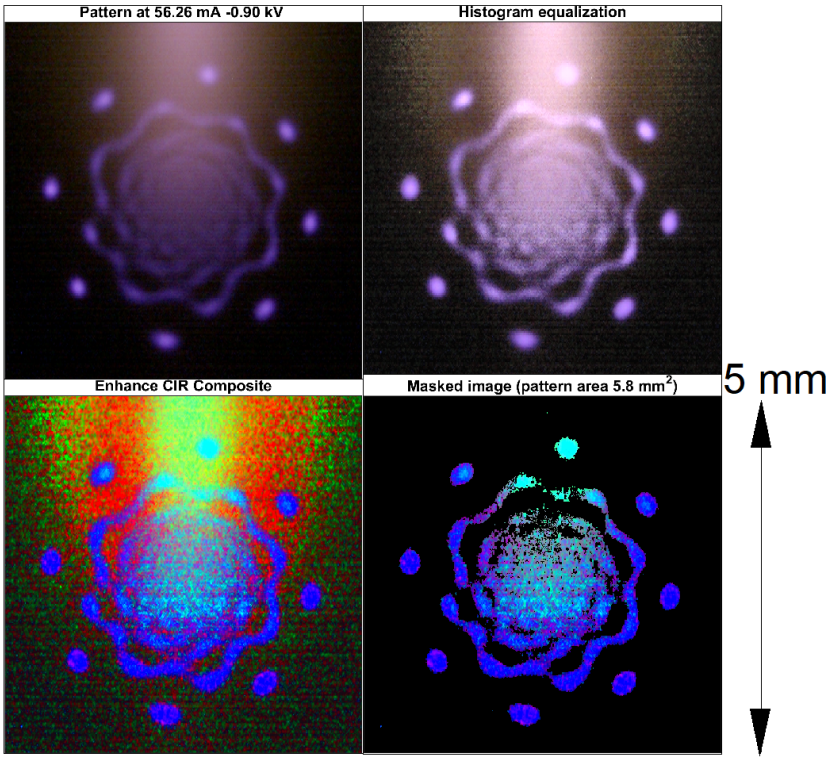

Figure 3.4: Estimation of the pattern area using post-processing and color spectrum filter

3.2.3 Schlieren Diagnostics

Schlieren imaging is a classical diagnostic method used to visualize the fluid flow field. The diagnostic is sensitive to variations in density gradients due to pressure from high-speed flow or expansion from heat as these give rise to variations in refractive index [14]. The fundamental principle is to have a collimated light beam in z direction pass through the objects of interest in which refractive-index gradients $\partial n/\partial x$ and $\partial n/\partial y$ refract light rays in a small angle. The refracted rays are brought into a sharp focus by a parabolic mirror and then blocked by a razor edge or spatial, leaving the undisturbed rays. Thus, the image with prominent contrast is registered where dark regions indicate the density gradient and bright regions correspond to the homogeneous medium. Such diagnostic is proved to be straightforward and has been successfully used in many plasma sources since the gas phase is transparent and heat convection usually coexists with a discharge [15].

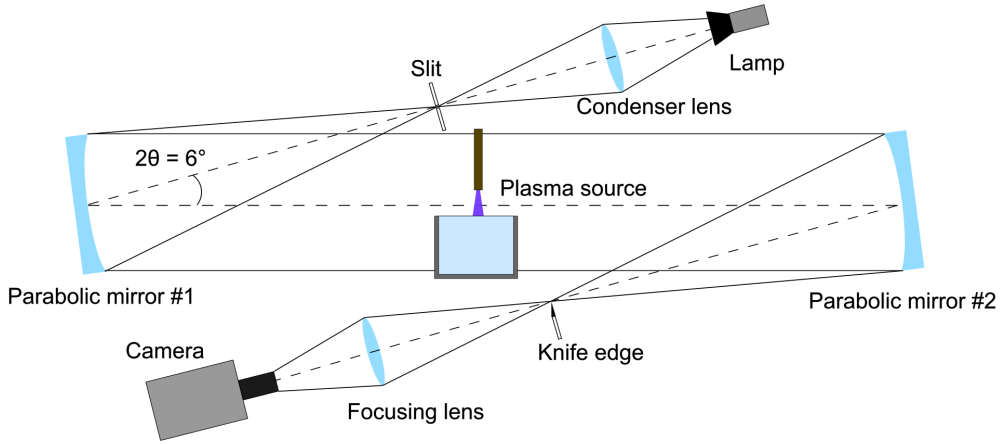

Figure 3.5: Schematic of a Z-Type Schlieren setup

Fig 3.5 illustrates a Z-Type Schlieren setup that is used to visualize the fluid flow of the glow discharge with a liquid anode. It consists of a halogen lamp as the light source, a condenser lens to concentrate the lamp light towards the mirror, an adjustable slit (0.5 mm opening) to configure the measurement range, a pair of parabolic mirrors to create the collimated rays (focal length 75 cm, $f/D = 10$), another slit used as knife edge to change the sensitivity, a focusing lens to concentrate the rays into the camera, and a digital camera (Photron FASTCAM miniUX100) to record the image.

3.3 Plasma Column Dynamics

3.3.1 Basics and Structure

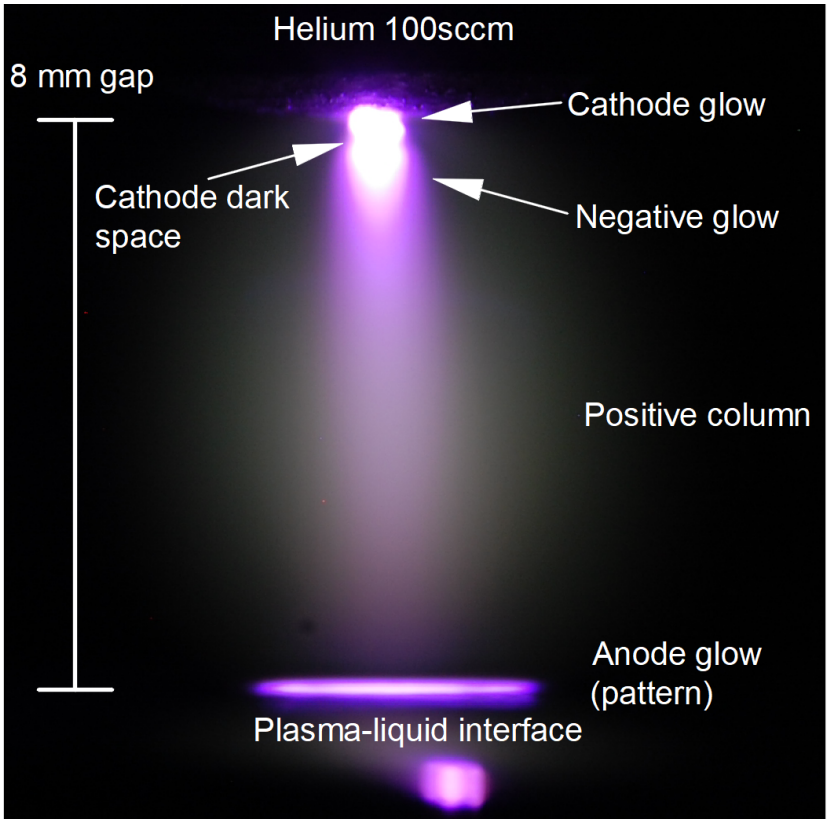

Figure 3.6: Structure of the discharge column (discharge at 30 mA, -930 V)

Observing the shape of an atmospheric plasma is especially important since the high pressure would greatly decrease the particles' mean free path and thus the macroscopic geometry is more constricted and informative. A snapshot of the discharge over the liquid anode is shown in Fig 3.6. Surprisingly, its features are analogous to a low-pressure glow discharge. A bright cathode fall region lies under the electrode nozzle and comprises cathode glow, cathode dark space, and negative glow. Cathode glow's thickness is estimated to be 200 µm. As was discussed in the section 1.2, the thickness of the cathode, and anode glow region depends on the order of the electron mean free path which is about 66 µm according to Eq 1.2. This can explain the very thin cathode dark space that is barely seen between the cathode glow and the negative glow. The cathode and anode voltage drop can be estimated by the linear curve of the discharge voltage as a function of the discharge gap when extrapolating it to zero gap. Normally, the positive column has an electric field strength between 600-800 V/cm, and subtracting it leaves one with the cathode and anode voltage

drop that ranges between 290-450 V which is close to 370 V for an air discharge in between brass electrodes [16]. An electric field over 20 kV/cm is estimated via the emission ratio of $N_2^+(B-X)$ versus $N_2(C-B)$ whose excitation threshold is different [17].

Near the end of the negative glow follows the less bright and diluted positive column. Interestingly, the positive column is not homogeneous in the transverse direction where the center is purple and surrounded by sparse hot air emission as a bulb shape. OES suggests that the purple emission is mostly from nitrogen's second positive system ($N_2(C-B)$) whereas the bulb shape is from $OH(A-X)$ emission. The differences between the brightness and density are owing to the weaker electron energy distribution function (EEDF) at the periphery of the positive column at a high energy range not only due to the faded electric field but also stronger collisional loss with the neutral molecules. On the other hand, nitrogen $N_2(C-B)$ emission has the electron energy threshold of 11.2 eV [18] whereas $OH(A-X)$'s 4 eV threshold [19] is much lower and thus easier at low EEDF.

On the plasma-liquid interface, a bright planar anode glow can be observed and its size grows with the positive column and current. This size change is to accommodate the additional current for constant current density and heat balance which will be elucidated later. The anode glow is organized due to the negative space charge gathering near a relatively positive electrode surface and becoming a sheath. On metallic electrodes, the glow resembles a small but bright spot whereas a sophisticated pattern is formed on a liquid anode. Although a SOP's diameter is correlated with the positive column and as is the anode current density, no corresponding self-organized structure can be found in the positive column. The anode glow has a 100 μm thickness and its emission mostly consists of $N_2(C-B)$ and $N_2^+(B-X)$. An obvious emission of N_2^+ means a strong sheath electric field is formed which establishes the SOP while its radial field distribution is unknown and critical to understanding the detailed mechanism.

3.3.2 Plasma Column under Various Conditions

The operation variables can impose significant impacts on the discharge column as can be seen in Fig 3.7. The positive column at 30 mA is rather constricted since the gas temperature is low and does not fully expand the neutral gas. As the discharge current increases, so as the total discharge power, the diameter of the positive column experiences remarkable growth whose growth rate with medium current is fast but slower at high current. This size change comes from the need for heat balance and constant current density. In a self-sustained glow discharge, the potential drop over a cathode layer is constant and only changes when the electrode material or gas composition differs. This normal voltage drop across the cathode layer guarantees a critical ionization rate for producing electrons and ions to sustain the discharge, so a normal glow discharge would have

unchanged current density and the increased current would need a larger area to dissipate.

On the other hand, the size change can also be coupled with the heat transfer process. The positive column is a volumetric heat source that is cooled by the heat conduction at the cathode, heat transfer at the radial surface, and the evaporating heat exchange at the liquid anode. Here, we mainly discuss the last two processes since the cooling on the brass electrode is constant. The heat balance in a glow discharge column is:

$$Q = I(V_c + E \times d) = 2\pi R d \frac{k_1(T_g - T_0)}{R\ln(R_\infty/R)} + \pi R^2 k_2 (T_g - T_0) \tag{3.1}$$

where V_c is the cathode fall voltage drop which is constant; E and d are the electric field and length of the positive column, respectively; k_1 and k_2 are heat transfer coefficients at gas phase and plasma-liquid interface; T_0 is the ambient temperature; R is the positive column radius. If k_1, k_2 stays constant, the radius R has to increase to balance the climbing power. Otherwise, the increased temperature would further expand the gas volume and grow into a larger radius. More importantly, the contribution of heat transfer at the anode and radial surface are not the same at different radii. The heat transfer rate ratio between them is $(R^2\ln(R_\infty/R))/d$ and increases with the radius. This means the anode heat transfer becomes more important as the power increases. Because the surface area of a circle grows with the second order of radius, the increase in radius will be slower at a high current since the current density stays constant. Note that the comprehensive thermal dynamics is more complex where the evaporated water vapor, convective flow, and liquid circulation are evolved, but the increase of plasma column radial size with power is fundamental for heat balance and constant current density.

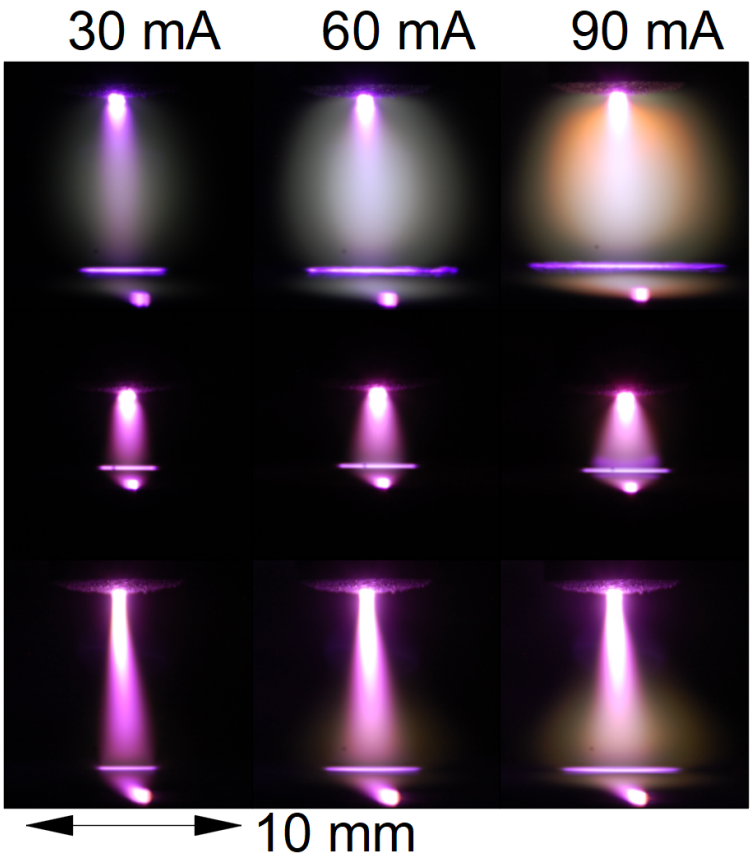

Figure 3.7: Discharge column at different gaps and helium flow rates (first row 100 sccm 8 mm gap, second row 100 sccm 4 mm gap, third row 300 sccm 8 mm gap)

When the discharge gap is halved as shown in the second row of Fig 3.7, the plasma column changes correspondingly where the radius of the positive column and the anode both decrease since the power of the plasma scales with gap d, so as the gas heating rate. Furthermore, the smaller gap also decreases the entrainment rate of air into the plasma column which means a larger mass fraction of helium atoms. This would decrease the attachment loss and energy input towards the vibrational excitation of molecules. $N_2(C-B)$ emission also contributes more because the evaporation is less intense and thus less OH is produced. The third row in Fig 3.7 shows the column at 300 sccm helium and shares many features with the small gap case. The radius of the positive column and anode are smaller than the low flow rate case since the higher flow rate decreases the overall gas residence time and a higher helium concentration in the plasma increases the overall thermal conductivity and lowers the discharge voltage needed as well as the gas heating rate. In fact, the plasma column resembles an atmospheric pressure plasma jet (APPJ) though it is mostly caused by the high-speed helium flow instead of the ionization wave found in an APPJ. A brighter emission is also observed since the higher helium mass fraction limits the gas heating and electron

loss to the collisions with ambient molecules, thus raising the electron energy.

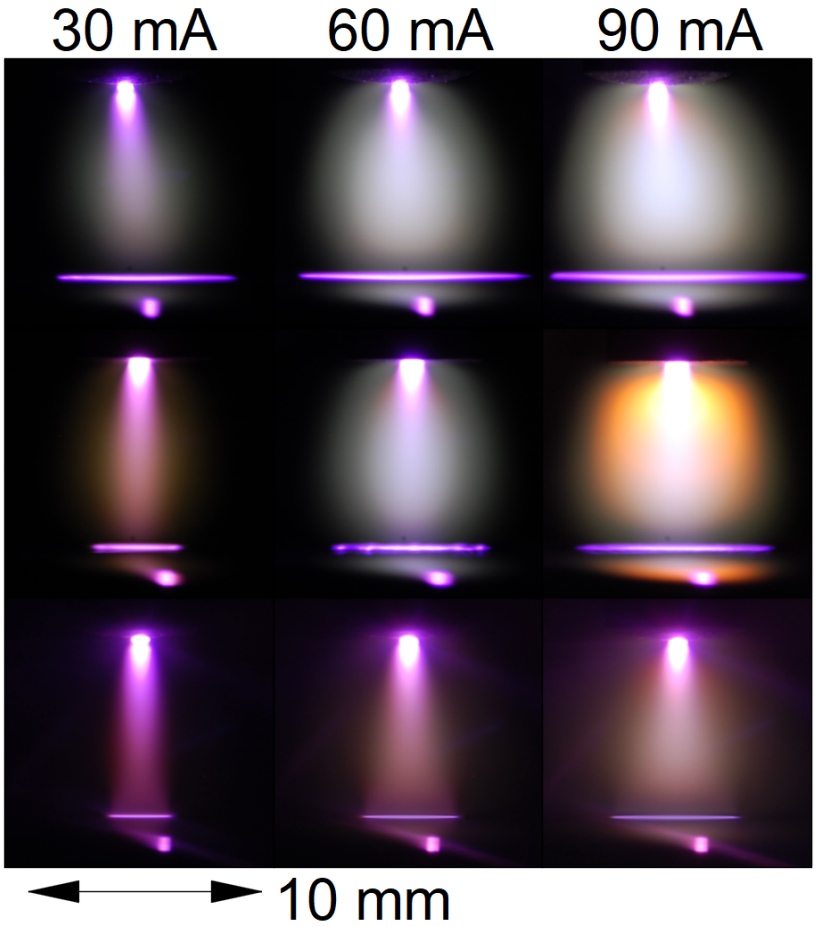

Figure 3.8: Discharge column at various conditions (first row 90 µS/cm liquid anode, second row 1 mm orifice, third row 4 % oxygen in ambient air)

In Fig 3.8, the plasma columns under special conditions are shown. In the first row, the liquid conductivity (90 µS/cm) is one order of magnitude lower than the other cases ($\sim$1 mS/cm). Note in this case there is a significant increase in the anode pattern radius which decouples from the positive column size. In a plasma-liquid interface, the anode sheath electric field not only depends on the plasma phase but also the ionic strength of the liquid phase [20]. Although the ionic strength is not linearly dependent on the conductivity, they are closely related at low-value range. The current density can be expressed in an exponential function of the liquid ionic strength:
Current density as a function of ionic strength[20]

$$j(I_s) = j_\infty \frac{1 - \exp(-\kappa I_s)}{\mathrm{erf}(\sqrt{\kappa I_s})} \tag{3.2}$$

where I_s is the liquid ionic strength, j and j_∞ are measured and maximum normal current density, κ is a scale factor. This inflicts an exponential decrease of the current density at low ionic strength and thus the large anode glow radius is correlated with the low current density. The larger anode spot is also ascribed to the space charge spreading near a lossy dielectric medium where accumulated space charge would enhance the local electric field. The second row shows the plasma column under the bigger nozzle orifice which does not change notably. However, the threshold of SOP was shifted and it is correlated with the weakened gas boundary layer since the helium is prone to diffuse at a lower flow speed. The plasma column under 3 % oxygen in the ambient air is shown in the third row where several differences are observed. The anode glow is thinner (∼50 µm) and smaller in radius since a low oxygen fraction gas phase manipulates the chemical reactions and gas heating in the positive column. A thinner and smaller anode region implies that the sheath electric field is weaker or there is simply more dissipation with a low oxygen level though a quantitative analysis is unavailable in this work.

3.3.3 Neutral Gas Density Gradient in the Plasma Column

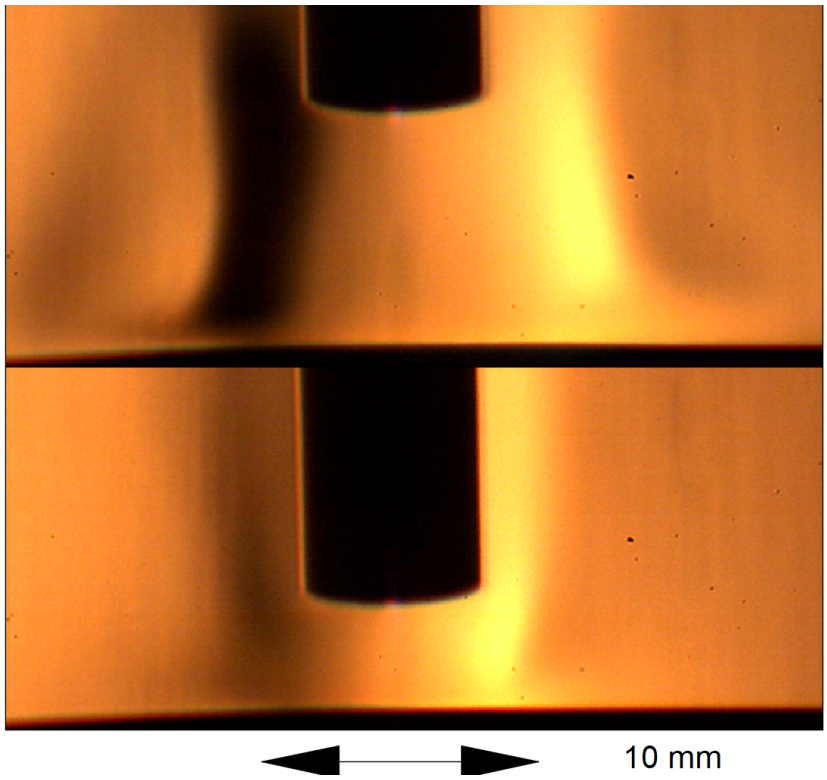

Figure 3.9: Neutral gas density gradient at different air gaps (Top: 8 mm gap, bottom: 4 mm gap)

The remarkable difference of positive column relies on many coupling processes among which the particle kinetics and thermal dynamics are the most important. Here a Schlieren imaging system is implemented to visualize the neutral gas density gradient at the positive column which is driven by the heat expansion so a thermal process can be indirectly analyzed. Fig 3.9 demonstrates the density gradient at various air gaps. At the 8 mm gap, the heat expansion of gas creates a boundary layer at 13 mm diameter. In contrast, the 4 mm gap forms a smaller boundary and gradient which reduces the gas mixing. This would suppress the air entrainment to the positive column and thus lower the gas heating rate. If the convection and heat expansion are critical for the air species mass transport in the plasma, the coupling between gap and plasma parameters such as electron temperature, and density is nonlinear.

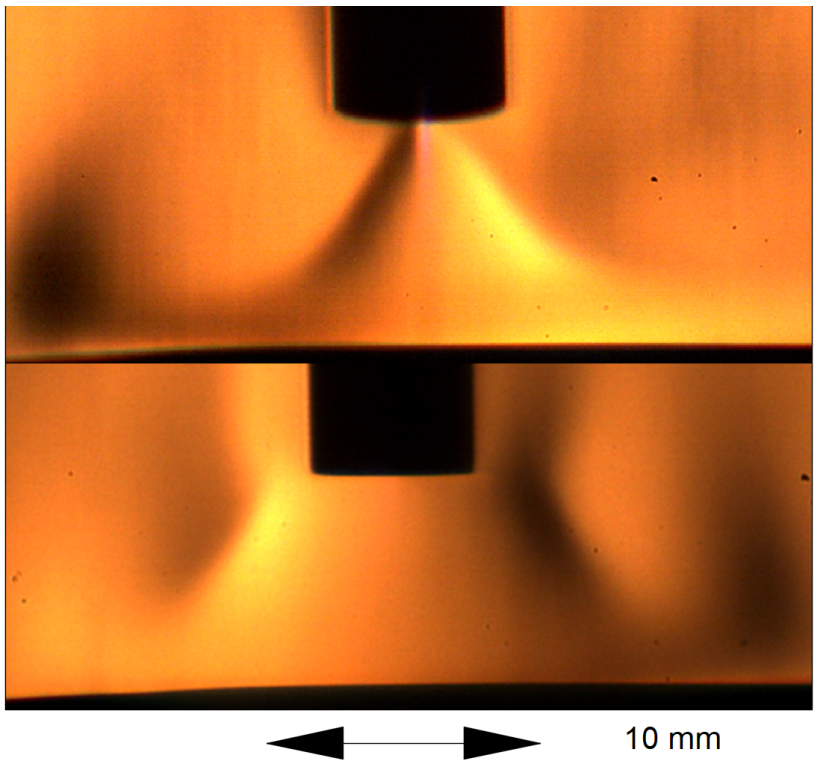

Figure 3.10: Neutral gas density gradient at 300 sccm helium flow rate (Top: 0.5 mm orifice, bottom: 1 mm orifice)

A higher flow rate of helium is also able to heavily affect the thermal process in the plasma by affecting the air species' mass fraction and chemical reactions. Fig 3.10 presents the neutral density gradient of a plasma with 300 sccm helium flow rate. Compared with 100 sccm case in Fig 3.9, a conical shape boundary layer is established near the cathode orifice revealing the nonlinear effect of flow rate. This jet structure would highly limit the entrainment of air and further reduce

the gas heating rate. Helium is an atomic gas and features a strong diffusion tendency which makes the flow speed a dominant factor in the plasma dynamics, not only the mass flow rate. The bottom image in Fig 3.10 shows the gas density at 300 sccm helium but with a larger orifice. The conical shape is replaced by a contracted "bottle neck" boundary layer that is wide and dissipated just like the 100 sccm case. A large opening would help the helium to diffuse radially and fail to form a jet which constricts the air mass transport and gas heating. This makes the low-speed but high-flow rate helium operating conditions have a lower effective performance for cooling, plasma properties, and pattern dynamics.

3.3.4 Current-voltage Characteristics

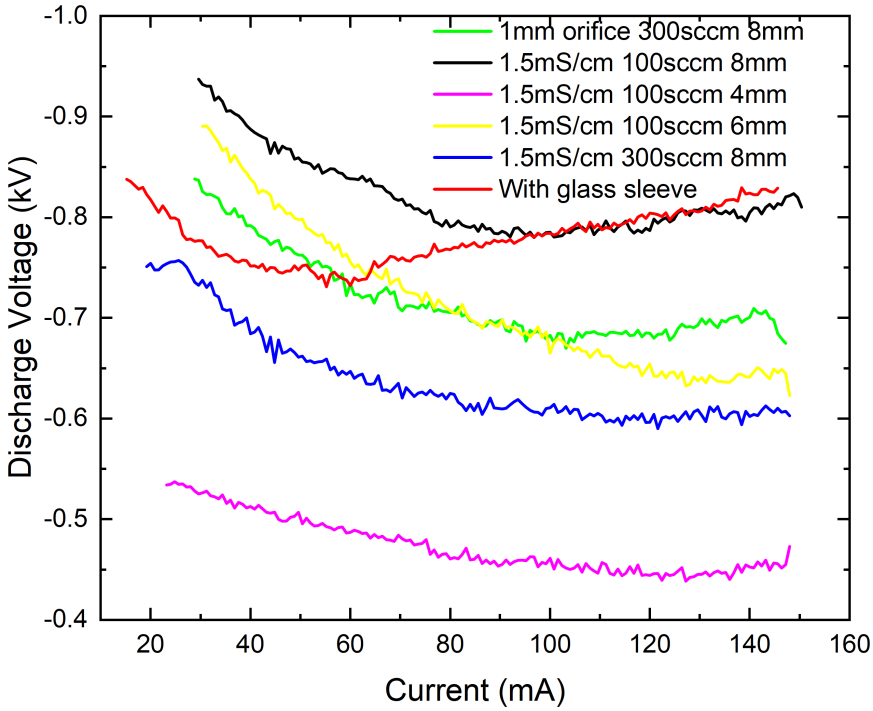

Figure 3.11: Current-voltage characteristic curve of plasma operated at different air gaps and flow rates (conductivity 1.5 mS/cm)

Fig 3.11 plots the I-V characteristic curve of a glow discharge at different air gaps and flow rates with liquid anode. Note that the current signals frequently come with fluctuations in the $\sim$ 100 µA scale. These fluctuations are from the disturbance of the liquid surface, the spark on the brass cathode, plasma column movement by the ambient air convection, and the SOP dynamics. Overall, they do not remarkably affect the I-V characteristics. At low current, all the curves indicate a negative slope $\mathrm{d}V/\mathrm{d}I$ which was also reported in other research [5, 2]. This is partially related to

the Joule heating in the positive column that a rising gas temperature with current reduces the local neutral density thus reducing the need for electric field for a constant E/N. At the same time, the growth of the discharge column and anode glow radius with current inflict the decrease of current density that corresponds with the negative slope of I-V. A larger plasma column cross-section along with the increased gas temperature and reaction rate both contribute to the reduced plasma impedance at a high current.

Following the negative slope region, the discharge voltage enters a plateau regime where the voltage is independent of the current. This is a manifestation of constant current density which suggests the discharge is truly a normal glow discharge. The yellow and pink curves in Fig 3.11 plot the smaller gap's I-V characteristics where the discharge voltage is correspondingly decreased with the gap since the positive column has a uniform electric field. The blue curve shows the plasma impedance at a higher flow rate is lower than the 100 sccm case. This is mostly attributed to the low breakdown voltage of noble gas [21]. A higher helium flow can also decrease the electron loss to the gas heating and vibrational excitation of the molecule species. On the other hand, the discharge column and anode have a smaller radius and higher current density while it fails to raise the impedance and counteract the helium's cooling effect. Interestingly, not only the total flow rate but also the cathode orifice can affect the plasma impedance which is shown in the green curve. With a bigger opening at the nozzle, the boundary layer would be larger and introduce more air mixing thus effectively weakening helium's cooling effect just as using a lower flow rate. The higher gas heating rate also makes the plasma column less contracted and allows more air entrainment which has been discussed in the Schlieren results. Finally, a specific condition shown in the red curve represents the plasma I-V when a glass sleeve (10 mm diameter) is implemented around the plasma. In this case, the rate of ambient air entrainment is lower and shall be equivalent to a higher helium flow for cooling the plasma. However, the plasma column size is physically restricted by the sleeve like a chamber wall, and the plasma impedance starts to increase at a higher current since the column could not expand to compensate for the higher power and current density starts to increase. It is also possible that electron loss to the wall may contribute to the change of I-V.

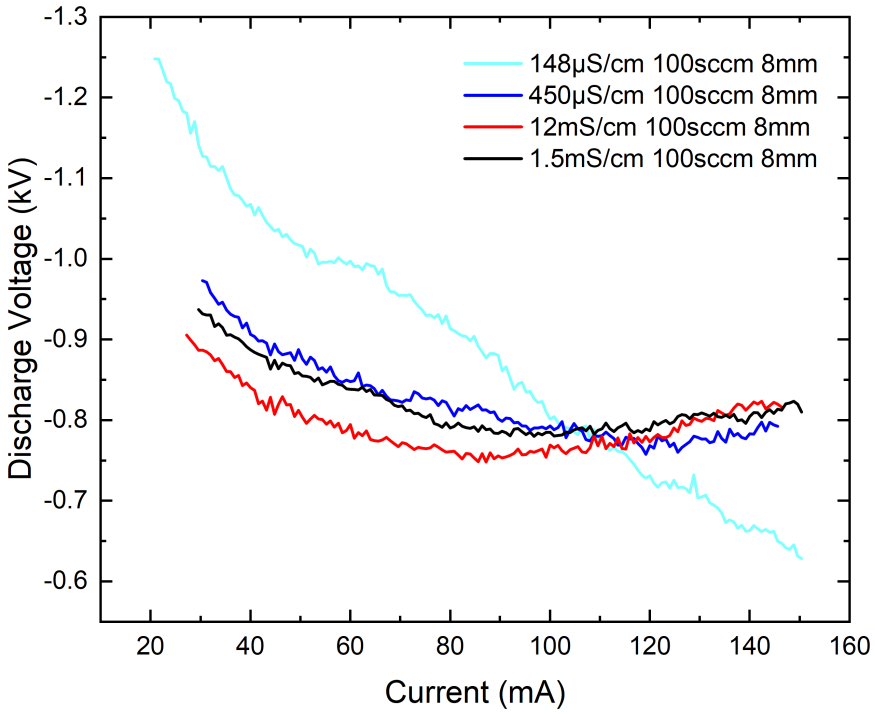

Figure 3.12: Current-voltage characteristic curve of plasma operated at different conductivities (8 mm gap, 100 sccm helium)

The impact of current density and anode size on plasma impedance can also be seen in Fig 3.12 where the 148 μS/cm liquid anode causes a steep negative slope of the plasma I-V characteristics. Note that the negative $\mathrm{d}V/\mathrm{d}I$ happens across the current range while all the other high conductivity cases have the same trend and same range of plasma impedance even though the conductivity is varied in different orders of magnitude. A similar result was reported in [2] where it was speculated the liquid conductivity increased with current at the same time during the experiment. In our case, the low conductivity water is fed by a tank although the liquid's local properties near anode attachment may be subject to a dynamic process. Across the different orders of magnitude conductivity, the plasma column impedance only has a strong variation on the low conductivity $\sim$ 100 μS/cm or 10 $\mathrm{k}\Omega \cdot \mathrm{cm}$. As Eq 3.2 suggests, the current density increases with ionic strength, and low conductivity, usually also means low ionic strength, would initiate a large anode spot to compensate for the low current density. Therefore, the development of anode size and positive column would induce a decrease in plasma impedance.

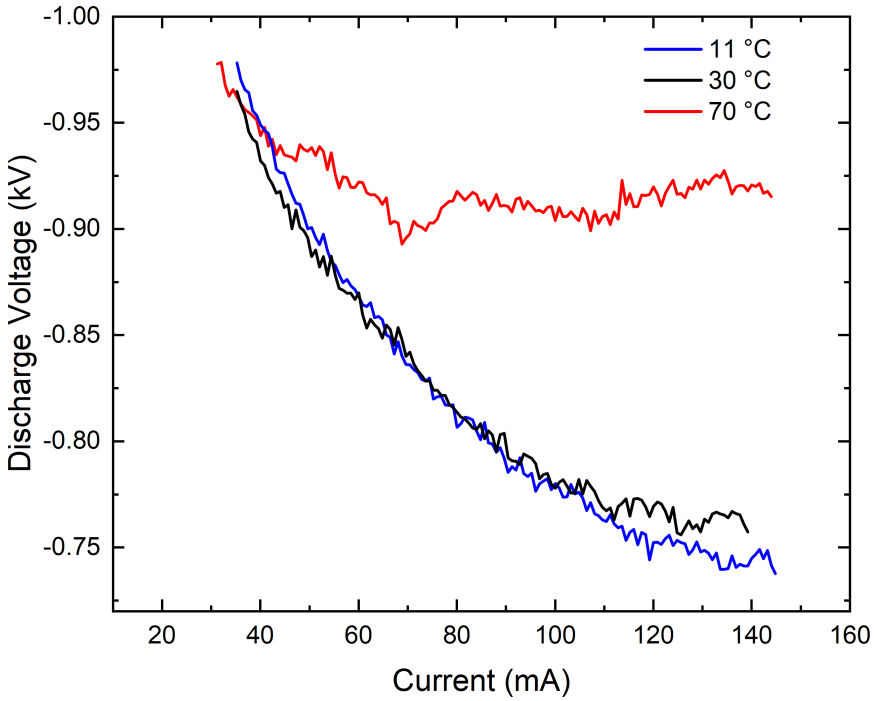

Figure 3.13: Current-voltage characteristic curve of plasma operated at different liquid temperatures (8 mm gap, 100 sccm helium)

Fig 3.13 plots the plasma I-V running with various liquid temperatures (conductivity is $\sim$ 875 µS/cm). The red curve representing the 70 °C case stands out significantly from the other low temperature results. A higher liquid temperature would increase the evaporation rate and lower the anode surface heat transfer rate due to a smaller temperature difference. This also causes a slower growth rate of anode size and increased current density that corresponds to the early plateau regime. The higher impedance is mostly attributed to the high vapor concentration which increases the electron attachment loss and lowers the mobility, thus increasing the plasma impedance. Plasma running over high temperature liquid has been proved to increase the sodium mass transport rate towards the plasma column by OES though the detailed mechanism may not be coupled with the evaporation [3]. Chapter 7 will illustrate our hypothesis where the sodium is carried by small droplets. Interestingly, these curves all start from the same level of voltage while ending up at different normal voltages indicating that the evaporation at low current is not a dominant factor no matter the liquid temperature.

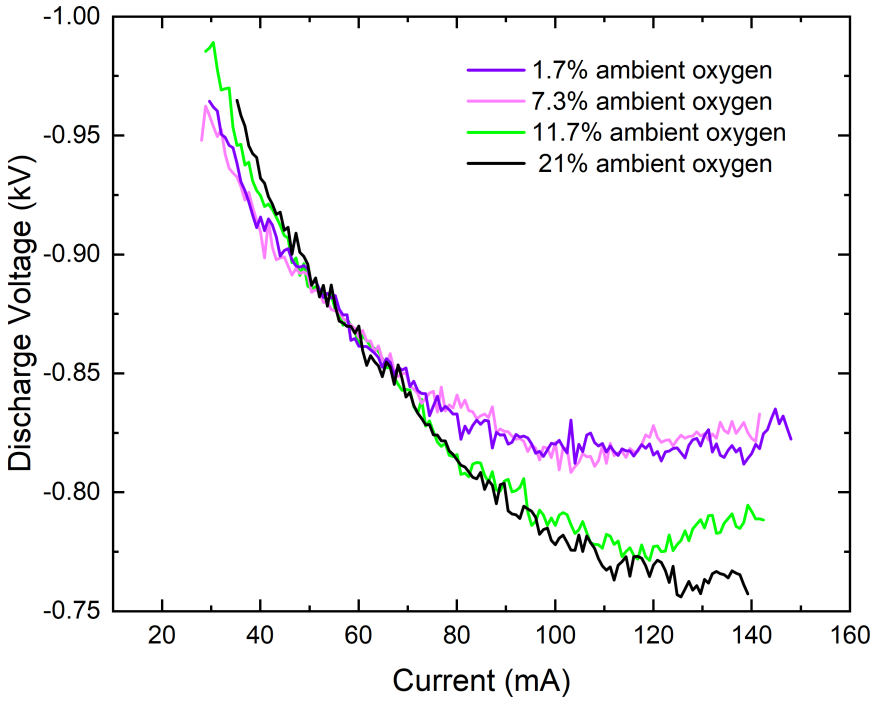

Figure 3.14: Current-voltage characteristic curve of plasma operated at different oxygen levels (8 mm gap, 100 sccm helium)

As indicated in Fig 3.14, the oxygen mass fraction in the gas phase does not inflict a serious variation on the plasma I-V. The green curve that represents 11.7 % oxygen level almost matches the nominal oxygen case (black curve) though the SOP already starts to decay into a featureless disk. At the threshold level of oxygen (7.3%), the entire SOP transforms into a diffusive disk, and the I-V curve suggests a larger normal voltage. This is mostly prompted by the small anode glow size which corresponds with a high current density. In any case, the oxygen mass fraction does not change the plasma I-V characteristics while it is surely a critical "ingredient" in the formation of SOP.

3.3.5 Electric Field at Positive Column

The reduced electric field in the positive column governs the electron temperature for it represents the energy balance between electrostatic force and collisional loss. Tab 3.1 lists the reduced electric field of a plasma under various conditions. The neutral density is calculated from the gas temperature that is based on the rotational temperature of $N_2(C-B)$. Note that only the emission at the plasma column's central axis is imaged on the spectrometer slit so the estimated temperature may not be able to represent the volumetric average value.

Table 3.1: Estimated electric field and E/N at positive column under various conditions

Conditions (50 mA, 100 sccm He, 1 mS/cm if unspecified)	Electric field (V/cm)	Gas temperature (K)	Reduced electric field (Td, $10^{-17}\mathrm{V}\cdot\mathrm{cm}^2$)
30 mA	900	2561	31.4
50 mA	750	2752	28.1
70 mA	600	2805	22.9
300 sccm	850	2237	25.9
152 µS/cm	483	2650	17.43
12 mS/cm	745	2611	26.38
$3\ \%\mathrm{O}_2$	820	2703	30.2
$80\,^\circ\mathrm{C}$	870	2482	29.4
Glass sleeve	370	2036	10.3

The reduced electric field and electric field both decrease as the discharge current increases. The high electric field at low current is attributed to the constriction of the positive column which corresponds to a high current density. Gas temperature rises with current inflicts the drop of neutral density at the positive column which then decreases the electric field for a constant E/N. At the same time, the lower neutral density also facilitates the electron mobility $\mu_\mathrm{e} = \frac{\mathrm{e}}{\mathrm{m}\nu_\mathrm{en}}$ and lowers the required E/N. For a higher helium flow rate, the gas temperature and reduced electric field are both reduced because of the cooling effect of helium. Nobel gas like helium is well-known for reducing the breakdown voltage and E/N when running an atmospheric plasma [16].

Interestingly, the electric field of the positive column over low conductivity liquid is remarkably low. It is not clear whether the positive column's current density is affected by the anode region. If so, a larger anode may provide more conductive channels and make the plasma more conductive. Higher conductivity, on the other hand, does not promote significant variation. No distinctive change happens in the E/N with a low oxygen mass fraction in the gas phase. Although oxygen is critical for anode pattern, the bulk plasma collisional loss is dependent mostly on nitrogen which dominates the ambient air. Gas temperature decreases with a higher liquid temperature which is not expected. It is speculated that the larger vapor concentration quenches (depopulation of the excited state by collisions without the emission of a photon) with the nitrogen species and falsely reduces the rotational temperature. On the other hand, if the quenching by water molecule does not reduce the lifetime of $\mathrm{N}_2(C)$ as fast as the rotational-translational relaxation time ($\sim$ 0.6 ns), the rotational state is thermalized and trustworthy as gas temperature. In this case, the

temperature decrease is due to the cooling by extra evaporated water molecules and collisional processes. Finally, a physical wall around the plasma column can significantly reduce the electric field, gas temperature, and E/N. This is mainly ascribed to the semi-closed wall establishing a higher ionization degree by decreasing the diffusion loss of electrons. At the same time, air molecules are harder to participate in the plasma and effectively increase helium's mass fraction and weaken the collisional loss by molecules. Note that this sleeve can extend the plasma column as far as 10 cm thanks to the very low discharge voltage and diffusion loss. This method can be useful if a low gas temperature or E/N is needed for a large volume glow discharge at atmospheric pressure.

It was reported that the pattern requires at least 16.6 Td to be formed in [22] which is only not satisfied in the glass sleeve case. However, the E/N in the low oxygen case is much larger but failed to establish the pattern. Either way, it is clear that the SOP is subjected to many coupling processes that make the identification of threshold confusing.

3.4 Self-organized Patter under Various Conditions

3.4.1 Evolution of Plasma Self-organized Pattern with Current

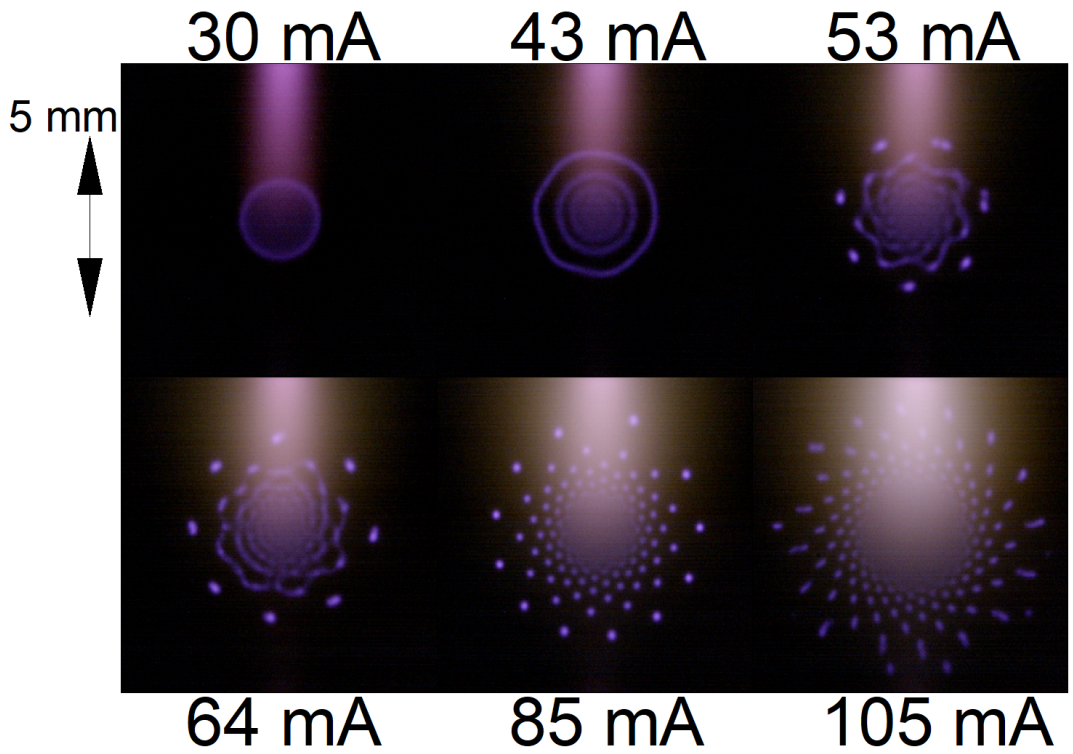

Figure 3.15: Plasma SOP at different currents (100 sccm helium, 6 mm gap, 1.2 mS/cm liquid)

Fig 3.15 shows the plasma pattern evolution with current (power). The evolving process is not linear while the consistent characteristics can be described. The attachment at a very low current ($\sim$15 mA) manifests as a small spot that is unstable and prone to extinguish. This is due to the negative slope of I-V curve at low current which is uncoupled with the circuit's load line [16]. As the current rises to $\sim$30 mA, a thin ring detaches from the disk while the center spot stays intact. Interestingly, the ring sometimes could transform into a hexagon that recalls the pattern found on Saturn's pole (Fig 1.6a). The ring increases its radius with the current, and multiple concentric rings would occasionally form. At $\sim$50 mA, the outer ring breaks into segments or dots and the inner ring or disk is also no more diffusive but reconstructed into a group of spots that resemble the shape of a dielectric barrier discharge pattern. At this moment the gas heating is prominent where the convective flow and plasma instability drive the pattern to rotate. Many of the dots or segments would also recombine or retreat away from the central part of the pattern and a new one would born quickly to fill the vacancy. Note that these cycles of events are more prominent when more

gas heating is involved, including low helium flow, a larger discharge gap, or a prominent ambient gas flow causing some dynamic motion. Schlieren imaging has revealed that these conditions can prompt more gas mixing and convection at the positive column. From this point, a further increase of current would only produce more but limited layers of dots or segments while the fundamental shape would not change.

Nonetheless, the pattern shown in Fig 3.15 only represents one of the evolution processes. For instance, a SOP can form many long spokes instead of spots or short dashes when the helium flow rate is high. Spokes, dashes, spots, and the central disk are the basic elements that establish a coherent pattern shape and they are essentially the excited space charge at anode sheath. In the theoretical study of SOP, bifurcation and multiple solutions theory are used to explain the process by which a small change in a controlling parameter leads to a remarkably different set of configurations, such as dissimilar patterns for the same value of the voltage and current [23]. Imagine the state of the plasma anode glow as a ball trying to find its lowest potential well whereas multiple valleys are around and each of the spots and spokes are balls that fall into the metastable valley. On the other hand, it is found that many controlling variables are critical to change or even preclude these metastable valleys. By recording the inflicted pattern evolution from controlled variables it is possible to resolve the condition that triggers the bifurcation events.

3.4.2 The Impact of Discharge Gap

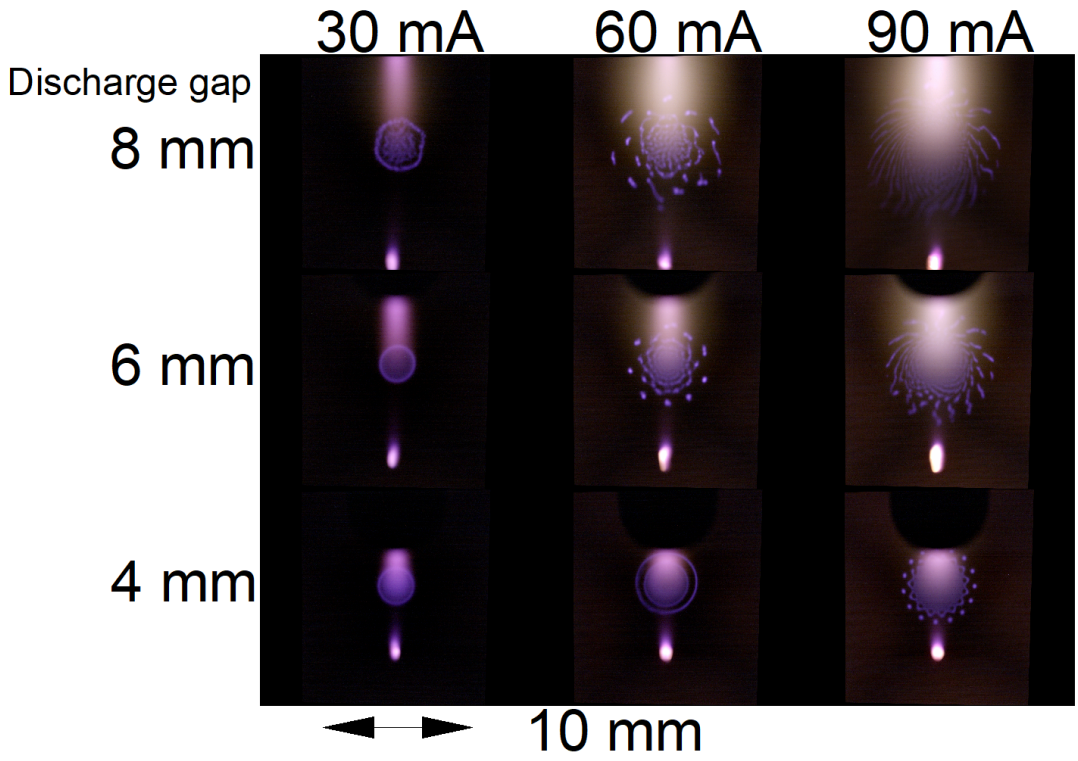

Figure 3.16: Plasma SOP at different air gaps (100 sccm, 890 μS/cm)

The SOP's variation at different air gaps is shown in Fig 3.16. The radius of the pattern becomes smaller with decreasing discharge gap because a shorter positive column generates less gas heating, thermal expansion, and a smaller anode area for heat exchange. A notable distinction is that a smaller air gap will delay the evolution of the SOP with current, i.e., the different phases of the pattern start at a higher current threshold. The shape of the pattern also changes dramatically at the 4 mm air gap where the number and layer of dissipated dots are much smaller and they are inclined to stay closer or attached to the center disk. There is a ring of bounded segments that form a polygon which is actually a group of attached dots. They failed to develop into isolated dots due to the restricted anode size from lower gas heating. At a smaller air gap (<2 mm), the anode glow will stay as a diffusive disk without evolution even at high current. A larger air gap (>8 mm) does not fundamentally affect the shape but only adds more dots and chaotic motion. Overall, the air gap affects not only the gas heating and convection rate but also the aspect ratio of the plasma column. In this case, a larger air gap allows more air species to transport into the plasma and thus lower the helium mass fraction. At the same time, anode glow size is correlated with the plasma

radius so as the outreach of the SOP and the complexity (layer of dots, dashes). The change of patterns with air gap hereby reveals that the SOP's size and complexity are coupled with the air entrainment.

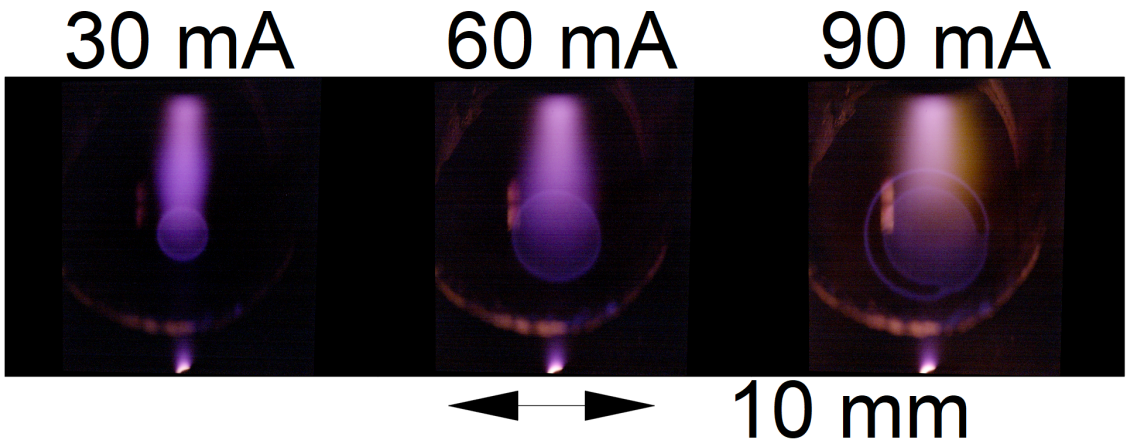

Figure 3.17: Plasma SOP with a 10 mm diameter glass sleeve (8 mm gap, 1.2 mS/cm)

The importance of air for SOP can also be justified in Fig 3.17 where a glass sleeve is put around the plasma column. It forms a physical wall around the plasma that blocks the air entrainment from the positive column. A physical boundary would reduce the diffusion loss of electrons and less air entrainment effectively weakens the collisional loss towards molecules excitation. This is proved by the exceptionally low gas temperature from OES and low discharge voltage listed in Tab 3.1. Interestingly, the pattern stays as a diffusive spot as the current is raised which suggests the importance of air in SOP. On the other hand, the anode sheath electric field distributions in radial and axial components are expected to be different as the glass wall can affect the space charge by its floating potential and a lower anode layer voltage from low electron temperature.

3.4.3 The Impact of Helium Flow Rate

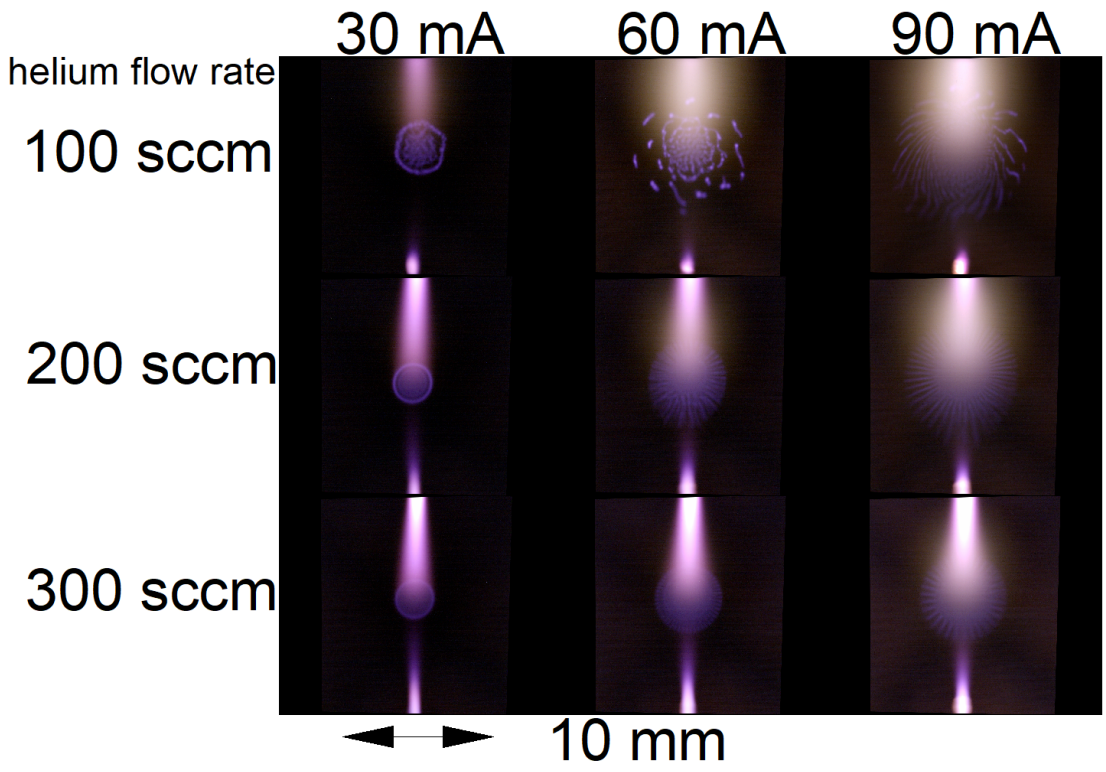

Figure 3.18: Plasma SOP at different helium flow rates (8 mm gap, 890 µS/cm)

Helium is well-known for its cooling effects as a working gas, not only because of the faster diffusion time but also the lower breakdown voltage and lack of vibrational excitation loss. Fig 3.18 supports the argument where the pattern is much more compact and organized which corresponds to the constricted positive column shown in Fig 3.7. Specifically, only spokes are formed in high helium conditions instead of a group of isolated spots featured in low helium flow rate. A large diffusive disk at the center guided the spoke and the whole pattern is stable under the strong helium flow. Whether the spoke is related to the reduced heat expansion or changed electric field distribution is unknown. Note that the spokes can rotate at a high rate whereas the central attachment is static. Overall, a higher helium fraction in the plasma reduces the complexion of the SOP. The positive column at a higher gas flow rate forms a higher neutral gas gradient, i.e., a boundary layer that limits the air entrainment as indicated by Schlieren results Fig 3.10. A lower gas heating limits the positive column expansion and thus a smaller anode. At the gas phase, the air gap and helium flow rate both tweak the mass fraction of air inside the plasma and thus affect the collisional process and energy transport.

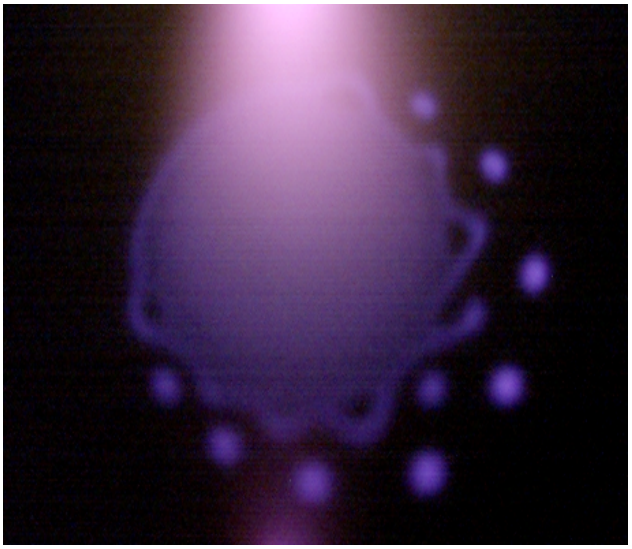

Figure 3.19: Plasma SOP with a 45-degree angled cathode (cathode is pointed from the left top towards the right bottom, 4 mm gap, 1.2 mS/cm)

Alternatively, the impact of helium on the pattern can be illustrated by an angled cathode which guides the helium flow non-normal relative to the liquid surface. As a result, an asymmetric SOP is observed and shown in Fig 3.19. Specifically, the angled nozzle guided the helium flow from the top left towards the bottom right of the image where the pattern's asymmetry is biased with the same orientation. The pattern near the cathode (top left of image) forms a diffusive disk whereas the right bottom side develops many spots. This peculiar phenomenon is supposed to be related to gas dynamics coupled with plasma physics. A research published recently performed a numerical simulation of a helium plasma jet impinging onto a wet surface at different angles [24]. The simulated various gas densities suggested that a strong vortex would form on both sides of the attachment point while the lateral speed on the side closer to the charged electrode would be slower. This would increase the residence time while the farther side developed a parallel streamline and lower the residence time. Electron density is also found larger at the side closer to the electrode. In our case, the flow speed is much lower (8.4 m/s) but the gas dynamic is still critically related. The gas at the top left near the cathode may stagnate and form a high helium fraction whereas the other side flows with higher speed and allows air mixing by convection.

3.4.4 The Impact of Electrode Nozzle Size

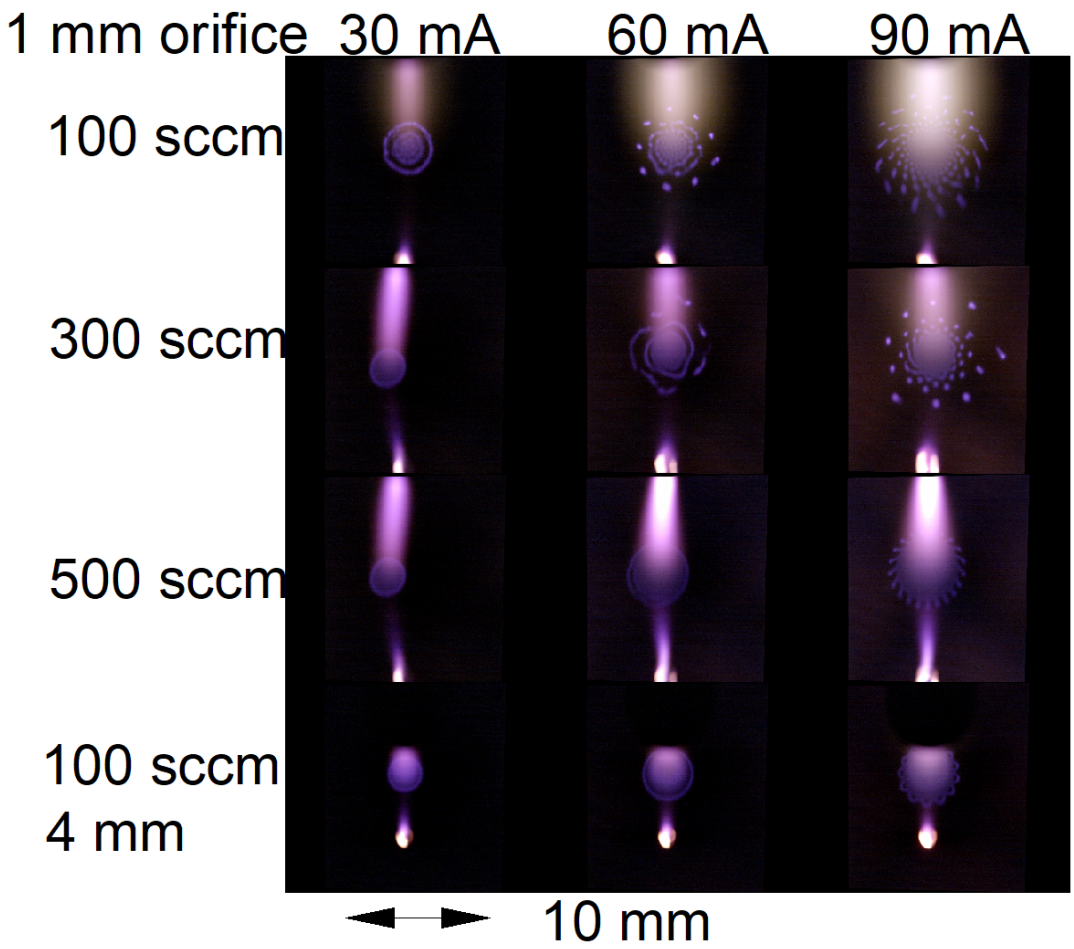

Figure 3.20: Plasma SOP with a 1 mm orifice diameter cathode nozzle

The effect of the cathode orifice is shown in Fig 3.20 where the 300 sccm flow rate almost produces an identical pattern evolution with 100 sccm's. As we discussed in the Schlieren results, a larger orifice effectively lowers the helium cooling performance since it does not form a strong boundary layer that makes the helium diffuse out and air transport inside the plasma. To achieve the equivalent cooling effect, a 500 sccm flow rate is used to produce a similar pattern as those at 300 sccm with a smaller orifice. Note that the pattern with the small gap and low flow rate resembles the similar evolution of the small orifice case. This means the helium's diffusion is less important at a small gap for the volumetric heating is weaker and air mass transport is also limited by the weaker convection and shorter boundary. Overall, SOP cares mostly about the mass fraction of air species and the correlated gas heating rate. By operating the plasma in the purge box, nitrogen, and oxygen will clearly show their differences in the mechanism of pattern dynamics.

3.4.5 The Impact of Oxygen Fraction

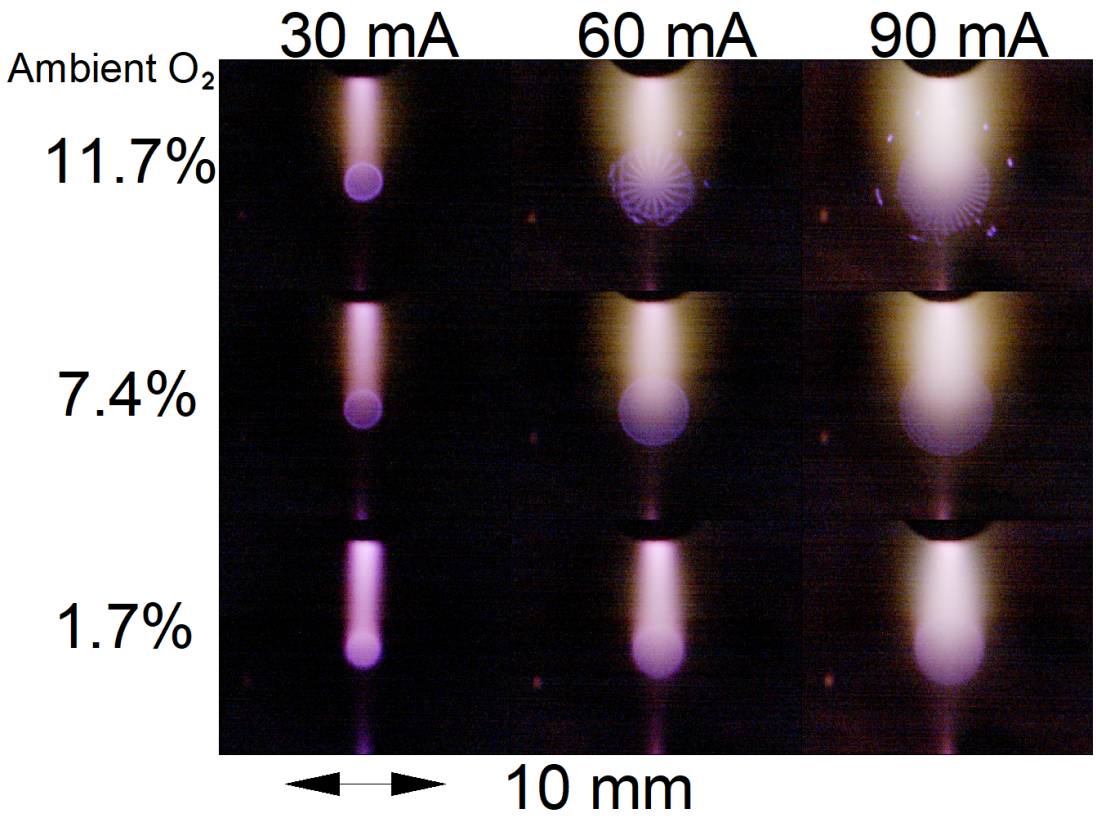

Figure 3.21: Plasma SOP at different oxygen mass fractions in the gas phase (8 mm gap, 100 sccm helium)

The above discussion has suggested that convection and air mass transport are both critical for pattern dynamics. This justifies that running the plasma in a nitrogen purge box is essential because it only changes the oxygen mass fraction in the gas phase without introducing any convection or mass transport process. Fig 3.21 shows the pattern under various levels of oxygen mass fraction in the gas phase. The pattern starts to change its shape with the oxygen level down to 12 % and entirely decays into a general attachment disk at 7 %. Note that the size of the anode glow decreases with diminishing oxygen volume fraction implying a higher current density and weaker gas heating rate. On the other hand, the anode glow is weaker and thinner implying a lower voltage drop at the anode layer. These results prove that only oxygen, not nitrogen, is critical for the SOP establishment in the case of the air species mass transport and particle kinetics. It is well-known that oxygen can sharply decrease the electron temperature by introducing many excitation, ionization, and dissociation processes that require relatively low activation energies[25]. However, nitrogen, not oxygen, dominates the ambient air, and nitrogen also has many excitation states of

low energy and can greatly decrease the electron temperature [26]. Thus, it is possible that the purge box further decreases the electron temperature by increasing the nitrogen mass fraction and finally weakening the anode layer voltage. But the anode sheath voltage is not the only factor, or else the enhanced anode layer on low conductivity liquid would form a non-diffusive pattern. The detailed mechanism of how oxygen could affect the SOP will be discussed in Chapter 4.

3.4.6 The Impact of Liquid Conductivity

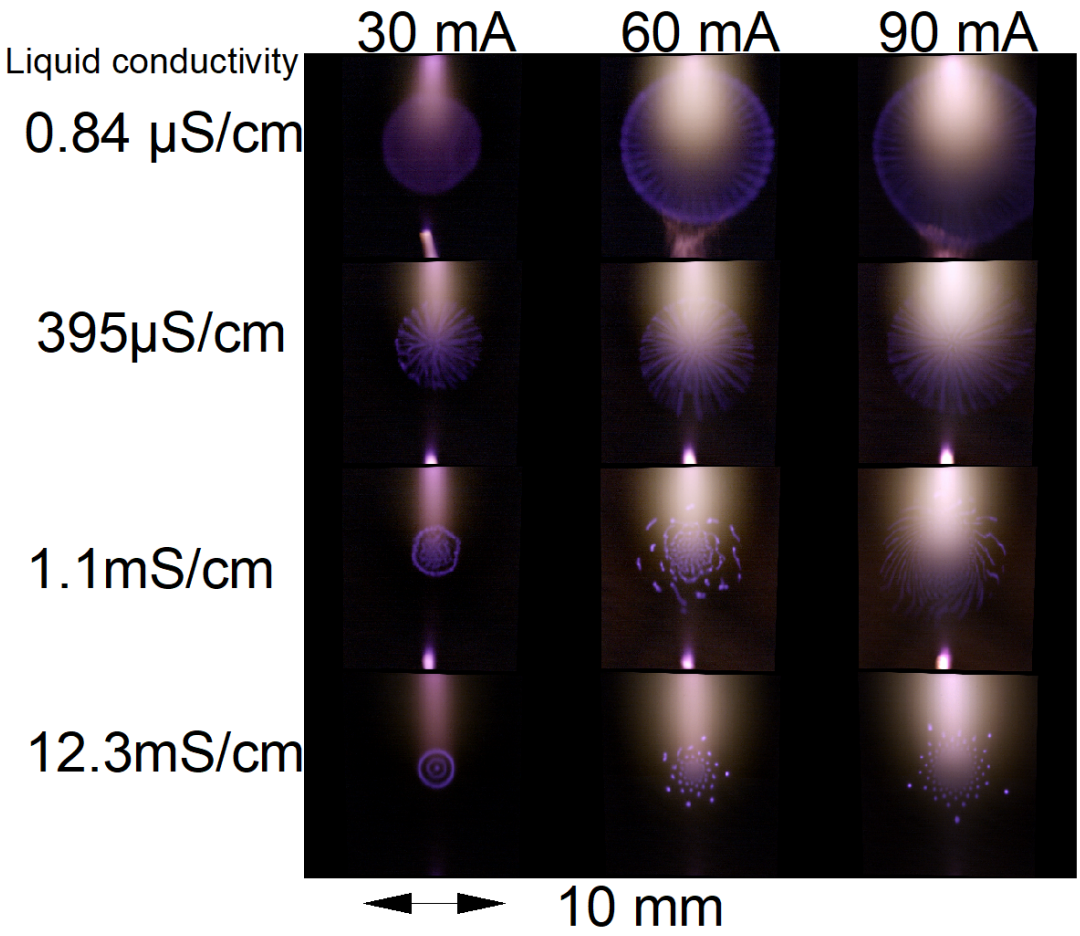

Figure 3.22: Plasma SOP at different liquid conductivities (8 mm gap, 100 sccm helium)

Apart from the gas phase variables, a strong reaction of SOP is observed when liquid conditions are changed. Fig 3.22 presents the pattern evolution at various liquid conductivity. When using the deionized water (0.84 μS/cm), SOP does not perform a major shape evolution but only increases its size with the current. The deionized water would behave like a dielectric medium where $\tau = \epsilon(\text{permittivity})/\sigma(\text{conductivity}) \approx 7\mu s$ that is much slower than the plasma fre-

quency. The space charge would have time to accumulate at the anode layer and form a stronger sheath. The locally-accumulated space charge has to spread along the surface just like a low-frequency dielectric barrier discharge and hence a diffusive pattern shape is established. This also leads to a remarkably larger anode glow surface area which can be related to the low current density estimated from Eq 3.2. Numerous filaments can be observed in the pattern and there is an obvious rim that encircles the filaments. At higher conductivity, space charge has less time to accumulate and thus the anode surface is smaller. At 395 μS/cm, the diffusive pattern transforms into a fireworks burst shape where numerous, active filaments move around the center resembling the shape of dielectric barrier discharge. Note that the outer rim is not formed and filaments are more scattered and dynamic as the conductivity rises. As the conductivity further increases, the long spokes reorganize into round spots and convene a cohesive formation. In fact, the 12 mS/cm case has a rather stable and coherent pattern that looks like a five-pointed star which is usually observed in small gap conditions. Unfortunately, it is unknown whether a peculiar shape pattern is correlated with the salt ion in the electrolyte [9]. In general, the space charge would rather repel each other and form numerous spots at high conductivity while a more uniform and homogeneous attachment is formed at low conductivity. The detailed mechanism has to be correlated with the transport process at the plasma-liquid interface which is out of the scope of this work.

3.4.7 The Impact of Liquid Temperature

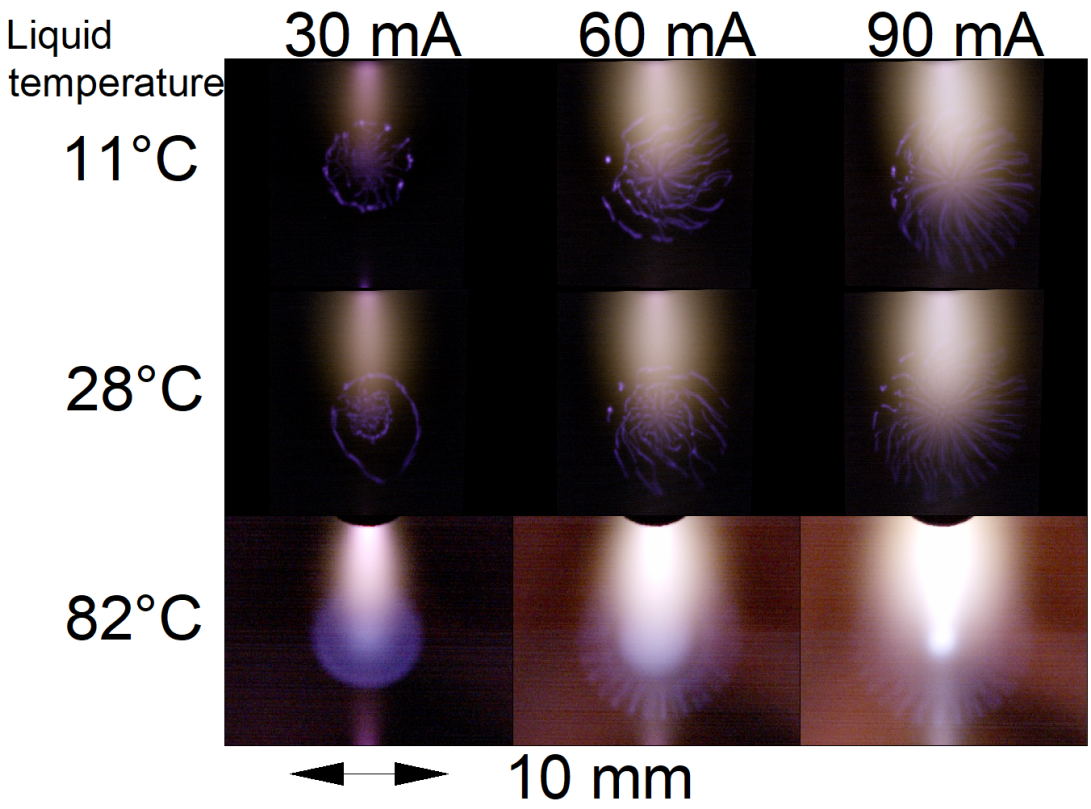

Figure 3.23: Plasma SOP at different liquid temperatures (8 mm gap, 100 sccm helium)

The liquid temperature also demonstrates its impact on SOP in Fig 3.23. The pattern only responds dramatically with the high temperature liquid where a "Gear" pattern is formed. Such a shape is often observed in the high helium flow condition whereas its size is smaller. The size of the pattern is larger than the other case because the heat transfer rate depends on the temperature difference and the high temperature liquid needs more contact area to achieve the thermal balance. Interestingly, a bright and dense hot spot can be observed at the center of the pattern which is similar to the anode attachment on a conductive metallic electrode. A possible explanation is that the effective conductivity would increase with liquid temperature whereas the pattern does not look like the high conductivity case in Fig 3.22. Another plausible mechanism is that the increased vapor concentration would introduce more electron loss through attachment and dissociative electron-ion recombination which reduce the excitation towards oxygen. The development of a SOP is sensitive to the oxygen. Indeed, a high helium flow condition inhibits dot formation and produces a "Gear" shape which also reduces the entrainment of oxygen. On the other hand, the water vapor is not identified as a triggering element in [22] for the vapor layer removal time is much longer than the

pattern formation time scale. The lack of enough oxygen in the purge box also shows no pattern even if a large amount of vapor is evaporated.

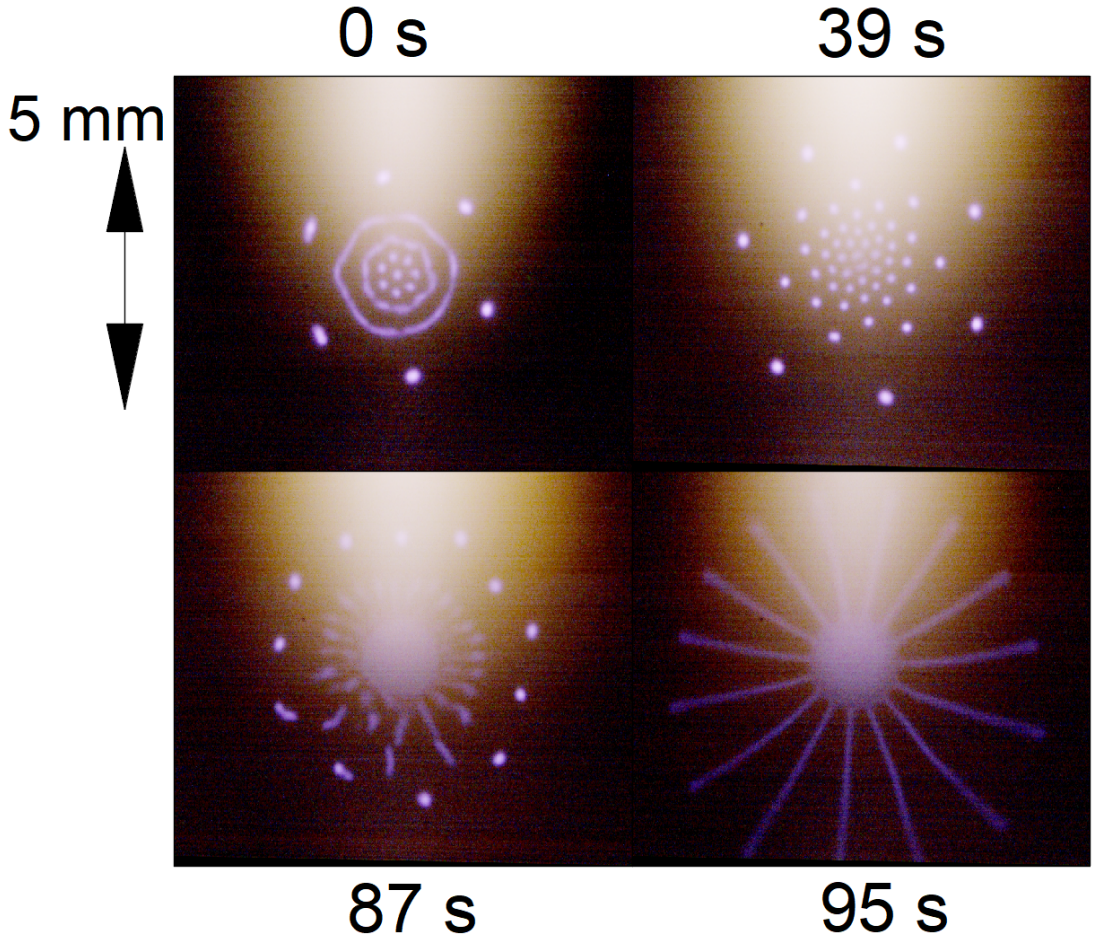

Figure 3.24: Plasma SOP evolution without liquid phase recycled (8 mm gap, 3.4 mS/cm, 60 mA)

An important feature of the liquid phase is the longer relaxation time compared with the gas phase. This is mostly because of the large volume, restricted mass, and energy transport at the plasma-liquid interface. It is found that SOP would develop a different shape when the relaxation time of liquid shortened. Conveniently, the relaxation time is shortened when the circulation loop is not used and the temperature, conductivity, and reactive species density would rise in the liquid phase. Fig 3.24 shows the evolution of the pattern when the liquid stops circulating. During the recording, the liquid surface height dropped 0.4 mm in one minute and the discharge voltage was increased to keep a constant current. At the start, the evolution of the pattern is ascribed to the dropping of liquid surface height and power increase. However, the pattern starts to grow a group of spokes that start to expand and unify with the outer spots. At 95 seconds, the pattern stops

evolving and stabilizes as an Inca sun shape where the spokes are longer and the central disk is smaller than a wagon wheel shape that is observed in the high helium flow case. Interestingly, a similar evolution can be produced in lower conductivity liquid but takes a longer time to reach the final stage. On the other hand, a circulated high temperature liquid or high conductivity failed to replicate this evolution or the Inca sun shape. In this case, it is speculated that a complicated and localized balance among chemical species, heat, and mass transport is established in 2 minutes when the glow discharge interacts with an isolated liquid phase. The pattern shape implies a strong radial gradient of species around the attachment. The whole process is self-consistent and would be interrupted immediately if the liquid phase is circulated again. This phenomenon also suggests the importance of keeping a static liquid phase property or the coupling process would manipulate the liquid phase locally and affect SOP.

3.5 The Evolution and Threshold of the Self-organized Pattern

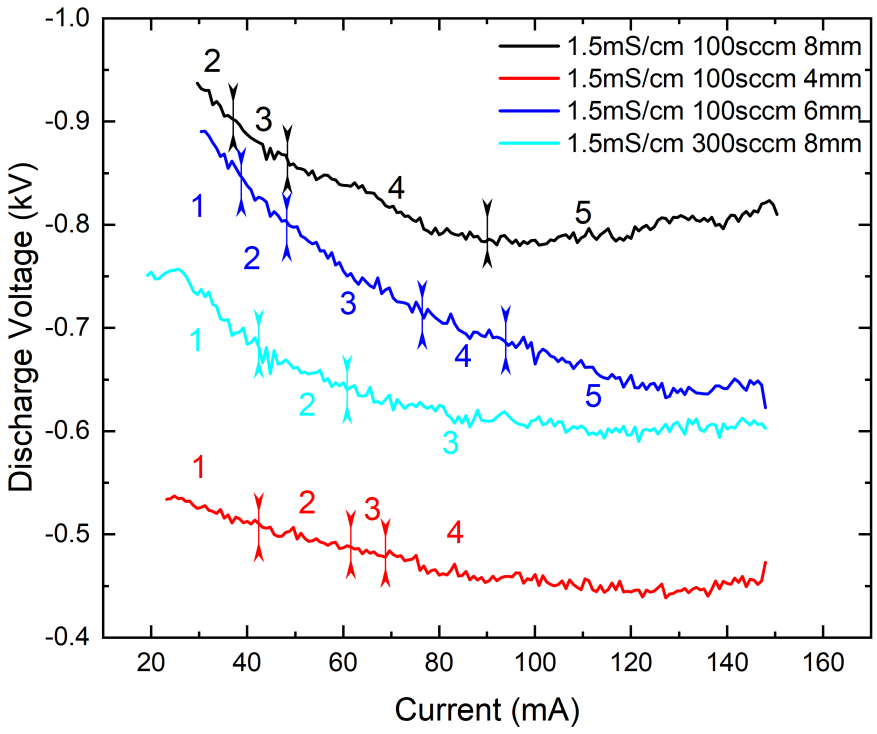

Figure 3.25: Threshold of evolution phases of the self-organized pattern under the impact of the gas condition (1.5 mS/cm)

The aforementioned discussions on the impact of conditions are elucidated with the image of SOPs at certain currents. This is because a SOP manifests the conductive channels at the plasma-liquid

interface and can affect the plasma impedance. However, it is also instrumental to discuss the impact of experimental variables on the evolution of SOP and the threshold. Indeed, the thresholds of different evolution phases are subject to change with different gas and liquid conditions. More importantly, the geometries of evolution phases transform nonlinearly. In the following figures, the shape of SOP is highlighted by the color filter for easier recognition.

The thresholds and evolution phases under different discharge gaps and flow rates are shown in Fig 3.25 and Fig 3.26, respectively. When the discharge gap is decreased, the thresholds of the pattern phases (indicated by numbers on the plots and illustrated in Fig 3.26) are shifted to the higher current. A smaller discharge gap reduces the voltage and the higher current threshold is needed to provide a similar power. However, their discharge power at the thresholds did not match meaning that it is not a linear effect. Smaller gaps or higher helium flow all increase the helium fraction which suppresses the excitation of molecules and cools the volumetric heating. In the last section, it was shown that the heat expansion can affect the pattern area while the effect on the shape is unknown.

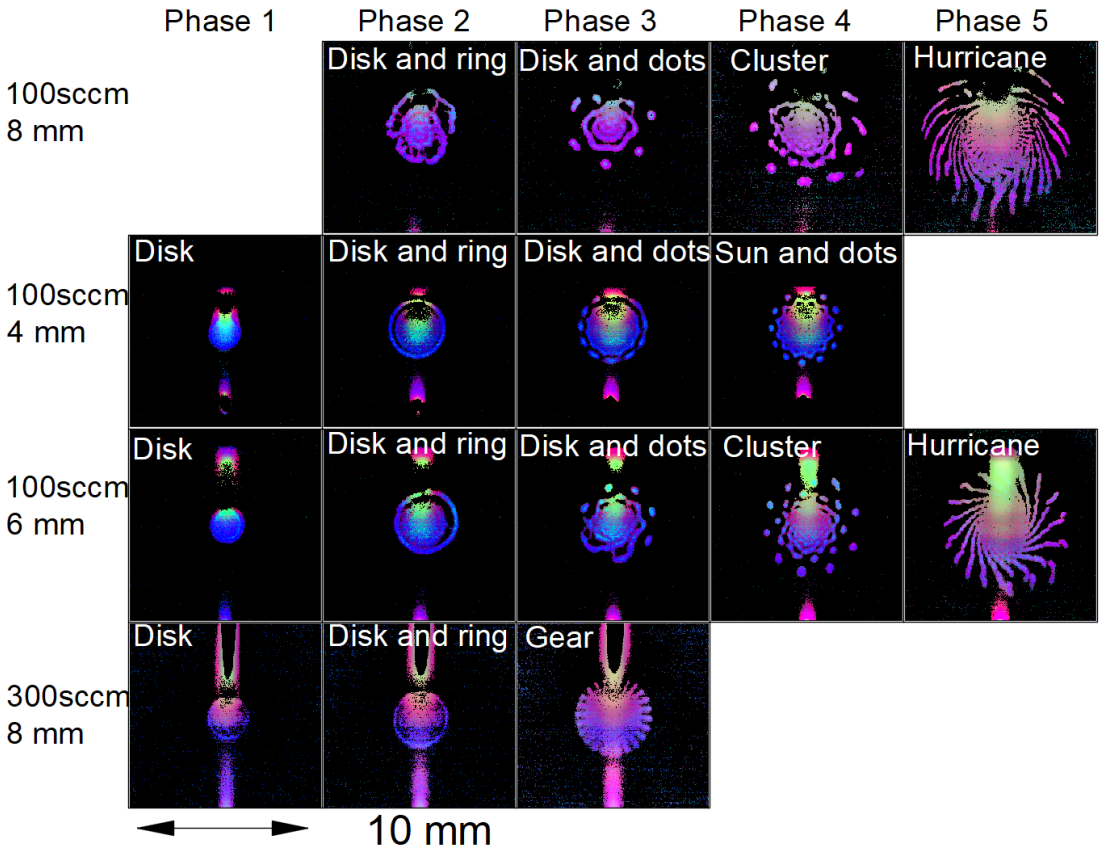

Figure 3.26: Various evolution phases of the self-organized pattern under the impact of the gas condition (1.5 mS/cm)

In Fig 3.26, the SOP under the 8 mm discharge gap is highly unstable and exhibits dynamic motion. This is mainly due to the thermal instability where the helium is unable to cool down the plasma thoroughly at a large gap. When the discharge gap is decreased, the SOP becomes more stable and cohesive. This can be justified by the differences in phase 4 "Cluster" shape between 8 mm and 6 mm gap where dots and central disk are more symmetric. The smaller gap has a higher helium fraction in its plasma column and helps mitigate the thermal instability. Interestingly, the 4 mm gap not only enforces more cohesion but also stops the further development of pattern evolution. The higher helium flow rate also restricts the evolution to three phases and the pattern is highly symmetric and lacks those scattered dots. Overall, the size of the discharge gap and helium flow rate govern the molecule fraction in the plasma and more entrainment of oxygen can facilitate the pattern evolution to a more complex and scattered form.

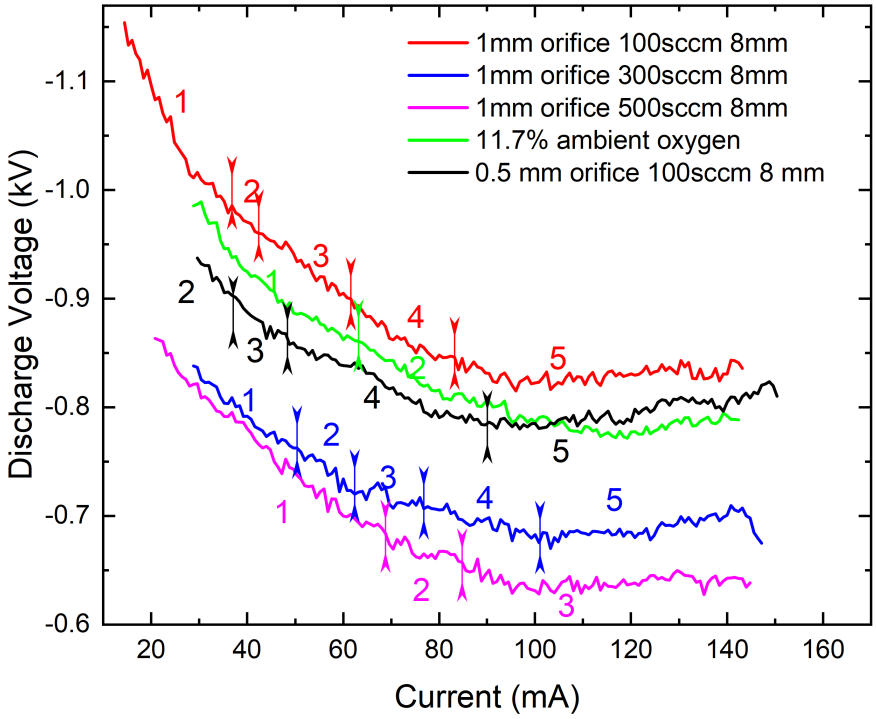

Figure 3.27: Threshold of evolution phases of the self-organized pattern under the impact of the additional gas condition (1.5 mS/cm)

In Fig 3.28, a larger orifice would weaken the helium's impact where the evolution of the SOP under 300 sccm helium flow resembles the 100 sccm case. At 500 sccm, the evolution is prominently limited and indicates the "Gear" shape. A larger orifice slows the helium flow speed and undermines the boundary layer which allows more diffusion of air. All in all, the change of SOP geometry and the evolution are mostly decided by the oxygen fraction. At low oxygen fraction

(11.7%), the SOP is almost featureless where the center region is filled with numerous streaks. In this case, the oxygen is critical for the evolution. As for the threshold, Fig 3.27 indicates a similar trend where the current shifts to a higher value when the overall discharge impedance is lower, i.e., less air mixing and volumetric heating.

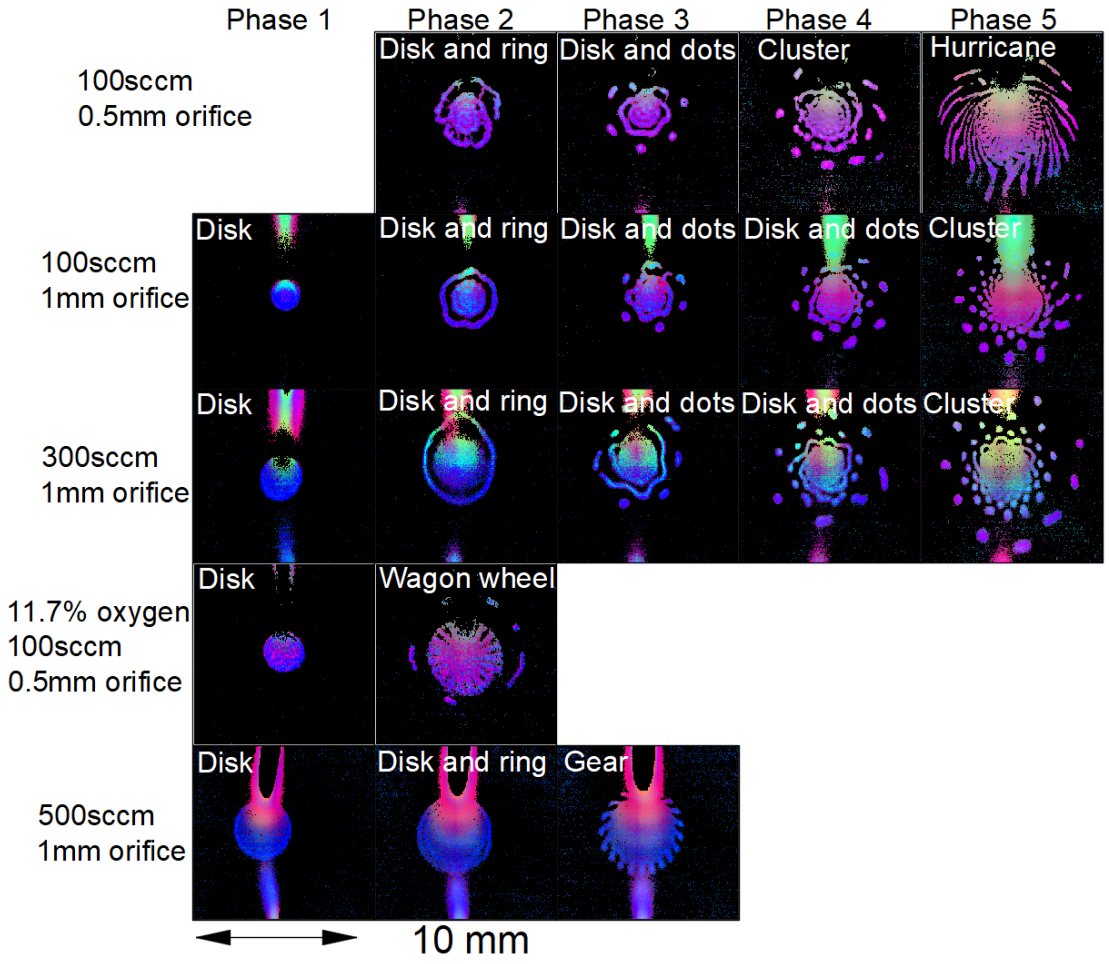

Figure 3.28: Various evolution phases of the self-organized pattern under the impact of the additional gas condition (1.5 mS/cm)

The gas phase conditions including high helium flow rate, small discharge gap, and low oxygen volume fraction can not only suppress the evolution of SOP but also prohibit the establishment of SOP. It means that the anode attachment stays as a featureless disk no matter how high the discharge current is. A few pattern images at threshold conditions are shown in Fig 3.29. Normally, SOPs can evolve simultaneously at all radial positions while the repression from threshold conditions only allows it to grow at peripheral. Fig 3.30 shows the regime where the SOP cannot be established at conditions above the curve. The X and Y axes are two important parameters, helium

flow and the discharge gap, thus the curve also shows the scaling law between them. Essentially, a rich oxygen fraction favors the establishment of SOPs and it is correlated with the length of the air gap. Helium flow rate, however, reduces the oxygen entrainment and concentration thus suppressing the SOPs. This competition leads to a linear graph that separates the regime of the pattern formation.

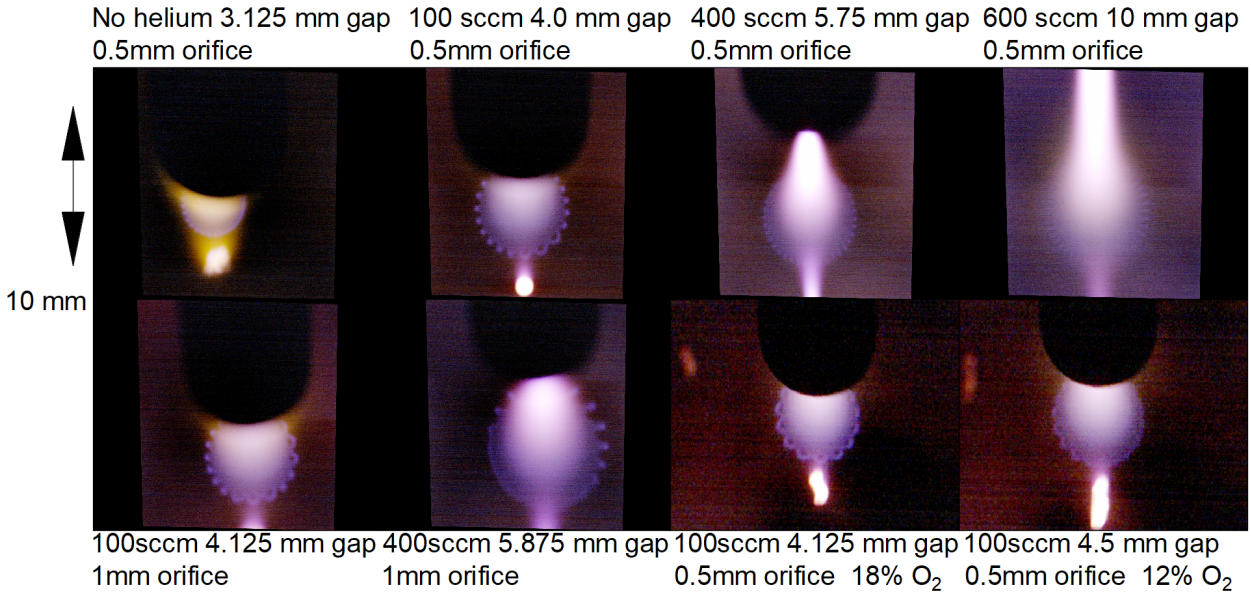

Figure 3.29: Anode attachments on the brink of establishment of the self-organized pattern under various gas phase conditions

Importantly, a small discharge gap (3 mm) inhibits the SOP evolution even without helium gas in the plasma. Note that a small gap also leads to high current density which can potentially forbid the expansion of space charge, i.e., the development of SOP. As the discharge gap increases, more helium flow is needed to repress the pattern. However, this trend is nonlinear at a larger discharge gap (> 7 mm) where helium flow prevails over the large gap. This can be explained by the boundary layer restriction illustrated in Fig 3.10. A high helium flow not only reduces the volumetric fraction of air by flushing but also limits the entrainment rate. On the other hand, this mechanism can be weakened by the large orifice which has a linear trend even at the large gap (blue curve). The regime for pattern is also limited by the volumetric fraction of oxygen where a lower oxygen fraction increases the gap threshold. At 7% oxygen, no pattern is allowed and thus the regime of SOP does not exist.

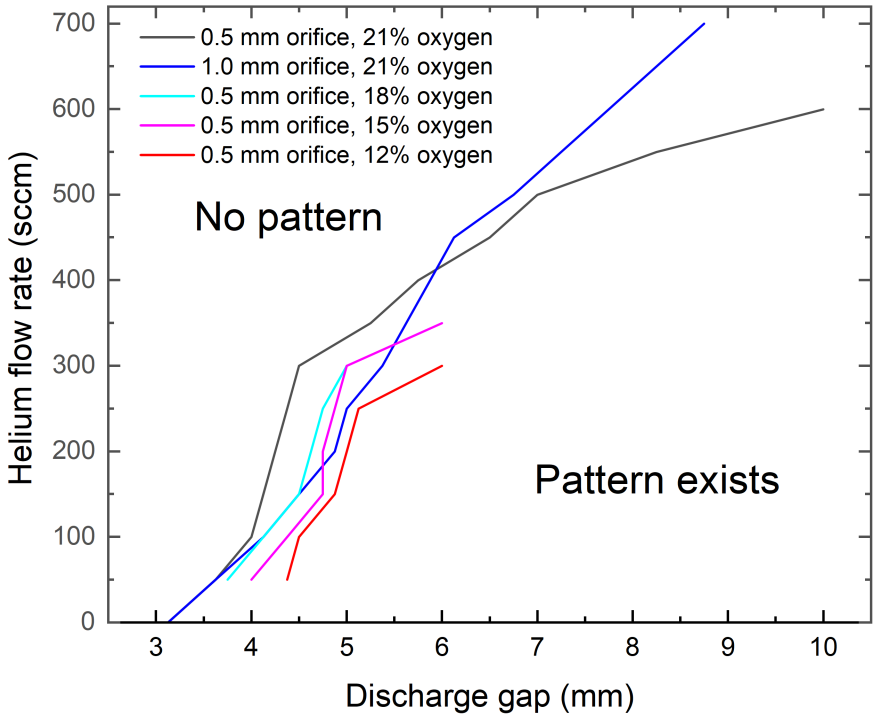

Figure 3.30: The regime of self-organized pattern at various gas phase conditions (conditions above the curve prohibit the SOP formation)

The liquid phase dominantly affects the evolution and geometry of a SOP at low conductivity. This is strongly illustrated in Fig 3.31 where no high-order phases are allowed with a low conductivity liquid anode. In Fig 3.32, the resistive liquid anode (148 µS/cm) favors the accumulation of space charge which in turn leads to a localized saturation in the attachment and thus forbids a complex, scattered geometry. At a larger current, a "Wagon wheel" geometry is observed where numerous filaments are encircled by a rim. At liquid conductivity of 450 µS/cm, the outer rim is gone and the filaments are more dynamic and scattered. In time, they are broken into round dots and form the "Cluster" geometry. It is profound that salt solution with high conductivity (12 mS/cm) supports the establishment of a more coordinated shape across all phases. For instance, the outer dots of the "Cluster" phase form a pentagon or hexagon. These patterns may be a result of increased surface mobility. Additionally, if the water is not highly conductive, intuitively one might expect more localized less complex patterns. Here the job of the attachment is to support the current which includes higher deposition locally to satisfy the required charge transport across the interface. In the case of highly conductive fluids, the attachments can take place at multiple locations since the charge transport is less resistive across the interface. Interestingly, a high-temperature liquid also inhibits the development of a range of complex patterns and forms a "Gear" shape. It is possible that the additional evaporation cools down the plasma and inhibits

thermal instability. Overall, the liquid phase affects the SOP through the complex plasma-liquid interaction and the observed results can provide insights to a further study in the future.

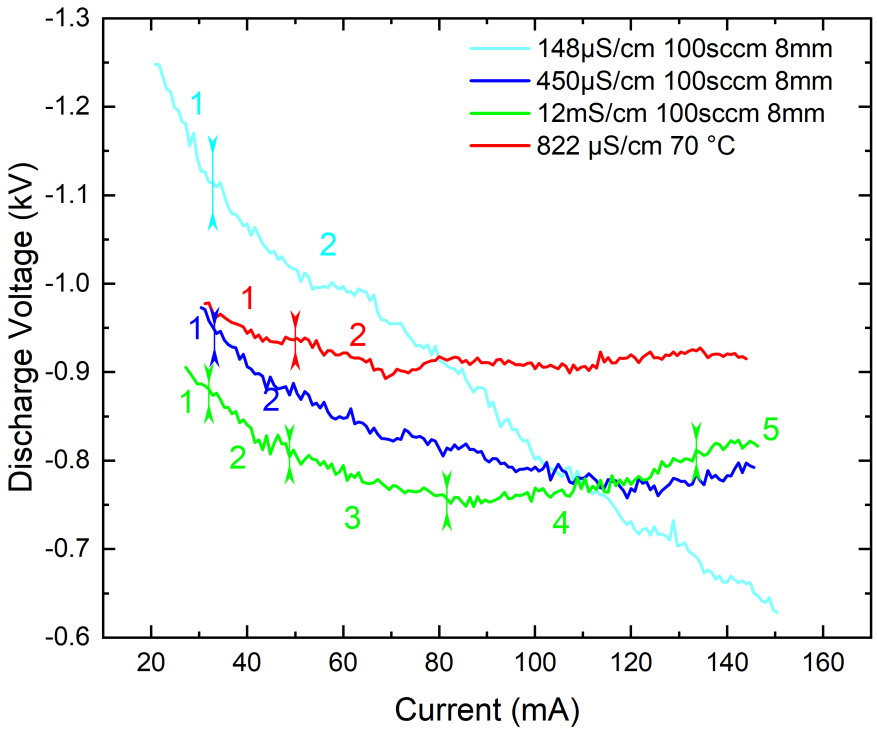

Figure 3.31: Threshold of evolution phases of the self-organized pattern under the impact of the liquid condition (8 mm gap, 100 sccm helium)

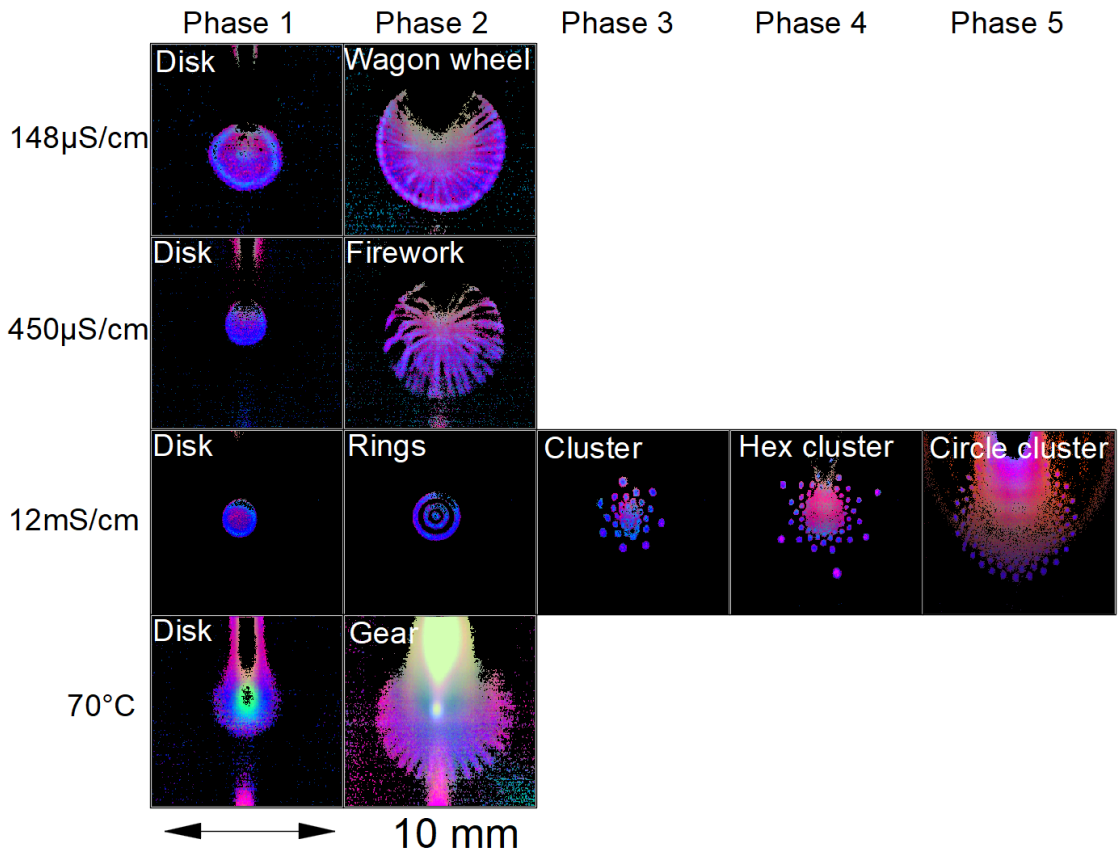

Figure 3.32: Various evolution phases of the self-organized pattern under the impact of the liquid condition (8 mm gap, 100 sccm helium)

3.6 Self-organized Pattern Size and Anode Current Density

The pattern size is another important parameter that decides the anode current density. Unlike the constant cathode current density, the positive column and anode layer are subject to many coupling processes and their size variation would affect the dynamics of the plasma and SOP. Specifically, the size of a pattern is defined as the perimeter of a SOP, not the surface area of the emission. This is due to the difficulty of precisely measuring the area when the pattern in high-speed motion creates a trail in the image. Another huge error source is the intense positive column emission that interferes with the pattern image which makes the pixel filtering rather intricate. At least the outreach of a pattern is correlated with the positive column boundary which is informative for the current density estimation. The following size estimations all have a 12 % error.

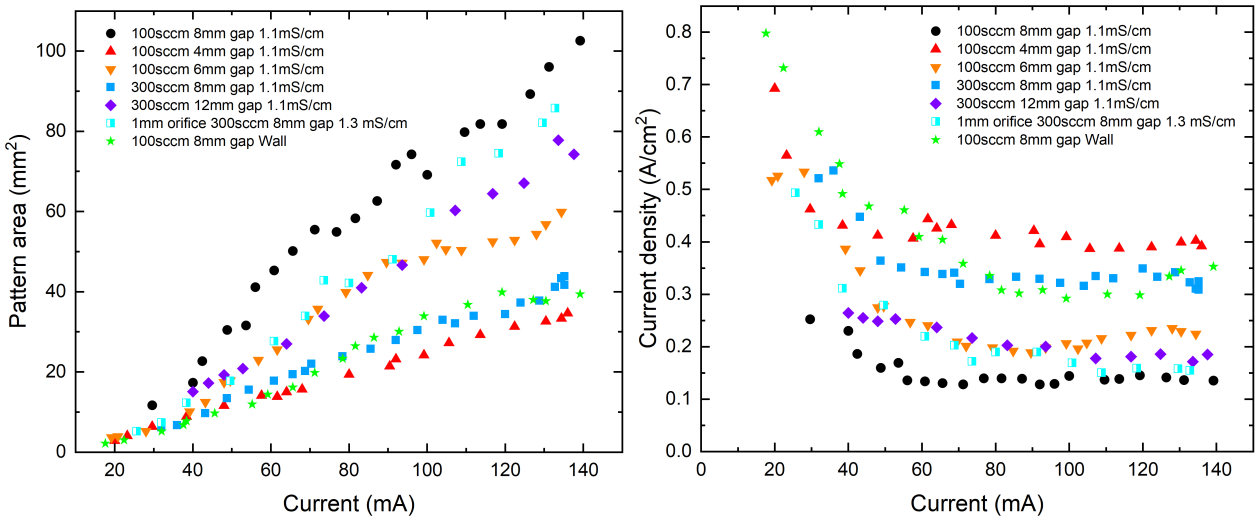

(a) Pattern size

(b) Current density at anode

Figure 3.33: Impact of air gap and helium flow rate

3.6.1 Impact of Gas Phase

Fig 3.33 plots the impact of the air gap and helium flow rate on pattern size and current density. As discussed before, the gas phase affects the plasma mainly by the variation of mass transport of air, helium cooling rate, and the boundary layer of convection. The air gap controls the length of the column boundary where air entrainment happens. It also decides the volumetric heating rate thus affecting the heat expansion directly. On the other hand, the helium flow rate directly manipulates the mass fraction of air. It also constricts the plasma column by controlling the boundary layer that governs the air entrainment. The boundary layer is also affected by the nozzle orifice due to the helium's short diffusion time and change of the boundary layer. Finally, a glass sleeve can directly block the air convection and increase the helium mass fraction. All in all, the larger air gap, lower helium flow rate, larger orifice, and absence of plasma column restriction all favor the air entrainment and gas heating which then cause the heat expansion, and vice versa. The impact of oxygen mass fraction is plotted in Fig 3.34 where a low oxygen level in the gas phase favors a smaller pattern and high current density. Thus, the current density and anode size are heavily affected by the gas mixing and oxygen mass fraction at the gas phase.

These relationships can be all found in the plots and the current density is ranged within $1\mathrm{A}/\mathrm{cm}^2$. Interestingly, the current density all have a rather high value at low current which reflects the negative $\mathrm{d}V/\mathrm{d}I$ in Fig 3.11. Note that less air entrainment can support a more stable anode attachment and enable the plasma to operate at low current as far as possible though the pattern will become featureless and diffusive. The thermal instability might be related to the pattern

dynamics although no measurement is available.

3.6.2 Impact of Liquid Phase

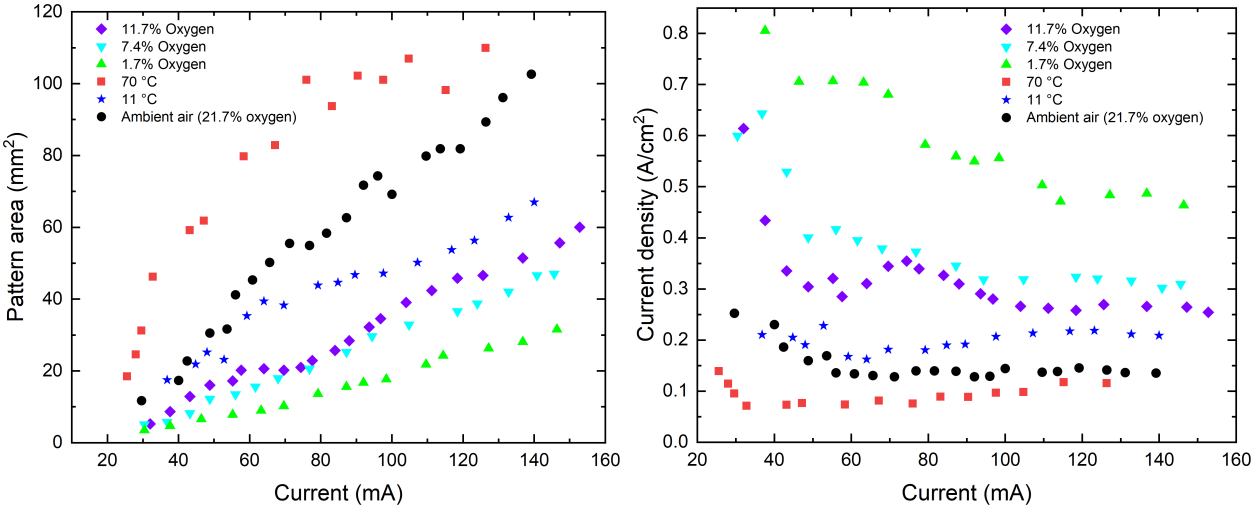

(a) Pattern size

(b) Current density at anode

Figure 3.34: Impact of oxygen and liquid temperature

The coupling between the liquid phase and SOP is rather complicated since it involves the gas and liquid phase species, plasma physics, and the energy mass transport at the interface. Liquid temperature can affect the heat transfer rate which depends on the temperature difference. A larger temperature difference at colder liquid supports a stronger heat transfer rate and smaller attachment area if the discharge power and gas heating rate stay the same. This is shown by Fig 3.34 in the 11 °C case. On the other hand, a high-temperature liquid causes a lower heat transfer rate which requires a larger anode surface to compensate. In Fig 3.35, the pattern size and current density under the impact of liquid conductivity change more dramatically. This can be attributed to the current density's exponential dependence on ionic strength in Eq 3.2. The size of the anode is also indirectly affected to accommodate the current density limited by liquid conductivity.

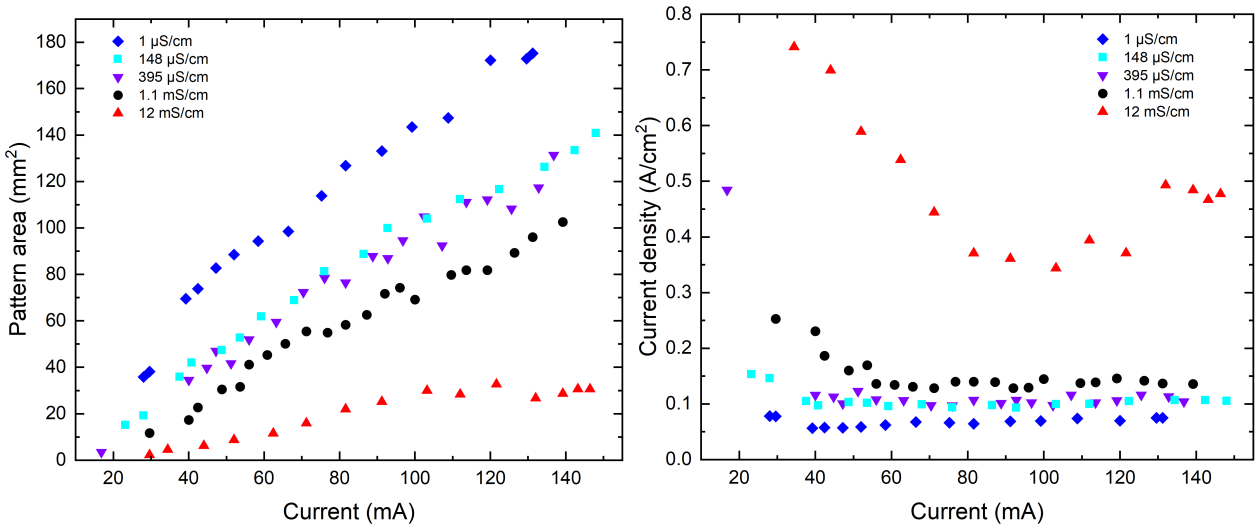

(a) Pattern size

(b) Current density at anode

Figure 3.35: Impact of liquid conductivity

3.7 Summary

In this chapter, the operation of the plasma column and its anode under the influence of many variables are investigated. The plasma column structure reveals the fundamentals of glow discharge at atmospheric pressure. It is found that the thermal dynamics and chemical reactions of reactive species are responsible for the morphology. The noble gas mass fraction and air mass transport are critical variables for they strongly affect the particle's kinetics and the gas heating. Analysis of I-V curve demonstrates that the plasma impedance at different conditions. Overall, although the trend is not significantly different, the discharge voltage range is different when the air mass fraction or liquid properties are affected. The estimated reduced electric field at the positive column is also estimated and used to analyze. The pattern evolution and its variation with different conditions are discussed. In the gas phase, a larger air gap, lower helium flow rate, larger orifice, or absence of plasma column restriction all favor the air entrainment and gas heating which then enable a more developed and complicated pattern. Conversely, opposite gas phase conditions restrict the oxygen's diffusion into plasma and inhibit the high-order phase of SOP while the geometry is more stable due to the mitigation of thermal instability. Results show that enough level of oxygen concentration (> 7%) in the gas phase is paramount for SOP formation. In the liquid phase, the conductivity of the liquid can affect the current density by changing the space charge accumulation at the plasma-liquid interface and the anode voltage. A low conductivity provokes the transverse spreading of space charge along the liquid surface and a larger, diffusive pattern whereas a high

conductivity prompts a more stable and peculiar shape. The liquid temperature only indicates its impact when it is high and the pattern is approximated to the shape of high helium condition, possibly due to the vapor concentration affecting the plasma properties. It is clear that SOP is more sensitive to the gas phase where the air fraction affects the thermal dynamics and the anode size. The pattern complexity is also related to the gas dynamics and oxygen concentration. A more detailed mechanism for SOP would require a comprehensive kinetic model to tell the plasma parameters under the influence of various conditions.

References

[1] Naoki Shirai, Satoshi Uchida, and Fumiyoshi Tochikubo. Influence of oxygen gas on characteristics of self-organized luminous pattern formation observed in an atmospheric dc glow discharge using a liquid electrode. *Plasma Sources Science and Technology*, 23(5):054010, 2014.

[2] Tiny Verreycken, Peter Bruggeman, and Christophe Leys. Anode pattern formation in atmospheric pressure air glow discharges with water anode. *Journal of Applied Physics*, 105(8), 2009.

[3] Naoki Shirai, Kosuke Ichinose, Satoshi Uchida, and Fumiyoshi Tochikubo. Influence of liquid temperature on the characteristics of an atmospheric dc glow discharge using a liquid electrode with a miniature helium flow. *Plasma Sources Science and Technology*, 20(3):034013, 2011.

[4] Naoki Shirai, Satoshi Uchida, Fumiyoshi Tochikubo, and Shozo Ishii. Self-organized anode pattern on surface of liquid or metal anode in atmospheric dc glow discharges. *IEEE Transactions on Plasma Science*, 39(11):2652–2653, 2011.

[5] David Staack, Bakhtier Farouk, Alexander Gutsol, and Alexander Fridman. Characterization of a dc atmospheric pressure normal glow discharge. *Plasma Sources Science and Technology*, 14(4):700, 2005.

[6] VA Titov, VV Rybkin, SA Smirnov, AN Kulentsan, and H-S Choi. Experimental and theoretical studies on the characteristics of atmospheric pressure glow discharge with liquid cathode. *Plasma chemistry and plasma processing*, 26:543–555, 2006.

[7] Shu Yi Miao, Chun Sheng Ren, Yu Tao Zhang, Bing Qi, You Nian Wang, et al. Conical dc discharge in ambient air using water as an electrode. *IEEE transactions on plasma science*, 36(1):126–130, 2008.

[8] Shiqiang Zhang and Thierry Dufour. Self-organized patterns by a dc pin liquid anode discharge in ambient air: Effect of liquid types on formation. *Physics of Plasmas*, 25(7), 2018.

[9] Yao E Kovach, Maria C Garcia, and John E Foster. The variation in self-organized anode plasma pattern structure with solution electrolyte type in 1 atm dc glow discharge. *Plasma Sources Science and Technology*, 30(1):015007, 2021.

[10] Naoki Shirai, Shinji Ibuka, and Shozo Ishii. Self-organization pattern in the anode spot of an atmospheric glow microdischarge using an electrolyte anode and axial miniature helium flow. *Applied Physics Express*, 2(3):036001, 2009.

[11] Xuechen Li, Shuai Zhou, Kun Gao, Junxia Ran, Kaiyue Wu, and Pengying Jia. Temporal evolutions of self-organized patterns formed on the water-anode surface of an atmospheric pressure glow discharge. *IEEE Transactions on Plasma Science*, 50(6):1717–1722, 2022.

[12] Jan Voráč, Lukáš Kusýn, and Petr Synek. Deducing rotational quantum-state distributions from overlapping molecular spectra. *Review of Scientific Instruments*, 90(12), 2019.

[13] Andrew J Woods, Tom Docherty, and Rolf Koch. Image distortions in stereoscopic video systems. In *Stereoscopic displays and applications IV*, volume 1915, pages 36–48. SPIE, 1993.

[14] Gary S Settles. *Schlieren and shadowgraph techniques: visualizing phenomena in transparent media*. Springer Science & Business Media, 2001.

[15] Enrico Traldi, Marco Boselli, Emanuele Simoncelli, Augusto Stancampiano, Matteo Gherardi, Vittorio Colombo, and Gary S Settles. Schlieren imaging: a powerful tool for atmospheric plasma diagnostic. *EPJ Techniques and Instrumentation*, 5:1–23, 2018.

[16] Alexander Fridman and Lawrence A Kennedy. *Plasma physics and engineering*. CRC press, 2004.

[17] P Paris, M Aints, F Valk, T Plank, A Haljaste, KV Kozlov, and HE Wagner. Intensity ratio of spectral bands of nitrogen as a measure of electric field strength in plasmas. *Journal of Physics D: Applied Physics*, 38(21):3894, 2005.

[18] Yukikazu Itikawa. Cross sections for electron collisions with nitrogen molecules. *Journal of physical and chemical reference data*, 35(1):31–53, 2006.

[19] R Riahi, Ph Teulet, Z Ben Lakhdar, and A Gleizes. Cross-section and rate coefficient calculation for electron impact excitation, ionisation and dissociation of h 2 and oh molecules. *The European Physical Journal D-Atomic, Molecular, Optical and Plasma Physics*, 40:223–230, 2006.

[20] Paul Rumbach, Jean Pierre Clarke, and David B Go. Electrostatic debye layer formed at a plasma-liquid interface. *Physical Review E*, 95(5):053203, 2017.

[21] Alexander Fridman, A Gutsol, and YI Cho. Non-thermal atmospheric pressure plasma. *Advances in Heat Transfer*, 40:1–142, 2007.

[22] Tanubhav Srivastava, Marien Simeni Simeni, Gaurav Nayak, and Peter J Bruggeman. Self-organized patterns at the plasma–liquid anode interface in a helium glow discharge: temporal development and mechanisms. *Plasma Sources Science and Technology*, 31(8):085010, 2022.

[23] MS Benilov. Multiple solutions in the theory of dc glow discharges and cathodic part of arc discharges. application of these solutions to the modeling of cathode spots and patterns: a review. *Plasma Sources Science and Technology*, 23(5):054019, 2014.

[24] Guy Parsey, Amanda M Lietz, and Mark J Kushner. Guided plasma jets directed onto wet surfaces: angular dependence and control. *Journal of Physics D: Applied Physics*, 54(4):045206, 2020.

[25] Davide Mariotti, Yoshiki Shimizu, Takeshi Sasaki, and Naoto Koshizaki. Gas temperature and electron temperature measurements by emission spectroscopy for an atmospheric microplasma. *Journal of applied physics*, 101(1), 2007.

[26] Delin Kong, Ping Zhu, Feng He, Ruoyu Han, Bingyan Yang, Manyu Wang, and Jiting Ouyang. Influence of nitrogen and oxygen admixture on the development of helium atmospheric-pressure plasma jet. *Journal of Applied Physics*, 129(10), 2021.

CHAPTER 4

Influence of Oxygen and Negative Ions in Self-organized Pattern Dynamics

4.1 Introduction

Molecular species consume a substantial amount of plasma power (often more than 95%) through additional inelastic processes such as vibration for their vibrational quantum (N_2 0.29 eV, O_2 0.2 eV) and rotational excitation. The level spacing for such inelastic processes is much less than the equilibrium electron energy thus making them especially important in plasma chemical kinetics. Different channels of relaxation and chemical reactions rely on these vibrational excited molecules to participate in [1]. Within the air, the oxygen molecules feature two very low energy metastable singlet states with long lifetimes (Tab 4.1), and their electronic excitation energy is close to the typical energy of vibrational excitation and therefore the relative concentration of such metastable particles in the discharges can be very high and important.

Table 4.1: Lifetimes and Energies of the Metastable Diatomic Molecules (on the Lowest Vibrational Level) [1]

Metastable molecule	**Electronic state**	**Energy of the state (eV)**	**Radiative lifetime (s)**
N_2	$A^3\Sigma_u^+$	6.2	13
N_2	$a'^1\Sigma_u^-$	8.4	0.7
N_2	$a^1\Pi_g$	8.55	2×10^{-4}
N_2	$E^3\Sigma_g^+$	11.9	300
O_2	$a^1\Delta_g$	0.98	3000
O_2	$b^1\Sigma_g^+$	1.63	7
NO	$a^4\Pi$	4.7	0.2

Oxygen can also form anions as the electronegative gas which consists of molecules with a

high electron affinity and attract electrons. In this case, the additional electron loss term, electrons attachment to electronegative neutrals, can heavily affect the electron balance. The negative ions formed as a result of electron attachment can be neutralized quite easily and extremely fast by recombination of negative ions and positive ions. This process is volumetric and could drive the plasma into the attachment-controlled regime rather than the diffusion-controlled regime which requires a higher electron temperature and a higher reduced electric field to sustain the discharge [1]. At atmospheric pressure, a noble gas feed glow discharge would have a larger electron density gradient near its periphery where negative ions would form. Near the electrode or dielectric, negative ions can affect the sheath by their low mobility and enhance the local electric field radially [2]. The importance of negative ions in the weakly ionized molecular gas discharge instability has been analyzed and determined to stimulate an attachment instability wave mode [3]. Interestingly, the pattern dynamics have been proven to be sensitive to oxygen which is an electronegative gas [4]. Acidic electrolytes H_2SO_4, HCl, HF were found to lower the pattern complexity as the author speculated that electrolysis products such as O_2, Cl_2, F_2 with increasing electron affinity restrict the pattern formation [5]. It is then of interest to investigate the role of oxygen negative ions in the mechanism of SOP.

Diagnostics of negative ions include mass spectrometry [6] or the laser-induced photodetachment method [7]. Both methods are well-established in the study of low-pressure plasma. At atmospheric pressure, the thin sheath and less diffusive plasma make mass spectrometry more challenging though skimmers and differential pumping methods can be used to sample the ion species. The laser photodetachment method involves the use of a tunable laser to illuminate a plasma within its beam area with photon energy exceeding the negative ion's electron affinity. Free electrons are formed in the detachment process and are detected as the increase of electron density, thus a Langmuir probe is generally used to measure the electron saturation current. However, the atmospheric plasma's thin and collisional sheath does not fulfill the requirements of the Langmuir probe measurement. In this case, the electron density increase due to detachment can be measured within the circuit as a temporal increase in discharge current. Sasaki *et al* recently measured the negative ion species in an atmospheric glow discharge over metallic and liquid cathode [8]. Results suggested that O^- and OH^- derived from the dissociative electron attachment of H_2O_2 were the dominant negative ions. On the other hand, the negative ion species and density have not been conducted for the glow discharge with liquid anode. It should be noted that patterns are typically absent in glow discharges with liquid cathodes.

In this chapter, a laser photodetachment experiment on the negative ions in the atmospheric glow discharge plasma with a liquid anode is performed including a discussion of negative ion density and the identification of dominant species of negative ions. The impact of negative ions depletion on the SOP dynamics is also examined.

4.2 Experimental Setup and Method

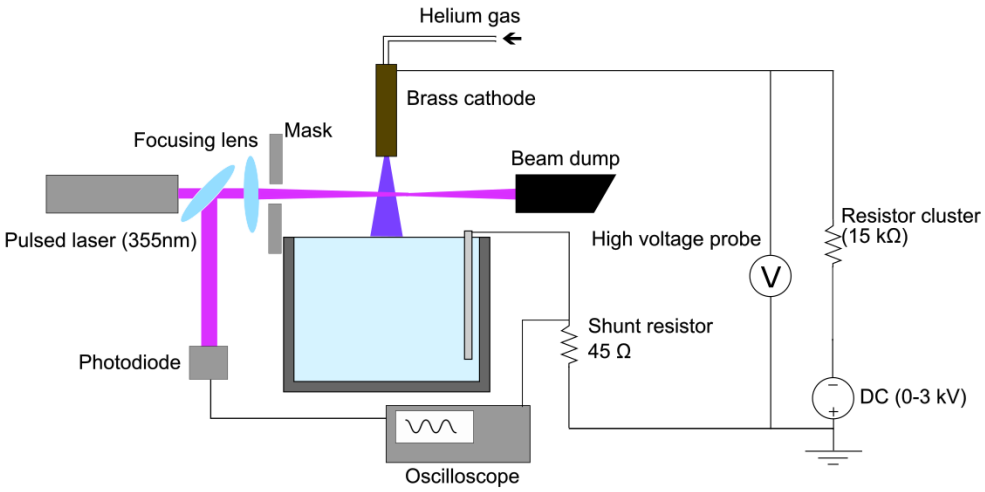

Figure 4.1: Schematic diagram of laser photodetachment setup

Table 4.2: Electron affinity and photodetachment cross section of major negative ions

Negative ion	**Electron affinity (eV)**	**Cross-section at 355 nm** ($\times 10^{-22}\mathrm{m}^2$)	**Reference**
O_2^-	0.448	3.64	[9]
O^-	1.44	9.52	[10]
OH^-	1.83	9.31	[11]
$O_2^- \cdot (H_2O)$	2.25	2.58	[9]

Fig.4.1 shows the schematic of the laser photodetachment experiment. A tunable Nd:YAG pulsed laser (wavelength of 355 nm, photon energy 3.49 eV) outputting a maximum 100 mJ beam energy at 4 ns pulse width is used to perform the detachment. Tab 4.2 lists the major negative ions presumably present in a plasma running in humid air. O_2^- is produced by three-body electron attachment [12, 13], while abundant singlet oxygen can participate in the dissociative attachment by energetic electrons and yields O^- [14]. OH^- is produced from the dissociative attachment of water molecules [15]. The energy of photons at 355 nm is higher than the attached electron binding energy for all the listed negative ions and thus produces photodetachment nonselectively. The other possible negative ions such as H^-, O_3^- are negligible in the experiment. The theoretical ratio of the detached negative ions versus all negative ions α can be calculated by:

$$\alpha = \frac{\Delta n_-}{n_-} = 1 - \exp(-\frac{\sigma \lambda E}{hcS}) \tag{4.1}$$

$$\frac{\Delta I}{I} \cong \frac{\Delta n_-}{n_e} = \frac{n_-}{n_e} \times \frac{\Delta n_-}{n_-} = A \times \alpha \tag{4.2}$$

where n_- represents the negative ion density, σ is the photodetachment cross-section, E, S are the laser pulse energy and beam area, respectively; h, c are Planck constant and speed of light. The increased current ratio $\Delta I/I$ scales with the detached negative ions to free electrons $\Delta n_-/n_e$ if we assume the discharge current is mainly carried by them. Then the detachment current ratio can be represented by the multiplication of the negative ion detachment ratio α and the local negative ion density over the free electron's $A = n_-/n_e$ in Eq 4.2. The local density ratio A depends on not only the density difference but also the volume of plasma that the laser illuminates. The measured current ratios at different laser energies are fitted with the theoretical detachment ratio times the local density ratio A as a constant. When compared with the known species's curve, A is used to normalize the $\Delta I/I$ into $\Delta n_-/n_-$ to show the relative difference of the detachment cross-section. Note that the detachment ratio α depends on the laser fluence at constant photon energy (wavelength) which is the energy per area and will be saturated at enough high fluence. When higher laser energy is unavailable, a focusing lens was placed between the plasma column and laser output port to increase the laser fluence. A laser viewing card measures the effective beam area. The laser beam energy was adjusted by a delay generator and the value was measured by a laser power meter. A small portion of the laser beam was diverted by a beamsplitter towards a photodiode to acknowledge the laser pulse on the oscilloscope. A beam dump was set at the back of the plasma to trap the laser beam for safety.

The discharge setup was similar to the one illustrated in section 2.1 except for the current measurement. The detachment current signal happens on a nanosecond time scale that corresponds to the laser pulse and such current change would only be detectable on the anode where free electrons drift. Therefore, a shunt non-inductive resistor is put between the liquid and earth ground whose voltage is measured directly by an oscilloscope. An intensified CCD camera (PIMAX 4) was implemented and synchronized with the pulsed laser to observe the SOP dynamics when negative ions are destroyed by the photodetachment. A 300 ns gate width was used to receive enough emission of the pattern so that any pattern change could be registered.

4.3 Results and Discussion

4.3.1 Current Change at Photodetachment

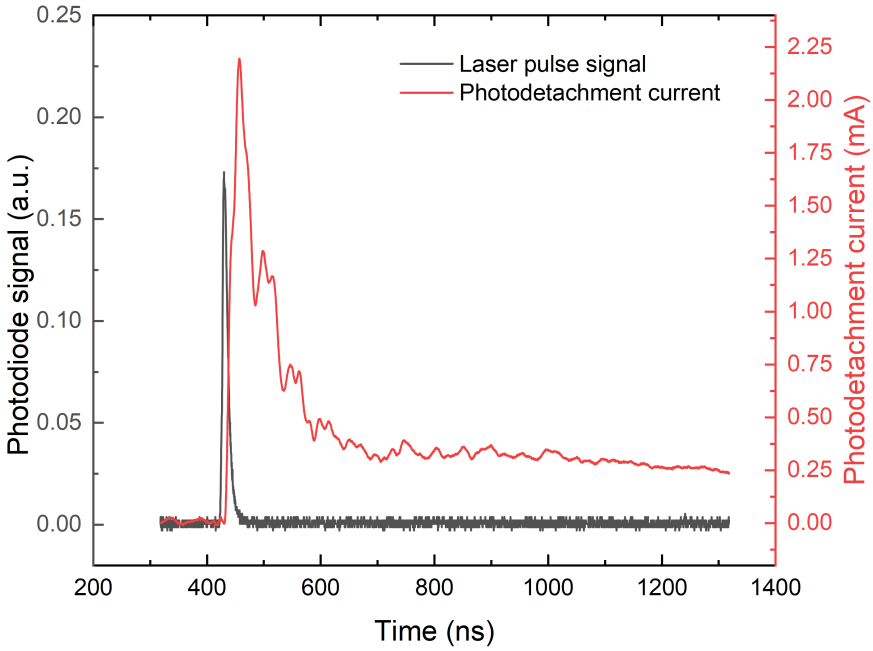

Figure 4.2: Photodetachment current temporal change at a 97 mJ laser pulse (discharge current 32 mA, beam diameter 8.6 mm)

Typical temporal variation of discharge current as photodetachment laser reached is shown in Fig 4.2. The laser energy is 97 mJ and the beam is unfocused with 8.6 mm diameter. The beam covers the majority of the plasma column and should detach all the negative ions. The black curve represents the laser pulse that starts 8 ns earlier than the current signal due to the position difference between the photodiode and plasma column. In principle, the photodetachment happens almost immediately after the laser illuminates the plasma. The current pulse had a rise time $\sim$20 ns and then decayed exponentially with a time constant of 58 ns. The fast decay implied that the free electrons are reattached with electronegative gas. Note there is also a slower-falling part in the curve whose origin is unknown. The current signal is also not smooth but coupled with several peaks. It is plausible the signal transmission is interfered with the impedance in the circuit. Another possible source is the reflected laser rays shine the plasma column later than the major beam and generate these secondary peaks which was discussed in [16]. Curtains and masks were placed around the plasma to reduce this effect as much as possible.

4.3.2 Photodetachment Current Ratio

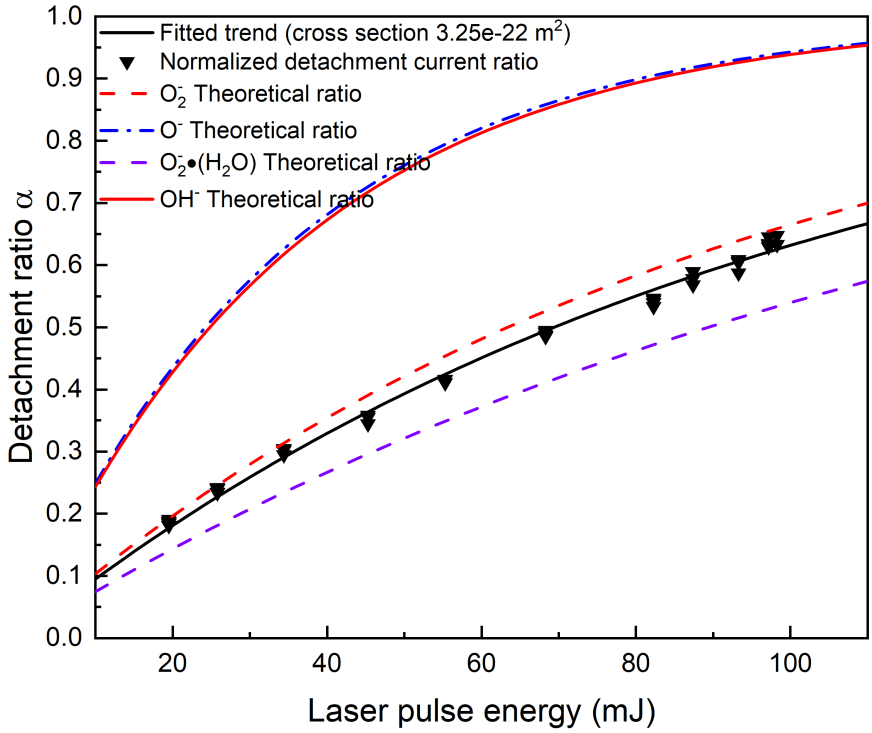

Figure 4.3: Normalized photodetachment ratio at an 8.6 mm diameter laser beam (discharge current 32 mA, laser pulse 97 mJ, density ratio 0.104, effective cross-section $3.25 \times 10^{-22}\mathrm{m}^2$)

According to Eq 4.1, the percentage of detached negative ions should increase and then saturate if the laser pulse fluence is high enough. This percentage corresponds to the change of detachment current $\Delta I/I$ where the largest $\Delta I/I$ is achieved when the detachment ratio $\Delta n_-/n_-$ is saturated to unity. Fig 4.3 plots the change of normalized detachment ratio as a function of pulse energy. Surprisingly, the detachment ratio only reaches 62 % at the highest pulse energy and fails to saturate. The pulsed laser is expected to provide enough fluence for saturation if the major negative species is O^- as [8] showed. Because the laser beam area and the photon energy are known. The overall detachment cross section can be deduced from fitting the data with Eq 4.2 where the local density ratio A and effective photodetachment cross section are set as unknown parameters. An atmospheric pressure glow discharge has electron density of $10^{13}\mathrm{cm}^{-3}$ [17], thus the density ratio $A = n_-/n_e$ 0.104 means $\sim 10^{12}\mathrm{cm}^{-3}$ negative ion density present in the plasma column. It was also reported in [18] that the negative ion density shall be two orders of magnitude smaller than the electron density. The fitted effective cross section apparently lies between O_2^- and $\mathrm{O}_2^- \cdot (\mathrm{H_2O})$ and far below the O^- and OH^- suggesting that O_2^- is the dominant negative ions. Normally, the negative ions in a low-pressure plasma with oxygen are dominated by O^-, although research suggests

that the percentage of O_2^- increases with the chamber pressure since the charge transfer between O^- and O_2 ($a^1\Delta_g$) become more important at higher pressure (>10 mTorr)[19]. Another study also pointed out the importance of this reaction if a larger reduced electric field and small current density (<10 $\mathrm{mA/cm^2}$) exists and O_2^- can become dominant even at low pressure [20]. In this work, we believe the bulk plasma column has a low electric field (<30 Td, see Tab 3.1) that does not favor the dissociative attachment of water and oxygen, thus the three-body attachment is dominant and produces O_2^- [21]. The low electric field also diminishes the contribution from the dissociative attachment of water molecules which can be a more important electron loss mechanism compared to oxygen [22].

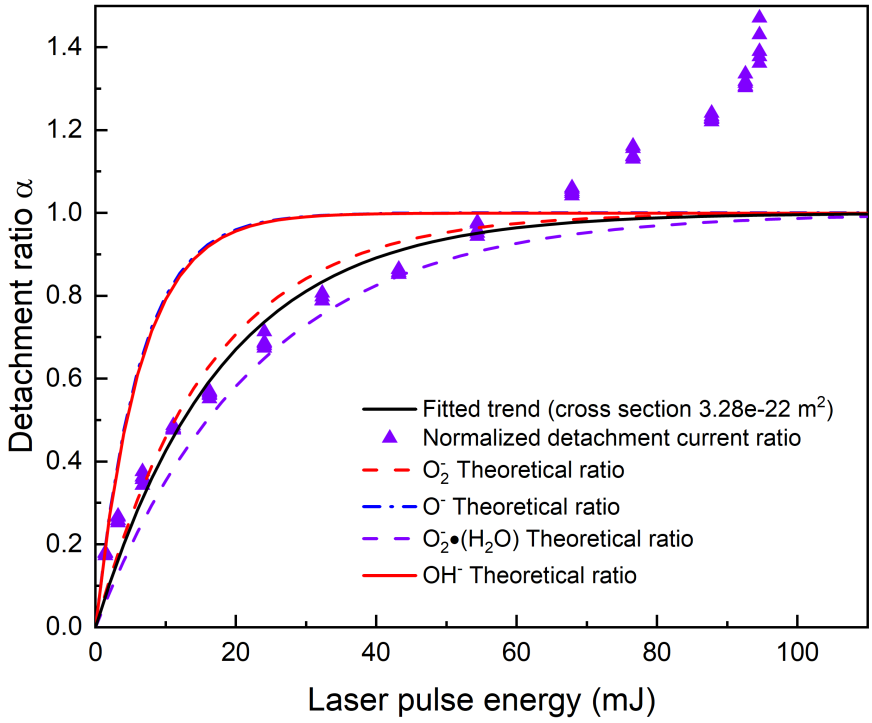

Figure 4.4: Normalized photodetachment ratio at a 3.7 mm diameter laser beam (discharge current 34 mA, local density ratio 0.0434, effective cross section $3.28 \times 10^{-22}\mathrm{m}^2$)

Although the laser pulse energy was limited, the detachment ratio is correlated with the laser fluence which is energy per area. Therefore, more negative ions per unit volume can be detached if the laser beam is focused into a smaller beam. On the other hand, a smaller beam would not be able to cover the whole plasma and the detachment current only represents the negative ions detached from the plasma volume within the beam coverage. Therefore, a smaller local density ratio is expected. Fig 4.4 shows the detachment ratio at a beam diameter of 3.7 mm. As anticipated, the data is closer to saturation, yet the detachment current abnormally increases beyond a certain

beam energy, deviating from the theoretical trend. This anomaly was also found in similar research and is attributed to the laser ablation of the probe surface contacting the beam [16, 23, 24]. Indeed, a very strong current signal can be found when the laser beam covers the cathode surface. It also becomes extremely serious when a highly focused beam is used which can form photoionization electrons. Except for the anomaly, the data at smaller pulse energy does follow the trend and the fitted effective cross section is very close to the unfocused beam result.

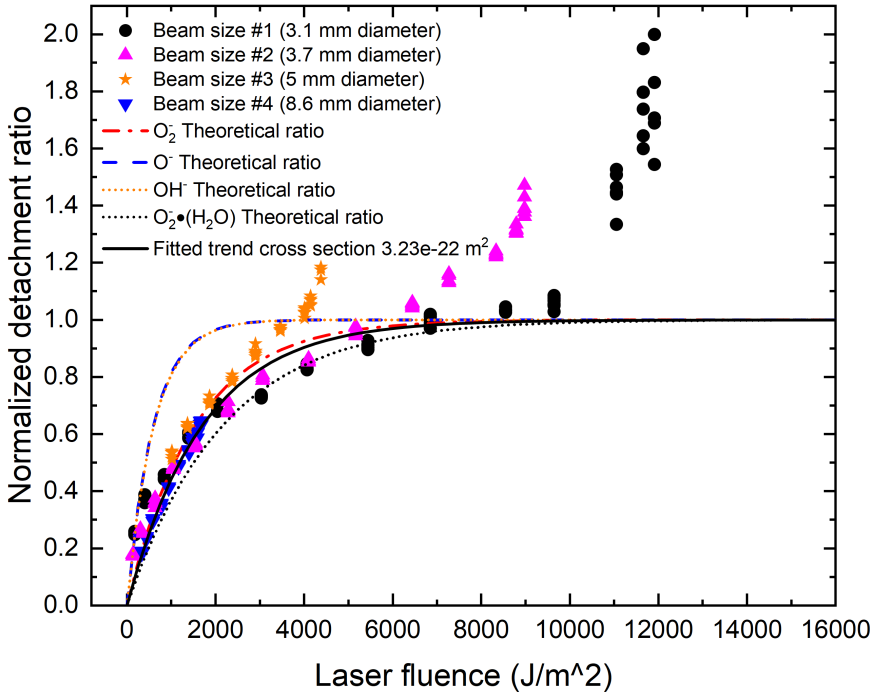

Figure 4.5: Normalized photodetachment ratio as a function of laser fluence with various beam sizes

Fig 4.5 shows the detachment ratio as a function of laser fluence from four different beam sizes. By plotting the data as a function of laser energy per area, different beam sizes can be compared with the theoretical curve together where the detailed fitting results can be found in Tab 4.3. The smaller the beam area, the higher the laser fluence and the higher the chance to reach saturation of photodetachment. Although the anomaly persists at the higher beam energies, the fitted effective photodetachment cross sections across these beam sizes are only narrowly dispersed. A smaller beam also limits the volume of plasma having photodetachment and thus a smaller local density ratio is found. The effective cross sections from four different beam sizes are all close to the O_2^-. It is convincing that the experiment indicates a glow discharge at atmospheric pressure is dominated by O_2^- negative ions whereas the exact mechanism requires a kinetic model to be fully understood. Note that the data is prone to deviate from the theoretical curve at smaller laser energy when a

smaller laser beam is used. Although the precise reason for the deviation is unclear, a tightly focused beam should be avoided in the photodetachment experiment in future work.

Table 4.3: Effective photodetachment cross section and negative ion density ratio from various beam size

Beam diameter (mm)	**Local density ratio**	**Effective cross-section at 355 nm** ($\times 10^{-22}\mathrm{m}^2$)
8.6	0.104	3.25
5.0	0.0566	3.28
3.7	0.0434	3.28
3.1	0.0215	3.12

4.3.3 Impact at Self-organized Pattern

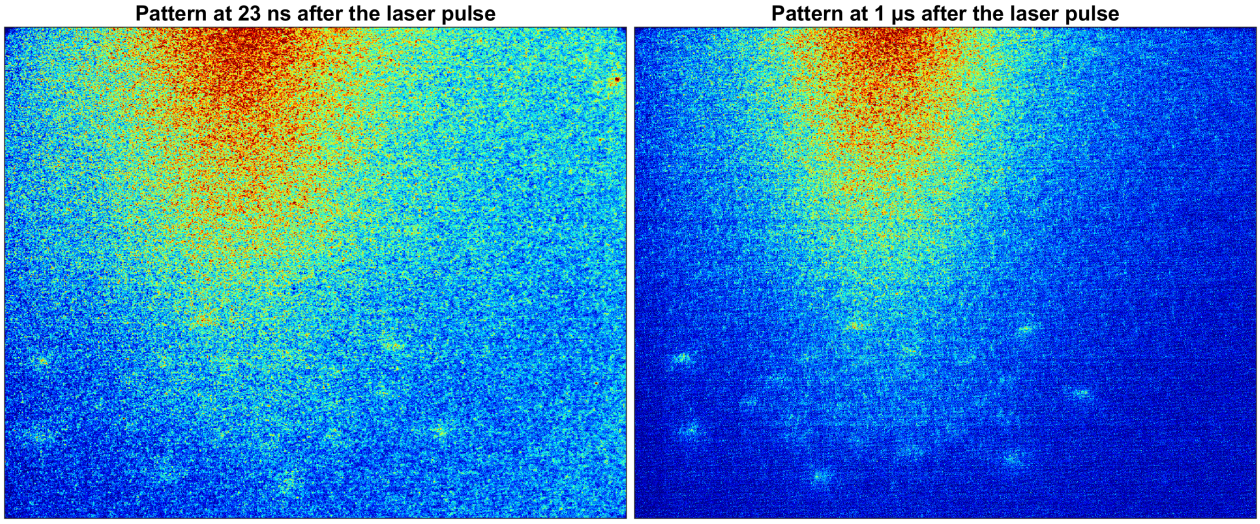

Figure 4.6: Self-organized pattern with laser photodetachment (Laser pulse 97 mJ, beam diameter 8.7 mm, discharge current 52 mA)

Identifying the dominant negative ions O_2^- again indicates the importance of oxygen gas in atmospheric glow discharge. However, SOP exhibits no impact during photodetachment as shown in Fig 4.6. The original images are 16-bit grayscale which is transformed into a color one for better contrast. Due to the intense reflection of laser rays toward the camera, the earliest image was taken at 23 ns after the laser pulse whereas no prominent deviation is observed. Given that the rise time of the photodetachment current is 20 ns in Fig 4.2, it is believed that at least 62% of

negative ions have been detached at this moment. The right image of Fig 4.6 shows the pattern image at 1 μs after the laser pulse and no observable change exists. In fact, different orders of delay time scale from nanoseconds to a few hundred microseconds were examined, yet no impact from photodetachment was found. Based on these results, the plasma self-organization does not appear to be correlated with the negative ion mechanism at least over the range investigated here. A pulsed DC glow discharge experiment was performed and the results suggested that the pattern is established in ∼100 μs which is a rather long time scale compared with the kinetic processes [25]. Negative ions are also known to exist around the periphery of the plasma column where the ambient oxygen attaches with diffusing electrons, thus it is plausible that these regions may need further probing.

4.4 Summary

A laser photodetachment experiment was described in this chapter to investigate the role of negative ions in the mechanics of SOP. A prominent discharge current increase could be detected when photodetachment was engaged and should increase with laser energy until saturation. However, the laser energy was not high enough to reach saturation, and O_2^- was found as the dominant negative ion species according to the fitted effective photodetachment cross section. The factor between the current ratio and the detachment ratio can be used to estimate the negative ion density which is about $\sim 10^{12}\mathrm{cm}^{-3}$. A focused laser beam increased the laser fluence and led to a more intense photodetachment while an abnormal current spike was also observed probably due to the ablation of the exposed electrode. An examination of the SOP dynamics from the ICCD camera revealed no change under the photodetachment condition. This means the self-organization at atmospheric glow discharge with liquid is not dependent on the 62% negative ions that are detached by the laser. Nevertheless, the current experiment cannot fully ascertain the mechanism of negative ions in SOP unless the photodetachment is performed thoroughly at a larger energy and length scale.

References

[1] Alexander Fridman and Lawrence A Kennedy. *Plasma physics and engineering*. CRC press, 2004.

[2] Ansgar Schmidt-Bleker, Seth A Norberg, Jörn Winter, Eric Johnsen, S Reuter, KD Weltmann, and Mark J Kushner. Propagation mechanisms of guided streamers in plasma jets: the influence of electronegativity of the surrounding gas. *Plasma Sources Science and Technology*, 24(3):035022, 2015.

[3] Roger A Haas. Plasma stability of electric discharges in molecular gases. *Physical Review A*, 8(2):1017, 1973.

[4] Naoki Shirai, Satoshi Uchida, and Fumiyoshi Tochikubo. Influence of oxygen gas on characteristics of self-organized luminous pattern formation observed in an atmospheric dc glow discharge using a liquid electrode. *Plasma Sources Science and Technology*, 23(5):054010, 2014.

[5] Shiqiang Zhang and Thierry Dufour. Self-organized patterns by a dc pin liquid anode discharge in ambient air: Effect of liquid types on formation. *Physics of Plasmas*, 25(7), 2018.

[6] JPJ Dubois, K Achkasov, D Kogut, A Ahmad, JM Layet, A Simonin, and Gilles Cartry. Negative-ion surface production in hydrogen plasmas: Determination of the negative-ion energy and angle distribution function using mass spectrometry. *Journal of Applied Physics*, 119(19), 2016.

[7] JR Legorreta, JL Patiño, and FB Yousif. Laser induced photo-detachment of o2 in dc discharge. *Plasma Science and Technology*, 20(7):075401, 2018.

[8] Koichi Sasaki, Ryohei Hosoda, and Naoki Shirai. Negative ion species in atmospheric-pressure helium dc glow discharge produced in ambient air. *Plasma Sources Science and Technology*, 29(8):085012, 2020.

[9] LC Lee and GP Smith. Photodissociation and photodetachment of molecular negative ions. vi. ions in o2/ch4/h2o mixtures from 3500 to 8600 å. *The Journal of Chemical Physics*, 70(4):1727–1735, 1979.

[10] Matthieu Génévriez, Kevin M Dunseath, Mariko Terao-Dunseath, Alan Hibbert, Arnaud Dochain, Raphaël Marion, and Xavier Urbain. Absolute total, partial, and differential cross sections for photodetachment of o-. *Physical Review A*, 98(3):033410, 2018.

[11] Lewis M Branscomb. Photodetachment cross section, electron affinity, and structure of the negative hydroxyl ion. *Physical Review*, 148(1):11, 1966.

[12] LM ao Chanin, AV Phelps, and MA Biondi. Measurement of the attachment of slow electrons in oxygen. *Physical Review Letters*, 2(8):344, 1959.

[13] D Spence and GJ Schulz. Three-body attachment in o 2 using electron beams. *Physical Review A*, 5(2):724, 1972.

[14] Thomas Jaffke, Martina Meinke, Reza Hashemi, Loucas G Christophorou, and Eugen Illenberger. Dissociative electron attachment to singlet oxygen. *Chemical physics letters*, 193(1-3):62–68, 1992.

[15] Yukikazu Itikawa and Nigel Mason. Cross sections for electron collisions with water molecules. *Journal of Physical and Chemical reference data*, 34(1):1–22, 2005.

[16] Shin Kajita, Shinichiro Kado, and Satoru Tanaka. Eclipse laser photodetachment method for avoiding probe surface ablation in negative ion measurement. *Plasma Sources Science and Technology*, 14(3):566, 2005.

[17] Yao E Kovach, María C García, and John E Foster. Optical emission spectroscopy investigation of a 1-atm dc glow discharge with liquid anode and associated self-organization patterns. *IEEE Transactions on Plasma Science*, 47(7):3214–3227, 2019.

[18] Peter Bruggeman, Tiny Verreycken, Manuel A Gonzalez, James L Walsh, Michael G Kong, Christophe Leys, and Daan C Schram. Optical emission spectroscopy as a diagnostic for plasmas in liquids: opportunities and pitfalls. *Journal of Physics D: Applied Physics*, 43(12):124005, 2010.

[19] JT Gudmundsson, IG Kouznetsov, KK Patel, and MA Lieberman. Electronegativity of low-pressure high-density oxygen discharges. *Journal of Physics D: Applied Physics*, 34(7):1100, 2001.

[20] Vladimir V Ivanov, Konstantin S Klopovsky, Dmitriy V Lopaev, Alexandr T Rakhimov, and Tatyana V Rakhimova. Experimental and theoretical investigation of oxygen glow discharge structure at low pressures. *IEEE Transactions on plasma science*, 27(5):1279–1287, 1999.

[21] J de Urquijo, O González-Magaña, E Basurto, and AM Juárez. Two-and three-body attachment, electron transport and ionisation in water-air mixtures. *Journal of Physics D: Applied Physics*, 57(12):125205, 2023.

[22] Željko Mladenović and Saša Gocić. Influence of air and water vapor on eedf, plasma parameters, and the main rons in atmospheric pressure low temperature helium plasmas: Global model approach. *Physics of Plasmas*, 29(10), 2022.

[23] JW Bradley, SD You, R Dodd, and PM Bryant. Negative ion density measurements by laser photo-detachment in rf and dc reactive magnetron discharges. *Laser*, 1:R1, 2010.

[24] N Sirse, N Oudini, A Bendib, and AR Ellingboe. Measurement of electronegativity at different laser wavelengths: accuracy of langmuir probe assisted laser photo-detachment. *Plasma Sources Science and Technology*, 25(4):04LT01, 2016.

[25] Tanubhav Srivastava, Marien Simeni Simeni, Gaurav Nayak, and Peter J Bruggeman. Self-organized patterns at the plasma–liquid anode interface in a helium glow discharge: temporal development and mechanisms. *Plasma Sources Science and Technology*, 31(8):085010, 2022.

CHAPTER 5

Spatially Resolved Plasma Parameters of a DC Glow Discharge with Liquid Anode

5.1 Introduction

In plasma science, optical emission spectroscopy (OES) is a well-established and widely-used diagnostic method [1]. Excited neutrals and their ions radiate electromagnetic waves during kinetic processes that can be analyzed and provide insight into the corresponding dynamics and plasma properties. One of the most prominent advantages of OES is the non-invasive nature which only requires an optical port and does not interfere with the plasma or experimental setup. On the other hand, the interpretation of the recorded spectra needs to be correlated generally with a kinetic model that comprehensively describes the various kinetic processes in the plasma. Another drawback comes from the difficulty of obtaining spatially resolved information since the radiation is integrated along the line of sight and recorded by a fiber in most cases. Unfortunately, these issues are more pronounced when diagnosing atmospheric plasma. Atmospheric plasma is generally in a non-equilibrium state where different species do not have the same translational energy and molecules' different degrees of freedom (excitation, translation, rotation, vibration) are also out of equilibrium. To understand the plasma properties thoroughly, multiple temperature parameters have to be measured and analyzed. Running a plasma with ambient air means nitrogen, oxygen, and water molecules participate in the reactions and introduce a prodigious amount of species and sophisticated radiation bands. Although their presence enables multiple channels to gather the plasma properties, it further complicates the interpretation of the plasma radiation. Atmospheric pressure also greatly enhances the collision rate of those reactions with neutral species and limits the diffusion of charged particles. As a result, these fast kinetic processes usually induce the correlated species to develop a non-Maxwellian distribution and perplex the analysis. Finally, atmospheric plasma is nonuniform and unstable where its properties and emission vary spatially and temporally [2]. Despite these difficulties, OES is widely used in atmospheric plasma diagnostics

owing to the non-invasive nature and unavailability of conventional techniques such as Langmuir probe [3].

The gas temperature is an important plasma parameter as many kinetic processes are exponentially dependent on its value thus greatly affecting the performance of plasma applications. It also gives insight into the efficiency of plasma ionization because the vibrational excitation of molecules and other exothermic reactions consumes a large amount of electron energy. In the case of applications involving heat-sensitive medium treated by plasma, the measurement and control of gas temperature is paramount. The general methods for obtaining the gas temperature in OES include the rotational temperature of diatomic molecules [4], van der Waals broadening of spectral atomic lines at low gas temperature (T_g<350 K) [5, 6], Doppler broadening of spectral atomic lines at higher gas temperature (T_g>2000 K) [7]. Among these methods, the rotational temperature of diatomic molecules is frequently chosen since it does not require additional atomic gas and can cover a wider temperature range. On the other hand, the time for thermalization of a rotational distribution has to be much shorter than the radiative lifetime of the rotational excitation state. Otherwise, it would cause a non-Maxwellian distribution and make the kinetic model invalid. A non-equilibrium between the rotational distribution and translational population also put the estimation in vain.

OES has also been used to estimate electron density and temperature. Stark broadening of the atomic line (usually H_β for its linear Stark effect) is widely used although special care has to be paid to the spectral line fine structure at low densities [8]. Specifically, Doppler broadening and van der Waals broadening would contribute comparable or even larger degrees at $n_e < 10^{16}\mathrm{cm}^{-3}$ and both components are correlated with gas temperature. Electron temperature can also be estimated by comparing the H_β and H_α. Different spectral lines' broadening depends differently on the electron density and the temperature which can be simulated with a kinetic model and the temperature can be deduced from calculated electron density [9]. Continuum radiation from free-free bremsstrahlung interactions between electrons and neutral atoms becomes important if the atmospheric plasma density is high [10]. With a good knowledge of the species and their bremsstrahlung cross-section, the measured emission is fitted with the theoretical one to calculate the electron temperature and density.

This work performs a spatially resolved optical emission spectroscopy on the atmospheric glow discharge over a liquid anode. Species' spatial distribution is presented based on their emission result. Gas temperature is estimated by the rotational temperature of $\mathrm{N}_2(C^3\Pi_\mathrm{u} \rightarrow B^3\Pi_\mathrm{g})$ at various plasma conditions. Spatially resolved electron density and reduced electric field measurement are also attempted while the weak emission at low density region causes a high degree of uncertainty. The variation of plasma properties' spatial distribution reveals its correlations with the dynamics of SOP.

5.2 Experimental Setup

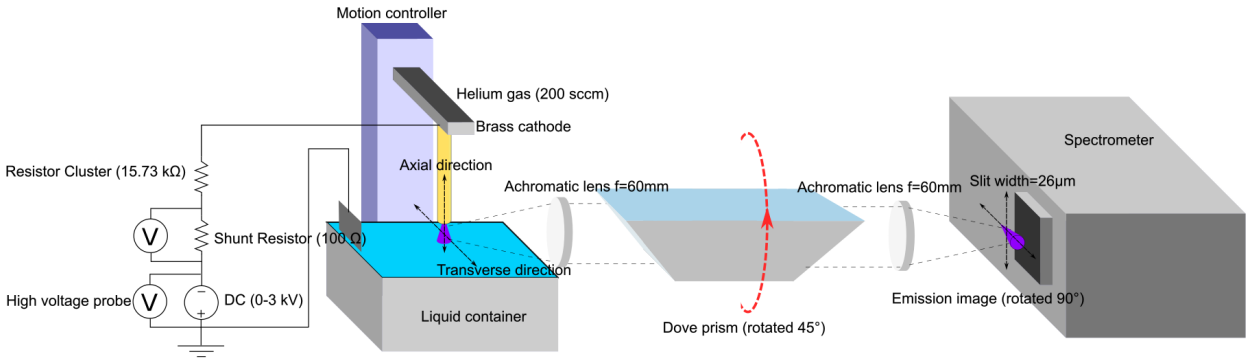

Figure 5.1: Schematic of the spatially resolved spectra measurement setup

Fig 5.1 illustrates the instrument used in the spatially resolved OES measurement. The discharge part is the same as illustrated in section 2.1. The liquid circulation to a reservoir is critical for a stable and static acquisition where the plasma-liquid interface will stay at the same height. When measuring the radial distribution of plasma emission, an achromatic lens (focal length 60mm) is used to focus the scattered emission into a collimated beam for the following dove prism. The prism is rotated 45 degrees to make a 90-degree rotation of the plasma image. Then, another achromatic lens is used to focus the rotated image to its original size at the entrance slit. The distance between the first achromatic lens and plasma column s and the distance between the slit and second achromatic lens s' would define the magnification ratio $M = \frac{s'}{s}$. For radial distribution measurement, both distances are 60 mm which yields a real image on the ICCD with a spatial scale of 26.7 μm/pixel. When the axial distribution is measured, only one achromatic lens is used to project the plasma image. The magnification ratio is set to 0.63 with a spatial scale of 40 μm/pixel otherwise the 256 rows of pixels cannot accommodate the whole 8 mm long plasma column.

The plasma emission is diffracted by a Czerny-Turner configuration spectrometer (Acton SP2300i) of 0.3 m focal length equipped with an 1800 grooves/mm holographic grating. A fast ICCD camera (PI-MAX3) is coupled with the spectrometer to record the diffracted emission on a 1024×256 pixels sensor. The number of rows of the sensor times the spatial scale determines the spatial range of the spectra while the width corresponds with the wavelength range. The slit opening is set the same as the physical size of the pixel (26 μm) in PI-MAX3 to maximize the useful resolution. The measured spectral resolution is 0.04 nm.

5.3 Methods of Spatially Resolved Optical Emission Spectroscopy

5.3.1 Data Acquisition

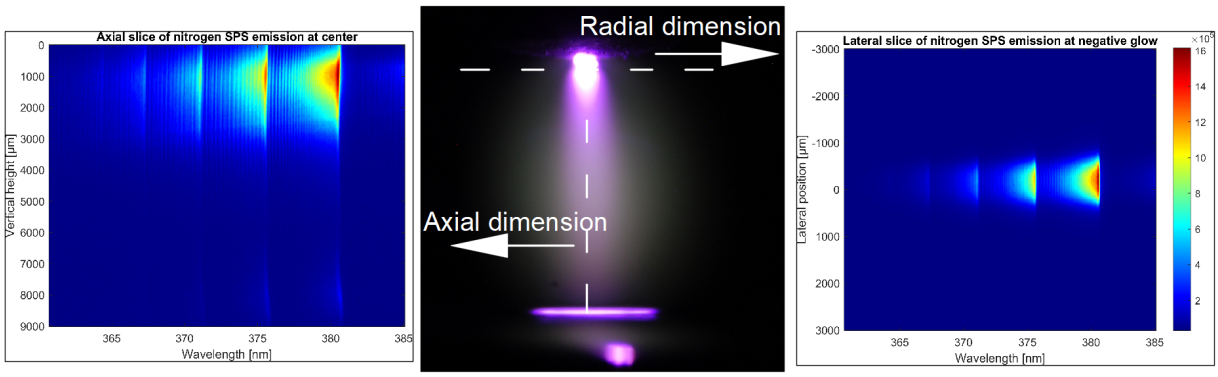

Figure 5.2: Illustration of the spatial resolved spectra acquisition

Spatially resolved OES is desirable considering the nonuniform distribution of plasma parameters in the atmospheric plasma. For a normal glow discharge, the variation along the axial (vertical) coordinate is due to the change of electric field and space charge density while the radial distribution depends on diffusion and attachment loss. Studying and analyzing the spatially resolved emission spectra of a plasma can be challenging when using a conventional method. In default, an optical fiber collects all the emissions within its numerical aperture and transmits them onto the spectrometer's slit. It is a simple and compact method whereas the information loses its spatial distribution. When a focusing lens is used, an upside-down image of the emission can be projected on the slit and preserve its spatial distribution. The slit has to be implemented to control the spread of the angle of incident light on the diffraction grating and this is essential for a decent wavelength resolution. However, this also greatly narrows the emission in the horizontal (radial) dimension while the vertical (axial) dimension is preserved as long as the image is within the slit's height. Alternatively, a dove prism can be used to rotate the emission image 90 degrees where the horizontal (radial) dimension is preserved when it is aligned with the slit but the axial dimension is narrowed at this arrangement. When the incident light is diffracted by the grating and reflected onto the ICCD, a data matrix is obtained where the horizontal axis corresponds to the wavelength, and the emission's radial or axial distribution is allocated to the vertical axis. As illustrated in Fig 5.2, each matrix is a vertical or horizontal slice of the plasma emissions depending on the orientation of the plasma image relative to the entrance slit. By moving the plasma and the optical lens together

horizontally, the relative position of the slit versus the image will be shifted, then a vertical slice of the plasma emission at different lateral positions can be examined and vice versa for the horizontal slice. The scan was performed with a step size of 100 μm generally, though a bigger step was also used when the emission indicated insignificant change at the positive column. For a 2D plot, there is no extra dimension that could represent the distribution of different spectral lines in the same band. Instead, the strongest band head is picked to represent the characteristics of the species emission. By combining each slice's band head lateral distribution across the axial dimension, the entire map of plasma emissions can be obtained as shown in Fig 5.3 where the X-axis represents the lateral position, the Y-axis corresponds to the vertical distance to the cathode, and the intensity is shown by the logarithmic color bar. Alternatively, the emission map can also be obtained by combining the vertical slices across the radial dimension.

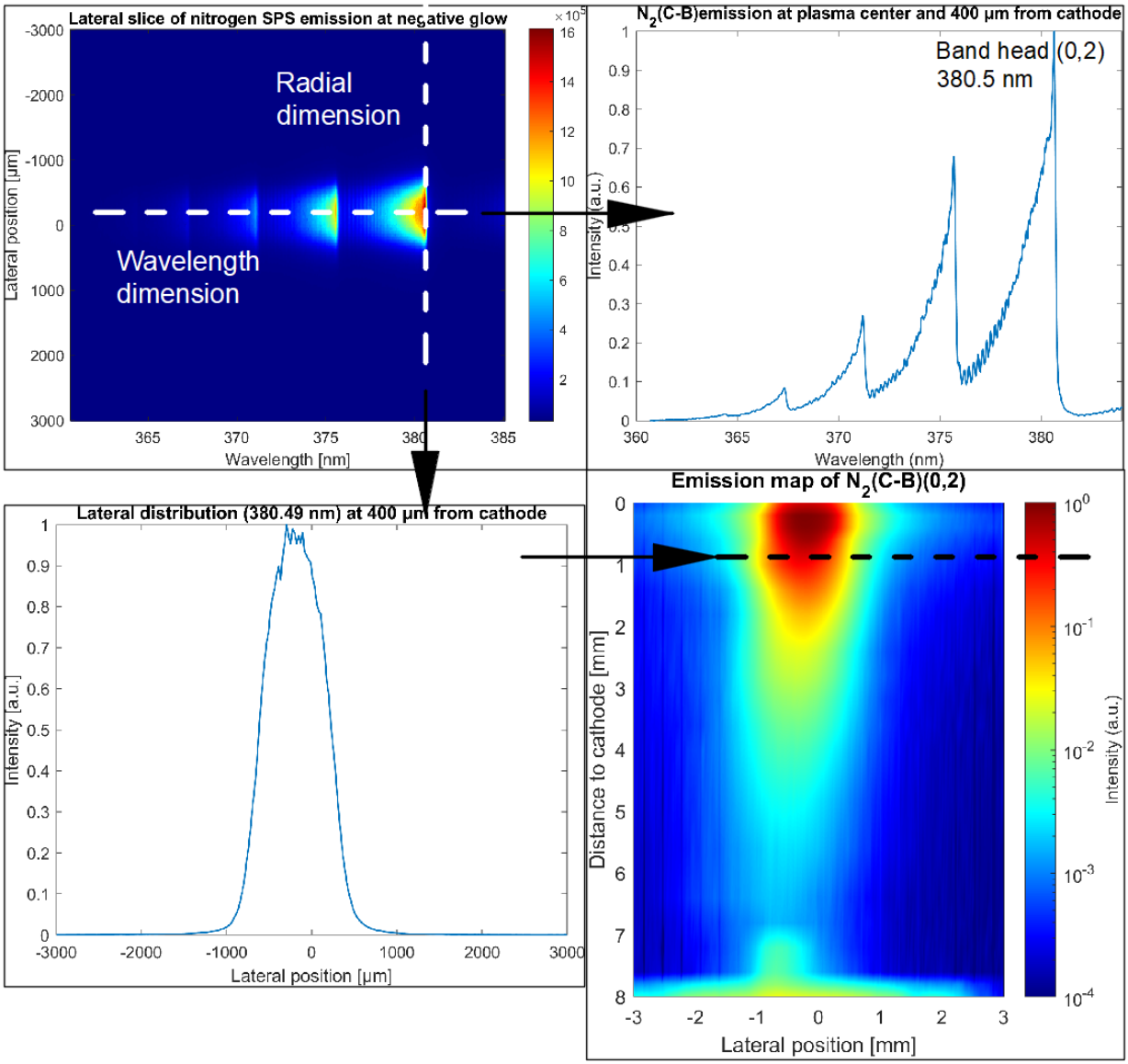

Figure 5.3: Illustration on the acquisition of full emission map of $N_2(C-B)$(380.49 nm). Left top: data matrix of a horizontal slice; right top: emission at the center as a function of wavelength; left bottom: lateral distribution of the emission band head (0,2); right bottom: the combined emission map

The spatial scale calibration is performed by recording a ruler picture with ICCD's image mode. The non-uniformities in gain from pixel to pixel are also calibrated on the ICCD camera to ensure a consistent response. A pre-calibrated tungsten lamp was used to provide a known continuum black body radiation which is divided by the acquired emission data. The result is a normalization matrix which is used to correct the raw data to reduce the systematic error. Other systematic errors are mainly from the movement of plasma and the optical aberration of the lens and spectrograph.

5.3.2 Gas Temperature Estimation

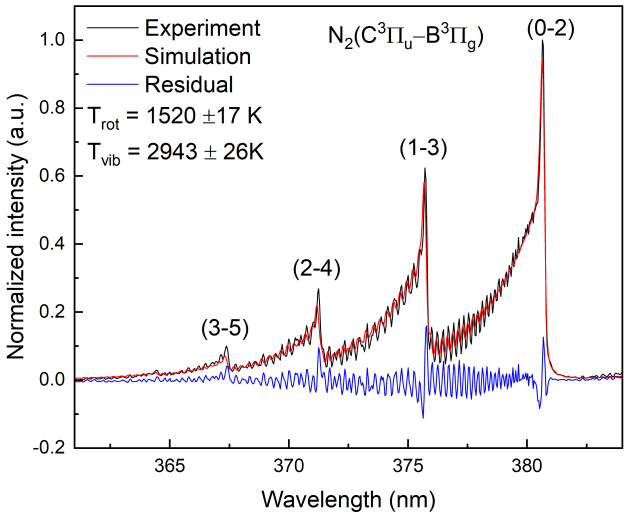

Figure 5.4: Experimental and simulated spectra of $N_2(C-B)$ in negative glow region at 50 mA, 1520 K and 2943 K are estimated for rotational and vibrational temperature, respectively.

The rotational temperature of excited molecules is usually used as an estimation of the gas temperature (translational temperature). This is because the rotational energy is quantized by a constant that is inversely proportional to the moment of inertia $I = (1/M_1 + 1/M_2)r^2$. On the other hand, vibrational energy is usually larger since its constant is inversely proportional to the square root of moment of inertia. A nitrogen molecule has a rotational constant of 2.48×10^{-4} eV whereas its vibrational constant is 0.29 eV. This order of magnitude difference makes the rotational level well-populated and the rotational-translational relaxation very fast compared to the vibrational-translational relaxation. Therefore, the rotational temperature of molecular gas in plasma is usually very close to the translational temperature even in nonequilibrium discharges, while vibrational temperatures can be significantly higher [11].

For gas temperature estimation, the rotational temperature of nitrogen second positive band $N_2(C^3\Pi_u \rightarrow B^3\Pi_g)$ is chosen instead of the more abundant $OH(A^2\Lambda^+ \rightarrow X^2\Pi)$ band. Research has suggested that $OH(A-X)$ is not a good representation of the gas temperature because the quenching process by water molecules (0.5 ns at 1850 K [12]) is at the same time scale of rotational energy transfer process (0.6 ns [13]) for thermalization [14]. In addition, the dissociative excitation of water molecules contributes a large portion of the $OH(A)$ production and induces a higher rotational temperature which is non-Boltzmann. $N_2(C)$, conversely, is dominantly produced by electron impact excitation in nitrogen gas and thus thermalized. It also suffers less impact from quenching since the time of thermalization ($\sim$100 ps [4]) is faster and yields a good estimation

of the gas temperature. This was also justified by a comparison among the rotational temperature method using $\mathrm{OH}(A-X)$, $\mathrm{N_2}(C-B)$, and Rayleigh scattering where the rotational temperature of $\mathrm{N_2}(C)$ is more reliable and similar with the result of Rayleigh scattering [15]. In this work, the transition of $\mathrm{N_2}(C-B, \Delta\nu=-2)$ in the range 360-380 nm is measured and fitted with simulated spectra using *massiveOES* [16] for the estimation of gas temperature. A fitting example is shown in Fig 5.4 which indicates a rotational temperature of 1520 K in the negative glow region at 50 mA. The uncertainty of the results is within 3.3 % which is based on the standard deviation between the measured spectra and the analytic one.

5.3.3 Electron Density Estimation

The electron density is determined by the Stark broadening of H_β line (486.13 nm). It is more suitable than H_α which features a smaller full width at half maximum (FWHM) and thus only applicable at larger electron density (>$5 \times 10^{14}\mathrm{cm}^{-3}$) [17]. The fine structure of a H_β line is decided by a variety of broadening mechanisms that result in a Voigt profile, a convolution of Lorentzian and Gaussian broadening profiles. The detailed calculations of each broadening mechanism are shown as follows:

1) *Instrumental broadening*

Acquisition of the spectral lines experiences additional broadening unrelated to plasma processes. Optical instrument broadening is inevitable in the measurement system and thus it represents a systematic error. It is mostly determined by the dispersion through optical elements, the spectrometer slit width (diffraction effects), and dispersion in the spectrometer itself. This broadening is estimated by measuring a single-mode He-Ne laser's spectrum fitted with a Gaussian profile. Since the laser has a negligible dispersion, the FWHM of the profile can represent instrumental broadening $\Delta\lambda_I$. The measured instrumental broadening is 0.065 nm.

2) *Doppler broadening*

Doppler broadening is inflicted by the relative motion of an emitter to the detector leading to a shifted frequency of photons, i.e., the Doppler effect. Assuming the emitters have a Maxwellian distribution, the line shape of Doppler broadening resembles a Gaussian profile and depends on the temperature:

$$\Delta\lambda_D = \frac{1}{2}\lambda_0\sqrt{\frac{8\mathrm{k_B}T_g\ln 2}{mc^2}} = 3.48\times10^{-4}T_g^{1/2} \tag{5.1}$$

where λ_0 is the transition emission's wavelength (nm), m is the mass of the emitter (u), and T_g is the gas temperature given that the emitter is a heavy particle. The equation can be simplified since the mass of hydrogen and transition energy of H_β are already known.

3) *Van der Waals broadening*

Van der Waals broadening is due to the dipolar interaction between an excited atom (the emitter) with the dipoles induced by this emitter over the background of polarizable perturber atoms in the ground state. It becomes important if a plasma has an ionization degree lower than 10^{-4} with high neutral density [18]. This broadening is calculated with

$$\Delta\lambda_{vdw} = 8.18 \times 10^{-26} \lambda_0^2 (\overline{R}^2)^{0.4} T_g^{0.3} N \sum_i (\frac{\alpha_i^{0.4} \chi_i}{\mu_i^{0.3}}) \tag{5.2}$$

where N is the neutral density (cm^{-3}), i and α represent different perturbers and their polarizability, μ and χ are the reduced mass and fraction of perturber, respectively. For an air plasma, Eq 5.2 can be simplified as

$$\Delta\lambda_{vdw} = \frac{3.6}{T_g^{0.7}} \tag{5.3}$$

where coefficient 3.6 is calculated to include the effects of helium and air [3].

4) *Stark broadening*

Stark broadening is due to the Coulomb interaction between the emitter and the charged particles present in the plasma, mostly electrons. The broadening resembles a Lorentzian shape and can be estimated by

$$\Delta\lambda_S = 3.67 \cdot (\frac{n_e}{10^{23}\mathrm{m}^{-3}})^{\frac{2}{3}} \Rightarrow n_e = 10^{17} \cdot (\frac{\Delta\lambda_S}{3.67})^{\frac{3}{2}} (\mathrm{cm}^{-3}) \tag{5.4}$$

which is applicable for $10^{13} < n_e < 6 \times 10^{14} \mathrm{cm}^{-3}$ [19].

The other broadening mechanisms such as resonance broadening and natural broadening are negligible and can be excluded from calculation [8]. The process of electron density estimation starts with fitting the measured line profile with Voigt shape. The Voight profile's FWHM is a convolution of both Lorentzian and Gaussian broadening profiles:

$$\Delta\lambda_V \approx \sqrt{(\frac{\Delta\lambda_L}{2})^2 + \Delta\lambda_G^2} + \frac{\Delta\lambda_L}{2} \tag{5.5}$$

where the Gaussian and Lorentzian profiles' FWHM are

$$\Delta\lambda_G = \sqrt{\Delta\lambda_I^2 + \Delta\lambda_D^2} \tag{5.6}$$

and

$$\Delta\lambda_L = \Delta\lambda_{vdw} + \Delta\lambda_S \tag{5.7}$$

which can be estimated by the $\Delta\lambda_V$ and $\Delta\lambda_G$ by transforming Eq 5.5

$$\Delta\lambda_L \approx \Delta\lambda_V - \frac{\Delta\lambda_G^2}{\Delta\lambda_V} \tag{5.8}$$

With gas temperature estimated by $N_2(C-B)$, the $\Delta\lambda_{vdw}$ and $\Delta\lambda_D$ can be calculated and the $\Delta\lambda_S$ can be deduced which yields the electron density according to Eq 5.4. Fig 5.5 plots the line shape of H_β in negative glow region and an electron density $1.2\times10^{14}\mathrm{cm}^{-3}$ is calculated which is typical for a DC plasma at atmospheric pressure. Note that the line profile of H_β would split into different components at low electron density (<$4\times10^{13}\mathrm{cm}^{-3}$) and large systematic errors can be introduced from the deconvolution process [8, 20]. Apart from the fine structure splitting error, the electron density of low-temperature atmospheric pressure plasma calculated from the Stark broadening is usually only for estimation on the order of magnitude [19].

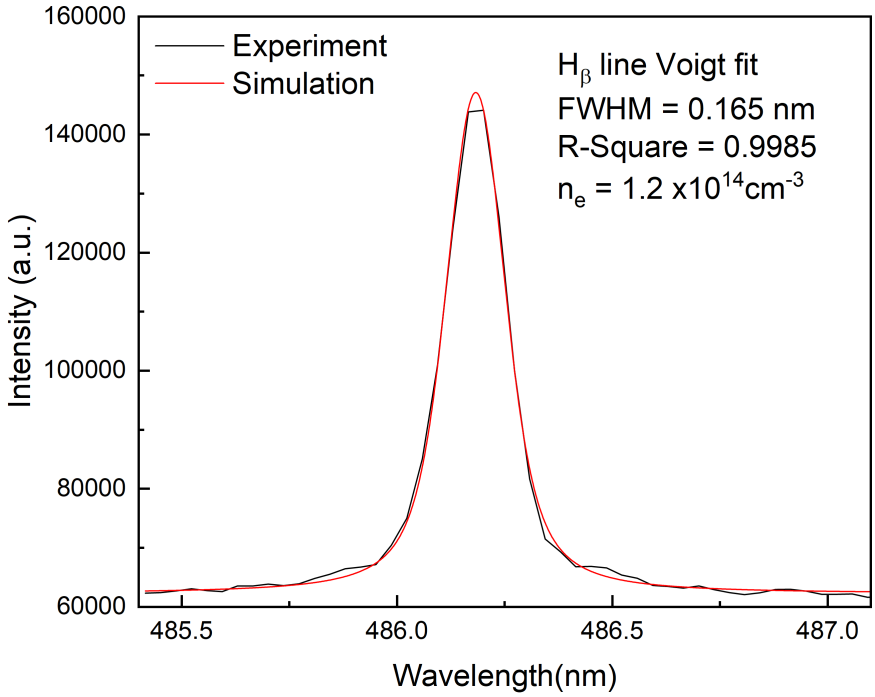

Figure 5.5: Experimental and fitted line shape of H_β in negative glow region at 50 mA, 1520 K and $1.2\times10^{14}\mathrm{cm}^{-3}$is estimated for electron density.

5.3.4 Abel Inversion for Radial Distribution

Measuring the plasma emission by side view means the recorded data is integrated along the line of sight across the medium, thus collected light does not contain any spatial information. Interpretation of such emission is problematic if the emission is highly nonuniform. The Abel transform method is an integral transform to analyze axially symmetric functions and its inverse form Abel inversion can deduce the radial distribution function from a spatially varying plasma [21]. This method has been applied in [22, 23, 24] and proven to be particularly advantageous in small length scale and nonuniform plasma sources. However, several assumptions have to be met to use this

method: 1) the object of interest must be cylindrically symmetric; 2) the target has to be optically thin; 3) the object should be stable in space and time during the measurement thus providing an unambiguous interpretation of the plasma state. A normal glow discharge can satisfy the first two criteria whereas additional attention has to be paid to the last assumption. Usually, a static emission scan can be achieved by a shorter exposure time which also decreases the signal-to-noise ratio.

The Abel transform is given by

$$I(x_0) = \int_{-y_0}^{y_0} f(r)dy \tag{5.9}$$

where y_0 is the transverse range of plasma at lateral position x_0. The equation means the detected emission $I(x_0)$ is the integral of emission distribution $f(r)$ across the plasma. To deduce the radial distribution from measured $I(x_0)$, inverse Abel transform is used

$$f(r) = -\frac{1}{\pi}\int_r^{\infty} \frac{I^{'}(x)}{\sqrt{x^2 - r^2}}dx \tag{5.10}$$

Solving the above equation requires a numerical method since the measured data is discrete and cannot be solved analytically due to discontinuity. In this work, the *Hankel–Fourier method* is implemented [25] which transforms the coordinate variable to a frequency variable k. The Fourier transform of the distribution is

$$F(k) = \int_{-\infty}^{\infty} I(x)\exp(ikx)dx \tag{5.11}$$

Transforming Eq 5.11 to polar coordinates yields

$$F(k) = 2\pi\int_0^{\infty} f(r)J_0(kr)rdr \tag{5.12}$$

where $J_0(kr)$ is the zero-order Bessel function of the first kind. The emission function $\epsilon(r)$ is obtained by the inverse of Hankel transform

$$f(r) = \frac{1}{2\pi}\int_0^{\infty} F(k)J_0(kr)kdk \tag{5.13}$$

Spline smoothing [26] is used to reduce the noise of the lateral distribution data $I(x)$ for a stable result of Hankel transform. To validate the accuracy of this numerical method, two theoretical radial distributions were used to generate the lateral emission data

Bell curve

$$g(r) = \begin{cases} 1 - 2r^2 & \text{for} \quad 0 \leq r \leq 0.5 \\ 2(1-r)^2 & \text{for} \quad 0.5 < r \leq 1 \end{cases} \tag{5.14}$$

Off-axis peak curve

$$h(r) = \begin{cases} \frac{3}{4} + 12r^2 - 32r^3 & \text{for} \quad 0 \leq r \leq 0.25 \\ \frac{16}{27}(1 + 6r - 15r^2 + 8r^3) & \text{for} \quad 0.25 < r \leq 1 \end{cases} \tag{5.15}$$

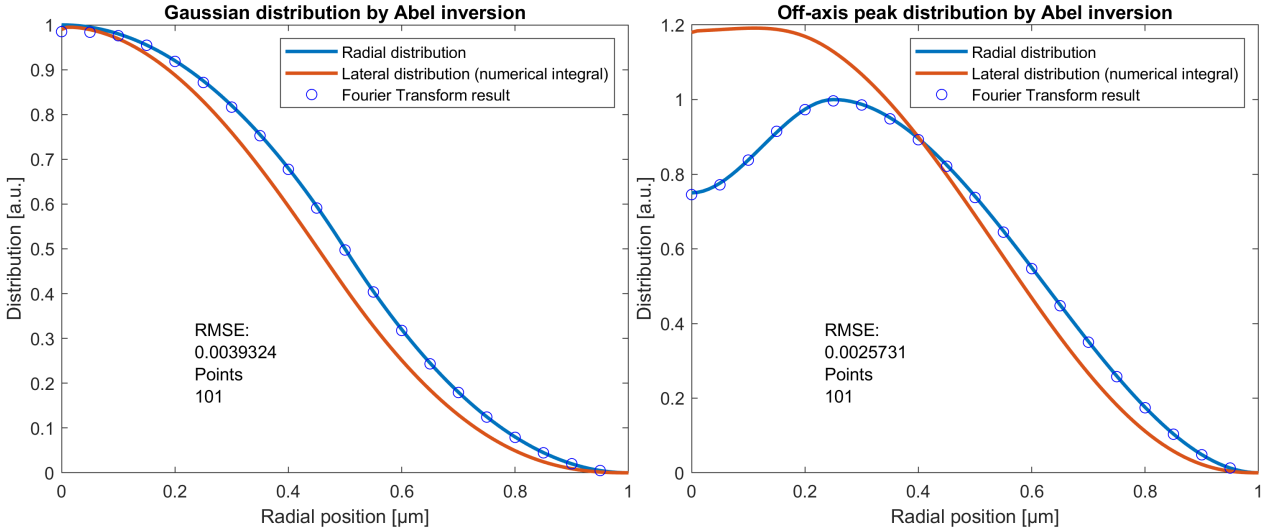

(a) Bell curve

(b) Off-axis peak curve

Figure 5.6: Benchmark of Hankel transform Abel inversion algorithms

Fig 5.6 shows the comparison between the theoretical distribution and the numerical result calculated from the lateral distribution. Clearly, the Hankel transform can deduce the emission function with complex distribution. The frequency k is limited up to 10 for saving computational resources.

5.4 Results and Discussion

5.4.1 Species Emission and Distribution

The excited species' emission in a spatially resolved OES provides the intensity, spectral profile, and distribution information altogether that can help with diagnostics and control of plasma conditions. The emission's intensity scale changes dramatically across the plasma column, and therefore a logarithmic color bar is used to differentiate the distribution at various locations. Fig 5.7 shows

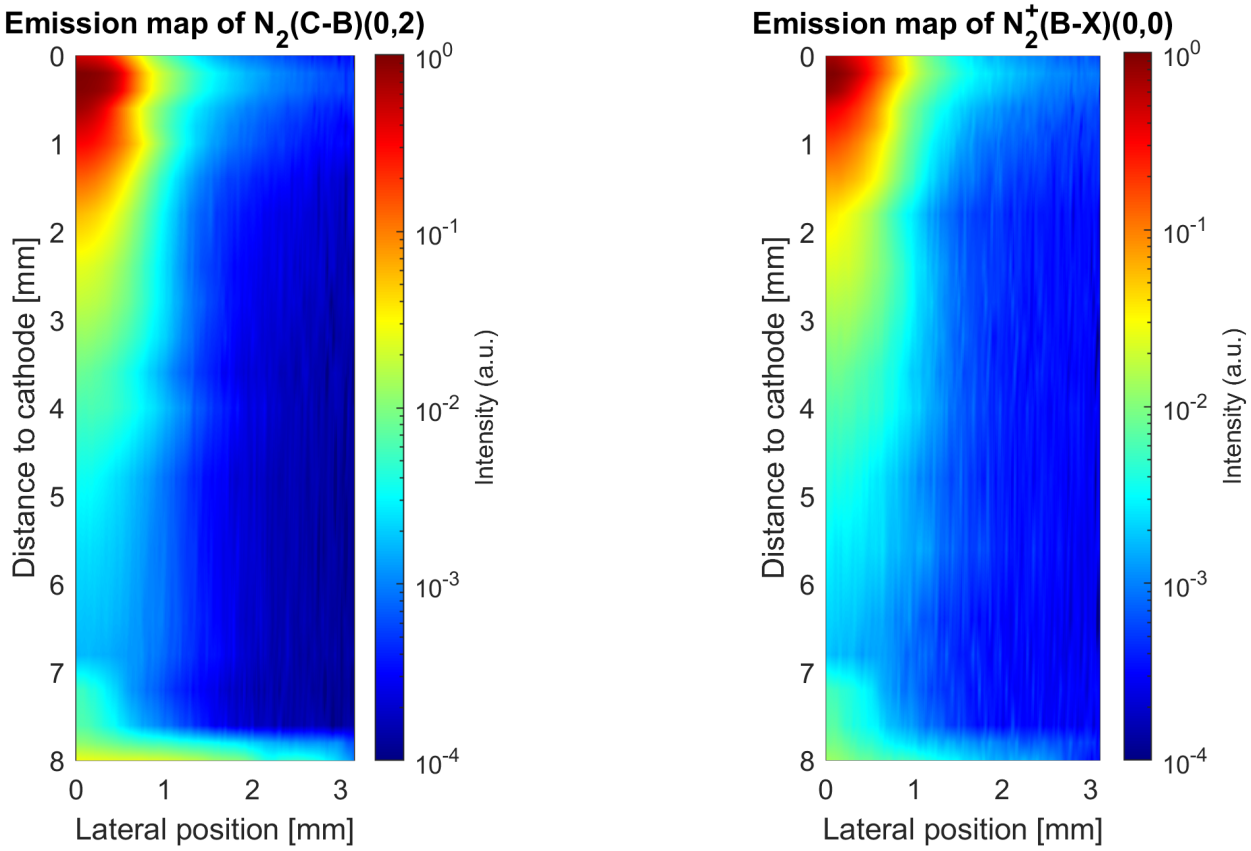

(a) Emission map of $\mathrm{N}_2(C-B)(0,2)(380.49\ \mathrm{nm})$

(b) Emission map of $\mathrm{N}_2^+(B-X)(0,0)(391.44\ \mathrm{nm})$

Figure 5.7: Emission intensity distribution of nitrogen species' emission (horizontal slice combined)

the emission map of nitrogen species combined by horizontal slices. Since a high fraction of electron energy is localized on the vibrational excitation of molecules for atmospheric plasma, the emission of excited nitrogen second positive system $\mathrm{N}_2(C-B)$ (upper-level energy 11.1 eV) is ubiquitous in the plasma column and features a high intensity. This emission is due to the direct electron excitation [27]:

$$\mathrm{e}^- + \mathrm{N}_2(X^1\Sigma_\mathrm{g}^+) \rightarrow \mathrm{N}_2(C^3\Pi_\mathrm{u}) + \mathrm{e}^- \tag{5.16}$$

and metastable pooling reaction [28]:

$$\mathrm{N}_2(A^3\Sigma_\mathrm{u}^+) + \mathrm{N}_2(A^3\Sigma_\mathrm{u}^+) \rightarrow \mathrm{N}_2(C^3\Pi_\mathrm{u}) + \mathrm{N}_2(X) \tag{5.17}$$

According to the distribution map, the emission is the strongest near the cathode glow region where high-energy electrons are present. At 560 µm vertical position, a contraction can be observed which

corresponds to the cathode dark space. The positive column also comprises the emission although the intensity is one to two orders of magnitude lower because the local average electron temperature is much lower than the excitation threshold. The cathode layer electric field is approximately 30-40 kV/cm, two orders of magnitude larger than the 700 V/cm in the positive column. Near the liquid surface, the distribution develops a protrusion region that distinctively grows from the anode towards the positive column about 1 mm. At first glance, this is possibly associated with the anode fall electric field which boosts the electron impact excitation. However, the anode fall region is correlated with the Debye length ($\sim 100\,\mu\mathrm{m}$), which is much smaller than the protrusion length scale and cannot affect the electron energy there. Alternatively, the axial distribution of gas temperature exhibits a steep decline at this position and can result in a higher neutral density and larger electric field. Finally, a strong emission can be found on the liquid anode which expanded radially further than the cathode glow. In fact, $\mathrm{N_2}(C-B)$ contributes the major part to the emissions of the SOP whose radial size corresponds to the emission's expansion. On the other hand, the emission is less bright than the cathode layer due to the quenching of vapor and weaker anode fall voltage.

Emission of $\mathrm{N_2^+}(B-X)$ (threshold energy 18.9 eV) is also observed in the plasma although it is less pronounced than $\mathrm{N_2}(C-B)$. The Penning ionization from metastable helium (19.82 eV) is efficient in producing this species [29]:

$$\mathrm{He^*} + \mathrm{N_2}(X^1\Sigma_\mathrm{g}^+) \rightarrow \mathrm{N_2^+}(B^2\Sigma_\mathrm{u}^+) + \mathrm{He} + \mathrm{e^-} \tag{5.18}$$

In addition, charge exchange between $\mathrm{N_2}$ and $\mathrm{He^+}$ can also produce the nitrogen ions. Due to the higher energy of $\mathrm{N_2^+}(B^2\Sigma_\mathrm{u}^+)$ state, its absolute intensity is weaker and the spatial distribution is limited. This is also the case for the anode fall region where the emission is dimmer than excited nitrogen neutrals. It was estimated that the cathode layer's electric field is three times larger than the anode layer's which is also below the electrohydrodynamic instability criterion 24.6 kV/cm [30]. The distinction between electric field and electron energy would have a greater impact on excited species with higher energy levels and thus more sensitive to the EEDF.

Fig 5.8 plots the distribution of other species' emissions that can be normally found in atmospheric plasma. The H and O are produced by electron-impact dissociation of water molecules and oxygen [31, 32, 33].

$$\mathrm{e^-} + \mathrm{H_2O} \rightarrow \mathrm{H}(n=1) + \mathrm{OH}(X) + \mathrm{e^-} \quad \text{threshold} \quad 5.1\mathrm{eV} \tag{5.19}$$

$$\mathrm{e^-} + \mathrm{H_2O} \rightarrow \mathrm{O}(^3P) + \mathrm{H_2}(X) + \mathrm{e^-} \quad \text{threshold} \quad 5.03\mathrm{eV} \tag{5.20}$$

$$\mathrm{e^-} + \mathrm{O_2} \rightarrow \mathrm{O}(^3P) + \mathrm{O}(^3P) + \mathrm{e^-} \quad \text{threshold} \quad 6\mathrm{eV} \tag{5.21}$$

while their excited states $\mathrm{H}(4d)$ and $\mathrm{O}(3p)$ have energy level of 12.75 eV and 10.74 eV, respec-

tively. Besides, the electron-ion dissociative recombination with O_2^+ and H_2O^+ become important production channels at low electron temperature regime [34]. The emission distributions of $O(3p-3s)$ and $H(4d-2p)$ are alike except for the region near liquid. This is due to the strong reaction between $O(3p)$ and water molecule which reduce the density [35, 36]:

$$O(3p) + H_2O \rightarrow OH(X) + OH(X) \tag{5.22}$$

Emission of $He(3d-2p)$ has an almost identical distribution with H_β though its high excitation energy level (23.1 eV) causes a weaker absolute intensity. The anode layer supports a comparable density of excited helium atoms as the cathode region. This is not seen in the emission of H_β or $O(3p-3s)$ since helium has a lower quenching rate with water.

The presence of sodium in the plasma column is believed to be transported by droplets [37, 38] since the evaporation is unable to bring salt ions into the gas phase. The emission of $Na(3p-3s)$ is distributed broadly thanks to the low energy level (2.1 eV). The emission is also presented in the positive column but not significantly near the anode. In this case, the sodium emission mostly depends on its transport mechanism in which the droplets would evaporate closer to the cathode glow and release the salt particles. This can also be justified by the spatial nonequilibrium of emission that is due to the fluctuation of emission between the acquisition of each horizontal slice. The average time between the acquisition of vertical position can be 30 seconds which is much longer than the relaxation time of the collisional process. On the other hand, the mechanical transport by droplets may give rise to a long relaxation time.

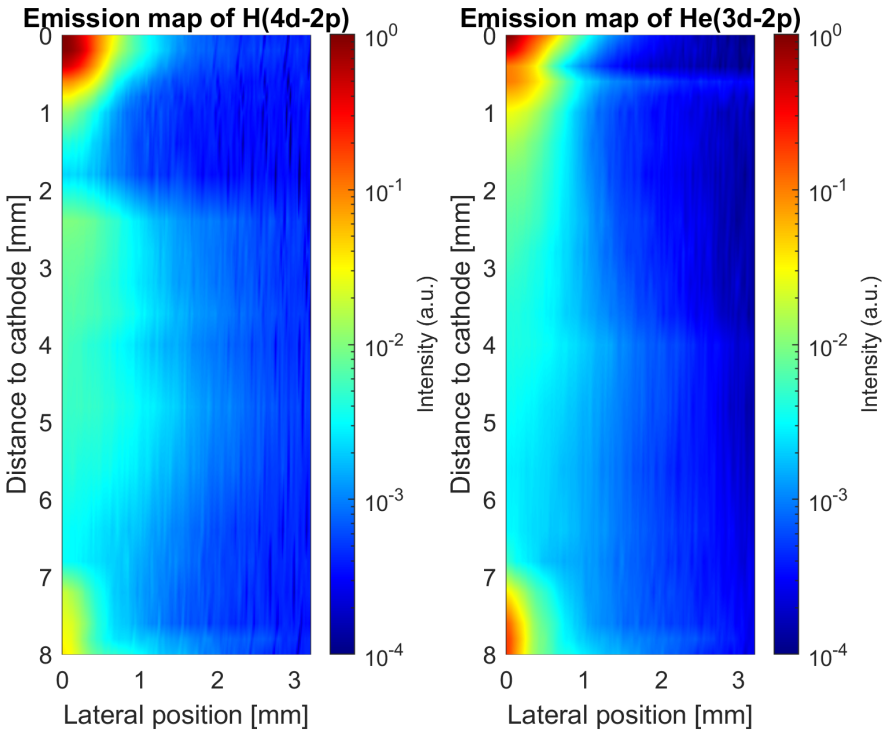

(a) Emission map of $\mathrm{H}(4d-2p)$(486.13 nm)

(b) Emission map of $\mathrm{He}(3d-2p)$(587.56 nm)

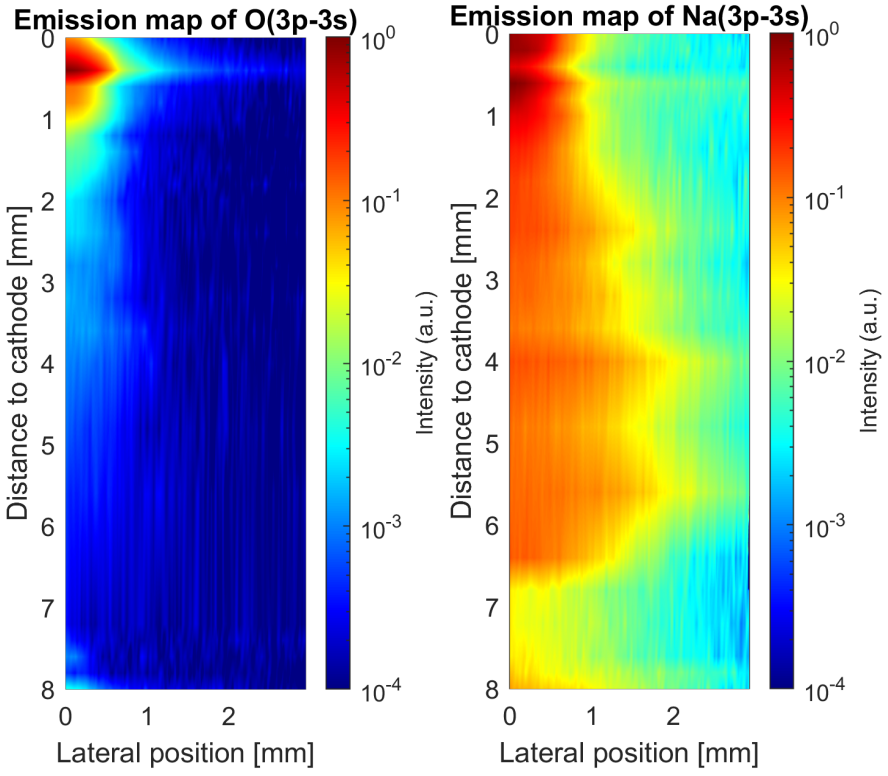

(c) Emission map of atomic oxygen $(3p-3s)$ (777.42 nm)

(d) Emission map of sodium atom $(3p-3s)$ (589.00 nm)

Figure 5.8: Spatial distribution of various species' emission intensity (horizontal slice combined)

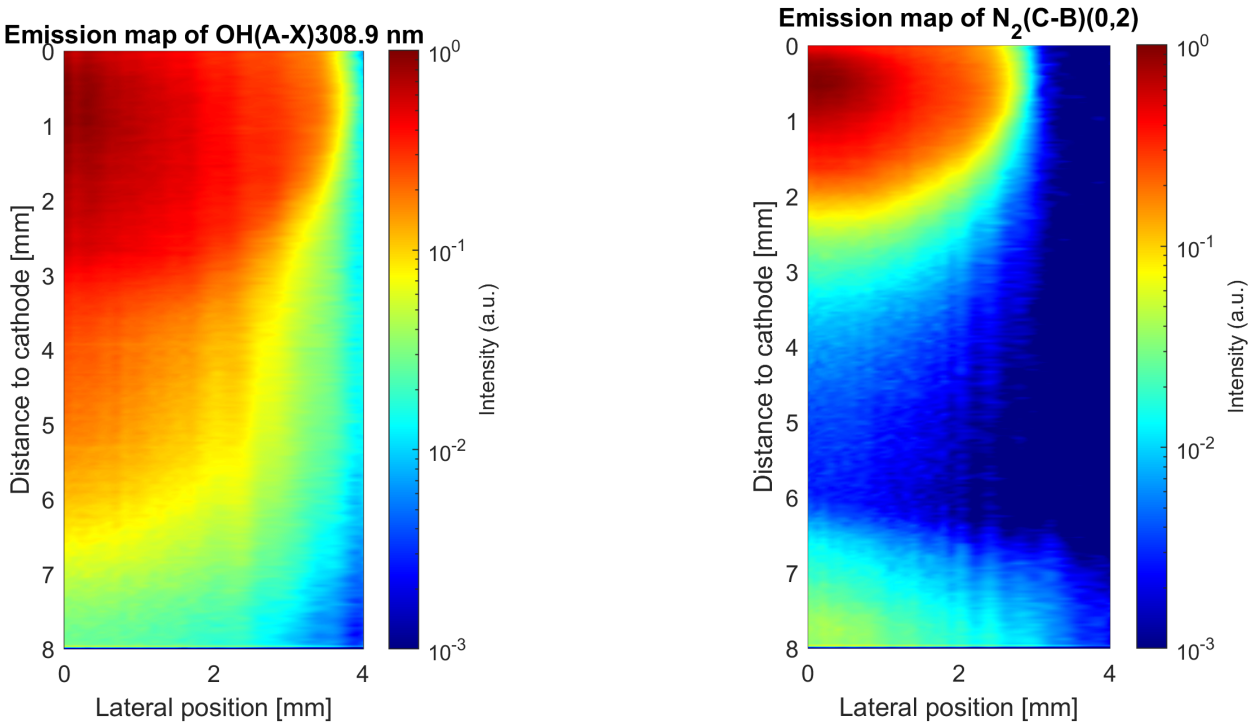

(a) $\mathrm{OH}(A-X)$(308.9 nm)

(b) $\mathrm{N_2}(C-B)(0,2)$(380.49 nm)

Figure 5.9: Emission intensity distribution of $\mathrm{N_2}(C-B)(0,2)$(380.49 nm) and $\mathrm{OH}(A-X)$(308.9 nm) from combining vertical slices

During the experiment, a peculiar issue was noticed in which the two arrangements of acquisition yielded different emission distributions. In Fig 5.9b, the emission map of $\mathrm{N_2}(C-B)(0,2)$ is obtained by combining the spectra slice along the axial directions. It indicates a significantly larger radial distribution extended to 3.6 mm in radius which is larger than that in Fig 5.7a, though the emission map matches qualitatively. A closer comparison to the plasma column image in Fig 5.2 can prove that the large radial distribution is false. This issue is probably coming from the unrestricted numerical aperture at the input slit. When the slit captures the emission along the axial direction, light rays from adjacent lateral positions would also be collected and increase the emission intensity falsely. Note that a similar issue could happen when a horizontal slice is captured and the light rays from adjacent axial positions would be collected too. But the Dove prism limits the spread of light rays and mitigates this issue. The emission of $\mathrm{OH}(A-X)$ at 308.9 nm is shown in Fig 5.9a by combining the vertical slices. Due to the low transparency of the long Dove prism at UV range, any emission wavelength below 360 nm cannot be detected when a horizontal slice is examined. Remarkably, $\mathrm{OH}(A)$ exhibits very low intensity near the liquid anode and in the SOP. $\mathrm{OH}(A)$ is mostly produced by the dissociative excitation of water molecules in Eq 5.19. As discussed before, the quenching of $\mathrm{OH}(A)$ by various species in air plasma prohibits its use in gas

temperature estimation if the quenching rate is faster than the state's lifetime or the thermalization is not slow [4]. If the formal condition is met, then quenching can also reduce the radiative lifetime of $\mathrm{OH}(A)$ near the liquid surface and therefore inhibit the emission detection. A recent study measured the absolute density of $\mathrm{OH}(X)$ using laser-induced fluorescence (LIF) spectroscopy and showed a strong OH presence near the liquid surface [39].

5.4.2 Axially Resolved Gas Temperature Distribution

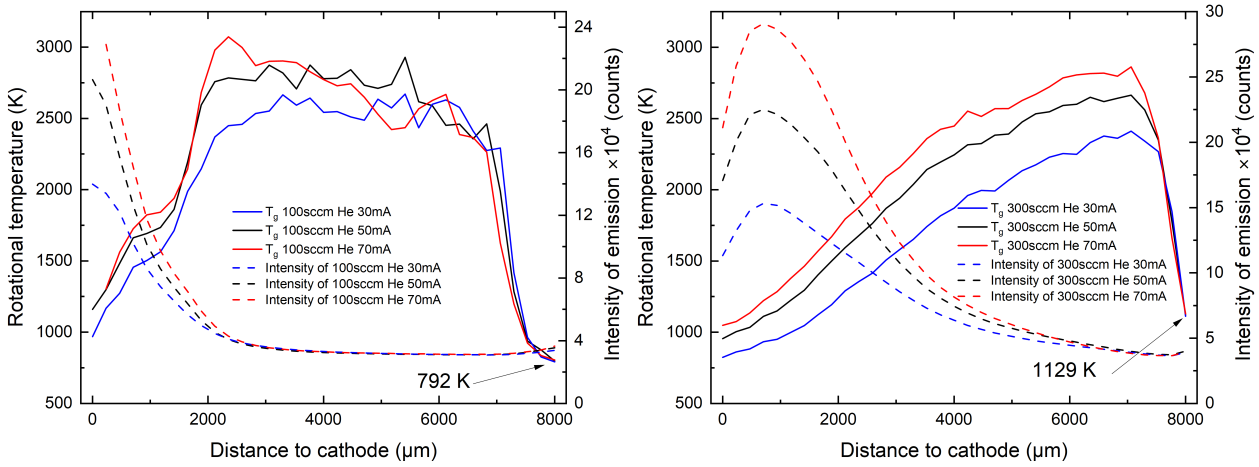

(a) 100 sccm helium flow rate

(b) 300 sccm helium flow rate

Figure 5.10: Axial distribution of gas temperature and emission intensity at different helium flow rates (8 mm gap, 1 mS/cm liquid conductivity)

The emission of $\mathrm{N}_2(C-B)$ at various locations can also reveal the change in gas temperature. Fig 5.10a plots the axial distribution of gas temperature and emission intensity when the 100 sccm helium flow is used. The gas temperature starts at $\sim$ 1000 K near the cathode layer thanks to the high helium mass fraction. As more molecules from the ambient air join in, the energy fraction that goes into the helium ionization and excitation goes down while more vibrational excitation and chemical reactions of molecules are invested by electrons. This causes the rising gas temperature at 754 K/mm until it reaches the peak position at 2.2 mm downstream from the cathode. From this point, the gas temperature is stable at 2500-2800 K since the heat exchange and gas heating are balanced. At 1.2 mm above the liquid surface (anode), the gas temperature declines significantly and fast at 2179 K/mm (50 mA), stronger than the cathode fall gradient. Such a significant temperature gradient corresponds to a vapor layer originating from the evaporation and functions as a "cushion" that cools down the gas temperature. The temperature gradient also indicates an intense heat flux towards the liquid phase, indicating its importance in thermal stabilization. The trend in the

gas temperature distribution does not change dramatically with elevated discharge power (current) though a higher gas temperature can be found near the cathode fall region by the extra gas heating rate. Surprisingly, the temperature is highly similar near the liquid anode region no matter the discharge power while higher discharge power decreases the temperature gradient from 2905 K/mm (30 mA) to 1899 K/mm (70 mA). Presumably, the vapor concentration increases with power providing extra cooling and alleviating the temperature gradient. On the other hand, the temperature of the liquid anode indicates 792 K despite the discharge power varies. This may arise from the coupling between gas heating and evaporation that is substantial and efficient to stabilize the gas temperature. On the other hand, the quenching from the water molecules can greatly affect the radiative lifetime of $N_2(C)$ and result in a false temperature estimation which is rather serious near the liquid surface. The gas temperature estimated from the rotational temperature of $N_2(C-B)$ and Rayleigh scattering was compared in [15] in which both methods are in good agreement and the temperature range (2700 K) is close with this work. Importantly, there is no obvious coupling between the emission intensity and rotational temperature. The emission intensity is intense at the cathode fall region and then declines tremendously as a result of the electric field.

The temperature distribution modifies itself notably as the helium flow rate is increased to 300 sccm in Fig 5.10b. The higher flow rate of helium restricts the gas heating by increasing the ionization efficiency and its high thermal conductivity. A remarkable modification happens in the cathode fall and positive column region where the temperature peak is delayed and occurs at 1 mm away from the liquid anode. A moderate temperature gradient (247 K/mm) is developed across the plasma column until reaching the peak temperature. A liquid anode temperature of 1129 K is also achieved at various discharge power levels and it is higher than the low helium flow case. This is ascribed to the higher current density at the liquid anode illustrated in Fig 3.33. On the other hand, the temperature gradient (2615 K/mm) near the liquid anode is very identical to the low flow rate, and so is the heat flux. Note that the delay of the peak temperature position also "squeezes" the expanse of the anode cooling region by 300 μm. A higher helium flow also extends the high electron temperature region which is indicated by the slower decline of emission distribution at the positive column. Notice the peak intensity is "delayed" to 706 μm due to the higher helium fraction there. Overall, the plasma column has lower gas heating at higher helium flow, and temperature distribution re-organizes.

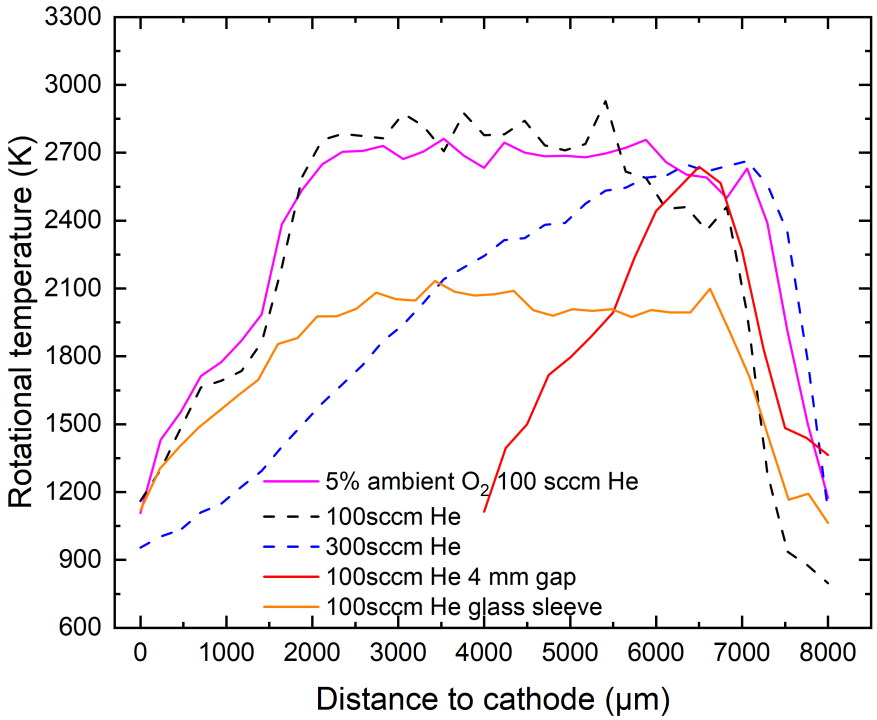

Figure 5.11: Axial distribution of gas temperature at different gas phase conditions (50 mA, 1 mS/cm)

Extra gas phase conditions' effect on the temperature distribution is shown in Fig 5.11. The purple curve indicates that the ambient oxygen level of 5% does not notably change the gas temperature. This indicates that nitrogen gas dominantly contributes to the gas heating in an air discharge. Nevertheless, Fig 3.21 confirms that oxygen is important for SOP establishment. Note that the low oxygen fraction modifies the temperature distribution near the liquid anode which is similar to the high helium flow rate case. The temperature starts to decrease at a closer position to the liquid implying a thinner vapor layer and therefore less heat conduction. When the discharge gap is halved in the red curve, the temperature gradients on both electrodes are decreased since the gas heating is also weakened. The higher current density also induces a higher anode temperature (1365 K) in the plot. A very special case is displayed in the orange curve where a glass sleeve is put around the plasma column and significantly reduces the air entrainment. As a result, the peak gas temperature is 2100 K and the lowered temperature gradient can be found on both electrodes. It is still uncertain whether the gas heating is critical for the SOP since the lowered oxygen fraction does not notably change it. However, a low temperature on the anode seems to favor the pattern formation.

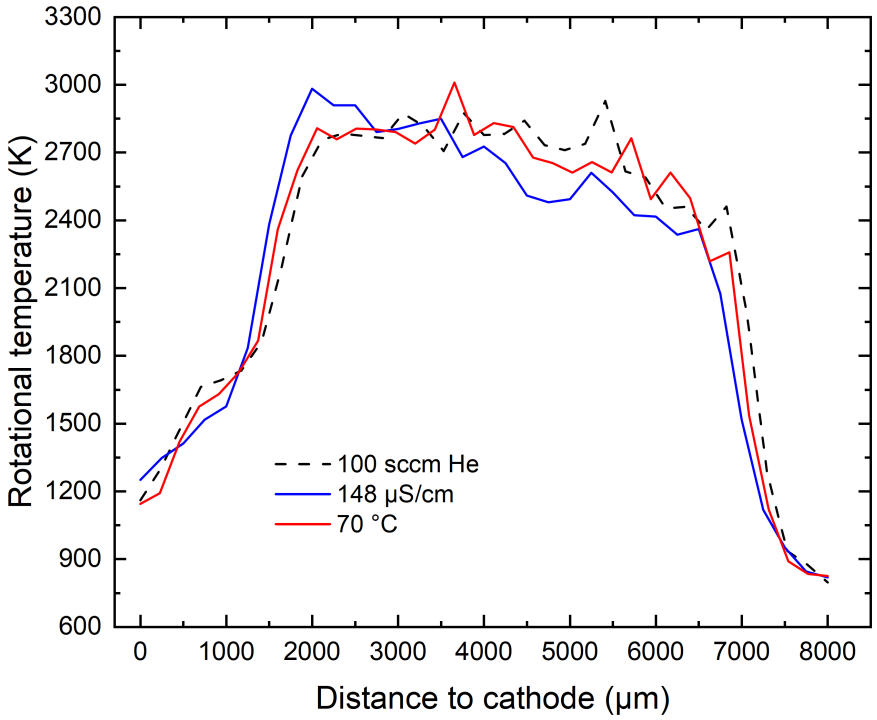

Figure 5.12: Axial distribution of gas temperature at different liquid phase conditions (50 mA, 100 sccm helium)

Fig 5.12 shows the temperature distribution when the liquid properties are changed. Interestingly, the high liquid temperature and low conductivity both decrease the temperature gradient. The stronger evaporation from high liquid temperature is responsible for providing extra cooling whereas the mechanism for a low conductivity case is unclear. It has been discussed in Chapter 3 that the liquid properties mostly change the anode sheath and pattern shape rather than the plasma gas heating. Indeed, the unchanged distribution indicates a similar thermal energy density and heat flux. This may also suggest the argument that the impact on SOP from the gas phase and liquid phase has very different mechanisms.

5.4.3 Radially Resolved Gas Temperature Distribution

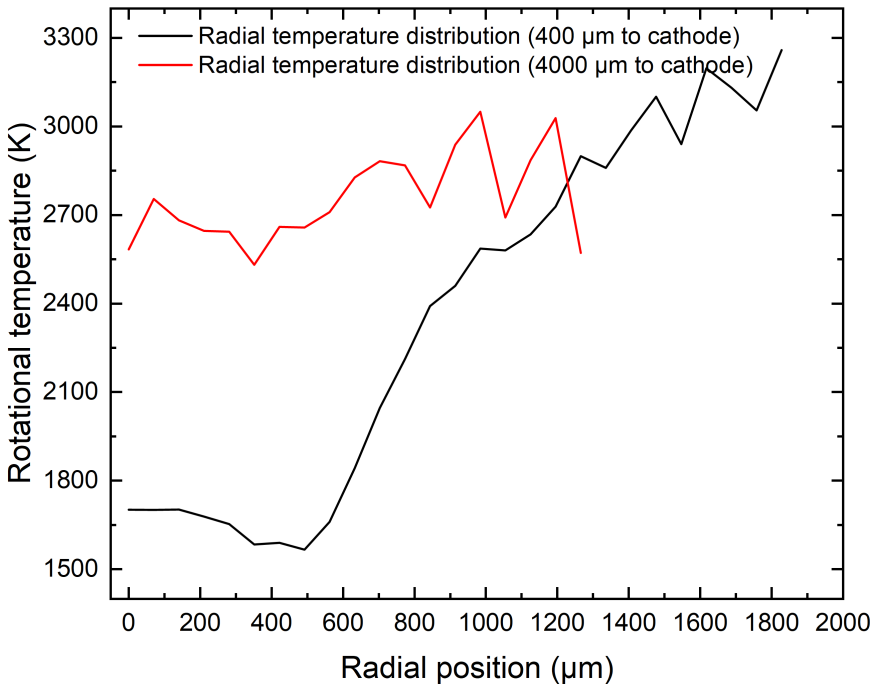

Figure 5.13: Radial distribution of gas temperature at different vertical position (50 mA)

The change of gas temperature along the radial dimension is plotted in Fig 5.13. The emission of $N_2(C-B)$ was gathered from the horizontal slice acquisition to assure an authentic distribution function. Near the cathode glow region (400 μm to cathode), the gas temperature is cooler near the center and increases dramatically at the radius of 560 μm. The low-temperature core at negative glow is due to the higher helium fraction which increases the electron temperature and lowers the energy fraction that is trapped in the vibrational excitation of molecules. On the other hand, the free electrons diffuse radially and become cooler from collisions which then facilitates the vibrational excitation process and causes the rise of gas temperature. Helium's cooling effect mostly prevails near the cathode. From the emission map of helium in Fig 5.8b, its presence deteriorates tremendously in the positive column. This is also verified by the radial temperature distribution at the middle of the plasma column (4000 μm to cathode) represented as the red curve in Fig 5.13. The temperature is already hot at the center and shows no change at a larger radial position. Note that the fidelity of temperature results declines significantly at larger radii mainly due to the weak emission of $N_2(C-B)$ and bad signal-to-noise ratio.

Fig 5.14 shows the intensity distribution of a self-organized pattern emission with the corresponding gas temperature. Interestingly, the temperature distribution does not have a strong coupling with emission intensity neither the lateral nor the radial profile. Instead, the temperature

stays roughly constant around 800 K which is usually found when a pattern is formed. The spatial-equilibrium temperature may be also due to the quenching of high-concentration water vapor. From the Abel inversion, the lateral emission function can be used to infer the radial distribution of a self-organized pattern which has a good correlation with its visible image. The two annular dots and the central diffusive disk can be recognized. The intensity profile clearly indicates the presence of the pattern.

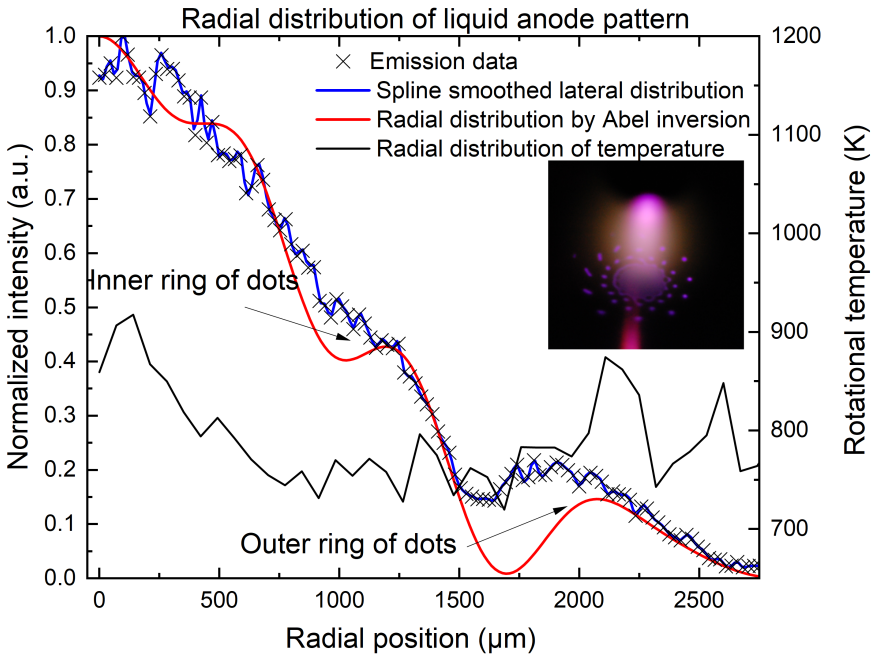

Figure 5.14: Radial distribution of a self-organized pattern emission and its gas temperature (50 mA)

5.4.4 Electron Density Distribution

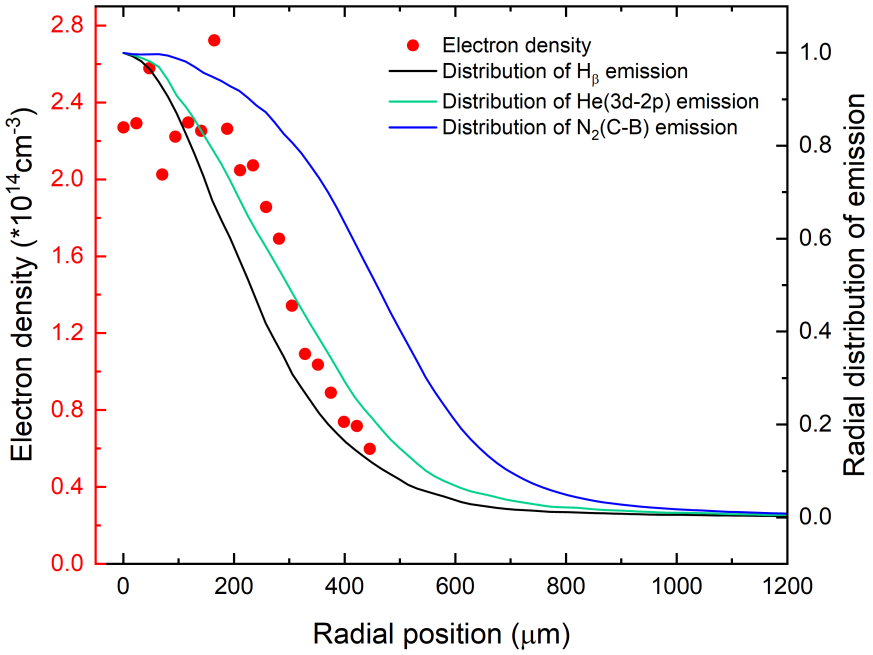

Figure 5.15: Radial distribution of electron density and normalized intensity of species emission at the cathode glow region

Compared to the spatially resolved gas temperature estimation, the electron density estimated from the deconvolution on the fine structure of the H_β is severely limited due to its weak line emission and scarce distribution. This causes most of the plasma column to be subject to poor signal-to-noise ratios and not be suitable for electron density estimation. Fig 5.15 illustrates the radial distribution of electron density and species emission at the cathode glow region. The electron density is $2.46 \times 10^{14}\mathrm{cm}^{-3}$ near the central cathode glow then drops substantially at the radius of 200 μm to $6.2 \times 10^{13}\mathrm{cm}^{-3}$ at 476 μm. Beyond this radius, the H_β emission is not suitable for analysis. Compared to the emission of $N_2(C-B)$, the excited helium and hydrogen have their distribution decreasing dramatically at a smaller radius. This is because both are produced by electron impact collisions while the pooling reaction (Eq 5.17) can contribute significantly to excited nitrogen [28]. The axial distribution of electron density across the plasma column is not available due to the scarcity of emission and high errors.

5.5 Summary

The variation of plasma properties at different locations is examined by spatially resolved optical emission spectroscopy. A lens set with the imaging spectrometer enabled the acquisition of a high spatial resolution of major species' emissions. The second positive system of nitrogen and OH(A-X) are widely found across the plasma column due to the low excitation thresholds and abundance of nitrogen and water molecules. SOP mostly comprises $\mathrm{N}_2(C-B)$ and $\mathrm{N}_2^+(B-X)$. The measured OH(A-X) is remarkably scarce near the liquid surface as a result of the interference from the strong quenching. Excited helium and H_β are produced by the impact collisions of high-energy electrons and thus exhibit limited distribution. The spatially resolved gas temperature is obtained from the rotational temperature of $\mathrm{N}_2(C-B)$ and reveals the instrumental importance of liquid anode to thermal stability. The temperature gradient (heat flux) and gas temperature peak values change correspondingly with the gas phase conditions while the liquid phase has little impact. A lower gas temperature at the liquid anode is seemingly coupled when a complex pattern is formed. The radial distribution of gas temperature indicates a cooler core region near the cathode showing the helium's impact while the gas temperature at the liquid anode is in spatial equilibrium and stays at 800 K. Electron density is calculated by deconvolution of the line profile of H_β. Unfortunately, the weak emission prohibited spatial analysis of electron density in many locations. The cathode region had an electron density of $2.46 \times 10^{14}\mathrm{cm}^{-3}$ which decreased with radius. Emissions of species that heavily depend on the energetic electrons, including H_β and $\mathrm{He}(3d-2p)$, are coupled with the electron density distribution while $\mathrm{N}_2(C-B)$ is less affected due to the extra channel from pooling reaction. It has been shown that spatially resolved spectroscopy is a non-invasive and straightforward method for estimating the distribution of species' emissions and gas temperature if their radiative lifetime is long enough. On the other hand, the electron density estimated from Stark broadening strictly requires sufficient emissions and constitutes a lower limit of plasma density. Such measurements yield insight into discharge structure and energy transport.

References

[1] Hans R Griem. *Principles of plasma spectroscopy*. Cambridge University Press, 2005.

[2] Alexander Fridman, A Gutsol, and YI Cho. Non-thermal atmospheric pressure plasma. *Advances in Heat Transfer*, 40:1–142, 2007.

[3] Christophe O Laux, TG Spence, CH Kruger, and RN Zare. Optical diagnostics of atmospheric pressure air plasmas. *Plasma Sources Science and Technology*, 12(2):125, 2003.

[4] Peter J Bruggeman, N Sadeghi, DC Schram, and V Linss. Gas temperature determination from rotational lines in non-equilibrium plasmas: a review. *Plasma Sources Science and Technology*, 23(2):023001, 2014.

[5] C Yubero, MS Dimitrijević, MC García, and MD Calzada. Using the van der waals broadening of the spectral atomic lines to measure the gas temperature of an argon microwave plasma at atmospheric pressure. *Spectrochimica Acta Part B: Atomic Spectroscopy*, 62(2):169–176, 2007.

[6] A Rodero and MC García. Gas temperature determination of non-thermal atmospheric plasmas from the collisional broadening of argon atomic emission lines. *Journal of Quantitative Spectroscopy and Radiative Transfer*, 198:93–103, 2017.

[7] David V Tsu, RT Young, SR Ovshinsky, CC Klepper, and LA Berry. Ion and neutral argon temperatures in electron cyclotron resonance plasmas by doppler broadened emission spectroscopy. *Journal of Vacuum Science & Technology A: Vacuum, Surfaces, and Films*, 13(3):935–942, 1995.

[8] A Yu Nikiforov, Ch Leys, MA Gonzalez, and JL Walsh. Electron density measurement in atmospheric pressure plasma jets: Stark broadening of hydrogenated and non-hydrogenated lines. *Plasma Sources Science and Technology*, 24(3):034001, 2015.

[9] J Torres, JM Palomares, AJAM Sola, JJAM Van der Mullen, and A Gamero. A stark broadening method to determine simultaneously the electron temperature and density in high-pressure microwave plasmas. *Journal of Physics D: Applied Physics*, 40(19):5929, 2007.

[10] Sanghoo Park, Wonho Choe, Se Youn Moon, and Jaeyoung Park. Electron density and temperature measurement by continuum radiation emitted from weakly ionized atmospheric pressure plasmas. *Applied Physics Letters*, 104(8), 2014.

[11] Alexander Fridman and Lawrence A Kennedy. *Plasma physics and engineering*. CRC press, 2004.

[12] Masayuki Tamura, Pamela A Berg, Joel E Harrington, Jorge Luque, Jay B Jeffries, Gregory P Smith, and David R Crosley. Collisional quenching of ch (a), oh (a), and no (a) in low pressure hydrocarbon flames. *Combustion and Flame*, 114(3-4):502–514, 1998.

[13] MP Lee, R Kienle, and Katharina Kohse-Höinghaus. Measurements of rotational energy transfer and quenching in oh a 2 σ+, υ'= 0 at elevated temperature. *Applied Physics B*, 58:447–457, 1994.

[14] Peter Bruggeman, Daan C Schram, Michael G Kong, and Christophe Leys. Is the rotational temperature of oh (a–x) for discharges in and in contact with liquids a good diagnostic for determining the gas temperature? *Plasma Processes and Polymers*, 6(11):751–762, 2009.

[15] T Verreycken, AFH Van Gessel, A Pageau, and P Bruggeman. Validation of gas temperature measurements by oes in an atmospheric air glow discharge with water electrode using rayleigh scattering. *Plasma Sources Science and Technology*, 20(2):024002, 2011.

[16] Jan Voráč, Lukáš Kusýn, and Petr Synek. Deducing rotational quantum-state distributions from overlapping molecular spectra. *Review of Scientific Instruments*, 90(12), 2019.

[17] Marco A Gigosos, Manuel A Gonzalez, and Valentın Cardenoso. Computer simulated balmer-alpha,-beta and-gamma stark line profiles for non-equilibrium plasmas diagnostics. *Spectrochimica Acta Part B: Atomic Spectroscopy*, 58(8):1489–1504, 2003.

[18] C Trassy and A Tazeem. Simulation of atomic and ionic absorption and emission spectra for thermal plasma diagnostics: application to a volatilisation study in a plasma jet. *Spectrochimica Acta Part B: Atomic Spectroscopy*, 54(3-4):581–602, 1999.

[19] Sven Hofmann, AFH Van Gessel, Tiny Verreycken, and P Bruggeman. Power dissipation, gas temperatures and electron densities of cold atmospheric pressure helium and argon rf plasma jets. *Plasma Sources Science and Technology*, 20(6):065010, 2011.

[20] N Konjević, M Ivković, and N Sakan. Hydrogen balmer lines for low electron number density plasma diagnostics. *Spectrochimica Acta Part B: Atomic Spectroscopy*, 76:16–26, 2012.

[21] Clifford J Cremers and Richard C Birkebak. Application of the abel integral equation to spectrographic data. *Applied Optics*, 5(6):1057–1064, 1966.

[22] R Alvarez, A Rodero, and MC Quintero. An abel inversion method for radially resolved measurements in the axial injection torch. *Spectrochimica Acta Part B: Atomic Spectroscopy*, 57(11):1665–1680, 2002.

[23] A Sáinz, A Díaz, D Casas, M Pineda, F Cubillo, and MD Calzada. Abel inversion applied to a small set of emission data from a microwave plasma. *Applied spectroscopy*, 60(3):229–236, 2006.

[24] J Pender, M Buie, T Vincent, J Holloway, M Elta, and Mary L Brake. Radial optical emission profiles of radio frequency glow discharges. *Journal of applied physics*, 74(5):3590–3592, 1993.

[25] L Montgomery Smith, Dennis R Keefer, and SI Sudharsanan. Abel inversion using transform techniques. *Journal of Quantitative Spectroscopy and Radiative Transfer*, 39(5):367–373, 1988.

[26] Christian H Reinsch. Smoothing by spline functions. *Numerische mathematik*, 10(3):177–183, 1967.

[27] TG Finn, JFM Aarts, and JP Doering. High energy-resolution studies of electron impact optical excitation functions i. the second positive system of n2. *The Journal of Chemical Physics*, 56(11):5632–5636, 1972.

[28] NK Bibinov, AA Fateev, and K Wiesemann. On the influence of metastable reactions on rotational temperatures in dielectric barrier discharges in he-n2 mixtures. *Journal of Physics D: Applied Physics*, 34(12):1819, 2001.

[29] JM Pouvesle, A Bouchoule, and J Stevefelt. Modeling of the charge transfer afterglow excited by intense electrical discharges in high pressure helium nitrogen mixtures. *The Journal of Chemical Physics*, 77(2):817–825, 1982.

[30] GI Taylor and AD McEwan. The stability of a horizontal fluid interface in a vertical electric field. *Journal of Fluid Mechanics*, 22(1):1–15, 1965.

[31] Yukikazu Itikawa and Nigel Mason. Cross sections for electron collisions with water molecules. *Journal of Physical and Chemical reference data*, 34(1):1–22, 2005.

[32] CIM Beenakker, FJ De Heer, HB Krop, and GR Möhlmann. Dissociative excitation of water by electron impact. *Chemical Physics*, 6(3):445–454, 1974.

[33] PC Cosby. Electron-impact dissociation of oxygen. *The Journal of chemical physics*, 98(12):9560–9569, 1993.

[34] Alexandra Brisset, Matthew Bieniek, Laurent Invernizzi, Mohammad Hasan, James Walsh, Kari Niemi, and Erik Wagenaars. The formation of o and h radicals in a pulsed discharge in atmospheric pressure helium with water vapour admixtures. *Plasma Sources Science and Technology*, 32(6):065004, 2023.

[35] Kirsty McKay, Ding-Xin Liu, Ming-Zhe Rong, Felipe Iza, and Michael G Kong. Generation and loss of reactive oxygen species in low-temperature atmospheric-pressure rf he+ o2+ h2o plasmas. *Journal of Physics D: Applied Physics*, 45(17):172001, 2012.

[36] R Peyrous, P Pignolet, and B Held. Kinetic simulation of gaseous species created by an electrical discharge in dry or humid oxygen. *Journal of Physics D: Applied Physics*, 22(11):1658, 1989.

[37] Zimu Yang, Yao Kovach, Zhehui Wang, and John Foster. On the nature of droplet production in dc glows with a liquid anode: mechanisms and potential applications. *Plasma Sources Science and Technology*, 31(11):115008, 2022.

[38] Naoki Shirai, Goju Suga, and Koichi Sasaki. Mechanism of droplet generation and optical emission of metal atoms in atmospheric-pressure dc glow discharge employing liquid cathode. *Plasma Sources Science and Technology*, 29(2):025007, 2020.

[39] Yuanfu Yue, Stephen Exarhos, Jaehyun Nam, Dongho Lee, Suljo Linic, and Peter J Bruggeman. Quantification of plasma produced oh and electron fluxes at the liquid anode and their role in plasma driven solution electrochemistry. *Plasma Sources Science and Technology*, 31(12):125008, 2022.

CHAPTER 6

Coupling between Plasma Self-Organization and Induced Fluid Circulation*

6.1 Introduction

The intense evaporation and heat transfer at the plasma-liquid interface of DC glow discharge gives rise to convective flow within the liquid and at the surface. Such flows, in contrast to simple diffusive processes, speed up the transport of reactive species into the bulk solution. Indeed, there are many studies have shown that plasma irradiation of the liquid surface leads to the induction of fluid dynamical effect which can facilitate heat and mass transport faster than diffusion beyond the point of attachment [2]. These fluid effects can manifest in many forms such as Taylor cone formation, capillary waves on the interface [3], and plasma-induced liquid convection [4, 5, 6, 7]. Shirai *et al* presented evidence suggesting that the self-organized pattern may depend on the presence of water vapor in the gas phase [8]. Strong water vapor emission has been observed as inferred by laser-induced fluorescence spectroscopy in an atmospheric pressure helium DC glow discharge contact with NaCl solution [9]. These observations suggest many scientific questions, some of which with technological implications: What processes drive the convection in the liquid phase and how does it change when the plasma self-organizes? Also, the self-organized patterns evolve with input conditions such as discharge current and electrolyte type. Does the flow field vary appreciably as the pattern itself changes? Control and optimization of the plasma-induced flow velocity and spatial extent offer a potential opportunity regarding the mass transport of reactive species into the bulk and thus could offer a pathway or approach to scale up. In this chapter, we investigate the occurrence of plasma-induced flows using particle imaging velocimetry (PIV) to address the aforementioned scientific questions. Additionally, we compare the convection cell formation in liquid irradiated with a nanosecond pulsed plasma jet as well to yield some additional

*The text and discussion in this chapter have been previously published by Yang, Z., Kovach, Y., & Foster, J. (2021). Visualization and analysis of coupling between plasmas self-organization and plasma-induced fluid circulation in 1 atm DC glows with liquid anode. Journal of Applied Physics, 129(16). [1]

insight regarding mechanisms and to explore if there is any universal connection between different plasma regarding local conditions at the attachment point that drives circulation.

6.2 Experimental Method

Particle imaging velocimetry (PIV), a non-intrusive and quantitative laser diagnostic [10], was used to study plasma attachment induced convective flows in the liquid water anode. The basic layout of a PIV system is shown in Fig 6.1. The region of interest flow is seeded with tiny, neutrally buoyant particles called "tracers", e.g. oil or water aerosols in air and solid particles in fluids. A coherent light sheet, formed by passing a laser beam through a cylindrical lens, illuminates the particles in the flow. A camera perpendicular to the plane of the light sheet records the movement of tracers into consecutive frames which are further divided into small subareas named "interrogation windows". Using statistical correlation techniques a local displacement vector can be determined for each interrogation window where all particles within have moved homogeneously in the same direction and the same distance.

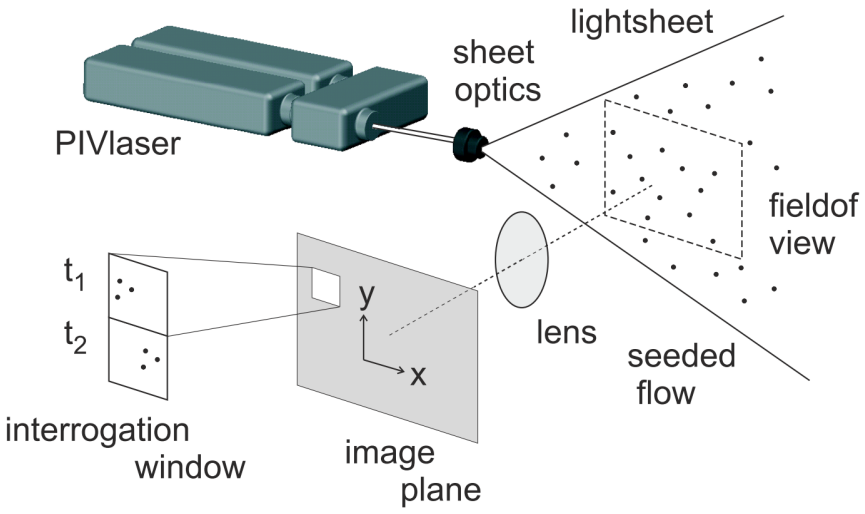

Figure 6.1: General setup of a 2D PIV system [11]

Fig 6.2 shows the experimental setup that implemented PIV to measure plasma-induced fluid motion in a DC glow discharge with a liquid anode. A laser beam (beam diameter: 1-2 mm) from a CW NdYAG laser (532 nm) was transformed into a sheet using a Powell lens to illuminate a single plane. Ceramic particles of $12\mu\mathrm{m}$ diameter were used as the tracer. A fast CMOS camera was used to acquire the flow field images with a $35 \times 27\mathrm{mm}^2$ field of view. Two planes of flow fields can be detected and they are perpendicular (vertical plane) and parallel (horizontal plane)

with the plasma-liquid interface, respectively. For imaging the horizontal plane, a mirror placed under the liquid phase container was placed at 45 degrees to reflect the scattered light from tracers at the horizontal plane towards the camera. The video results were then processed by the evaluation package DaVis [11] to calculate the flow vector. Deionized water and NaCl solution with different initial conductivity were used as liquid electrodes to establish various patterns. Note that the liquid is not circulated with the external tank so that the ambient flow motion is avoided.

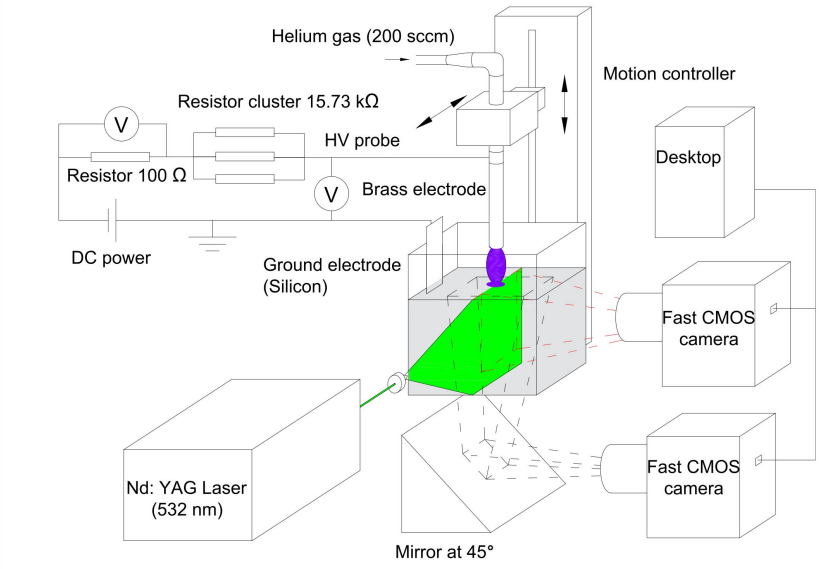

Figure 6.2: Experiment setup for detection of liquid phase movement at horizontal (black dash line) and vertical (red dash line) plane

We hypothesized that heat, mass transfer, and electrohydrodynamics forces together participate in the coupling of liquid convection; therefore, it was of interest to compare the plasma-induced flow observed under DC discharge with that observed in plasma jets which do not have significant heat transport. In this respect, the flow circulation stimulated by a plasma jet was also studied. While convection current in the liquid phase is present in the DC glow discharge, it is absent when the plasma jet irradiates a liquid water target. In both cases, however, local charge deposition occurs and thus charge and electrical field effects may be an important consideration in understanding the nature of plasma-induced flow in both systems. Fig 6.3 shows the schematic of a plasma jet which consists of a dielectric glass tube with one copper ring electrode on the outer wall and a metal wire inside the tube that functions as the high voltage electrode. The jet was powered using a nanosecond pulsed power supply (FID GmbH, FPG10-10KM). Note that the feed gas flow rate is set at 600 sccm where the formation of a plasma jet requires a critical flow speed [12]. On the other hand, the neutral gas flow speed is low enough to avoid significant interference with the bulk

fluid thanks to the large glass tube diameter.

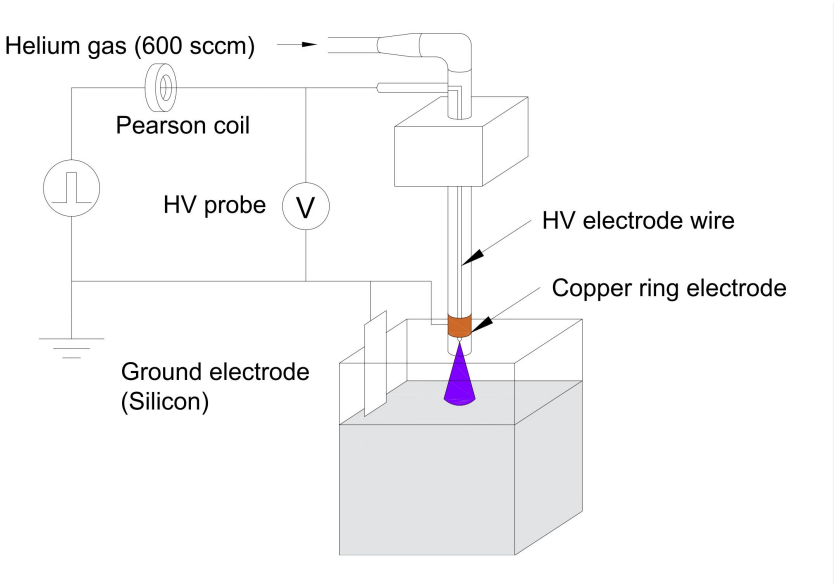

Figure 6.3: Experiment setup for detection of liquid phase movement under a pulsed atmospheric pressure plasma jet

6.3 Flow Field at Vertical Plane under Self-organized Pattern

In general, it was found that regardless of whether the attachment had SOP or not, plasma-induced circulation was present. With self-organization, however, the complexity of the flow field tended to increase. Fig 6.4 shows the general flow field just below the plasma attachment without a self-organized pattern. The background color indicates the magnitude of the velocity value while the arrows indicate the average direction. Note that the flow field diagram only presents the upper region of the field of view (40 mm x 32 mm) since the flow motion only happens near the interface ($\sim 8\mathrm{mm}$ depth) and does not appear to expand deeper. The flow field mainly consists of two parts: an ascending flow at the center and a toroidally shaped region associated with vortex flow. The ascending flow accelerates as it approaches the interface meaning a pressure gradient exists and we presume it is from the mass transfer at the interface caused by the evaporation. The maximum speed of the ascending flow as observed in the flow field is 1.5 cm/s. The vortex region around the central ascending flow had a circular cross-section which are rotational vortices. In the rotational vortices, the flow velocity is proportional to its distance to the center and such a vortex requires external forces to form. It was observed that the spatial size of the vortex grew with ascending flow speed and therefore, it is likely that the vortices are simply formed by the viscous stress from the nearby ascending flow. It would be intuitive to expect a downward flow caused by the helium gas

flow and the hot glow discharge does accelerate the gas flow speed from volume expansion. Note that we do not observe any appreciable flow at the water surface when the discharge is off and the helium gas is on.

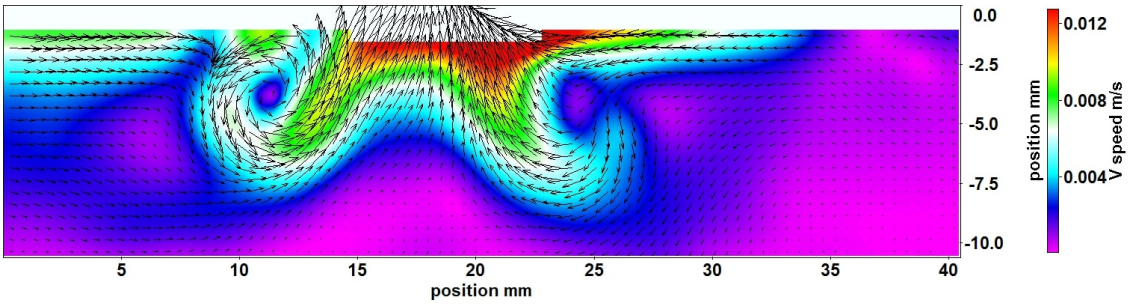

Figure 6.4: General vertical flow field without a self-organized pattern (Discharge current: 101 mA, Liquid anode: NaCl solution with initial conductivity 14 mS/cm)

As previously mentioned, it is suggested that predominantly localized evaporation is the origin of the ascending flow. To justify this speculation, we studied the effect of externally adding thermal energy to the liquid water using a butane jet mini-torch directed downwards with flame temperature $\sim$1800 K, which is in the same range of DC glow temperature measured by OES. Fig 6.5 shows the fluid motion under the butane jet torch and it has the qualitatively same pattern as the flow formed by DC glow discharge and the velocity magnitude is on the same scale. Thus, the ascending flow is mainly due to the evaporation of the fluid, and vortexes are formed by viscous stress. Note that the flow pattern in this case, as well as the discharge case without self-organization, was stable and static.

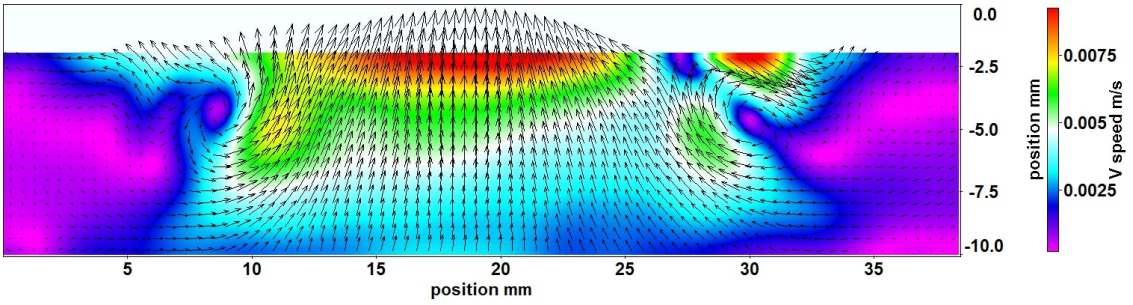

Figure 6.5: Vertical flow field induced by a downward butane jet (flame temperature 1800 K)

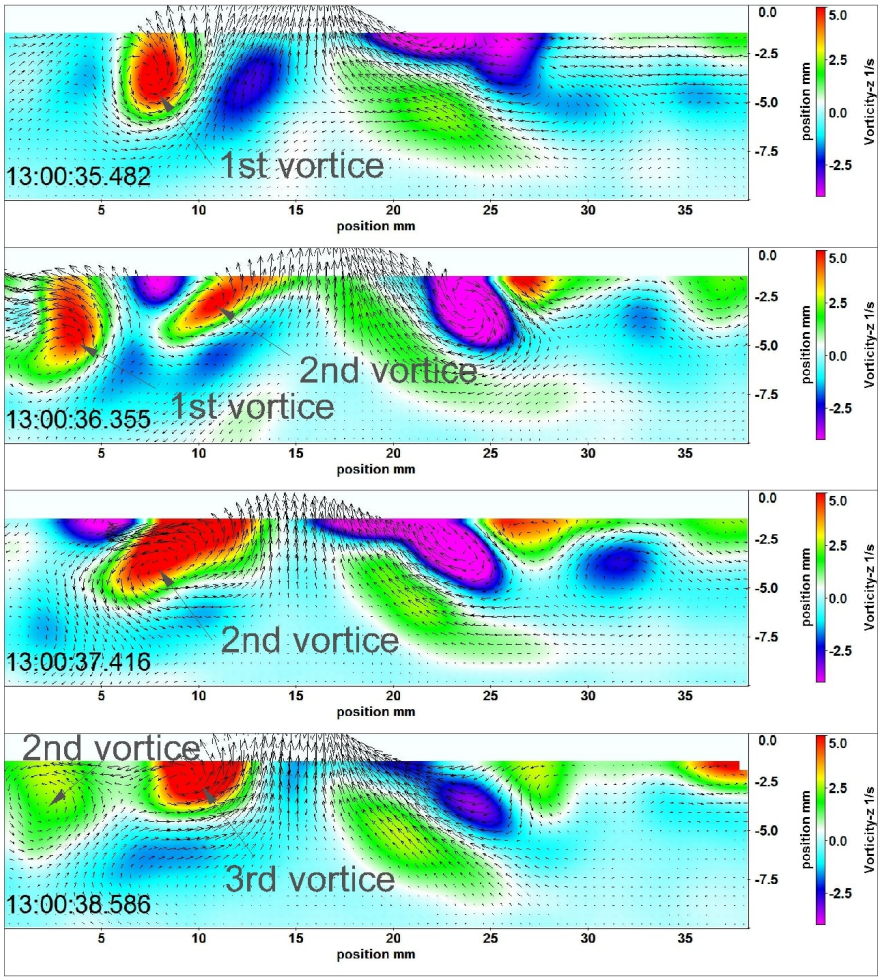

Figure 6.6: Dynamic vertical flow field under ring-with-spots SOP with vorticity evaluated in background color (Discharge current: 63 mA, Liquid anode: NaCl solution with initial conductivity 14 mS/cm)

Interestingly, the fluid motion under the interface is much more violent when a SOP appears. Fig 6.6 shows the evolution of flow vorticity ($w_z = \frac{\partial v_y}{\partial x} - \frac{\partial v_x}{\partial y}$) under a ring-with-spots pattern within 3 secs. Note that the background in this figure represents the vorticity in z-direction which helps identify the temporal evolution of vortices. It is obvious that the toroidal region of vortices is no longer static but instead shedded outward by the surface shear stress force and decays in the end. Then, new vortices are generated by viscous stress periodically and pushed outward again. Such dynamic flow patterns occur only when the discharge current is above 40 mA and a ring-with-spots pattern appears. This is the evidence showing that SOP introduces extra dynamics at the liquid

phase where the induced flow pattern is nonuniform in contrast to the non-self-organized case. We also observed a rotation movement on the pattern beyond this current threshold, which is also reported in [8]. Whether the dynamic vortex motion is related to the rotation of pattern, the fluid rotation itself, or some combination is still a mystery and they are probably related to the dynamic balance of local space charge and electric field. For the origin of dynamics in vortex transport, the surface stress force may come from the capillary wave or gas phase flow. Future work will be needed to confirm the presence of capillary waves using shadowgraph. The gas-phase coupling to surface processes will have to be explored using gas-phase PIV.

6.4 Flow Field at Horizontal Plane under Self-organization Pattern

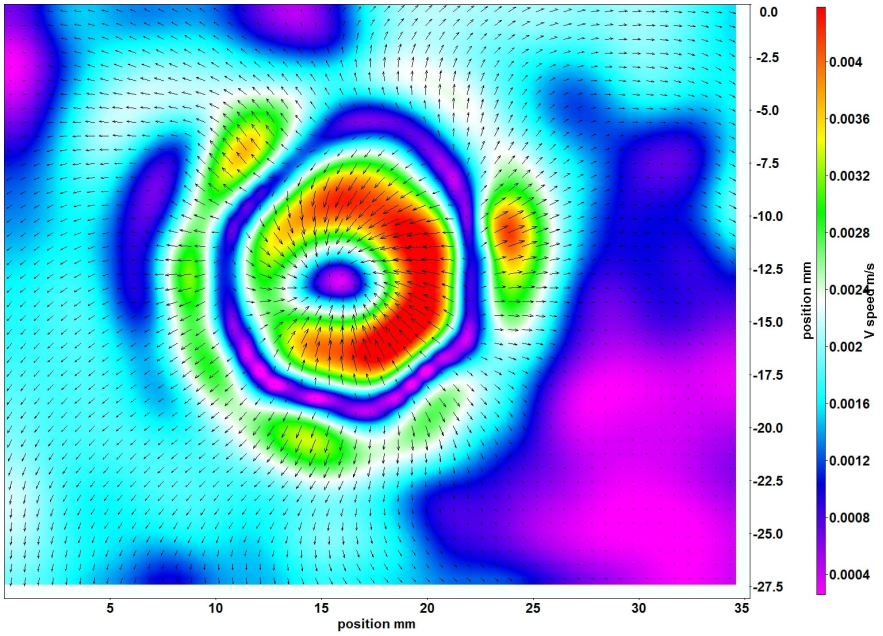

Figure 6.7: General horizontal flow field without self-organized pattern (Discharge current: 39 mA, Liquid anode: NaCl solution with initial conductivity 14 mS/cm)

It is noted that the evaporation rate of the liquid anode during the experiment is estimated at 0.27 mL/min or 0.1 mm/min for the fluid level change. The liquid level drop reduces the utility of PIV measurement at the actual liquid surface since that interrogation plane retreats over time. Therefore, all horizontal flow field measurements are made in a plane at 2 mm below the liquid surface. Fig 6.7 shows the general horizontal flow field without a self-organized pattern. It

reveals a layered structure where an annular region featuring zero velocity separates the radially inward flow and outward flow zones. If we compare this figure with Fig 6.4, it is straightforward that the flow field at the horizontal plane is the transverse component of the vertical plane flow field. The zero-velocity region is the center of vortices and radial flow motion corresponds to the horizontal cross-section of the vortex.

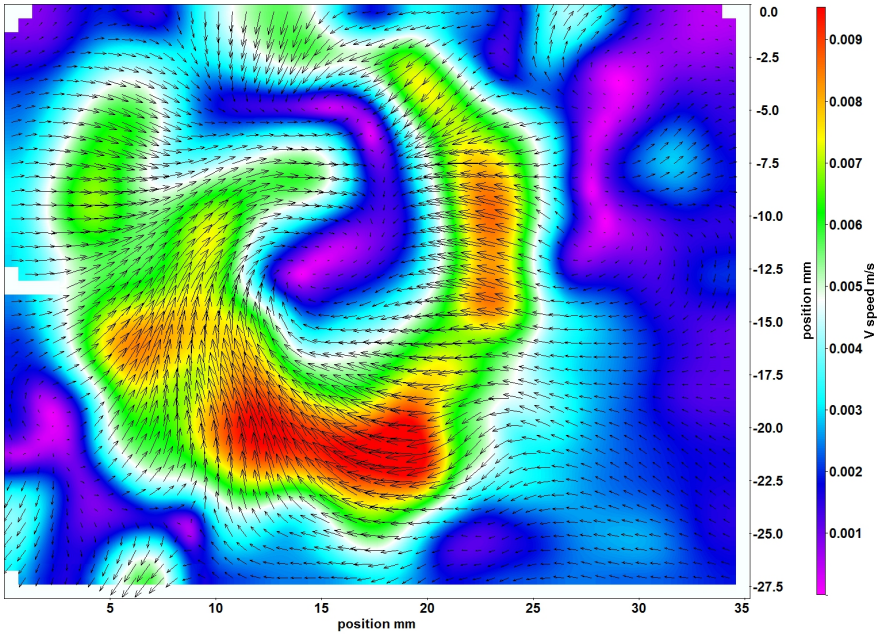

Figure 6.8: Dynamic horizontal flow field with gearwheel self-organization pattern (Discharge current: 71 mA, Liquid anode: NaCl solution with initial conductivity 32 mS/cm)

Interestingly, a highly dynamic and different horizontal flow field is established when a SOP is formed. As shown in Fig 6.8, an obvious clockwise swirl is apparent around the plasma attachment and the layered structure observed before no longer exists. We believe this swirl is strongly related to the electrohydrodynamic forces where the concentrated space charge, i.e., the plasma attachment pattern also rotates driven by the electric field. Because the pattern morphology dictates the locations of heat transport as shown in Fig 6.9, the flow field will follow its "fingerprint" as it shifts or rotates which distorts the static layered flow field and results in the swirl pattern. Note that this swirl mainly appears with self-organization and expands spatially at a higher current. Another candidate is the capillary wave controlled by electrohydrodynamic forces which can also help mixing the flow field underneath the surface. Besides the existence of the swirl, the second finding is that the rotation direction of the SOP is completely random and becomes more dynamic at higher discharge current. On the other hand, the flow field swirl appears to be more static with its overall flow direction invariant to discharge current variation. Fig 6.10 shows another

example of a complex, dynamical horizontal flow field for DI water anode where the rotation direction is counter-clockwise. The relationship among the swirl motion, rotation of SOP, and liquid conductivity are presently unknown.

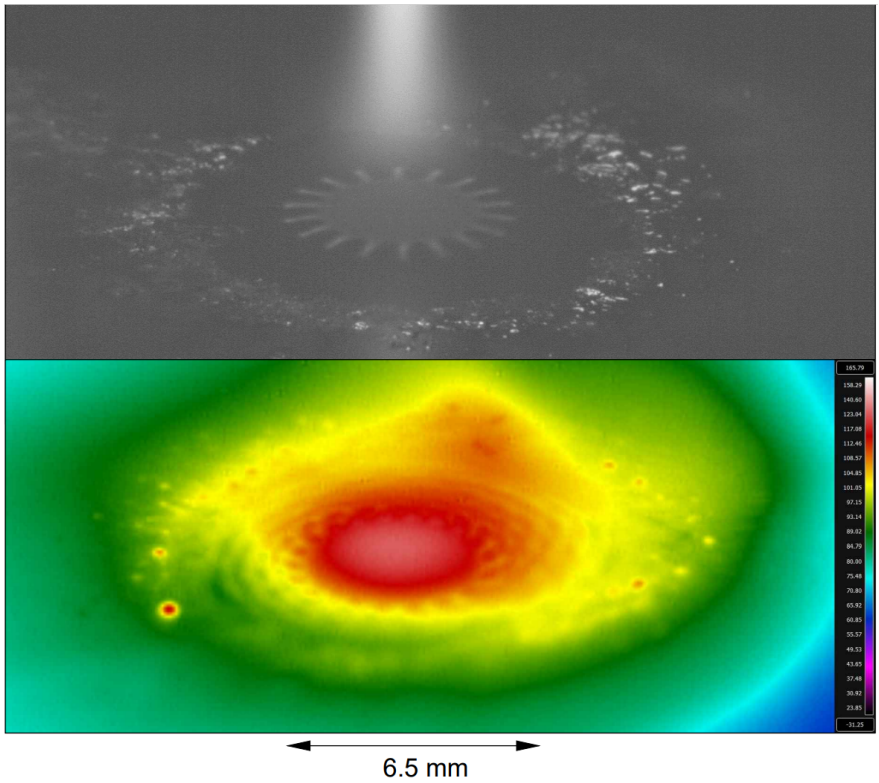

Figure 6.9: The temperature profile of the SOP and the surrounding liquid

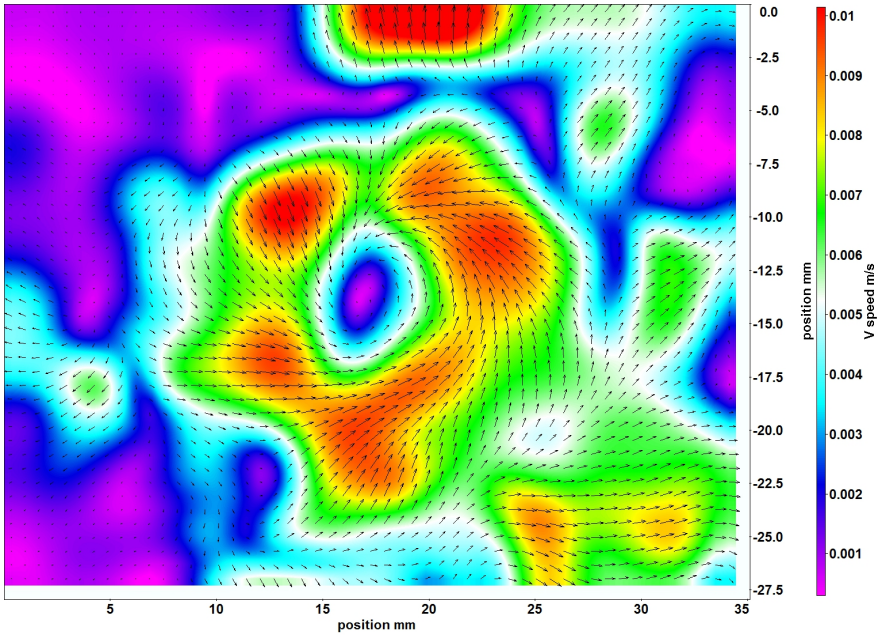

Figure 6.10: Dynamic horizontal flow field with gearwheel self-organized pattern (Discharge current: 80 mA, Liquid anode: DI water with initial conductivity 502 µS/cm)

6.5 Quantitative Results of the Flow Field

We have shown that the observed flow field was driven by the heating associated with the hot discharge column. Indeed, higher discharge power, i.e., higher discharge current would increase the attachment area and enhance the volumetric gas heating. Both of changes would increase the heat transfer rate towards the liquid phase. Therefore, the flow field momentum should be proportional to the power input; that is, the average flow velocity should scale with input power. Fig 6.11 plots the average velocities at the vertical and horizontal plane and it indeed justifies a linear relationship between the average velocity and input power. In the figures, each data point represents the flow field velocity averaged over its time-lapse (1 minute) and the field of view area. Interestingly, the curve is nearly a straight line with a constant slope until the current goes beyond 55 mA where the SOP starts to rotate and become unstable. Compared to the vertical plane flow field, the horizontal flow field's average velocity is nonlinear and in a lower velocity range since their flow field is partially the transverse component of the vertical flow field but is also strongly affected by the electric field and plasma attachment.

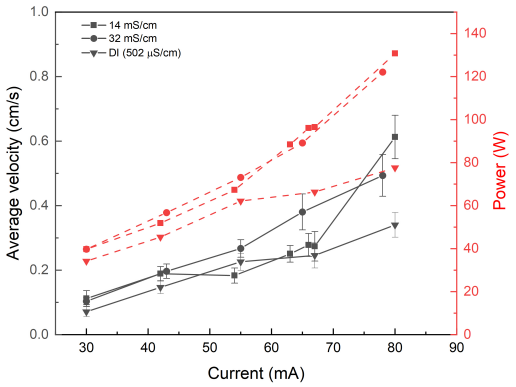

(a) Average velocity at vertical plane

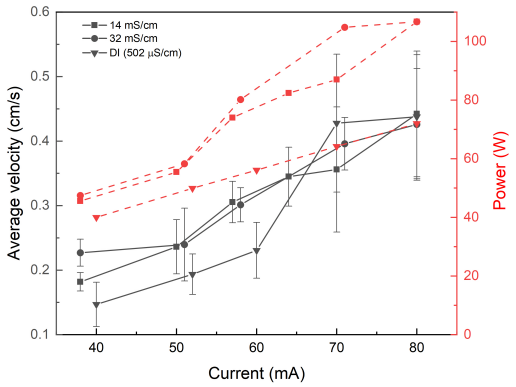

(b) Average velocity at horizontal plane

Figure 6.11: Time and spatial averaged velocity of the flow field

6.6 Induced Flow under Pulsed Power Helium Jet

Besides the heating effect, accumulated space charge will give rise to electrohydrodynamics force onto the plasma-liquid interface and will drive liquid motion. To explore this particular effect, a cold helium jet powered by a pulse generator is used. The atmospheric pressure plasma jet is useful for producing low-temperature plasma plumes consisting of reactive species in open space [13]. The plasma plume is also highly nonequilibrium in which neutral species are usually at room temperature. Such features are useful for the investigation of electrohydrodynamics forces excluding thermal effect. The helium jet configuration has similar features in Zhang et al [12] design while the feed gas flow speed is much lower (600 sccm or 0.5 m/s) to limit the jet flow interference at the liquid phase. The high-voltage electrode wire at the center of the quartz hollow tube can significantly enhance the local electric field and therefore lower the required breakdown voltage. It is noted that the tip of the high voltage wire is above the grounded liquid phase about 10 mm and such configuration also enhances the electric field near the plasma-liquid interface.

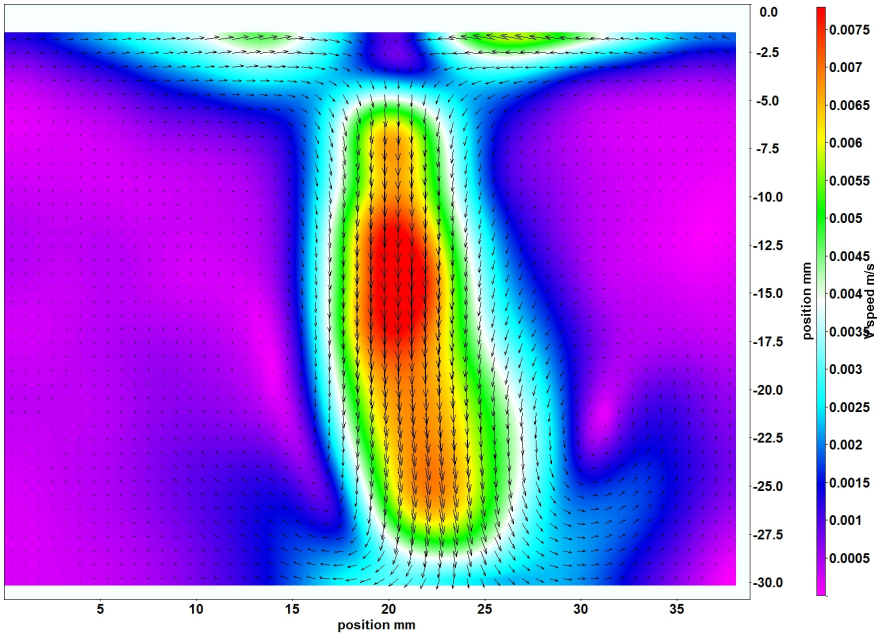

Figure 6.12: Vertical flow field in deionized water under helium jet (Pulse properties: 3 kV, 2.5 kHz, 34 W)

Fig 6.12 shows the vertical plane flow field in deionized water under the plasma jet. The jet appeared to penetrate the liquid surface and form a strong downward flow until it reached the bottom of the container. However, we did not observe any significant surface deformation at the impinge point. Compared to the flow under DC discharge, the flow velocity triggered by the jet is also on the scale of a few mm/s though no vortex or ascending flow is observed. On the other hand, the induced flow by DC discharge does not cross 8 mm depth below the surface while the flow under a cold plasma jet can propagate to the bottom of the container. In fact, a thorough propagation of flow is more efficient for bulk fluid mass transfer and suggests a great difference in the flow-driven mechanisms of plasma. A similar downward flow stimulated by the plasma jet has been found in other research using PIV [14, 15], and laser Schlieren [16] and they all suggest the flow is electrohydrodynamically driven. There are two theories for the origin of the strong electric field and the charge that triggers the electrostatic pressure. The injected ions from high voltage electrodes can be accelerated by an electric field or acoustic wave and impinge the liquid as the ionic wind [17] and give rise to a non-zero charge density in the liquid phase. With the help of fast imaging technology, it was observed that the plasma jet consists of continuous fast-moving structures namely “plasma bullets” [18] and their propagation speed is on a scale of 10 km/s, much higher than the feed gas speed. It is possible that these “plasma bullets” strike the liquid surface, inject the charge toward the liquid, and induce the electrohydrodynamics-driven flow, though the

detailed relationship between them is still unknown and requires further investigation. Another possible source of charge in the liquid is based on the process of dissociation and recombination of electrolytic species which is known as conduction pumping phenomena [19] and used in the electrohydrodynamics pump.

During the formation of the downward flow, it is noticeable that the PIV ceramic tracers around the flow structure are seemingly repelled by the flow channel and present a "dark trajectory" in the laser scattered image and this phenomenon is not observed for DC discharge results. Interestingly, the plasma jet will produce streamer-like discharge at high voltage (>7 kV) and the power consumption of the jet will spike to 60 W. At this condition, no downward flow presents but the results show an evaporation-induced flow pattern that is very similar to what we found in the DC discharge case. We believe the streamer in the plasma plume increases the gas temperature dramatically and achieves the same evaporation-induced mass transport at the interface.

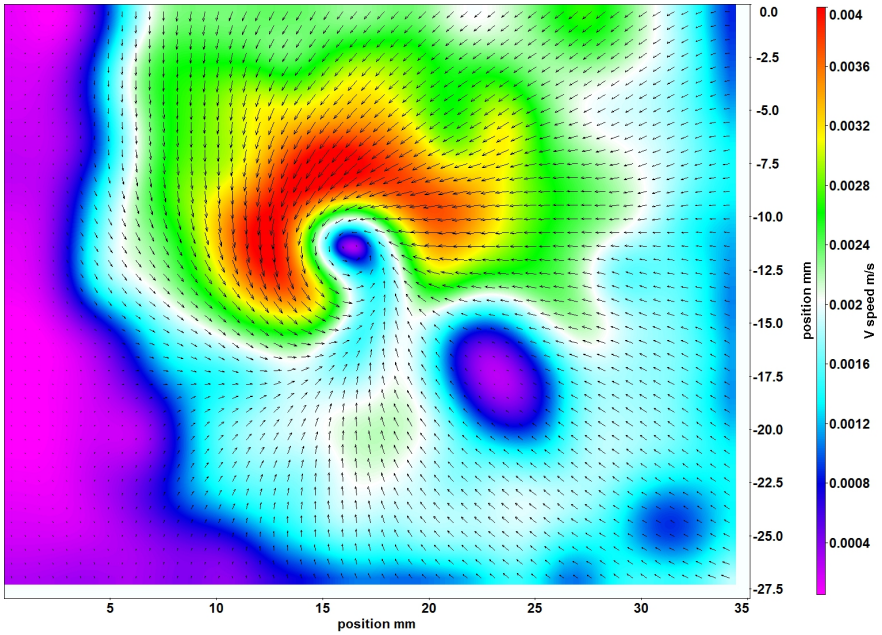

Figure 6.13: Horizontal flow field in deionized water under helium jet (Pulse properties: 2 kV, 3.5 kHz, 37 W

Fig 6.13 shows the horizontal plane flow field in deionized water under the plasma jet. Surprisingly, it presents a familiar swirl pattern around the center where the plasma plume front contact with the liquid surface. Certainly, the inertia force and friction by jet flow or plasma bullets will not be able to stimulate such a big scale and highly organized flow pattern on the horizontal plane. The electrohydrodynamics force in the bulk fluid probably induces this highly ordered flow motion since a large region of the parallel velocity vector at the right-hand side shows up where the

grounding electrode is located. It is expected to have a nearly parallel electric field that is stimulated between the high-voltage wire at the center and the grounding electrode sticking into the right-hand side of the liquid phase. The fluid, therefore, moves in parallel from the right and then converges into the center whereas no grounding electrodes are set on the left-hand side so that a distorted or "twisted" electric field is formed. Based on this reasoning, it is not surprising to find that the swirl fluid motion is stronger on the left side compared to the right side which supports the notion that a non-uniform electric field forms the swirl flow. A further investigation was performed by changing the grounding plate position and results show that the parallel flow region always stays near the plate and swirl flow concentrates near the opposite position. However, it is still unknown how the self-organization pattern can generate charges in the fluid which stimulates the swirl flow at the horizontal plane.

6.7 Summary

With the help of particle imaging velocimetry, the fluid motion in the liquid phase under the SOP in an atmospheric pressure DC glow discharge was measured and analyzed. In the plane normal to the plasma-liquid interface, the induced flow field consists of a strong ascending flow in the center at a maximum speed of 1.5 cm/s and a circle of vortices nearby. By using a butane torch, the ascending flow motion in this plasma-liquid interaction was qualitatively reproduced suggesting the water evaporation caused by the gas heating is the driving force. In addition, the formation of the pattern gave rise to flow structures that were non-static including periodic vortex/eddy shedding. In the plane parallel to the plasma-liquid interface, the flow field is an indication of the transverse component of vertical plane flow when no self-organized pattern is present. In the presence of self-organization, a single strong swirl flow was observed under the plasma attachment. A cold helium jet experiment using the same liquid as the ground stimulated a similar swirl flow at the horizontal plane and revealed that the driving mechanism could be the electrohydrodynamics force though a descending flow was also observed at the normal plane. SOP also reforms the heat transfer distribution whose rotation may contribute to the swirl flow mechanism. The magnitude of the flow velocity averaged over time and the field of view area suggests that flow speed is linear with increasing input power and increasing liquid electrical conductivity. Overall, the investigation indicates that flow field morphology is greatly impacted by the spatial distribution of the discharge attachment at the interface. A better understanding of these mass transport processes can therefore lead to some new approaches for plasma-liquid discharge optimization and thus new pathways for scaling up technologies in areas ranging from plasma-water treatment to nanoparticle synthesis.

References

[1] Zimu Yang, Yao Kovach, and John Foster. Visualization and analysis of coupling between plasmas self-organization and plasma-induced fluid circulation in 1 atm dc glows with liquid anode. *Journal of Applied Physics*, 129(16), 2021.

[2] Peter J Bruggeman, Mark J Kushner, Bruce R Locke, Johannes GE Gardeniers, WG Graham, David B Graves, RCHM Hofman-Caris, Dragana Maric, Jonathan P Reid, Elisa Ceriani, et al. Plasma–liquid interactions: a review and roadmap. *Plasma sources science and technology*, 25(5):053002, 2016.

[3] Bradley S Sommers, John E Foster, N Yu Babaeva, and Mark J Kushner. Observations of electric discharge streamer propagation and capillary oscillations on the surface of air bubbles in water. *Journal of Physics D: Applied Physics*, 44(8):082001, 2011.

[4] Tetsuji Shimizu, Yutaka Iwafuchi, Gregor E Morfill, and Takehiko Sato. Formation of thermal flow fields and chemical transport in air and water by atmospheric plasma. *New Journal of Physics*, 13(5):053025, 2011.

[5] Antonio Ramos. *Electrokinetics and electrohydrodynamics in microsystems*, volume 530. Springer Science & Business Media, 2011.

[6] Jasper FM Van Rens, Jan T Schoof, Fanny C Ummelen, Daan C Van Vugt, Peter J Bruggeman, and EM Van Veldhuizen. Induced liquid phase flow by rf ar cold atmospheric pressure plasma jet. *IEEE Transactions on Plasma Science*, 42(10):2622–2623, 2014.

[7] Selma Mededovic Thagard, Gunnar R Stratton, Mikhail Vasilev, Patrick Conlon, and Douglas Bohl. An experimental investigation of the liquid flow induced by a pulsed electrical discharge plasma. *Plasma Chemistry and Plasma Processing*, 38:719–741, 2018.

[8] Naoki Shirai, Kosuke Ichinose, Satoshi Uchida, and Fumiyoshi Tochikubo. Influence of liquid temperature on the characteristics of an atmospheric dc glow discharge using a liquid electrode with a miniature helium flow. *Plasma Sources Science and Technology*, 20(3):034013, 2011.

[9] Koichi Sasaki, Hiroaki Ishigame, and Shusuke Nishiyama. Density distributions of oh, na, water vapor, and water mist in atmospheric-pressure dc helium glow plasmas in contact with nacl solution. *The European Physical Journal Applied Physics*, 71(2):20807, 2015.

[10] Markus Raffel, Christian E Willert, Fulvio Scarano, Christian J Kähler, Steve T Wereley, and Jürgen Kompenhans. *Particle image velocimetry: a practical guide*. Springer, 2018.

[11] LaVision GmbH. Flowmaster product-manual for davis 8.4, 2017.

[12] Jialiang Zhang, Jiao Sun, Dezhen Wang, and Xiaogang Wang. A novel cold plasma jet generated by atmospheric dielectric barrier capillary discharge. *Thin Solid Films*, 506:404–408, 2006.

[13] Andreas Schutze, James Y Jeong, Steven E Babayan, Jaeyoung Park, Gary S Selwyn, and Robert F Hicks. The atmospheric-pressure plasma jet: a review and comparison to other plasma sources. *IEEE transactions on plasma science*, 26(6):1685–1694, 1998.

[14] Paul Rumbach, Nathaniel Griggs, R Mohan Sankaran, and David B Go. Visualization of electrolytic reactions at a plasma-liquid interface. *IEEE Transactions on Plasma Science*, 42(10):2610–2611, 2014.

[15] Ph Traoré, Michel Daaboul, and Ch Louste. Numerical simulation and piv experimental analysis of electrohydrodynamic plumes induced by a blade electrode. *Journal of Physics D: Applied Physics*, 43(22):225502, 2010.

[16] Vesna V Kovačević, Goran B Sretenović, Elmar Slikboer, Olivier Guaitella, Ana Sobota, and Milorad M Kuraica. The effect of liquid target on a nonthermal plasma jet—imaging, electric fields, visualization of gas flow and optical emission spectroscopy. *Journal of Physics D: Applied Physics*, 51(6):065202, 2018.

[17] Michael J Johnson and David B Go. Recent advances in electrohydrodynamic pumps operated by ionic winds: A review. *Plasma Sources Science and Technology*, 26(10):103002, 2017.

[18] Mounir Laroussi and Tamer Akan. Arc-free atmospheric pressure cold plasma jets: A review. *Plasma Processes and Polymers*, 4(9):777–788, 2007.

[19] Matthew R Pearson and Jamal Seyed-Yagoobi. Advances in electrohydrodynamic conduction pumping. *IEEE Transactions on Dielectrics and Electrical Insulation*, 16(2):424–434, 2009.

CHAPTER 7

Droplet Production Mechanism in DC Glow Discharge with a Liquid Anode*

7.1 Introduction

The non-thermal plasma interacting with the liquid solution can produce a host of reactive species: atomic oxygen, OH radical, hydrogen peroxide, and UV light [2]. These species can be utilized in applications ranging from water treatment to medicine. Our understanding of processes prevailing at the plasma-liquid interface however remains incomplete. The complexity of chemistry in the plasma-liquid interface partially comes from the coupling processes where thermodynamics and mass transport phenomena are correlated in the chemically reactive multiphase media. Based on a pin-to-water-surface discharge configuration, adding aerosols to the plasma can greatly expand the surface-to-volume ratio which enhances the transfer of activation energy from the plasma to the liquid, delivery of short-lived species, and controlling reactivity in the liquid [3]. The generation mechanisms of aerosols include evaporation, surface deformation, and external sources such as electrospray. The strong mist containing particles from cathodic electrolytes was reported in [4, 5]. Prominent surface deformation and aerosols from the Taylor cone are only found in cathodic electrolytes [5, 6, 7] while the anodic liquid surface features a relatively unperturbed surface where the plasma attachment can self-organize into intricate patterns accompanied by convection flow driven by heat. As we discussed in Chapter 3, the anode fall electric field (10 kV/cm) at the anodic electrolyte is too weak to trigger a Taylor cone deformation. However, an emission phenomenon of particles from molten droplets originating from the $FeCl_3$ liquid anode solution was reported before but the detailed formation mechanism was unclear [8]. Besides the Taylor cone or electrohydrodynamic process, another candidate that can account for this phenomenon is the jet droplet mechanism. Through high-speed camera imaging, the droplet ejection mechanism was

*The text and discussion in this chapter have been previously published by Yang, Z., Kovach, Y., Wang, Z., & Foster, J. (2022). On the nature of droplet production in DC glows with a liquid anode: mechanisms and potential applications. Plasma Sources Science and Technology, 31(11), 115008. [1]

studied and proved to be the jet droplets.

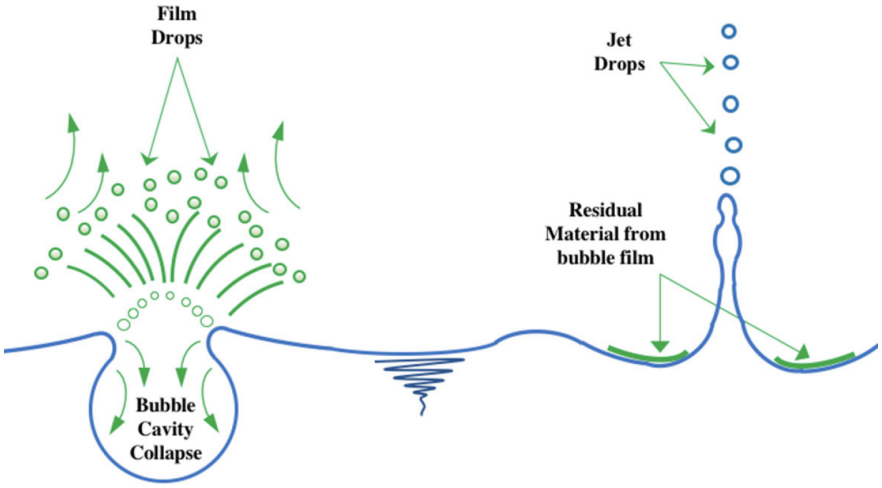

Figure 7.1: The formation of jet droplets [9]

The jet droplets process is ubiquitous and well known in the mass transport of sea aerosol into the atmosphere [10, 11]. They are formed when a gas bubble cavity collapses at the gas-liquid interface and forms a vertical upward jet that pins off into droplets (Fig 7.1). Interestingly this process also leads to the uptake of atmospheric gas by the liquid as well. A similar phenomenon can also be found in a melted liquid wall of tokamak plasma [12]. In the context of plasma science, the bubbles can either be dissolved air released by plasma gas heating or oxygen from electrolysis. In this regard, the process may be an important two-way mass transport mechanism that explains the observed particle emission.

After the ejection into the nonthermal plasma, the small are subject to a variety of forces including electrostatic forces due to droplet charging, thermophoresis, and gas dynamic drag force associated with convection. These forces along with gravity determine not only the motion of the droplets but also the duration of the interaction. Polarization effects driven by the electric fields as well as simple charge collection can lead to disruption, resulting in the production of even smaller droplets. A nonthermal plasma consists of an active zone associated with the ionization wave and the corona or afterglow region where droplets can deform and vaporize by the forces and thermal energy exchange. Such evaporation changes the size of the particles which in turn changes the magnitude of forces acting on the particle as well. The mass transport of species from the water into the discharge not only augments the gas-phase chemistry by providing a source of new reactants but also affects discharge impedance through cooling and the introduction of the charge and nanoparticles. Indeed, droplets may play an important role in charge transport between phases. The species introduced by the droplets can be quite complex especially if they are synthesized in solu-

tion such as glow discharge electrolytic cells with liquid anode or cathode electrode [13]. Droplets derived from these solutions can contain nanoparticles that ultimately interact with the gas phase plasma offering new opportunities for nonequilibrium processing as they transit the nonthermal plasma. This process can be used potentially for applications ranging from decontamination and agriculture to material processing [14].

This chapter focuses on the mechanism of droplet formation and the preliminary diagnostics of its impact on plasma properties via spectroscopy. Experiments described herein demonstrate that the source of the droplets is gas bubbles that upon breaking the surface generate a high-speed jet at the interface. These bubbles contain material produced within the liquid phase and thus are a mechanism for mass transport into the gas phase—such as metal ions and even nanoparticles. Optical spectroscopy is also used to reveal the droplet composition and its impact on plasma properties. This new mass transport mechanism suggests that material in the liquid can be processed by the plasma there thus providing a new approach to material processing and chemical synthesis.

7.2 Experimental Method

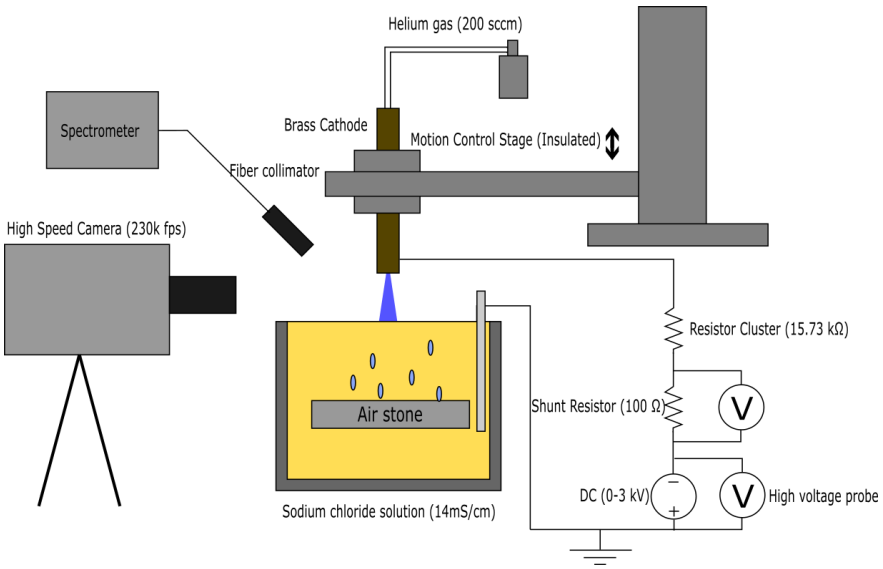

Figure 7.2: Experimental setup for jet droplets detection and analysis

Fig 7.2 illustrates a droplet detection setup which also facilitates the production mechanism. To capture the transient process at the liquid surface and trajectory of droplets, a high-speed camera (Phantom TMX 7510) coupled with a macro lens was used to record the events at 230k fps and 8×8 mm^2 field of view. Additionally, a fast medium-wave infrared camera (FLIR X8500sc) was

used to measure the thermal signature of the droplets. The open-source video analysis tool Tracker [15] was used to study the motion of droplets. The optical emission from the plasma and its interaction with droplets is captured using a Czerny–Turner type spectrometer (Acton Series, SP-2300i) with an 1800 grooves/mm holographic grating and a fast intensified CCD detector (PI-MAX3, Princeton Instruments). Optical emission from the positive column was collected using an optical fiber at its middle height region where the droplets most frequently burst. Different liquid electrolytes including deionized water (44 µS/cm), NaCl (14 mS/cm), $\mathrm{FeCl_3}$ (12 mS/cm), and $\mathrm{CuSO_4}$ (15 mS/cm) solutions were used to study the plasma response to the droplets.

The droplet ejection process is a fluid dynamics process driven by heat transfer and electrolysis which is not unique in this discharge configuration. Furthermore, the ejection of droplets and their emission near plasma was found to be highly random and discontinuous which makes the acquisition of emission spectra time-consuming. This might explain the paucity of published data on droplet formation with liquid anode systems. After identifying the mechanism of natural droplet formation and the issue of uncertainty, an air sparger was introduced to generate a stream of bubbles via the rupturing process. In this case, an aquarium air stone was placed underneath the liquid surface to boost and control the droplet ejection in a continuous manner. This experimental approach also enables a new method to enhance mass transport into the plasma through the production of aerosol at the interface.

7.3 Observation of Droplet Ejection

Our interest in droplet ejection originated from the observation of iron particle emission when using an $\mathrm{FeCl_3}$ electrolyte as shown in Fig 7.3. The composition of these particles was found to be iron nanoparticles from an electrolytic solution. At the time of that study, it was not known how these particles were emitted into the plasma. Thanks to the high-speed camera, the transient sequence of droplet formation was recorded and shown in Fig 7.4 where two typical examples of droplet ejection events were captured at a frame speed of 12.5k fps. Statistically, the observed droplets have an average speed of 3 m/s and a diameter range of 40-120 $\mu\mathrm{m}$. The generation of droplets starts with a rising jet which is then pinched off into a chain of droplets by an end-pinching process [16]. The top droplet at the jet tip usually has the highest velocity ranging from 1-9 m/s.

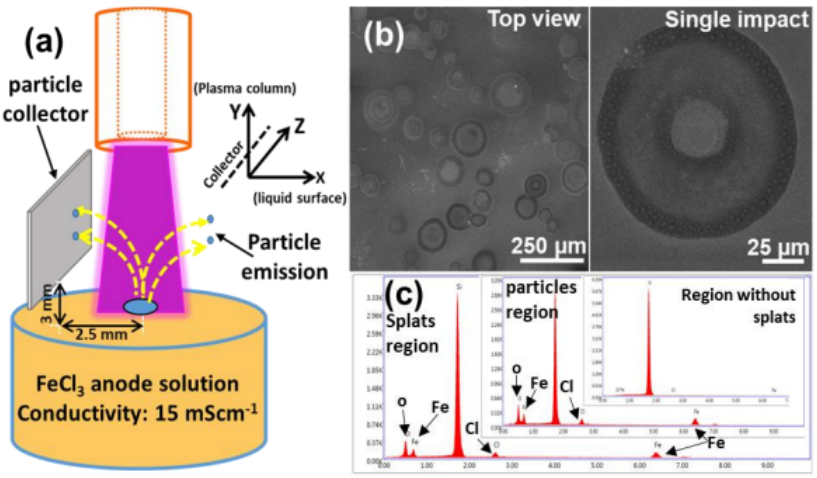

Figure 7.3: Identification of particle in droplets (a) schematic of particle collection setup, (b) scanning electron microscopy images of the resulting splats after the collection, (c) the composition spectrum detected using Energy Dispersive X-Ray Analysis [8]

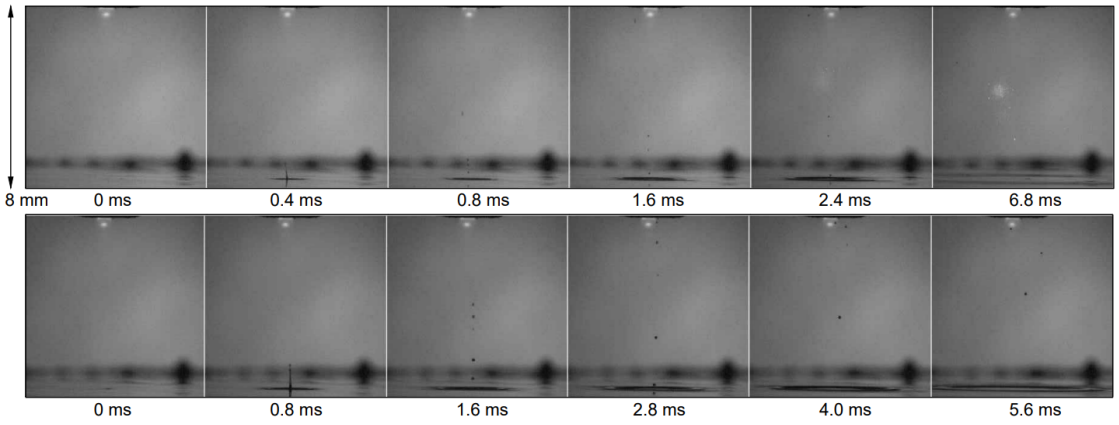

Figure 7.4: The droplet ejection under DC discharge. (90 mA, 12.5k fps, electrolyte: $FeCl_3$ with a conductivity of 12 mS/cm)

It is expected that as the droplets traverse the discharge, surface evaporation will lead to the introduction of liquid-derived species into the gas phase. Complete evaporation or rapid disruption is also possible during droplet transit. Indeed, droplet disruption in the gas phase can only happen if its size is small enough or the velocity is slow enough so that the droplets can completely evaporate. As shown in Fig 7.4, the progeny droplet in the first example (51 µm) is smaller than the example in the second row (90 µm) which did not vaporize. Other cases show the survival of droplets at a size of only 40 µm but having a speed of 8 m/s. As for the other electrolytes, we also observe

the droplet ejection from deionized water and NaCl solution. According to the high-speed camera imaging, the rate of droplet ejection does not depend on the type of electrolytes, while solutes such as Fe^{3+} and Na^{+} make the droplet ejection observable due to its bright emission upon vaporization. On the other hand, DI water droplet emission is difficult to detect owing to the absence of species having low excitation potential.

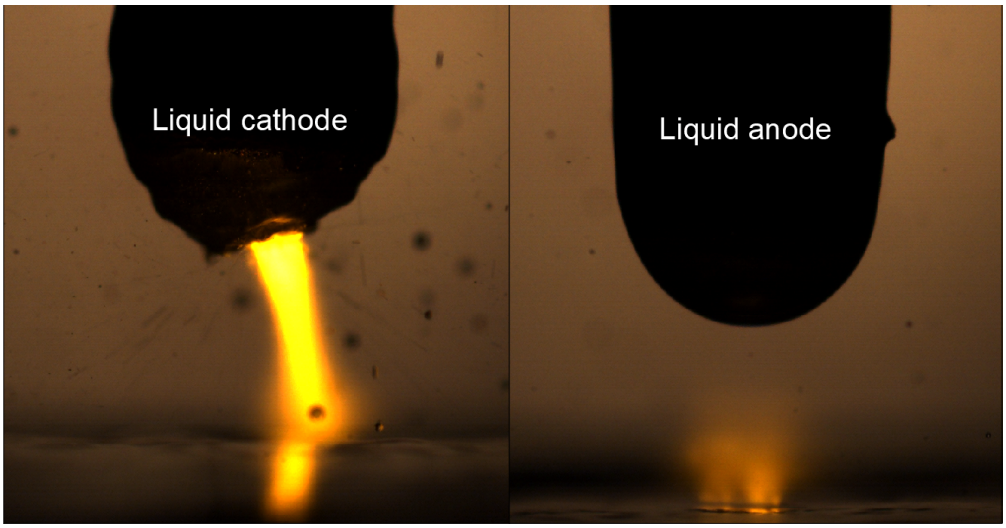

Figure 7.5: Capillary surface deformation on the liquid cathode and anode (NaCl solution, 40 mA discharge current)

It is well known that the liquid in a capillary tip would form a conical shape called the Taylor cone under a strong DC electric field [17]. Then the electrically charged fine droplets can be emitted from the liquid cone tip when the electrostatic repulsion by the charge on the surface exceeds the surface tension of the liquid. The strong cathode sheath electric field can generate fine droplets continuously from liquid cathode [5] which is not the case for a liquid anode. Two major differences between the Taylor cone droplets and the observed event shall be pointed out. First, the liquid anode droplet is ejected vertically via a single water jet that breaks into some progeny droplets. On the other hand, Taylor cone droplets are formed in large amounts and all directions at once, and the surface deformation can be seen clearly on the liquid cathode before the separation of the droplet where the intense sheath electric field tears off the cone tip and produce the aerosols. Secondly, the magnitude of aerosol flux at the liquid anode is independent of the magnitude of the local applied electric field. Fig 7.5 compares the response of liquid anode and cathode under the static DC electric field. Note that a pendent drop is attached to the charged brass electrode and its curved surface will enhance the local electric field intensity. For the liquid cathode, multiple droplets are ejected from the Taylor cone and a strong capillary wave can be observed on the

pendent drop whereas the liquid anode drop is highly stable. Thus, the liquid anode does not support Taylor cone formation.

Another possible mechanism related to electrohydrodynamic (EHD) instability should also be briefly discussed. Recently, linear perturbation analysis of the plasma-liquid interface including the sheath electric field on the EHD instability was performed [17]. An atmospheric pressure glow discharge has an electron temperature of 5 eV and density of $10^{14}\mathrm{cm}^{-3}$, and the corresponding critical surface potential is 3 kV for EHD instability including the ion impact. This value is even higher than the discharge voltage, therefore the EHD instability alone could not cause the formation of droplets.

7.4 The Mechanism of Jet Droplets Formation

One of the most important pieces of evidence to support the jet droplet mechanism comes from the two major processes that produce bubbles in the liquid phase. The first one is the solvated air in the liquid phase whose solubility decreases when the temperature is raised as the liquid is heated by the discharge. In fact, this explains why the droplet ejection is highly random and not readily apparent instantaneously after the plasma ignition—the liquid needs to heat up. A similar phenomenon can even be found in a tokamak where trapped gas in the melting metal wall surface forms a jet and bursting droplets [12]. In further support of the dissolved gas theory, the liquid anode solution is degassed by boiling and results show that the droplet ejection is significantly reduced but still exists suggesting incomplete degassing or that another gas source must be present. The immersed anode is another gas source that has to be accounted for. Oxidation of water at the anode gives rise to the production of oxygen gas bubbles as shown in Fig 7.6. These gas bubbles can also detach, rise, and rupture at the interface, forming droplets. However, the anode plate is usually placed away from the plasma attachment and this source is not dominant. At the plasma-liquid interface, many researchers also show that hydrogen can be generated through the reduction of protons by plasma electrons [18, 19, 20]. It is unknown whether the hydrogen gas could form gas bubbles at the surface since the solvated electrons can only exist under the interface around 12.3 nm [21]. A detailed measurement of the gas bubble's composition will need to be conducted in the future. In any case, bubbles are clearly present from two sources in our discharge.

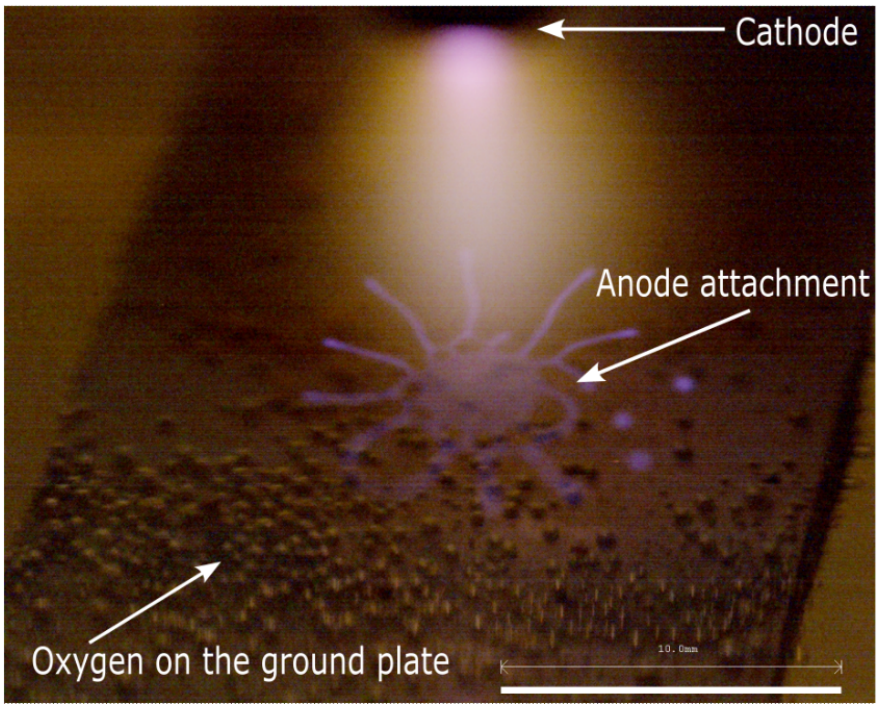

Figure 7.6: Gas bubbles due to electrolysis at the submerged anode (ground is a silicon plate)

When a gas bubble reaches a free liquid surface, its upper surface will protrude from the liquid-air interface, drain, and rupture due to the gravitational force [22]. The shattering of the cavity and capillarity forms a central jet which then breaks up into soaring droplets from the pinching-off process [23]. The radius of these droplets ranges from 2 to 500 μm and is related to the size of the bubble [24]. A similar phenomenon can be observed in diverse settings ranging from effervescent beer to the vast ocean surface. Research showed that the first droplet formed from end-pinching at the tip of the jet scales with the radius of the bubble [10]. A recent study further showed that this scaling law can be decoupled from the bubble radius by introducing the jet velocities as the function of the bubble radius [25]. The resulting expression is:

$$Bo_d = \frac{\rho g R_d^2}{\gamma} = 3.55(Fr_d We_d)^{-3/5} = 3.55(\frac{v^2}{gR_d}\frac{\rho v^2 R_d}{\gamma})^{-3/5} \tag{7.1}$$

where ρ, g, γ, R_d, v represent liquid density 977 $\mathrm{kg/m^3}$, gravitational constant, surface tension 64.4 mN/m, droplet radius, and jet velocity respectively; dimensionless parameters Bond number Bo_d (ratio of gravity to surface tension), Froude number Fr_d (ratio of fluid inertia to gravity), Weber number We_d (ratio of fluid inertia to surface tension) represent the ratio of different dynamic forces. Eq.7.1 can be simplified to:

$$R_d = \sqrt{3.55} v^{-1.2} \rho^{-0.2} \gamma^{0.8} \tag{7.2}$$

Fig 7.7 plots the experimental results and theoretical curve based on Eq.7.2 and most of the data fit within this scaling law within 30%. Thus the bursting droplets most likely come from a bubble rupture and water jet pinch-off. A schematic drawing is shown in Fig 7.8 to illustrate the sequence of bubble formation, rupture at the surface, water jet initiation, and pinch-off into droplets. The whole process is driven by released dissolved gas due to volumetric gas heating and electrolysis occurring at the anode charge transport. Although the consequent bubble rupture and droplet ejection are fluid dynamics phenomena that are not unique in this discharge configuration, it is indeed coupled with the plasma operation and the jet droplets serve as an additional transport process at the plasma-liquid interface. It works as a vehicle to carry the solute and solvent across the interface and it is practical to enhance its generation by controlling the rate of bubbles' formation in the plasma-activated electrolyte. Since the nature of the droplet mechanism is clear, it is then reasonable and justified to utilize external gas to increase the droplet ejection rate to help further investigation.

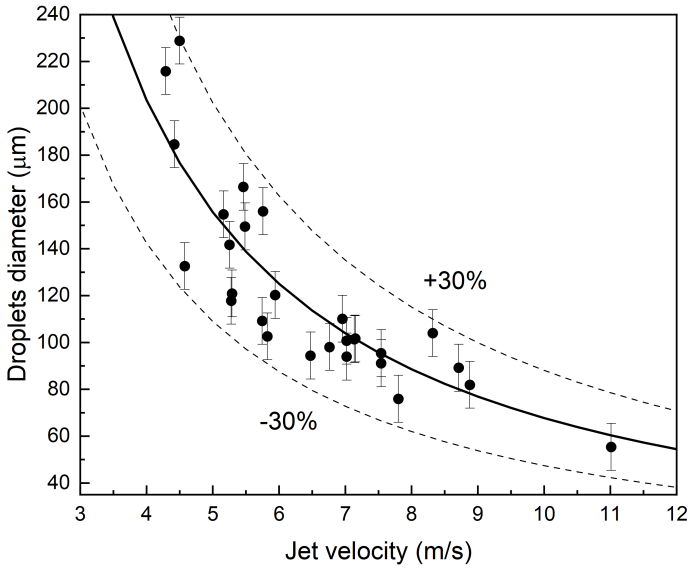

Figure 7.7: Jet droplets diameter vs. jet velocity. The solid curve represents the theoretical scaling law [25] and the dots with the error bar show the experiment results

As mentioned earlier, a given droplet will tend to evaporate and emit particles only if its speed or volume is small enough. This leads to the need to have fine bubbles (diameter < 100 μm) since the

droplet's diameter is highly dependent on the diameter of the bubble. Fig 7.8 shows fine droplet ejection and subsequent excitation of species contained within the droplet. These droplets were generated through bubble formation driven by gas injection through the air stone under the liquid anode. It also demonstrates a new method to enhance mass transport at the plasma-liquid interface.

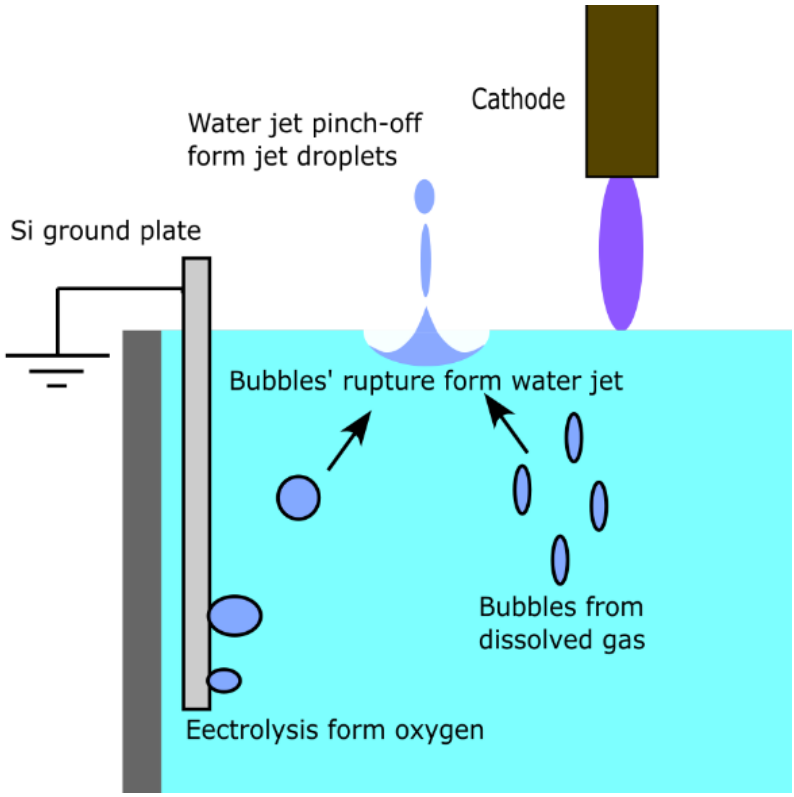

Figure 7.8: Schematic of droplet emission mechanism

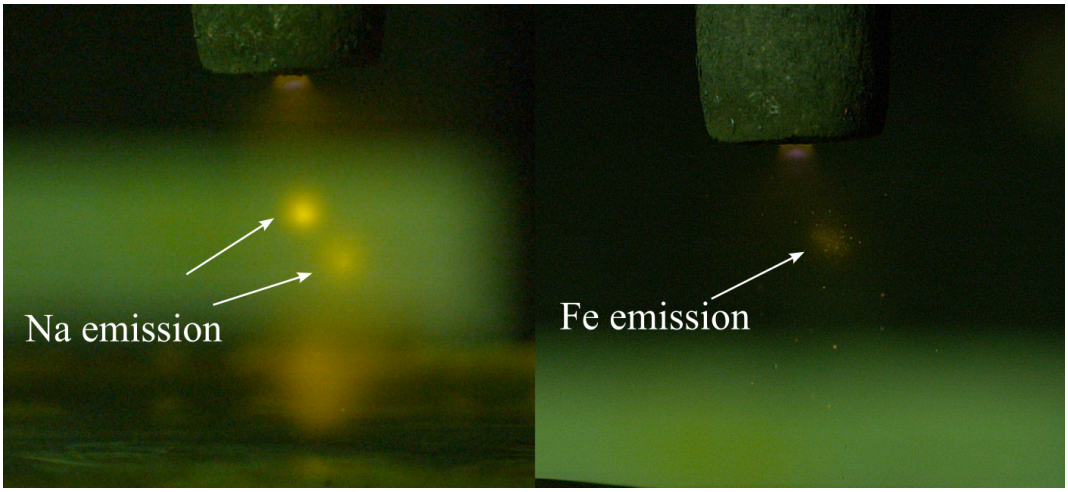

Figure 7.9: Evaporation of droplets and their subsequent optical emissions in the plasma. Note the differences in emission color. (Left: NaCl solution, right: $\mathrm{FeCl_3}$ solution)

7.5 Droplets Emission Species Analysis by Spectroscopy

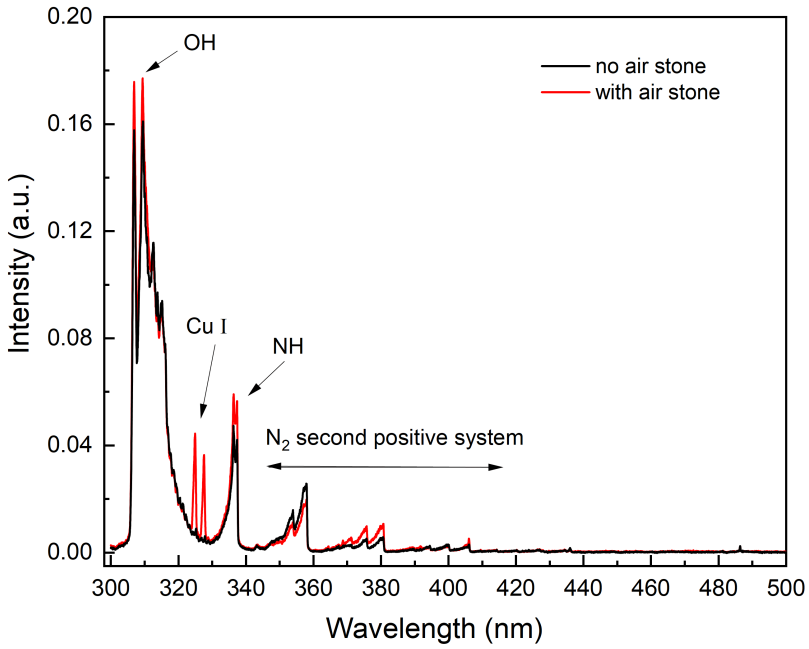

Figure 7.10: Optical emission spectra using a $CuSO_4$ liquid anode (Discharge current: 80 mA, Liquid anode $CuSO_4$ solution with initial conductivity: 15 mS/cm)

To study the composition of the droplets in a controlled manner, the air stone sparger was used to generate bubbles that burst at the interface thereby multiplying the droplet formation process. Some fraction of the generated droplets that pass through the plasma column will evaporate and cause intense optical emissions. The composition of the droplets is then inferred through optical emission spectroscopy. To distinguish the droplet emission from the plasma background emission, we compared the spectrum associated with the plasma at various discharge currents with and without droplet evaporation. Fig 7.10 shows the spectrum of DC discharge with a $CuSO_4$ liquid anode electrolyte. The most prominent change observed to occur with droplet emission is the appearance of Cu I (324.8 nm and 327.4 nm) emission lines. Similarly as observed with the sodium chloride solution, droplet emission gave rise to a 12-fold increase in emission intensity of the Na I over the baseline, unperturbed plasma as shown in Fig 7.11. A similar enhancement was also found in $FeCl_3$ solutions but the scale is much lower. These relative intensity differences in the observation with various salts can be attributed to variance in oscillator strength f_{ik} and upper energy level E_k magnitude. The emission from evaporation shows ejecting droplets in the gas phase is an efficient

way of adding salt ions, molecules, and nanoparticles from the liquid solution.

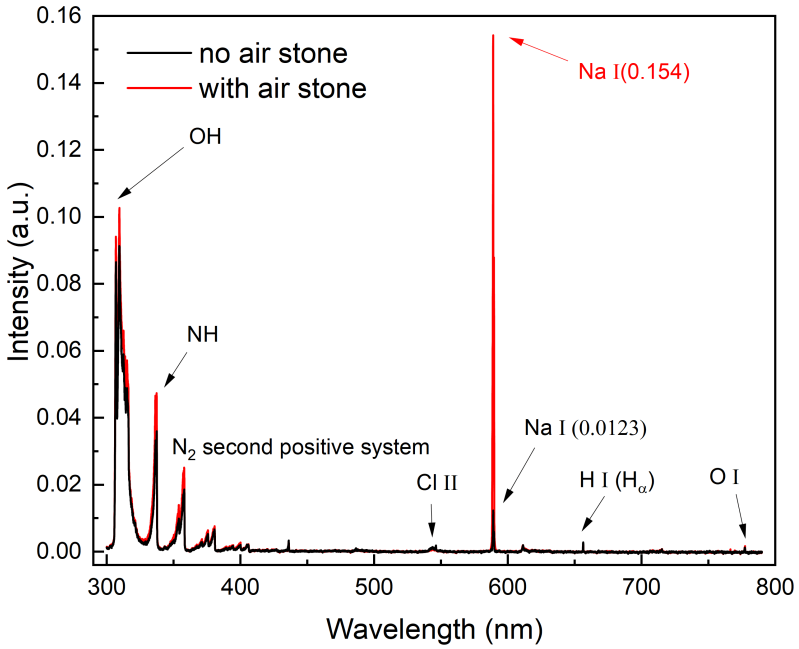

Figure 7.11: Optical emission spectra using a NaCl liquid anode (Discharge current: 50 mA, Liquid anode NaCl solution with initial conductivity: 14 mS/cm)

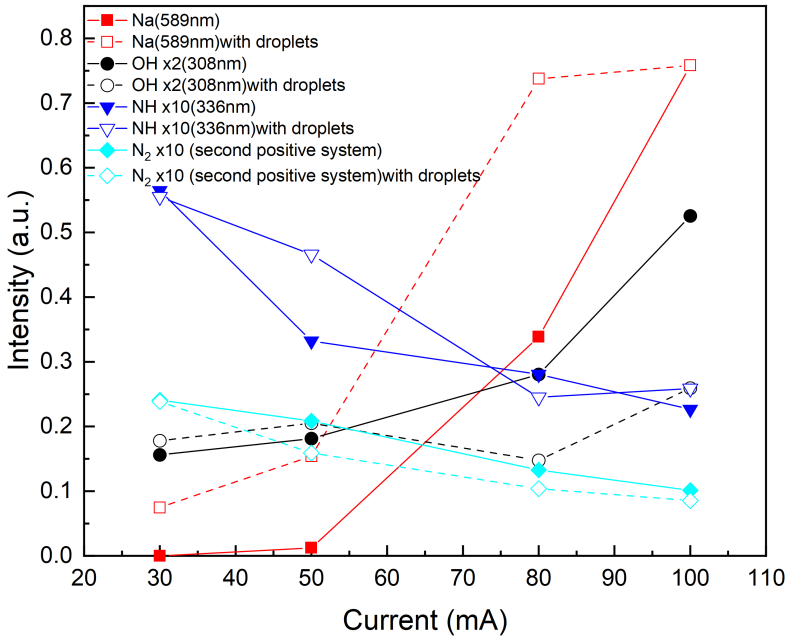

Figure 7.12: Excited species in plasma using a NaCl liquid anode (Liquid anode NaCl solution with initial conductivity: 14 mS/cm, some species' intensities are adjusted to fit the scale)

Fig 7.12 shows the relative excited species' emission intensities derived from a NaCl anode electrolyte. The hydroxyl radical species OH (307 nm and 309 nm) increases with current since the higher power provides a higher water evaporation rate and electron density. It should be pointed out that the additional droplet ejection tends to decrease the OH(A) emission at the high current. This reduction is possibly due to the electron temperature drop and a significant reduction in the OH(A) lifetime due to collisional quenching by water molecules [26]. Bruggeman *et al* [27] showed that the density of ground state OH(X) density can be proportional to the square root of water vapor concentration and its spatial profile is broader than the discharge region [28]. The emission of N_2 second positive system and the NH (336 nm) from the reaction between ambient nitrogen and water vapor show a downward trend due to a reduced air fraction in the plasma. Remarkably, the sodium (589 nm) is prominently enhanced by the additional droplets from the air stone. Such an effect is very significant at the low current where the sodium emission is extremely low due to the slow mass transport at the plasma-liquid interface. By mechanically ejecting droplets with various salts, the plasma excited species can be changed without adjusting the discharge properties. Another feature of droplet ejection is the time evolution of electrolyte emission as shown in Fig 7.13. The intensity fluctuations last for a millisecond, similar to the time gap between launch and

subsequent droplets burst according to the high-speed camera images. In comparison, the other strong emissions from species such as OH and NH feature a smaller magnitude (<11%) of change. We assume that each droplet burst can provide a pulsing dose of electrolyte into the gas phase and thus modify the natural concentration of such ions within plasma substantially. A more quantitative model of plasma chemistry is needed for further understanding of this result.

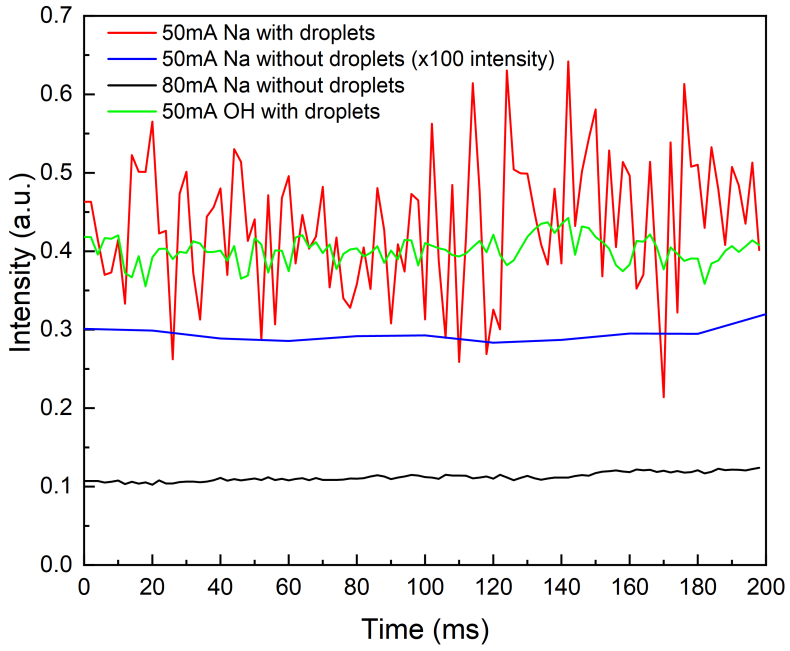

Figure 7.13: Emission line intensity as a function of time (Liquid anode: NaCl solution with initial conductivity: 14 mS/cm)

7.6 Influence of Droplets Evaporation on Plasma Properties

As discussed in the previous section, the transport of electrolyte species and other particles into the discharge should give rise to overall changes in discharge impedance, particularly at high droplet flux. Indeed, Fig 7.14 shows the modulation in the discharge current, discharge voltage, and discharge light emission (as inferred from a photodiode) with time. The time intervals among these peaks are in milliseconds which again coincides with the droplet ejection period. In the case of no droplets added, we also observe the minor magnitude change of the current-voltage waveform at $\sim$10 Hz and it is mainly from the small water level fluctuations due to the capillary wave motion near the plasma attachment. A photodiode that captures the time-resolved emission light intensity

indicates a pulsed signal that synchronizes the current-voltage waveform. If surface deformation is important, the voltage spike should happen before the photodiode signal change since the emission comes from evaporation which happens after the droplet ejection. This leads to the conclusion that those peaks are induced by gas-phase droplet evaporation and species interaction. For a weakly

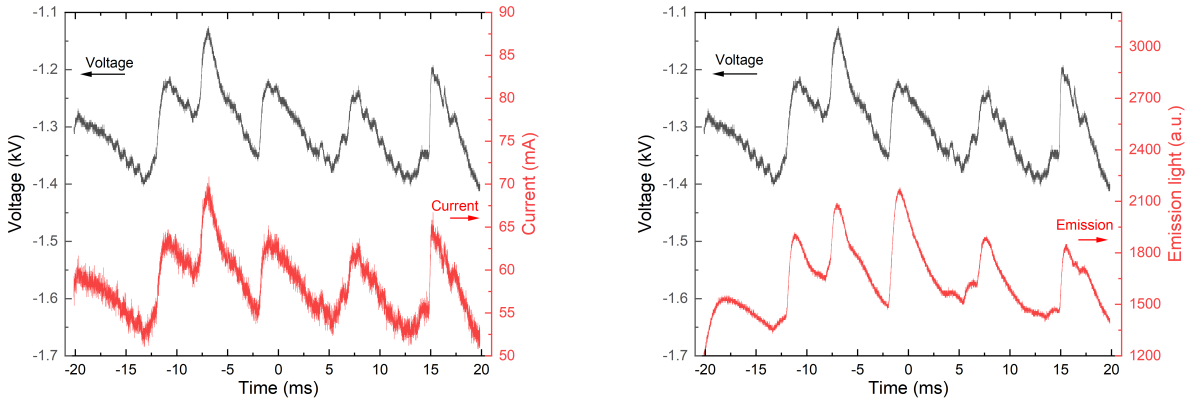

(a) Voltage and current signal

(b) Voltage and bulk emission intensity

Figure 7.14: Waveform of DC discharge with droplets burst at 50mA (Liquid anode: NaCl solution with initial conductivity: 14 mS/cm)

ionized and non-equilibrium plasma, its conductivity mostly depends on the electron mobility and density which is $\sigma = \frac{n_e e^2}{m\nu_{en}}$. A sudden increase in plasma conductivity means the electron density has risen, or a reduction in the neutral-electron collision frequency. To examine gas-phase plasma properties, we have also investigated changes in gas temperature and electron density by using emission spectroscopy following the method described in Section 5.3.2 and 5.3.3. Fig 7.15 shows the estimated rotational temperature of the plasma with and without droplet ejection. As the discharge current increases monotonically up to approximately 80 mA, above which there is a noticeable drop in temperature. The measured temperature behavior may be an indication that there is a competition between gas heating associated with dissipation in the discharge, which increases with the discharge current, and the rate of water evaporation, which also increases with the discharge current. At a fixed current, the additional water vapor from the vaporized droplets cools down the gas temperature in all cases. The data also suggest that the evaporation rate is comparable to the water introduced by droplets at the highest current.

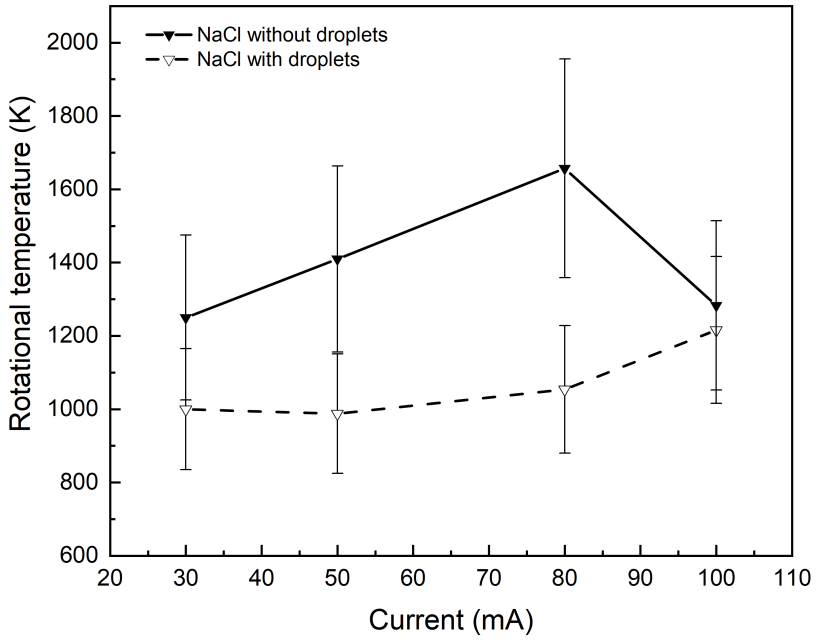

Figure 7.15: Rotational temperature at various conditions (Liquid anode NaCl solution initial conductivity: 14 mS/cm)

Next, the electron density is calculated from the Stark broadening of H_β (486.13 nm) Balmer transition. As Fig 7.16 shows the electron density increases monotonically with the discharge current. It is also found that with NaCl electrolyte droplets, the electron density increases suggesting that the low ionization potential sodium atoms derived from evaporating droplets are enhancing the plasma density and offsetting expected losses due to the increased water vapor density. Note that the spectrometer exposure time is relatively long during which multiple droplets have evaporated and released their emission. In that case, the density change may be transient and its sudden increase causes the plasma conductivity to change abruptly and gives the dynamics shown in Fig 7.14 electrical waveform.

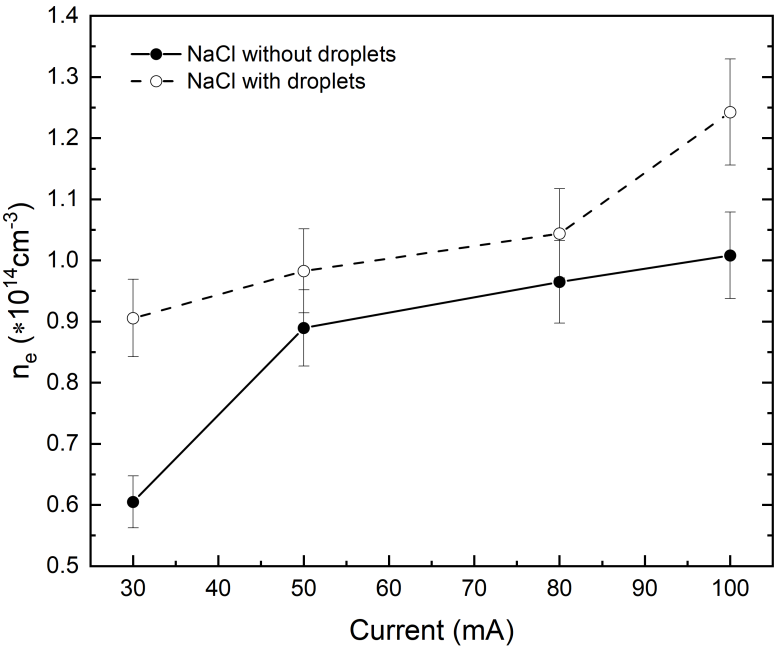

Figure 7.16: Electron density at various discharge conditions (Liquid anode NaCl solution initial conductivity: 14 mS/cm)

7.7 Summary

A new mass transport mechanism present in DC glows with liquid anodes—droplet emission is identified as jet droplets. Distinctive from the Taylor cone droplets generated in the liquid cathode, the droplets from the anodic electrolyte surface are produced by a liquid jet that originates from the gas bubbles' rupture at the plasma-liquid interface. It is not inherently a plasma process but the driving forces are provided by the discharge. Specifically, the electrolytic processes at the submerged electrode and gas heating give rise to the evolution of gas bubbles formed in the liquid solution. The scaling of the liquid jet speed with droplet diameters was found to be consistent with the jet droplet mechanism. Near the plasma column, the jet droplets vaporize and emit intense UV and visible light. To study the transfer process in a more controlled fashion, it was found that an air sparger could be used to artificially introduce fine bubbles into the liquid which subsequently formed droplets due to rupture in accordance with the jet droplets mechanism. Optical spectroscopy confirmed that these emissions are from salt particles in the electrolyte and excited OH radicals from the water molecule dissociation. From the current-voltage waveforms,

the ejected droplets and the associated salt particles were found to decrease the plasma resistance in a pulsing, intermittent fashion associated with the evaporation and subsequent disruption of a discrete number of bubbles at different times. Further analysis of the emission spectra revealed that the released sodium particles from the NaCl liquid anode can increase the electron density due to its low ionization potential. Overall, these findings substantiate a new approach to the mass transfer from the liquid and control of discharge maintenance by dispersing plasma-activated liquid into the gas phase and chemically and ionically enriching the plasma-liquid interaction.

References

[1] Zimu Yang, Yao Kovach, Zhehui Wang, and John Foster. On the nature of droplet production in dc glows with a liquid anode: mechanisms and potential applications. *Plasma Sources Science and Technology*, 31(11):115008, 2022.

[2] BR Locke, M Sato, P Sunka, MR Hoffmann, and J-S Chang. Electrohydraulic discharge and nonthermal plasma for water treatment. *Industrial & engineering chemistry research*, 45(3):882–905, 2006.

[3] Augusto Stancampiano, Tommaso Gallingani, Matteo Gherardi, Zdenko Machala, Paul Maguire, Vittorio Colombo, Jean-Michel Pouvesle, and Eric Robert. Plasma and aerosols: Challenges, opportunities and perspectives. *Applied Sciences*, 9(18):3861, 2019.

[4] Koichi Sasaki, Hiroaki Ishigame, and Shusuke Nishiyama. Density distributions of oh, na, water vapor, and water mist in atmospheric-pressure dc helium glow plasmas in contact with nacl solution. *The European Physical Journal Applied Physics*, 71(2):20807, 2015.

[5] Naoki Shirai, Goju Suga, and Koichi Sasaki. Mechanism of droplet generation and optical emission of metal atoms in atmospheric-pressure dc glow discharge employing liquid cathode. *Plasma Sources Science and Technology*, 29(2):025007, 2020.

[6] Peter Bruggeman, Jingjing Liu, Joris Degroote, Michael G Kong, Jan Vierendeels, and Christophe Leys. Dc excited glow discharges in atmospheric pressure air in pin-to-water electrode systems. *Journal of Physics D: Applied Physics*, 41(21):215201, 2008.

[7] Denise E Moon and Michael R Webb. Imaging studies of emission and laser scattering from a solution-cathode glow discharge. *Journal of Analytical Atomic Spectrometry*, 35(9):1859–1867, 2020.

[8] Yao E Kovach, Zhehui Wang, and John E Foster. Particle emission with identification from an atmospheric pressure plasma liquid interface. *Applied Physics Letters*, 119(13), 2021.

[9] Roger CK Law, Joseph HK Lai, David John Edwards, and Huiying Hou. Covid-19: Research directions for non-clinical aerosol-generating facilities in the built environment. *Buildings*, 11(7):282, 2021.

[10] Donald E Spiel. The number and size of jet drops produced by air bubbles bursting on a fresh water surface. *Journal of Geophysical Research: Oceans*, 99(C5):10289–10296, 1994.

[11] Luc Deike. Mass transfer at the ocean–atmosphere interface: the role of wave breaking, droplets, and bubbles. *Annual Review of Fluid Mechanics*, 54:191–224, 2022.

[12] Y Shi, G Miloshevsky, and A Hassanein. Boiling induced macroscopic erosion of plasma facing components in fusion devices. *Fusion engineering and design*, 86(2-3):155–162, 2011.

[13] Qiang Chen, Junshuai Li, and Yongfeng Li. A review of plasma–liquid interactions for nanomaterial synthesis. *Journal of Physics D: Applied Physics*, 48(42):424005, 2015.

[14] John E Foster, Yao E Kovach, Janis Lai, and Maria C Garcia. Self-organization in 1 atm dc glows with liquid anodes: Current understanding and potential applications. *Plasma Sources Science and Technology*, 29(3):034004, 2020.

[15] Douglas Brown, Wolfgang Christian, and Robert M Hanson. *Tracker: Video analysis and modelling tool*. Tracker, 2022.

[16] Alfonso A Castrejón-Pita, JR Castrejón-Pita, and IM Hutchings. Breakup of liquid filaments. *Physical review letters*, 108(7):074506, 2012.

[17] JT Holgate, M Coppins, and JE Allen. Electrohydrodynamic stability of a plasma-liquid interface. *Applied Physics Letters*, 112(2), 2018.

[18] Paul Rumbach, Megan Witzke, R Mohan Sankaran, and David B Go. Decoupling interfacial reactions between plasmas and liquids: Charge transfer vs plasma neutral reactions. *Journal of the American Chemical Society*, 135(44):16264–16267, 2013.

[19] A Hickling. Electrochemical processes in glow discharge at the gas-solution interface. In *Modern Aspects of Electrochemistry No. 6*, pages 329–373. Springer, 1971.

[20] Megan Witzke, Paul Rumbach, David B Go, and R Mohan Sankaran. Evidence for the electrolysis of water by atmospheric-pressure plasmas formed at the surface of aqueous solutions. *Journal of Physics D: Applied Physics*, 45(44):442001, 2012.

[21] Paul Rumbach, David M Bartels, R Mohan Sankaran, and David B Go. The solvation of electrons by an atmospheric-pressure plasma. *Nature communications*, 6(1):7248, 2015.

[22] Donald E Spiel. On the births of film drops from bubbles bursting on seawater surfaces. *Journal of Geophysical Research: Oceans*, 103(C11):24907–24918, 1998.

[23] Ferren MacIntyre. Flow patterns in breaking bubbles. *Journal of Geophysical Research*, 77(27):5211–5228, 1972.

[24] CF Kientzler, Arnold B Arons, Duncan C Blanchard, and AHhttps Woodcock. Photographic investigation of the projection of droplets by bubbles bursting at a water surface. *Tellus*, 6(1):1–7, 1954.

[25] Elisabeth Ghabache and Thomas Séon. Size of the top jet drop produced by bubble bursting. *Physical Review Fluids*, 1(5):051901, 2016.

[26] A Yu Nikiforov, Abdollah Sarani, and Ch Leys. The influence of water vapor content on electrical and spectral properties of an atmospheric pressure plasma jet. *Plasma Sources Science and Technology*, 20(1):015014, 2011.

[27] Peter Bruggeman, Gilles Cunge, and Nader Sadeghi. Absolute oh density measurements by broadband uv absorption in diffuse atmospheric-pressure he–h2o rf glow discharges. *Plasma Sources Science and Technology*, 21(3):035019, 2012.

[28] Qing Xiong, Zhiqiang Yang, and Peter J Bruggeman. Absolute oh density measurements in an atmospheric pressure dc glow discharge in air with water electrode by broadband uv absorption spectroscopy. *Journal of Physics D: Applied Physics*, 48(42):424008, 2015.

CHAPTER 8

Conclusion

8.1 Summary of Critical Findings and Conclusions

Among the various complex processes in plasma-liquid interactions, the appearance of self-organized patterns on the liquid anode surface of an atmospheric pressure DC glow discharge is indeed among the most fascinating and mysterious. Due to the miniature length scale and nonlinear nature, the direct diagnostics on a SOP is challenging and leaves us with a poor understanding of its formation mechanism. This dissertation focuses on the investigation of the coupling processes in an atmospheric pressure DC glow discharge with a liquid anode that impacts pattern formation. The processes involved include kinetic phenomena, induced volumetric gas heating, electrohydrodynamics, heat transfer, mass transport at the periphery and liquid, gas phase, and liquid phase convection. Insight gleaned from understanding the couplings between the dynamics of SOP and the aforementioned processes can enable us to understand the pattern mechanism indirectly.

As the root of a SOP, the physics of an atmospheric pressure glow discharge with liquid anode was explored by observing sensitivity to operating conditions. In the gas phase, pattern response to discharge gap size, discharge current, working gas flow rate, cathode orifice diameter, and the oxygen fraction in the ambient gas are explored. It was found that a smaller discharge gap, lower current (power), higher helium gas flow rate, and smaller cathode orifice would reduce the plasma column diameter and increase the current density. Schlieren imaging revealed that the entrainment rate is heavily affected by these conditions which constitute the thermal dynamics and convection boundary by the gas heating. The volumetric gas heating is strongly coupled with the nitrogen fraction and its entertainment rate, and the morphology of plasma is thus coupled with the thermal dynamics and chemical reactions of reactive species since a stronger heating rate requires a larger heat transfer flux and thus a larger surface area is needed. The extra heating causes gas expansion and affects the plasma impedance and current density at the liquid anode. The coupling between the SOP and gas phase conditions is based on the oxygen concentration. Those gas phase conditions limiting gas heating would also subdue the establishment or development on the SOP. More

importantly, it was found that the pattern requires at least 7% oxygen in the gas phase to form. In principle, the other gas phase conditions affect the pattern mechanics by altering the oxygen entrainment rate into the plasma column. In regards to the shape of SOP, a higher entrainment rate of ambient air would support a dispersive pattern with a more complex configuration while the nitrogen constitutes the gas heating rate and affects the dynamic motion of a pattern.

In the liquid phase, the conductivity of the liquid can affect the current density by changing the space charge accumulation at the plasma-liquid interface and the anode voltage. A low conductivity anodic solutions tend to favor the expanding of space charge and a larger, diffusive pattern whereas a high conductivity prompts a more stable and cohesive shape. High liquid anode temperature were found to give rise to patterns that are usually observed at high helium flow rates, possibly suggesting that the vapor concentration is affecting the plasma properties. Overall, SOP is more sensitive to the gas phase where the air fraction was found to affect the thermal dynamics and the anode size. The pattern complexity is also related to the gas dynamics and oxygen concentration. A more detailed mechanism for SOP would require a comprehensive kinetic model to self-consistently predict the local plasma parameters under the influence of various conditions in essentially an open system.

The role of oxygen in SOP was further investigated to test a hypothesis that suggested that the formation of oxygen negative ions modifies the space charge distribution and transport near the liquid anode leading to an instability that may give rise to the SOP [1, 2]. Laser photodetachment was used to determine the effect of negative ion concentration on discharge SOP. Here a laser was used to deplete the negative ions concentration and thereby allow one to assess the response of the pattern. A prominent current increase can be detected when negative ions are destroyed via photodetachment. The change of detachment ratio with laser energy density follows the Beer-Lambert law and can be used to estimate the effective detachment cross-section. The experiment suggested that the O_2^- ion is the dominant species in this discharge type. Using the discharge current perturbed to nominal ratio and the detachment ratio one can then estimate the negative ion density, which was found to be $\sim 10^{12}\mathrm{cm}^{-3}$. An examination of the SOP dynamics imaged with an ICCD camera revealed no change during photodetachment. This data suggests that the SOP is not sensitive to detachment of negative ion fraction up to 62 %. While these experiments suggest insensitivity to negative ion concentration, the current experiment cannot fully rule out the potential role of negative ions in SOP unless the photodetachment is performed thoroughly at a larger energy and length scale.

A spatially resolved optical emission spectroscopy study was also performed on the plasma to acquire the change in plasma properties at different locations along the plasma column. This was achieved by focusing the plasma emission through lenses and onto the imaging spectrometer. A dove prism was used to rotate the plasma image and enable the acquisition of the radial profile of

emission. Gas temperature and electron density were estimated from the rotational temperature of nitrogen second positive system and Stark broadening of H_β line, respectively. Major species emission profile was mapped and found to be concentrated in the cathode and anode regions. Their emission intensity and distribution are strongly dependent on the production mechanism. A steep temperature gradient near the liquid anode was found in the temperature distribution which shows the importance of cooling from liquid anode. The corresponding change from various operating conditions in temperature profiles showed that the SOP is more sensitive to the gas phase heating than the variation of liquid conditions. A thicker low-temperature region near the liquid anode was found to coexist with the establishment of a dispersive pattern. In addition, a lower anode temperature (800 K) is desirable to the complex and more developed SOP. The radial distribution of gas temperature at different axial positions indicates that the helium cooling effect is also limited in the radial dimension. The radial profile of electron density decreases dramatically at 200 μm and has a profound coupling with species whose production is heavily dependent on the energetic electrons. Overall, the temperature profile estimated from a spatially resolved OES is stable and robust if the radiative lifetime is long enough for thermalization. On the other hand, electron density calculated from Stark broadening requires a high signal-to-noise ratio and electron density threshold for an accurate result.

The coupling between the plasma and liquid phase motion was examined with the help of particle imaging velocimetry. In the plane normal to the plasma-liquid interface, the induced flow field consists of a strong ascending flow in the center at a maximum speed of 1.5 cm/s and a circle of vortices nearby. Such fluid motion is ascribed to the mass transport at the liquid surface driven by the evaporation. This conjecture was validated in an analogous experiment using a butane torch which qualitatively reproduced a similar flow. In addition, the formation of the pattern gave rise to flow structures that were non-static including periodic vortex/eddy shedding. In the plane parallel to the plasma-liquid interface, the flow field exhibited the transverse component of vertical plane flow. In the presence of self-organization, a single strong swirl flow was observed under the plasma attachment and shared a similar directional preference with the pattern motion. A cold helium plasma jet experiment with liquid ground stimulated a similar swirl flow at the horizontal plane suggesting that the driving mechanism could be the electrohydrodynamics force though a descending flow was also observed at the normal plane. The magnitude of the flow velocity averaged over time and the field of view area suggests that flow speed is linear with increasing input power and increasing liquid electrical conductivity. Overall, the investigation indicates that flow field morphology is configured by evaporation and the discharge attachment would redistribute the heat flux which induces complex fluid motion.

Lastly, a non-trivial mass transport mechanism at the plasma-liquid interface was reported and investigated. From the high-speed images, the sparking emission was identified as the burst of

droplets carrying salt ions from the liquid phase into the plasma column. Distinctive from the Taylor cone droplets generated with liquid cathode configuration [3], the droplets from the anodic electrolyte surface are produced by a liquid jet that originates from the gas bubbles' rupture at the plasma-liquid interface. It is not inherently a plasma process but the driving forces are provided by the discharge. Specifically, the electrolytic processes at the submerged electrode, the production of gaseous products, and gas heating give rise to the evolution of gas bubbles formed in the liquid solution. The scaling of the liquid jet speed with droplet diameters was found to be consistent with the jet droplet mechanism [4]. Near the plasma column, the jet droplets vaporize and emit intense UV and visible light. This mechanism can be exploited by using an air sparger which artificially introduces fine bubbles into the liquid and subsequently forms droplets. OES confirmed that emissions upon the bursting droplets in the plasma column are from salt particles in the electrolyte and excited OH radicals from the water molecule dissociation. From the current-voltage waveforms, the ejected droplets and the associated salt particles were found to decrease the plasma impedance in a pulsing, intermittent fashion associated with the evaporation and subsequent disruption of a discrete number of bubbles at different times. Further analysis of the emission spectra revealed that the released sodium particles from the NaCl liquid anode can increase the electron density due to its low ionization potential. Overall, these findings substantiate an important mechanism of mass transfer from the liquid and control of discharge maintenance by dispersing plasma-activated liquid into the gas phase and chemically and ionically enriching the plasma-liquid interaction.

8.2 Future Work

Due to the limited time and resources, this work cannot fully examine all the aspects of the glow discharge at atmospheric pressure and its coupling processes. Key areas of research suggested by this work include:

1) *Operation conditions impact*

Some operation conditions are intriguing and can have a significant impact on the SOP yet have not been explored. A coarse vacuum (1-760 Torr) would indeed greatly affect the kinetic processes and the gas heating. Does the pressure affect the threshold of pattern formation in the case of current, oxygen percentage? The gas heating mechanics can also be explored solely by applying an external cooling mechanism. When supplying a cryogenic feed gas, the plasma temperature could be cold enough that requires no evaporation for cooling and thus should affect the pattern formation. Alternatively, purging the box with helium can greatly reduce the fraction of nitrogen and suppress the gas heating. Observing the pattern under 80% helium and 20% oxygen can be instrumental in the investigation of pattern physics.

2) *Negative ions effect*

As Chapter 4 pointed out, the laser photodetachment does not fully break all negative ions in the plasma. The concentration of negative ions may be higher at the periphery of plasma due to runaway electrons. In any case, the laser photodetachment shall be performed more thoroughly in energy and spatial dimensions. An unfocused and powerful laser beam is required for this purpose. On the other hand, using sulfur hexafluoride (SF_6), a stronger electronegative gas (EA = 1 eV) of high attachment rate [5], mixed with helium in working gas would inflict more negative ions and enhance its impact on the plasma physics.

3) *Electric field measurements*

It is rather difficult to measure the electric field at the liquid surface of an atmospheric pressure plasma. The non-invasive method such as using the intensity ratio of nitrogen emission is not suitable for a nonequilibrium plasma [6]. Instead, laser diagnostics such as coherent anti-Stokes Raman scattering (CARS) [7] and electric-field-induced second-harmonic generation (E-FISH) [8] are generally more applicable. A good measurement of the profile of the electric field near the anode would be desired. If a double sheath exists, then the pattern spots are indeed miniature "anode" spots. This measurement combined with the variation of operating conditions can also reveal the threshold of the electric field for pattern formation.

4) *Capillary wave at liquid surface*

It has been reported that capillary waves arising from the electrostatic Maxwell pressure on the plasma-liquid interface can establish a particular oscillating mode of pattern [9]. The capillary wave is also correlated with the gas phase convection where an impinging jet induces the oscillation and wave propagation. Using a modulated speaker can initiate a similar capillary wave and its impact on the pattern dynamics can be investigated.

References

[1] Naoki Shirai, Satoshi Uchida, and Fumiyoshi Tochikubo. Influence of oxygen gas on characteristics of self-organized luminous pattern formation observed in an atmospheric dc glow discharge using a liquid electrode. *Plasma Sources Science and Technology*, 23(5):054010, 2014.

[2] Shiqiang Zhang and Thierry Dufour. Self-organized patterns by a dc pin liquid anode discharge in ambient air: Effect of liquid types on formation. *Physics of Plasmas*, 25(7), 2018.

[3] Naoki Shirai, Goju Suga, and Koichi Sasaki. Mechanism of droplet generation and optical emission of metal atoms in atmospheric-pressure dc glow discharge employing liquid cathode. *Plasma Sources Science and Technology*, 29(2):025007, 2020.

[4] CF Kientzler, Arnold B Arons, Duncan C Blanchard, and AHhttps Woodcock. Photographic investigation of the projection of droplets by bubbles bursting at a water surface. *Tellus*, 6(1):1–7, 1954.

[5] D Smith, NG Adams, and E Alge. Attachment coefficients for the reactions of electrons with ccl4, ccl3f, ccl2f2, chcl3, cl2 and sf6 determined between 200 and 600 k using the falp technique. *Journal of Physics B: Atomic and Molecular Physics*, 17(3):461, 1984.

[6] P Paris, M Aints, F Valk, T Plank, A Haljaste, KV Kozlov, and HE Wagner. Intensity ratio of spectral bands of nitrogen as a measure of electric field strength in plasmas. *Journal of Physics D: Applied Physics*, 38(21):3894, 2005.

[7] Tsuyohito Ito, Kazunobu Kobayashi, Sarah Mueller, Dirk Luggenhölscher, Uwe Czarnetzki, and Satoshi Hamaguchi. Electric field measurement in an atmospheric or higher pressure gas by coherent raman scattering of nitrogen. *Journal of Physics D: Applied Physics*, 42(9):092003, 2009.

[8] Sai Raskar, Keegan Orr, Igor V Adamovich, Tat Loon Chng, and SM Starikovskaia. Spatially enhanced electric field induced second harmonic (seefish) generation for measurements of

electric field distributions in high-pressure plasmas. *Plasma Sources Science and Technology*, 31(8):085002, 2022.

[9] Jinyu Yang, Oles Dubrovski, Paul Rumbach, Felipe Veloso, Hsueh-Chia Chang, and David Go. A transport-limited theory for the coalescence/de-coalescence plasma patterns on a plasma-liquid interface. *Bulletin of the American Physical Society*, 2023.